Electron crystallography of nanodomains in functional materials

Sara Passuti

Normandie Université

UNIVERSITÉ CAEN NORMANDIE

THÈSE

Pour obtenir le diplôme de doctorat

Spécialité **CHIMIE**

Préparée au sein de l'**Université de Caen Normandie**

Electron crystallography of nanodomains in functional materials

Présentée et soutenue par

SARA PASSUTI

Thèse soutenue le 30/10/2024

devant le jury composé de :

M. PHILIPPE BOULLAY	Directeur de recherche au CNRS - ENSICAEN	Directeur de thèse
M. EMMANUEL GUILMEAU	Directeur de recherche au CNRS - ENSICAEN	Président du jury
M. ADRIAN DAVID	Maître de conférences - Université de Caen Normandie (UCN)	Membre du jury
M. MAURO GEMMI	Professeur - Istituto Italiano di Tecnologia	Membre du jury
MME REGINA CIANCIO	Professeur - AREA Science Park	Rapporteur du jury
MME MURIEL VÉRON	Professeur des universités - PHELMA GRENOBLE	Rapporteur du jury

Thèse dirigée par **PHILIPPE BOULLAY** (Laboratoire de cristallographie et sciences des materiaux (Caen))

ED 591 PSIME

RISMA

Acknowledgements

I surely would like to start by thanking the entire NanED group, firstly Prof. Mauro Gemmi, as well as all the supervisors for building up a network for us students to grow together and create connections in the field of Electron Microscopy. Thanks to TESCAN as well for hosting me in their team and for giving me the opportunity to explore new avenues. I would like to thank all the NanED ESR which walked this path with me for sharing their work, ideas and issues, and for creating a collaborating environment that made facing my own obstacles easier. In particular, thanks to ESR 9, a.k.a. Marco Santucci, without whom I probably would not be where I am today, and ESR 13, a.k.a. Erica Cordero Oyonarte, for sharing every step of this journey and for the mutual support.

Thanks to CRISMAT staff, from researchers to PhD students for the support and help, first of all Dr. Philippe Boullay for the supervision during these years and for the effort in giving me the best possible inputs for advancing my work. I would like to thank the committee for the availability, whose feedback will be precious for my growth. I will certainly take their advice to heart and use it to improve.

Thank you to all my old friends, who always made me feel so close to them even if physically I was far. And of course, thanks to all the friends I made through the PhD, both in Caen and across Europe, which are now like family to me. The path we chose will

take us (and for many, it already has) in different parts of the world, but I am so grateful for having had the opportunity to know all of you, and hope we will keep meeting halfway, because I am surely not done with my souvenir posters. I would also like to thank a person that jumped on board at the last moment completely unexpected, because I'm so grateful he decided to stay. Donc Alain, merci pour tout. Pour chaque jour où tu voudras rester, je serai un Pitou heureux.

Lastly, I would like to thank my family, so I will do it in italian. Grazie di cuore a mamma e papà, Lia, Luca, Daniele e Alessandro, Simonetta, Stefano, Elena e Matteo, e tutti i nonni, Gisella, Giancarlo, Carmen e Vanni, per aver avermi sostenuta in questo viaggio impegnativo, per essere sempre fieri di me anche quando io non lo sono, ed aver reso ogni mio giorno di ritorno in Italia un momento di festa.

Table of Contents

Introduction

Electron diffraction for structural crystallography has grown considerably after the development of dedicated protocols for data acquisition and analysis, to the point where it was listed in Science magazine as one of the major scientific breakthroughs of the year 2018 [1]. The so-called 3D Electron Diffraction (3D ED) is a novel method for atomic structure determination of inorganic, organic and macromolecular compounds when their crystal size falls in the scale of few tens of nanometer or even below. In many cases, compounds of high commercial value or with medical applications, are in fact available only as nanocrystals or show phase/polymorphic transitions during crystal growth. 3D ED is an extraordinary new tool to disclose the nature of all these nanocrystalline materials, shedding new light and bringing new knowledge into different scientific fields, from materials science to physics of diffraction, from instrument engineering to chemical production and pharmacology.

Up to now, the development of 3D ED has remained limited to a few laboratories and has been slowed by the lack of young researchers trained in this field at PhD level. To address this issue, several European scientists active in the field and a group of small and large companies have decided to join forces (Panel 1). This took shape within the framework of the Marie Skłodowska-Curie European Innovative Training

Networks (ITN), where the Electron Nanocrystallography (NanED) project has been selected under the grant agreement N°956099.

As a training program, NanED aims to form a new generation of electron crystallographers, able to master and develop 3D ED techniques in an interdisciplinary and interconnected network. An intensive program was planned, with participation in several schools and periods of secondment to academic and industrial partners (see list in Appendix A), for a total of about 6 months of activities. As a research program, NanED aims to boost the dissemination of 3D ED in academic and industrial laboratories with two main objectives:

1. Develop 3D ED to make it more efficient and accessible by establishing optimized and portable strategies for sample preparation, data collection and analysis

2. Apply 3D ED to different types of compounds and materials, from cement to macromolecules.

These objectives are reflected in 4 scientific work packages and involve 14 PhD students in 7 academic centers. Each PhD student is assigned an "early stage re-

search" (ESR) project. The work presented in this manuscript is part of the work package 4 (WP4) entitled "Crystallography beyond nanocrystals" and concerns the ESR 12 *electron crystallography of nanodomains in functional materials* (Panel 2). WP4 aims to expand the applicability of 3D ED to complex nanomaterials and define a "Road Map to Nano".

Panel 2. The scientific part of the NanED project is divided into 4 work packages. The work carried out as part of this thesis falls within work package number 4.

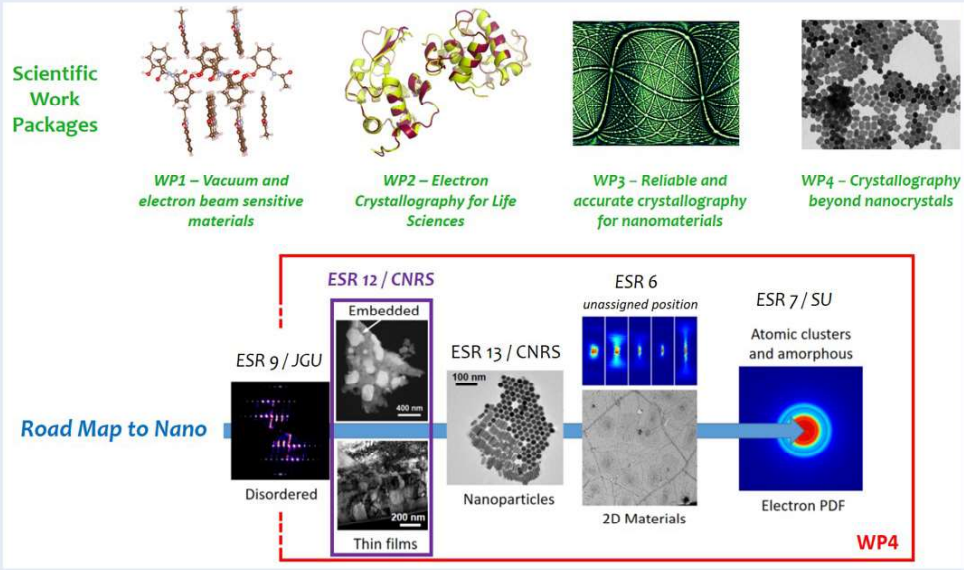

Nanoparticles and nanostructured materials in general are nowadays produced by large-scale industry and are spread in our daily life due to a large variety of uses as functional materials: high mechanical quality materials, absorbents, smart glasses, battery electrodes, cosmetics, food additives or health care. In this work, we will determine the ultimate spatial resolution of 3D ED and its potential for the investigation of functional materials synthesized in form of dense ceramics or deposited in the form of thin films. For the latter, the epitaxial growth of a thin film also introduces additional stresses by being clamped onto a thick crystalline substrate, giving rise to what is known as "strain engineering" [2]. The possibility to have a single crystal data collection on strained nanocrystals would open the prospective

of mapping the structure modifications and distortions due to the film/substrate interaction.

After introducing these types of functional materials and the techniques which are commonly used to characterize their crystal structure (Chapter 1), some reminders of the experimental and theoretical prerequisites needed to understand this work will be given. Then, an initial study will present some examples of state-of-the-art 3D ED experiments applied to nanostructured materials (Chapter 2). We will then consider a different approach to 3D ED data collection, moving from a single pre-defined area to the simultaneous analysis of multiple Regions of Interest (ROI), to which we will refer as SPET (Scanning Precession Electron Tomography) (Chapter 3). In this protocol, we will combine 3D ED with a scanning procedure of the electron beam on the sample, enabling this way an accurate analysis of different ROIs with from a single SPET acquisition. After discussing the advantages of this new approach and its requirements in terms of data analysis, we will apply it to thin films (Chapter 4) and ceramic materials prepared as TEM lamellae (Chapter 5). In the first case, our primary focus will be on analyzing the sample along its thickness (line scan) to accurately evaluate the evolution of its crystal structure.In the second, we will perform the analysis on a 2D area of the sample (area scan) to characterize the nano-sized domains being investigated. Where applicable, different approaches for data processing will be compared in order to determine which one leads to the best results. Finally, we will review the challenges SPET poses in terms of data processing, highlighting unresolved issues and proposing suggestions for further development of the technique.

CHAPTER 1

Nanosized domains in functional materials

1.1 Introduction to nanosized materials

The term "nanosized materials" refers to the class of materials where at least one controllable dimension extends for less than a hundred nm, or having internal structure or surface structure in the nanoscale. The ability to control the size of this class of materials is fundamental to tune their physical properties for obtaining the desired performances [3]. These materials can be classified according to the dimensions affected by the size limit, going from nanoparticles to one-dimensional, two-dimensional and bulk nanostructured materials.

Nanoparticles, in which the size limit applies to all the directions, hold a significant interest for a wide range of applications due to their unique features, including size-dependent properties (for optics and electronics), high surface area and enhanced reactivity (for catalysis), improved mechanical and thermal properties (for lubricants and composites), targeted drug delivery (for healthcare), energy conversion and storage (for cells and batteries) or environmental benefits (for purification

from toxic materials) [4]. 1D-nanostructures, such as nanotubes, nanowires, and nanofibers, showed remarkable light capture, electron and ion transmission and mass diffusion properties, making them suitable for fields of application such as energy storage and conversion, electrocatalysis, photocatalysis, nano-optoelectronic devices, sensing and biomedicine [5]. 2D-nanomaterials, including transition metal dichalcogenides, and complex oxides thin films, thanks to their high surface area, represent ideal candidates for applications in catalysis and super-capacitors [6]. Of particular interest for this work, complex oxides thin films constitute a layer, usually of tens of nm in thickness, which is deposited on a bulk substrate. Bulk materials can also be characterize by nano-sized crystalline regions, to which we will refer in this work as nanodomains. They may have a different crystal structure or orientation compared to the surrounding crystalline regions. These nanodomains will be typically found for materials science in ceramics, minerals or thin films, and their features strongly affect their properties in various functional materials (piezoelectrics, ferroelectrics, multiferroics, etc... [7, 8]).

Being able to accurately characterize the crystal structure of the nanodomains in these materials and understand how it is linked to their physical properties is therefore crucial for being able to tune their features for the desired applications. In this thesis, a new approach for the crystal structure characterization of nanodomains in functional materials is proposed and tested specifically on epitaxial thin films and ceramic materials. We will therefore have an introduction to these classes of materials before moving to the techniques that can be used for their characterization.

1.1.1 Epitaxial thin films

As previously introduced, thin films are constituted by a layer of (usually) tens of nm in thickness which is deposited on a bulk substrate. Epitaxial thin films can be obtained in several ways (MBE, PLD, MOCVD, sputtering, ...). Concerning the samples here presented, they are deposited by PLD (Pulsed Laser Deposition): in a vacuum chamber, a high-power pulsed laser impinges on the rotating target, which

consists of the material intended for deposition. In here, the material is vaporized due to the high temperature in a process known as ablation. The vaporized material forms a plasma plume, and then condenses on the nearby substrate forming a film.

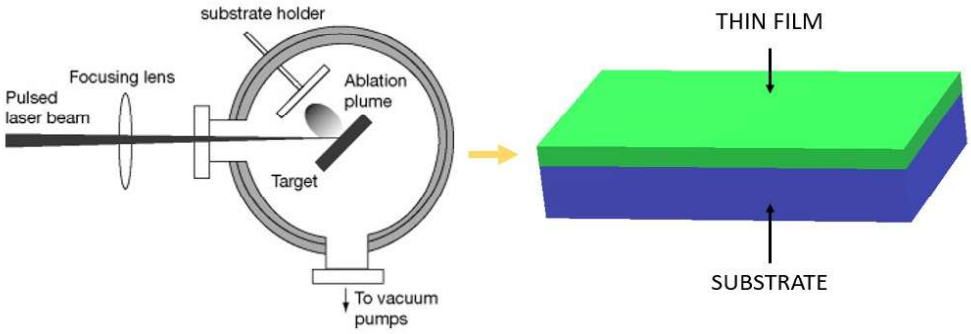

Figure 1.1: Schematic representation of the PLD setup and the obtained thin film sample [9].

Using epitaxy and substrate-induced deformation, oxide thin films can be elastically deformed by a few percent, well beyond the limits that the same material could withstand in its bulk form. Under these conditions, the intrinsic properties of these oxides can undergo substantial changes. One of the most important effects of epitaxial deformation is the modification of the crystalline structure of thin films. When subjected to deformation, the crystalline lattice of the film adapts to that of the substrate, resulting in distortion of the lattice. This distortion can manifest itself as changes in bond angles and bond lengths, which in turn can radically alter the electronic, magnetic and optical properties of the material. These deformation-induced structural changes are not merely superficial; they can fundamentally alter the energy landscape of the material, stabilizing phases that are not accessible in bulk form and enabling the exploration of new functionalities in thin oxide layers. The strain can be tensile or compressive, according to the lattice mismatch between the two materials. If the substrate shows a larger unit cell, the film will undergo tensile strain, while in the opposite case we will have compressive strain (Fig. 1.2). Moreover, an epitaxial oxide thin film can differ from the correspondent bulk mate-

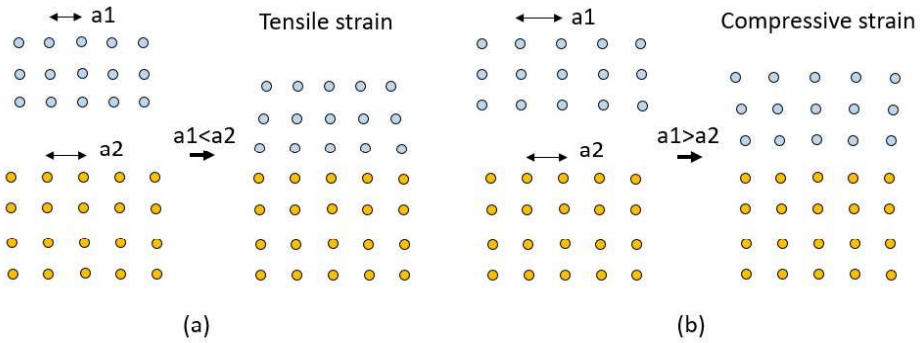

Figure 1.2: Schematic representation of (a) tensile strain and (b) compressive strain experienced by a thin film according to the lattice mismatch.

rial also in grain size, preferential orientation, crystallinity and composition [10]. As the film grows thicker and moves further away from the interface with the substrate, it will gradually recover its bulk crystal structure, provided the film is sufficiently thick. This is because the strain induced by the substrate diminishes with distance. This phenomenon is known as strain relaxation.

By properly customizing their lattice strain, procedure known as "strain engineering", we can thus tune the properties of these materials, enlarging their fields of application. In particular, functional oxide thin films with perovskite structure and formula ABO_3, have shown some interesting features, such as ferroelectricity, magnetism and insulator-to–metal transitions, making them an appealing field of study [11, 12, 13, 14].

1.1.2 Ceramic meterials

Concerning bulk nanostructured materials, we took into account the class of ceramics. A widespread procedure for synthesising ceramics consists in mechanical alloying where a fine powder is obtained by ball milling. This is then densified through spark plasma sintering (SPS) or microwave sintering. In the first case, the sample is subjecting it to high pressure and to a large current, creating plasma, joule heating, electromigration, and electroplasticity effects. As an outcome, high densification is

achieved in a short period of time [15]. In the second case, microwaves are directed into a multimode cavity where the sample is placed. They are then absorbed by the specimen according to its electric field distribution, causing a rapid and uniform heating, which leads to high levels of densification [16]. The final sample is typically characterized by a nanodomain-like morphology.

Among ceramics, copper-based sulfides stand out as a significant source of materials for energy applications and, notably, thermoelectrics [17]. Thermoelectrics can convert heat in electrical energy according to the Seebeck effect and find applications in energy recovery from waste heat. Copper-based sulfides show advantages as earth-abundant minerals, with non-toxicity and a low costs. It has been observed how, in copper sulfides, the transport properties of these materials originate from the Cu^{I}-Cu^{II} mixed valence allowing p-type carrier delocalization over the Cu-S network [18].

Alumina (Al_2O_3) represents another type of widely used ceramic, which finds application, among the others, as electrical insulator, in protective coating, in the biomedical field and in the industrial field [19, 20]. Among its polymorphs, α-alumina represents the most common and thermally stable phase, making it particularly valuable for applications that require durability and resistance to high temperatures. Research has shown that the properties of α-alumina can be further enhanced through doping with other materials. In 2015, it was in fact demonstrated that the incorporation of magnesium oxide (MgO) as a dopant in α-alumina significantly improved the efficiency of microwave sintering processes, leading to better densification of the material [21]. This improvement is particularly important for applications that require high-density ceramics with enhanced mechanical properties.

1.2 Crystal structure characterization of nanosized domains

The crystal structure of the previously seen kinds of functional materials can nowadays be characterized with a variety of techniques, the most spread being through X-Ray Diffraction (XRD) and Transmission Electron Microscopy (TEM). In this section, we will have an overview on these techniques, their advantages and limits, applied to the characterization of functional materials.

1.2.1 X-Ray characterization

For many years, X-Ray Diffraction has been the main technique for crystal structure characterization, given the simplicity of the experimental setup and the high accuracy in the determination of relevant structural parameters of the samples, including the cell parameters or the atomic positions.

In the cases where relatively large single crystals are available (in the range of tens of µm), Single Crystal XRD (SCXRD) can easily provide crystal structure determination with excellent Figures of Merit. This is accomplished by selecting a single crystal which is rotated around several axes, in such a way that the whole reciprocal space of the sample can be probed. However, when the dimension of the single crystals go beyond the range of the µm, performing SCXRD becomes challenging if not impossible to perform. In these cases, Powder XRD (PXRD) can give useful information about the sample.

Once the sample is crushed in a fine powder, PXRD can be performed in transmission geometry (Debye-Scherrer configuration), where the powder in inserted into a borosilicate glass capillary with diameter generally ranging between 0.2 mm and 0.8 mm. The capillary is fixed onto an steel holder which is finally mounted into the goniometer head, whose screws allow a precise vertical alignment of the capillary in front of the x-ray source. The capillary is allowed to spin on its axis during the

measurement, while the detector rotates around the capillary itself, measuring the diffracted intensities at different scattering angles 2θ. This way, a diffractogram showing the intensity versus the position 2θ is obtained (Fig. 1.3).

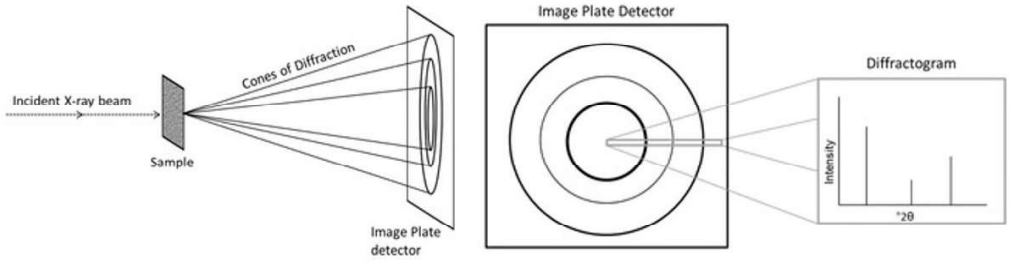

Figure 1.3: Schematic representation of the resulting PXRD pattern and of the final diffractogram obtained with a linear detector [22].

Alternatively, the experiments can be performed in reflection geometry (Bragg-Brentano configuration), where the powder is homogeneously dispersed on a holder and the radiation diffracted at an angle 2θ (considering an incident radiation at angle θ) is measured by the detector.

PXRD can allow phase identification, also in the case of polyphasic samples, by indexing the diffraction peaks, and through the estimation of the diffracted intensities it is possible to perform phase quantification. A precise estimation of the unit cell parameters is possible as well through Le Bail refinement, while Rietveld refinement of the diffractogram also allows for an accurate estimation of structural parameters such as atomic positions, occupancies and thermal factors.

Despite it is possible to perform *ab initio* structure solution through PXRD, it shows many limitations, in the first place the overlapping of different reflections. The structure solution becomes even more challenging if the sample shows modulations or large cell parameters, which will generate a larger amount of reflections that can overlap. In addition, these kind of measurements give a averaged signal over the probed crystals, which is problematic when different crystallographic phases are present in the same sample/material. Moreover, small grain/domain size will cause peaks broadening which might complicate the analysis.

For the characterization of epitaxial thin films, Bragg-Brentano represents the standard configuration (Fig. 1.4), given the usual thickess of the sample which prevents measurements in transmission geometry and because the signal of interest comes from its superficial part where the film is deposited. In this case, a divergent X-ray beam impinges on the sample and is later re-focused before reaching the detector, in such a way to obtain a stronger diffraction signal.

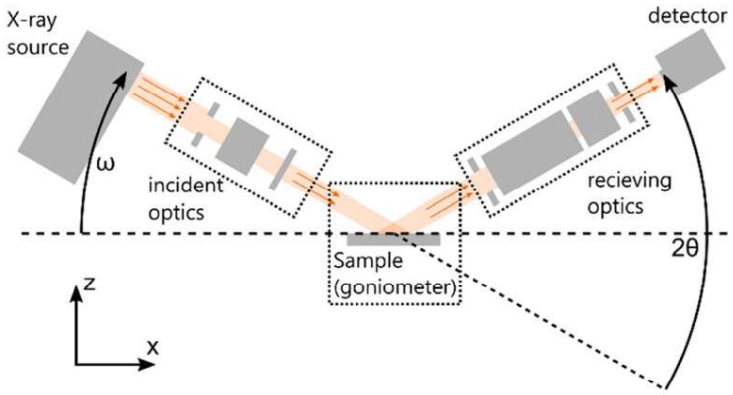

Figure 1.4: Scheme of an X-ray diffractometer setup in reflection configuration, typical of measurements on an epitaxial thin film [10].

Even in this configuration, obtaining structural information on these samples is challenging. The epitaxial relationship between the substrate and the film, normally giving a small lattice mismatch, causes significant overlapping of the peaks from the two. Additionally, the much larger volume of the substrate leads to a significantly more intense signal with respect to the one of the film, making the isolation of the two contributions difficult. Moreover, being the sample fixed instead of rotating, the visible diffraction peaks are very limited in number, allowing only an estimation of the in plane parameters [23]. From the acquired diffractometers it is however possible to assess the quality of the deposited film and to estimate its thickness, since the presence of atomic layers parallel to the substrate surface gives rise to fringes in the diffractogram, whose d spacing is related to the sample thickness.

Despite being nondestructive, not requiring a vacuum system and offering accurate results for bulk materials, X-ray acquisitions in reflection configuration preclude

a large part of the reciprocal space from being probed, leading to a limited number of measurable reflections.It's important also to consider that, in the normal $2\theta/\omega$ scan, where the incident angle ω is kept equal to the half of the scattering angle 2θ, the Bragg condition is respected for the atomic planes that are parallel to the sample surface. Therefore, the out-of-plane directions are excluded from the probed reciprocal space [10].

However, information on the out-of-plane direction of the deposited film can be obtained by performing Reciprocal Space Mapping (RSM). In this case, the diffraction intensity distribution is recorded by scanning on both the diffraction angle and the sample rotation axes, plotting the result in a 2D map in reciprocal space. This kind of measurement can provide details about orientation relationships, thickness, lattice mismatch, relaxation, layer tilt, mosaicity, defects, crystallinity and preferred orientation [24]. We can see some representative examples in Fig. 1.5. It is also possible to evaluate atomic positions by refining the crystal structure.

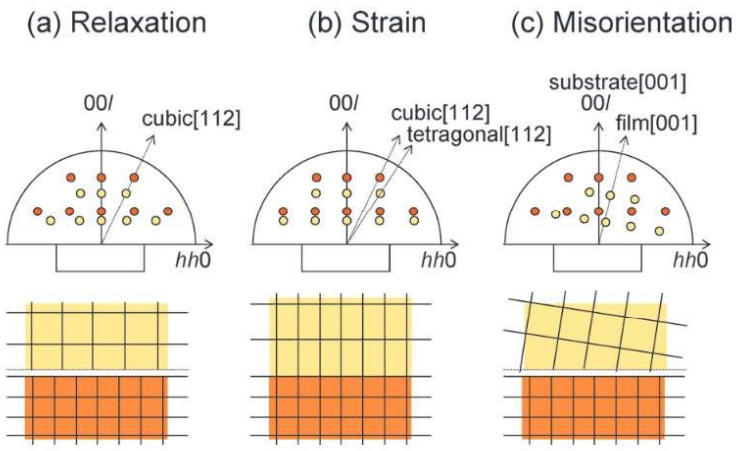

Figure 1.5: Schematic representation of (a) relaxed film, (b) strained film, and (c) misoriented film, and their corresponding RSM [24].

However, to obtain reliable results this requires to probe as many reflections as possible, which becomes largely time-demanding in terms of both acquisitions and data analysis. Moreover, the number of accessible reflections is usually limited by the geometry of the sample and the experimental setup, increasing this way the

uncertainty on the final results [25].

In case of complex samples composed of nanodomains of one single or multiple phases, or in the case of epitaxial thin films, where we cannot easily access accurate structural information through X-ray diffraction, we can exploit other characterization techniques, such as Electron Diffraction (ED), as we will see in the next section.

1.2.2 Transmission Electron Microscopy

The Transmission Electron Microscope (TEM) represents a multi-functional instrument for material characterization, since it can be used for both imaging and diffraction, and is normally equipped with some EDX/EELS detectors for chemical analysis. A Transmission Electron Microscope (TEM) is composed by a column, where the electron beam is generated and directed to the sample, and then to the detector, with a system of electromagnetic lenses [26]. In our case, a JEOL F200 TEM working at 200kV has been used to perform experiments on the considered samples. Its structure with the main components is shown in Fig. 1.6.

In the Jeol F200 TEM, the electron beam is generated by a cold FEG (Field Emission Gun): A sharp tungsten crystal emitter is kept at a high negative voltage (in our case 200 kV) close to two nearby anodes, in such a way that the voltage gradient causes electron emission. Successively, the electrons are accelerated and their path is deflected exploiting magnetic fields created by electromagnetic lenses, according to the Lorentz force:

$$\mathbf{F} = q(\mathbf{v} \times \mathbf{B}) \tag{1.1}$$

where F is the Lorentz force [N], q is the electron charge [C], v is the electron velocity [m/s] and B is the magnetic induction [T] [26].

Firstly, the electron beam passes through the deflection coils. It is directed to the condenser group, where we find the lens system that tunes the spot size and

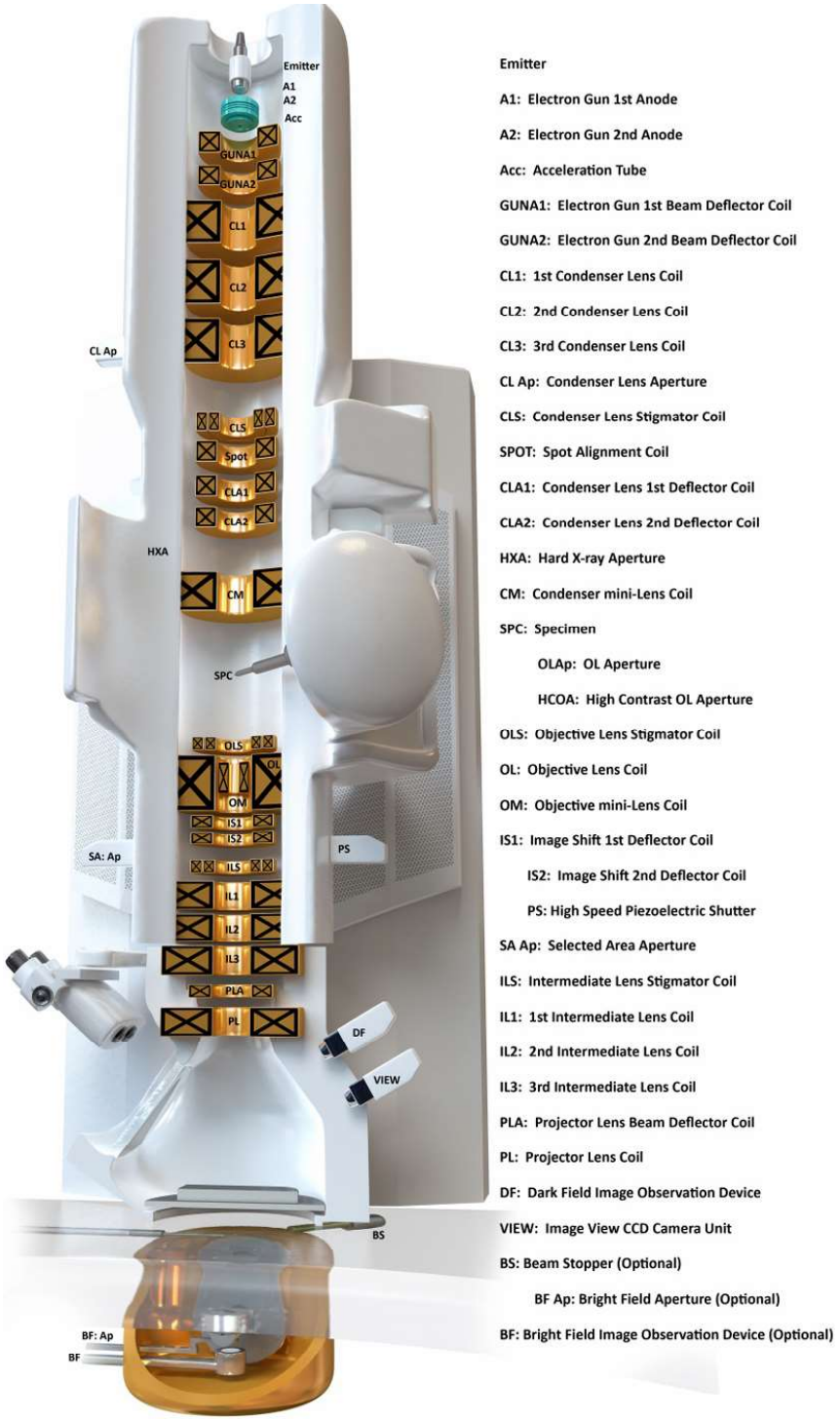

Figure 1.6: Jeol F200 TEM column in section with its components [27]

the convergence of the beam. Afterwards, it passes through the condenser aperture (usually in our experiments set to be the smallest available, i.e. 10 μm), which sets the lateral dimensions of the beam, before it impinges on the sample.

The main phenomena occurring at this point from the electron beam interaction with the sample are summarized in Fig. 1.7.

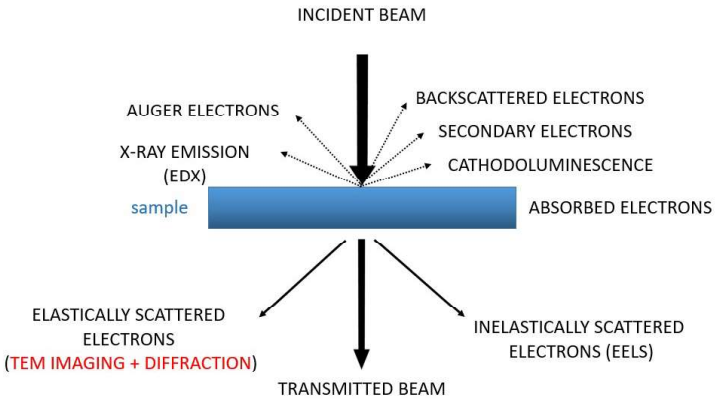

Figure 1.7: The main phenomena resulting from the interaction of the incident electron beam with the sample in a TEM.

In a TEM, the elastically scattered radiation, together with the transmitted beam, is exploited to form an image of the sample or to observe the diffraction pattern it generates (see setion 2.1.1), while X-rays emissions can be collected to perform Energy Dispersive X-ray (EDX) analysis. In this case, the elements which are present in the sample can be identified by counting the intensity of the emitted X-rays versus their energy (in keV), since each one of them will produce a characteristic X-ray emission depending on the atomic energy levels. By scanning the electron beam across an area of the sample and contemporaneously acquiring the EDX spectra, a map representing the chemical composition of the specimen can also be created [28].

Inelastically scattered electrons can instead be detected for Electron Energy Loss Spectroscopy (EELS). In this case, the energy loss of the scattered electrons (in eV) is plotted against the intensity of the signal. EELS represents a complementary technique with respect to EDX, since it can be more complex experimentally and

requires thin samples, but provides a larger amount of details on their chemistry and electronic structure of the atoms, which in turn lead to information, among the others, about their bonding/valence state, the nearest-neighbor atomic structure, the band gap if present, the specimen thickness, and others [28].

After impinging the sample, the beams which are transmitted or diffracted by the sample go through the objective lens, which creates the first magnified image of the sample. Successively, they pass through a system of intermediate and projector lenses and finally reach a fluorescent screen or a digital detector. The intermediate lenses in particular, allow to position on the detector plane either the back focal plane, and therefore to collect the diffraction pattern, or the image plane and therefore to collect an image of the sample [26].

The possibility of the transmission electron microscope of providing both images (direct space) and diffraction (reciprocal space) of the sample is a unique feature of this instrument. For the sake of sample visualization, TEM and STEM imaging mode can be used, constructing on the image plane respectively a bright-field or a dark-field image, depending on whether the transmitted or the diffracted beams are selected.

In TEM mode, the electron beam is kept still while the image is forming on the detector, which is positioned horizontally and perpendicular to the electron path. In bright-field images, the more electrons are scattered by the sample, the darker this will appear. Therefore, thinner samples will appear lighter than the thick ones. In this work modality, in order to visualize and collect diffraction patterns it is necessary to switch from image to diffraction mode in such a way to bring the back focal plane on the detector.

Differently, in STEM mode, a convergent electron beam is quickly scanned on the sample and the beams scattered at high angles (usually more than 5°) are revealed by the HAADF (High-Angle Annular Dark-Field) detector. Since the image has a Z-contrast, the brightest areas are those richer in heavy elements and thicker. In this case, once a suitable thin and well ordered crystal area is identified, we can

directly collect a sequence of patterns on it without changing the working modality but just by making the beam parallel [28].

In diffraction experiments, a quasi-parallel beam with a diameter typically below 100 nm and down to a few nm is used. Such a small parallel beam cannot be generated by currently available electron diffractometers, but is possible to reach for some TEM configurations. This method, known as parallel nanodiffraction mode (NED), allows to illuminate only the measured area of the sample, avoiding to damage not concerned parts of the latter [29].

High Resolution TEM imaging (HRTEM) can be also performed, which gives direct-space information about the atomic disposition in the sample with a resolution below the nm range. In a regular TEM, the spherical aberration (C_s) intrinsic to the electromagnetic lens system of the microscope can be exploited in order to obtain phase-contrast. This is implemented by compensating the wave distortion given by the spherical aberration with a negative defocus which produces an aberration of opposite sign. Since the introduction of spherical aberration correctors, the quality of the images that can be acquired increased significantly. With the corrector, it is possible to tune the value of C_s to obtain the best imaging conditions [30].

In the context of scanning diffraction techniques, 4D-STEM is a widely used protocol for morphology characterization for samples composed by multiple phases and/or domains. As depicted in Fig. 1.8, a convergent electron beam is focused on the sample and scanned across an area of interest while keeping the specimen oriented horizontally. For each position of the beam on the 2D ROI, a 2D diffraction pattern is acquired, generating therefore a 4D dataset [31].

From this kind of acquisition, it is possible to perform, among the others, virtual imaging, phase, orientation and strain mapping, measurements of medium-range order, evaluation of the sample thickness and tilt, and phase contrast imaging methods, including differential phase contrast, ptychography. When crystal orientation is computed automatically through computer image processing methods, we can refer to the technique as Automated Crystal Orientation Mapping (ACOM) [32, 33, 34,

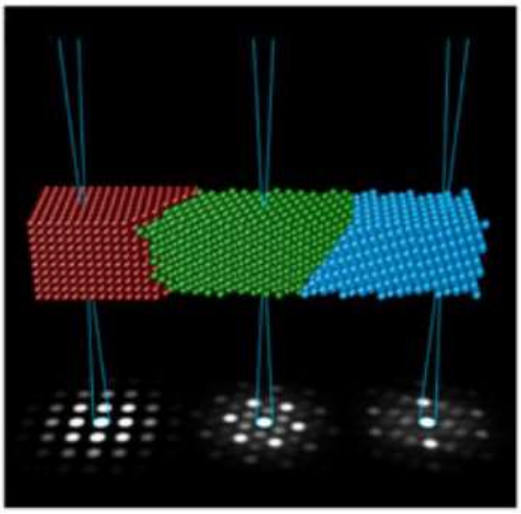

Figure 1.8: Schematic representing the operating method of 4D-STEM [31]. The electron beam is represented in blue while impinging a multidomain crystalline sample. The relative diffraction patterns are displayed below.

35, 36]. ACOM can rely on different methods for reconstructing the orientation map of the sample, for instance analyzing the Kikuchi lines in the CBED patterns, as for Schwarzer and Sukkau [34], or on ASTAR system by NanoMEGAS, which enables simultaneous beam precession and scanning over the desired sample area [37], as in the case of Kobler et al. [35].

This approach relies on the prior knowledge of the different phases that are present in the sample. From the reference crystal structure, in fact, a template consisting of all the possible diffraction patterns is computed. The structure can be imported as a .cif file, and the parameters such as the TEM acceleration voltage, maximum resolution and precession semi-angle can be tuned to match the experimental diffraction patterns. The template can be entirely visualized by tilting around X, Y and Φ, while the cell, symmetry and atomic parameters ar displayed on a separate panel (Fig. 1.9).

By comparing then the templates with the experimental patterns, a map of the different phases and relative orientation in the domains is created. Additionally, it is possible to visualize other outputs. For instance, the matching index map

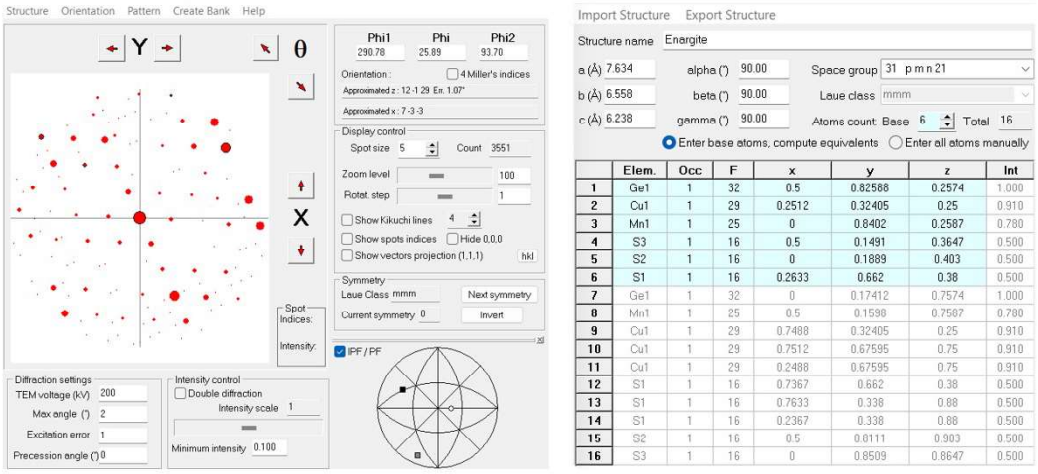

	Elem.	Occ	F	x	y	z	Int
1	Ge1	1	32	0.5	0.82588	0.2574	1.000
2	Cu1	1	29	0.2512	0.32405	0.25	0.910
3	Mn1	1	25	0	0.8402	0.2587	0.780
4	S3	1	16	0.5	0.1491	0.3647	0.500
5	S2	1	16	0	0.1889	0.403	0.500
6	S1	1	16	0.2633	0.662	0.38	0.500
7	Ge1	1	32	0	0.17412	0.7574	1.000
8	Mn1	1	25	0.5	0.1598	0.7587	0.780
9	Cu1	1	29	0.7488	0.32405	0.25	0.910
10	Cu1	1	29	0.7512	0.67595	0.75	0.910
11	Cu1	1	29	0.2488	0.67595	0.75	0.910
12	S1	1	16	0.7367	0.662	0.38	0.500
13	S1	1	16	0.7633	0.338	0.88	0.500
14	S1	1	16	0.2367	0.338	0.88	0.500
15	S2	1	16	0.5	0.0111	0.903	0.500
16	S3	1	16	0	0.8509	0.8647	0.500

Figure 1.9: ASTAR panel for diffraction pattern template generation from the reference crystal structure.

shows on a gray scale the correlation between the recorded diffraction pattern and the template pattern selected as matching. This map highlights features such as grain boundaries. The reliability map shows on a gray scale, for every location, the index representing the difference between the matching index of the two best matching solutions. The gray scales minimum and maximum values can be adjusted as needed. It is also possible to generate Virtual-Bright Field (VBF) and Virtual-Dark Field (VDF) images of the sample by selecting respectively the transmitted or one of the diffracted beams and integrating their intensity throughout the dataset (Fig. 1.10) [36].

Furthermore, recent developments are focused towards the expansion of this technique for 3D reconstruction of the grains in the sample. This is implemented by acquiring 4D-STEM datasets at different tilt angles, then coupling together the components at the different orientation angles and then using the "frozen-template" VDF images, created by using the template as a mask, for tomography reconstruction. Further information can be found in the article of Rauch et al. [38]. It is important to remember that, in these cases of study, the crystal structures under test are necessarily known, and that the objective is not *ab initio* structure solu-

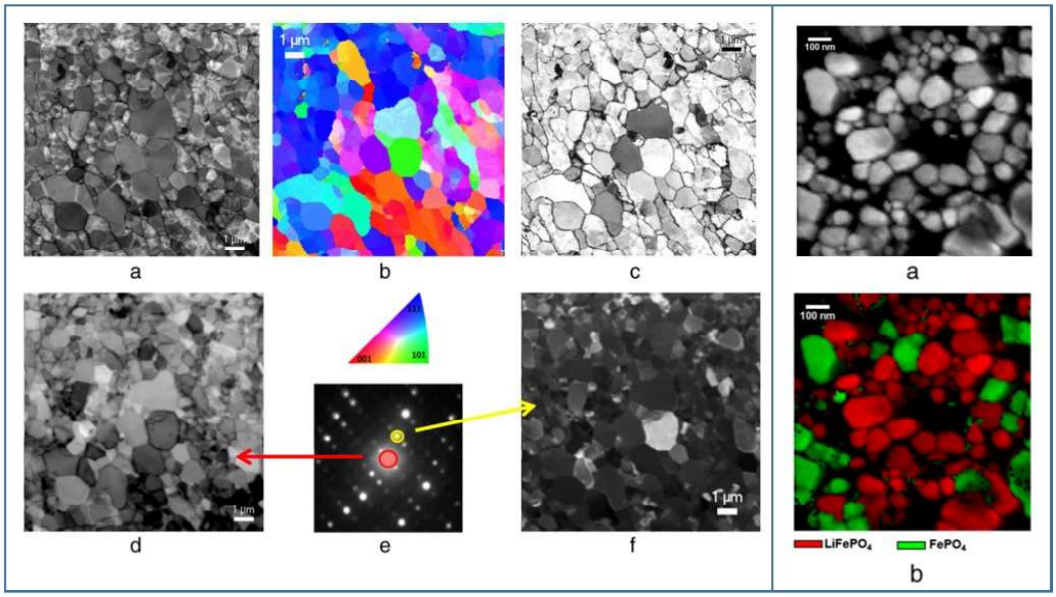

Figure 1.10: Left panel: ACOM-TEM results from acquisitions on a deformed sample of low carbon steel. (a) matching index, (b) crystal orientation (colour code shown in (e)), and (c) reliability alone. (d) Virtual-Bright field and (f) Virtual-Dark field images are generated by integrating (e) on the transmitted or one of the diffracted beam intensities at every position. Right panel: ACOM-TEM results from acquisitions on a partially charged lithium cell sample. (a) correlation index maps, (b) corresponding phase maps [36].

tion and accurate refinements, but rather gain microstructural information such as phases, orientations and morphology of domains in the samples.

CHAPTER 2

Crystal structure characterization of nanosized domains by 3D ED

In this chapter an overview of 3D electron diffraction techniques for crystal structure characterization will be given.

Starting from an introduction to the theory of diffraction, we will move on to the mostly spread 3D ED protocols. Successively, we will deal with the data processing strategy and finally the preliminary results on both thermoelectric materials and epitaxial thin films. Finally, we will introduce Scanning Precession Electron Tomography (SPET) as a tool for accurately characterize the crystal structure of nanodomains in the test samples and go through the details of SPET data analysis.

2.1 Introduction to 3D Electron Diffraction

When the size of the single crystals goes down the range of the µm, it is not possible to perform SCXRD anymore, given the difficulty in selecting and positioning a crystal to be analyzed in the X-Ray diffractometer. In these cases, 3D electron

diffraction, performed with a Transmission Electron Microscope, has proven its utility for accurately solving crystal structures.

Considering that, contrarily to X-Rays, which interact with the variations in electron density in the specimen (with scattering amplitude $f \propto \sqrt[3]{Z}$), electrons interact with variations in the electrostatic potential (with scattering amplitude $f_e \propto Z$). This implies electron beams being attenuated much more rapidly with respect to X-Rays. As a consequence, only thin samples can be probed by electron diffraction for solving its crystal structure, making it a complementary technique with respect to SCXRD [39].

For this reason, and with the latest development both concerning TEM technology and data processing, 3D electron diffraction made its way into structural characterization of nanomaterials. We will now see how its applications are still under expansion, and how we can exploit its potentialities for reaching accurate structure solution at the nanoscale in challenging samples.

2.1.1 The basis of diffraction techniques

In a 3D crystal structure, atoms adopt ordered and periodic arrangements, and therefore the whole structure can be described through the repetition in space of a unit cell (defining the lattice) according to specific symmetry operations, and the atomic basis, i.e. the atomic arrangement inside the unit cell.

As an electromagnetic wave interacts with crystalline matter, it will produce elastically scattered waves that will interfere with each other in a constructive or destructive manner, giving rise to the phenomenon of diffraction, provided that its wavelength is comparable to the inter-atomic distance. This phenomenon can be described in real space with the Bragg's law, or in momentum space with von Laue's description.

Bragg's law provides a correct description of diffraction as experimentally observed, though von Laue's formalism is more complete and is also suitable to describe diffraction of imperfect crystals. According to Bragg's law (eq. 2.1), the

electromagnetic wave impinging on a crystal are "reflected" by crystal planes at an angle θ equal to the incidence angle, as shown in Fig. 2.1.

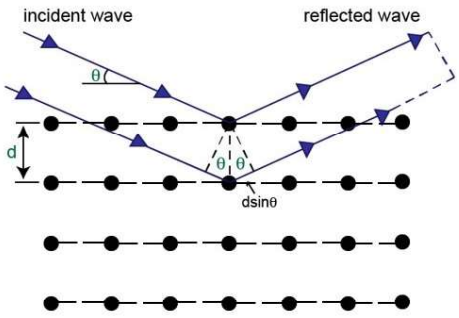

Figure 2.1: Schematic representation of the electromagnetic wave impinging on a crystal. The atomic planes that act as mirrors are shown with dotted line [40].

Two scattered rays will produce constructive interference and therefore a diffraction peak (also called "reflection"), whenever the difference in optical path equals an integer number of wavelengths. That is, whenever the following condition is satisfied [41]:

$$2d_{hkl} \sin\theta = n\lambda \tag{2.1}$$

d_{hkl} = distance between two parallel atomic planes of the (hkl) family

θ = incidence angle

λ = incident wavelength

n = integer

Conversely, if destructive interference occurs, no radiation intensity will be present in the given direction.

Von Laue's description of diffraction can be visualized in the geometrical construction shown in figure 2.2. We consider a diffraction experiment where the crystal is hit by the incident wavevector **k** and emits a diffracted ray with wavevector **k'**. We then draw a sphere having radius $|k| = |k'|$, translating the incident and the

diffracted wave vectors, in order that they both have their origin at the center of the sphere and their tip on the sphere surface. This construction is known as the Ewald sphere construction.

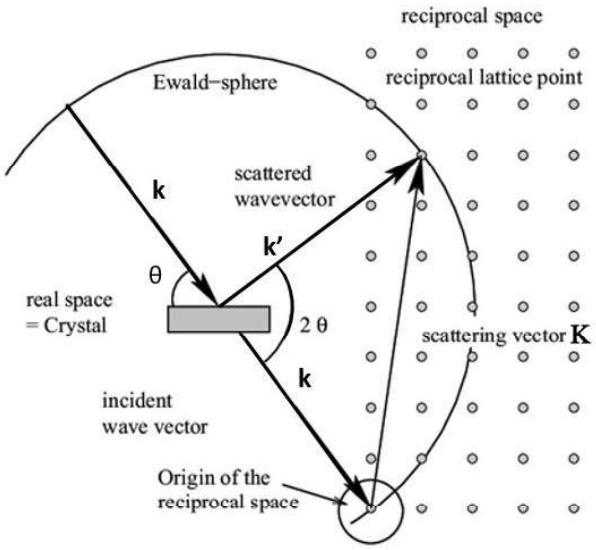

Figure 2.2: Geometric construction of the Ewald sphere. [42]

Finally, we draw the reciprocal lattice, having the caution to locate its origin on the Ewald sphere in correspondence with the tip of the incident wavevector. The orientation of the reciprocal lattice is tied to the crystal orientation and the vectors connecting each node with the lattice origin are reciprocal lattice vectors. With this construction, we can see that the Laue condition is satisfied for those reciprocal lattice points that lie on the Ewald sphere, since only for them the reciprocal lattice vector satisfies the equation $\mathbf{K} = (\mathbf{k}' - \mathbf{k})$. Thereby, as a point of the reciprocal lattice (h, k, l) intersects the Ewald sphere, it will give rise to a diffraction peak in direction of $\mathbf{k}'$ [43].

Being electrons associated to a shorter wavelength with respect to X-Rays (λ = 0.025 Å for an acceleration voltage V = 200 kV, opposed to $\lambda_{Cu_{K\alpha}}$ = 1.5406 Å commonly used for XRD), it is possible, in principle, to probe the reciprocal space of the sample up to higher resolution. In fact, having a larger wavevector, we will have a much larger Ewald sphere, and therefore a higher number of diffraction peaks

in Bragg condition, as shown in figure 2.3.

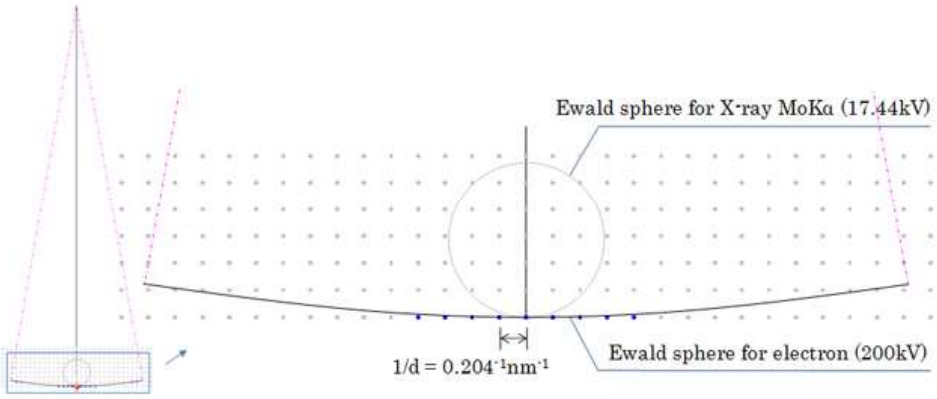

Figure 2.3: Comparison between Ewald spheres in the cases of x-rays ($V = 17.44\ kV$) and electrons ($V = 200kV$) [44]

By detecting the intensity of the diffracted radiation, changing the relative orientation of the crystal (and thus also of the reciprocal lattice) with respect to the direction of the incoming beam **k**, we can reconstruct the entire reciprocal space of the crystal, which provides important structural information. By measuring the position of several diffracted peaks, we can determine the full 3D reciprocal lattice, from which the unit cell parameters can be derived, representing a first information about the crystal structure of unknown samples. In fact, in the diffraction pattern, each reflection is attributable to a specific lattice plane, identified through the Miller indices (hkl) and characterized by specific interplanar distance (d_{hkl}), which is related to the angular position of the reflection through the Bragg's law. On the other hand, following the Laue condition, these indices identify a specific vector of the reciprocal lattice.

At first, we only consider the case of a single elastic scattering event per electron impinging the specimen, i.e. kinematic diffraction. In kinematic approximation, the physics of diffraction states that the integrated intensity of the peak in a specific position in reciprocal space (h,k,l) I_{hkl} is linearly proportional to the square modulus of the Fourier transform of the quantity responsible for the scattering: the electron density in the case of x-rays, the crystalline electrostatic potential in case

of electrons:

$$I_{hkl} \propto |F_{hkl}|^2 \tag{2.2}$$

The Fourier transform of the scattering quantity is known as structure factor and it is indicated as F_{hkl} [41]: The structure factor F_{hkl} can be expressed as a sum of waves as follows:

$$F_{hkl} = \sum_j f_j e^{2\pi i(hx_j+ky_j+lz_j)} \tag{2.3}$$

where h, k, l represent the components of the **K** vector, and j labels the atoms in the unit cell. Therefore, the structure factor is constituted by an amplitude and a phase. The structure factor has one wave terms for each atom in the unit cell. x_j, y_j, z_j are the coordinates of the atom j in the unit cell, while f_j represents its atomic scattering factor, and it is related to how efficiently it scatters the incident beam. f depends on the atomic species, the radiation type and wavelength and on the scattering direction. In the case of x-ray, it can be expressed as the Fourier transform of the atomic electron density $\rho(x, y, z)$:

$$f_j = \int \rho(x, y, z) e^{2\pi i(hx+ky+lz)} dV \tag{2.4}$$

while for electrons as the Fourier transform of the electrostatic potential $V(x, y, z)$ created by the nucleus of the atom and partially screened by the atomic electrons:

$$f_j = \int V(x, y, z) e^{2\pi i(hx+ky+lz)} dV \tag{2.5}$$

where x, y, z indicate the position with respect to the nucleus of the atom.

Therefore, the intensity of the peak will depend on the atomic species who are present in the unit cell, as well as their position, through the phase of the summed waves. Since the detected intensity is related to the square modulus of the structure factor, in a diffraction experiment we only obtain information about the amplitude of the scattered wave, while any phase information is lost. This is known as the phase problem in crystallography. It can be noticed that the scattering factors

$F(h,k,l)$ and $F(\overline{h},\overline{k},\overline{l})$ have the same magnitude but opposite phase, resulting in a centrosymmetric diffraction pattern. The reflections (h,k,l) and $(\overline{h},\overline{k},\overline{l})$ are referred to as Friedel pairs. Consequently, in a diffraction pattern, the two reflections will have the same intensity if the crystal has a centrosymmetric structure and different intensity otherwise.

It is noteworthy that eq.2.2 can be expressed as an equivalence in kinematical approximation for an ideal infinitely extended sample, that would produce infinitely sharp diffraction peaks. When we take into account crystal of limited dimensions, the peak intensity becomes related to the sample thickness as follows:

$$I_{hkl} = |F_{hkl}|^2 \frac{\sin^2(\pi t S_h)}{(S_h)^2} \tag{2.6}$$

where t is the sample thickness and $\mathbf{S_h}$ is the excitation error, the vector indicating the distance from the Ewald sphere of the specific reciprocal lattice point.

Therefore, the intensity of the diffraction peak with respect to $\mathbf{S_h}$, follows the square sinc trend, as shown in figure 2.4. As a consequence, a diffraction peak will have maximum intensity if its excitation error is null, while for an increasing distance of the point from the constructed Ewald sphere its intensity will diminish, making diffraction signal detectable for the case of electron scattering even if the corresponding reciprocal lattice vector is not lying exactly on the Ewald sphere (Fig.2.5)

We can observe as well how the decrease in the crystal thickness causes a broadening of the diffraction spots, making them, in the case of a platelet-like specimen, rod-shaped (Fig.2.5).

From the diffraction pattern, information about the symmetry of the crystal can also be extrapolated. By comparing the intensity of reflections related by possible rotational symmetry elements we can determine if these elements are present or not. Moreover, the centering and some translational symmetry elements can lead to *extinguished* or *forbidden* reflections, that is, reflections with intensity equal to

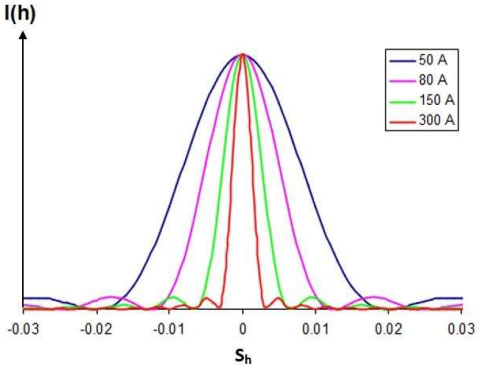

Figure 2.4: Graph reporting the computed intensity of the diffraction peak I(h) as a function of the excitation error S_h for different values of sample thickness in Å[45]

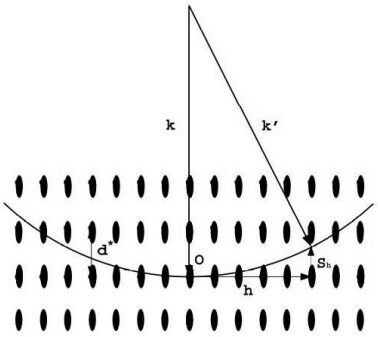

Figure 2.5: *In this figure, the reciprocal lattice points are shown distorted as a consequence of eq.2.6. The excitation error S_h for a point is also shown.*

zero in kinematical approximation, which are related to the fact that for specific atomic positions in the unit cell the structure factor will be equal to zero (see Eq. 2.3). Therefore, by examining the systematic absences in the *hkl* sections of the sampled reciprocal space caused by these forbidden reflections, we can have derive the possible space groups of the crystal structure.

As an example, considering a *bcc* structure, with one lattice point at the origin (0,0,0) and the other one at $(\frac{1}{2}, \frac{1}{2}, \frac{1}{2})$, we will obtain:

$$F_{hkl} = f[1 + e^{\pi i(h+k+l)}] \tag{2.7}$$

Which will in turn lead to:

- $F = 2f$ for (h+k+l) $= 2n$
- $F = 0$ for (h+k+l) $= 2n + 1$

with n integer. As a result, a body centered cubic structure, as the one of Fe, would generate a chess-like pattern observable on each reciprocal space section along one of the primary axes [28], as shown in Fig. 2.6.

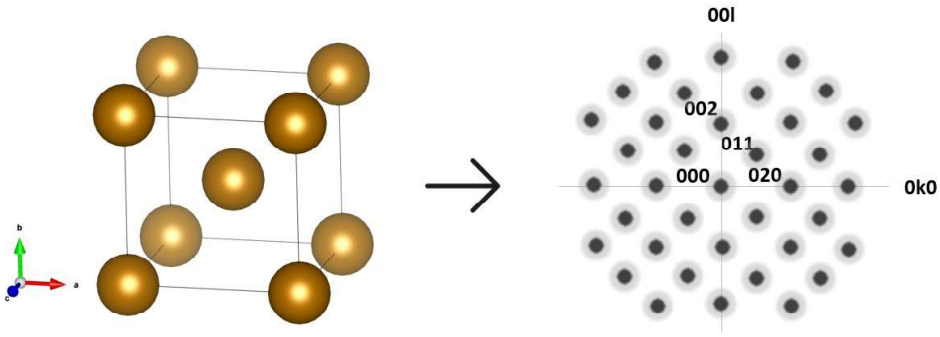

Figure 2.6: The *bcc* structure of Fe (SG: $Im\bar{3}m$, and the corresponding (0kl) section in reciprocal space. From the labeled reflections, we can notice the position of the missing ones.

2.1.2 3D ED experiments

In order to perform 3D ED experiments, the sample holder, usually a high tilt tomographic holder, is mounted onto a goniometer system that allows a fine rotation around its axis. In this way, the electron beam can impinge on the selected crystal from many different directions, the maximum tilt range being $\alpha = \pm 70°$, and consequently it is possible to acquire sequences of non-oriented reciprocal-space patterns covering a wide portion of reciprocal space. This technique, introduced in 2007 by Kolb et al. [46] and originally named Automated Diffraction Tomography (ADT), paved the way for 3D electron diffraction techniques, in contrast with the previously used 2D methods that required to orient the crystal along the zone axes in order to identify the unit cell and the correct space group [46]. By acquiring a sequence

of diffraction patterns at different orientations of the crystal we can thus obtain a highly accurate map of the reciprocal space, allowing an easier and more precise structure analysis.

Unfortunately, just a sequence of static patterns separated by fixed angular steps, might suffer from an incomplete sampling of the reciprocal lattice, since the portions of space lying in between two consecutive Ewald sphere positions will not be probed (see Fig. 2.5), which can lead to an underestimation of the diffracted intensities. This may be referred to as excitation error problem [45]. Despite there are many cases in which static ED patterns can be enough for structure solution, if we are interested in accurate determination of crystal lattice features it is necessary to probe as much of the reciprocal space as possible in order to allow a precise diffracted intensity determination.

There are several approaches in order to probe the missing wedge between two sequential positions: in RED (Rotation Electron Diffraction), discrete mechanical rotations of the sample can be combined with fine electron beam tilts while acquiring the diffraction patterns, while in continuous methods, also known as Integrated Electron Diffraction Tomography (IEDT)[47], continuous RED (cRED)[48] or microED [49], the sample is continuously rotated around the tilt axis while the detector records integrated snapshots at fixed time intervals/angular steps.

Another approach is based on the combination of ADT with a precession movement of the electron beam, which is tilted away from the optical axis of the microscope and rotated on a conical surface with its vertex on the surface of the sample. The precession semi-angle (ϕ) is defined by the inclination of the incident beam with respect to the TEM optical axis.

Precession electron diffraction was firstly introduced by Vincent and Medgley in 1994 [50], and in 2009 it was combined with ADT by Mugnaioli et al. [51] in the so called PEDT (Precession-assisted Electron Diffraction Tomography), in order to probe the reciprocal space with high completeness.

We can see the functioning method of PEDT sketched in Fig. 2.7.

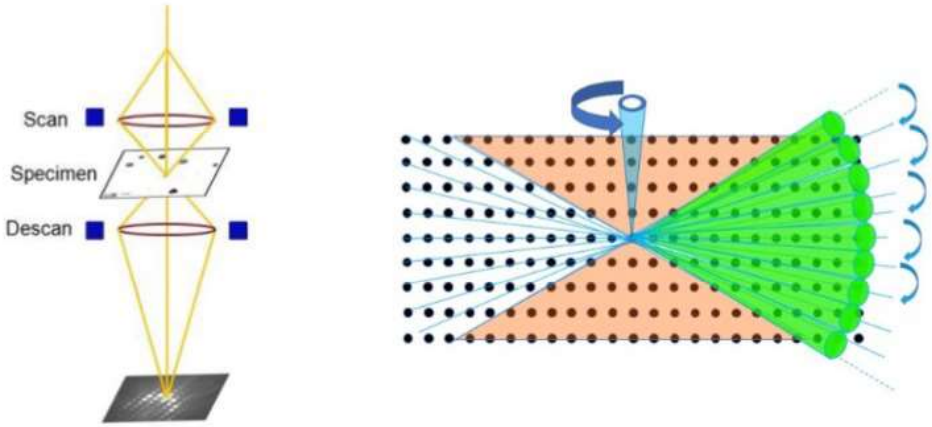

Figure 2.7: On the left, a scheme reporting the electron beam path in precession mode. On the right, a representation showing how a movement of the electron beam during a measurement in PEDT mode enables a sampling of the reciprocal space without gaps [52][45].

After passing through the specimen, the electron beam is then precessed in the opposite direction through the descan coils in order to avoid beam movement on the back focal plane and to obtain a stationary diffraction pattern.

The precession has an important effect on the acquired data: the beam precession movement makes the Ewald sphere to sweep the reciprocal space, enlarging the probed k-space for each acquired diffraction pattern, and therefore solving the extinction error problem, as displayed in Fig. 2.8 [45].

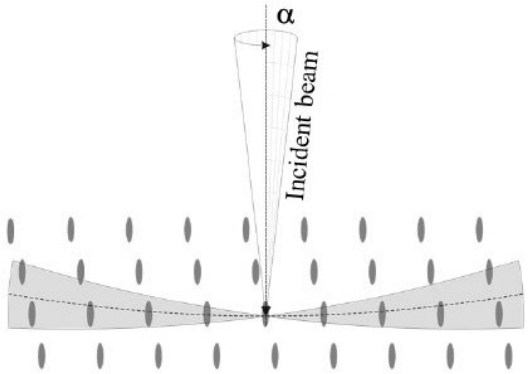

Figure 2.8: The rocking movement of the Ewald sphere in precession mode integrates the diffracted intensities over the spanned volume [53].

In our case, the precession motion of the electron beam in the TEM is generated and tuned using the NanoMEGAS DigiSTAR unit. Firstly, the precession should be properly aligned in such a way that the beam remains as steady as possible during the rocking process both on the sample plane and on the back focal plane. This way, the probed area on the specimen will be comparable in dimension to the condition without any precession, and the diffraction spots will be kept point-like on the detector. Generally, in our diffraction experiments, a precession semi-angle $\phi = 1.4°$ was set, in order to obtain an increase in the number of observed reflections but also to avoid the interaction of different Laue zones (a range considered $0.6° < \phi < 1.5°$) [54].

All these techniques are now referred to using the generic denomination 3D ED [45]. At the present time the most commonly used approaches are PEDT i.e. precession-assisted 3D ED and cRED i.e. continuous rotation 3D ED.

3D Electron Diffraction techniques have been proved to be suitable for structural characterization and accurate refinement of a large variety of crystalline samples, including thin films and ceramic materials, as we will illustrate in the next section. In addition, a new generation of extremely sensitive detector can be exploited to acquire more accurate diffraction patterns [45]. In our case, an ASI Cheetah M3 512×512 hybrid pixel detector was used, which allows to avoid background noise in data acquisitions.

2.1.3 3D ED data analysis workflow on PETS2

The acquired 3D electron diffraction data can be firstly processed using different software for peak indexation and integration, in order to determine the correct unit cell parameters and extract the intensity of the peaks, such as PETS2 (acronym standing for Precession Electron Tilt Series) [55], eADT [56] and XDS [57]. Being our data processed with PETS2, an insight on the workflow on PEDT data on this specific software will be given.

The program reads the input .pts or .pts2 file, where information about the

electron wavelength λ, orientation of the tilt axis of the sample holder with respect to the horizontal axis ω, the size in reciprocal Å of one pixel of the images, the precession angle ϕ, signal to noise ratio I/σ(I) and the reflection size in pixels are reported. Moreover, the acquired images of the diffraction pattern in .tiff format are listed in the file. Each image is associated to the corresponding tilt angle α, in such a way that the software can successively reconstruct the 3D sequence of diffraction patterns. Below the different steps that compose the workflow on PETS2 will be described. For more details please consult the PETS2 manual [58].

Peak search

The diffraction peaks are located on each image and selected according to the desired I/σ(I) value, minimum and maximum resolution shell selected by the user. Their position with respect to the image centre is also estimated. In our case, the image centre (transmitted beam) is determined through the Friedel pairs method, i.e. by identifying the reflection couples h, k, l and $\overline{h}, \overline{k}, \overline{l}$ and estimating the center as middle point between them. In figure 2.9 we can see an example of diffraction pattern, with the detected reflections indicated with a green circle. The calculated image centre is indicated by the blue crossed circle.

Refinement of the rotation axis ω

In this passage, the orientation of the rotation axis ω on the horizontal plane, and optionally its inclination with respect to the horizontal axis δ, is refined. As an output, a graph representing the peaks positions in cylindrical coordinates is generated. It is useful to estimate the quality of the data set and the accuracy of the parameters, by assessing how ordered the reflections appear. In figure 2.10 we can observe the graph for the refined value of the rotation axis angle, where a precise alignment of the detected peaks already gives a good hint about data and crystal quality.

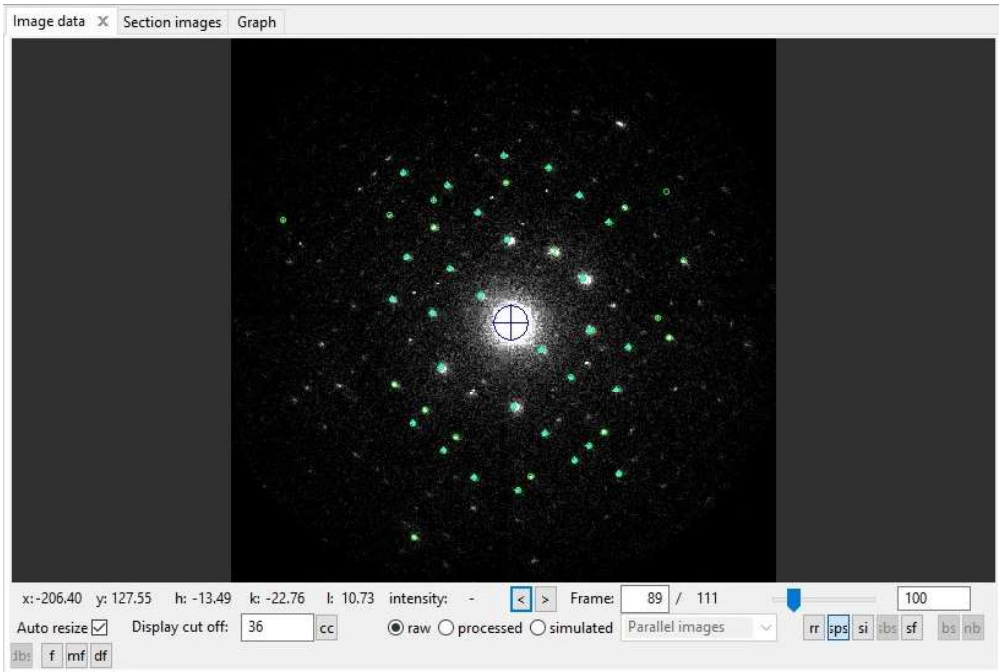

Figure 2.9: An example of diffraction pattern displayed on PETS. The found peaks, with intensity higher than the $I/\sigma(I)$ value, are indicated with a green circle. The calculated image centre is indicated with the blue crossed circle.

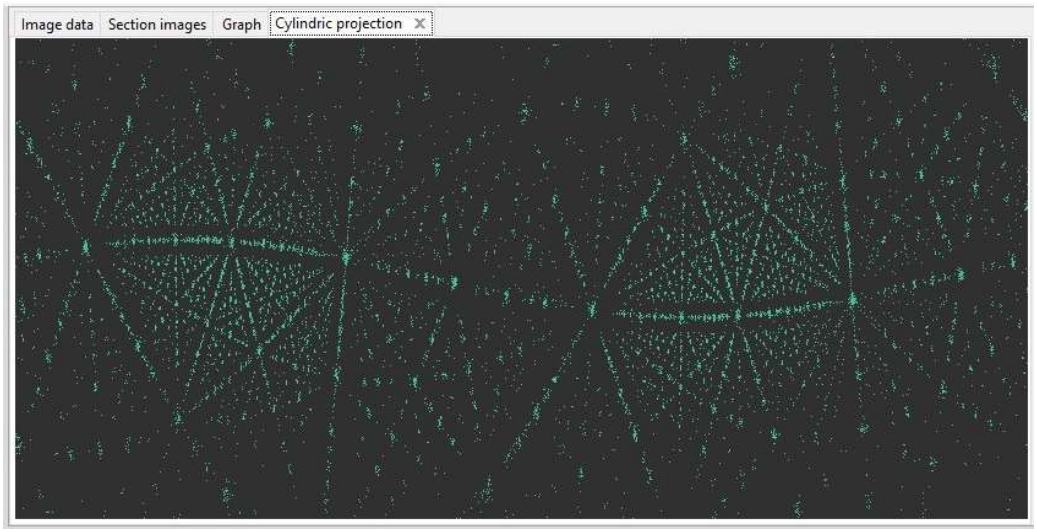

Figure 2.10: Graph representing the cylindrical projections of the reflections for the refined value of ω.

Peak analysis

During this step, firstly, all reflections measured on consecutive frames are clustered. Then, the centers of the clusters are used instead of individual peak positions. Successively, difference vectors between the peaks are calculated and then clustered applying the same procedure. We can check the correctness of these steps by observing the resulting graphs representing the trend of inter-peak distances with its derivative and its analogue for difference vectors. The graphs should resemble the one in figure 2.11.

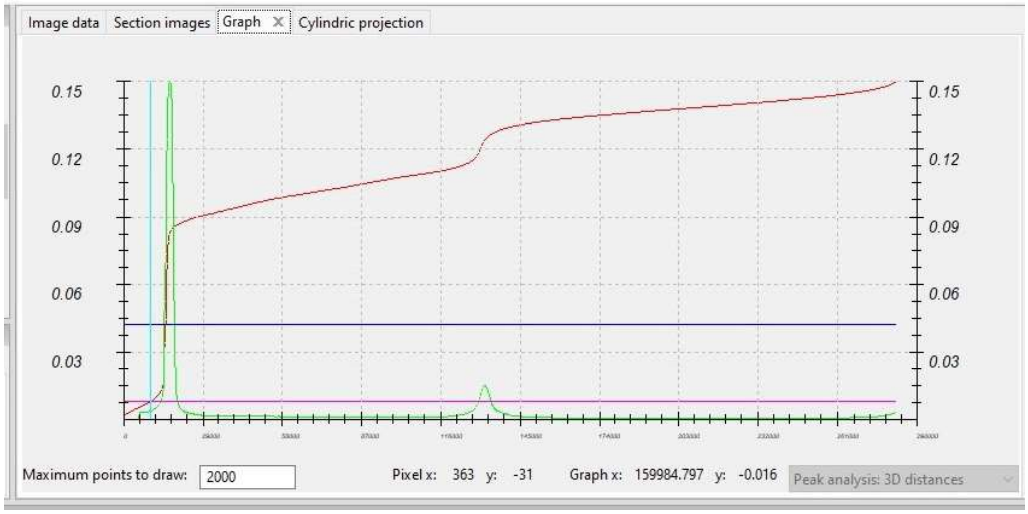

Figure 2.11: An example of graph resulting from peak analysis. In red, the trend of inter-peak distances is shown, while its derivative is shown in green. For a good data set and a correct cluster formation, the graph should display, as in this case, sharp peaks and clear jumps in the derivative.

Unit cell determination

Knowing the position of each peak in 3D, an option is offered to automatically calculate the most suitable unit cells together with their orientation matrix, and index the peaks accordingly (Fig. 2.12).

The percentage of peak indexing is shown for every unit cell, as well as its parameters, its Bravais lattice and its orientation matrix. This step can also be

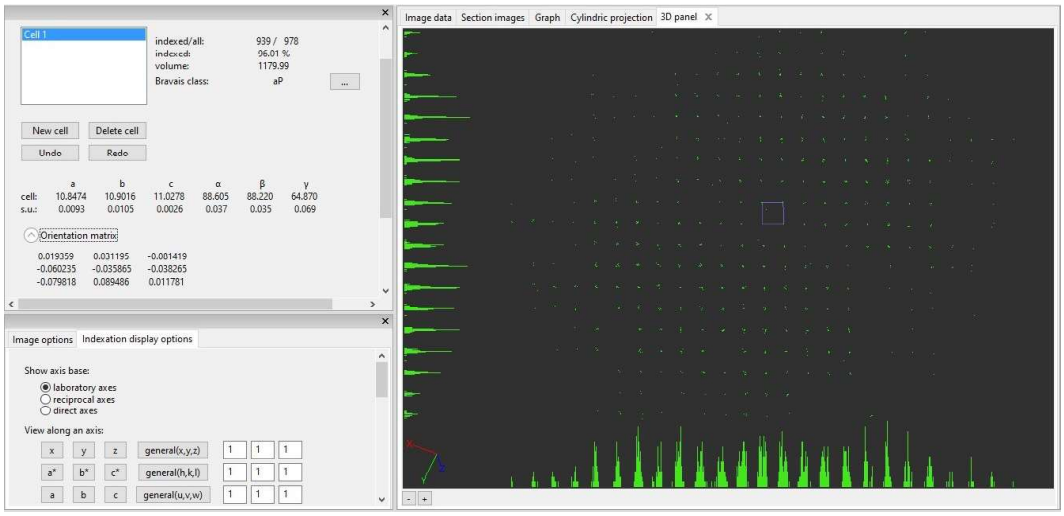

Figure 2.12: An example of 3D diffraction pattern reconstructed by Pets, viewed from the $b*$ axis of the computed unit cell. The reciprocal space cell is shown in blue.

carried out manually, if the automatic process fails or does not give satisfactory results. In Fig. 2.12, an example of 3D diffraction pattern reconstructed by PETS2 is reported. Afterwards, the selected unit cell can be refined and modified by using a transformation matrix. In the cell refinement step, also the distortions relative to the microscope electron optics can be calculated and refined, in order to obtain a more truthful unit cell parameters. In standard mode, magnification, barrel-pincushion distortion, spiral distortion, elliptical amplitude with its orientation, and the radial component of the shift caused by parabolic distortion (radial S_g para) can be refined. In Fig. 2.13 the effect of the main distortions on the diffraction patterns are depicted, as comprehensively described by Brázda et al. [59].

Process frames for integration

In this step, the peak positions in each frame are calculated according to the selected unit cell parameters and orientation matrix, and their intensity is determined by integration. As an output, the rocking curve is displayed, where we can observe the profile height plotted against the excitation error for both the experimental and

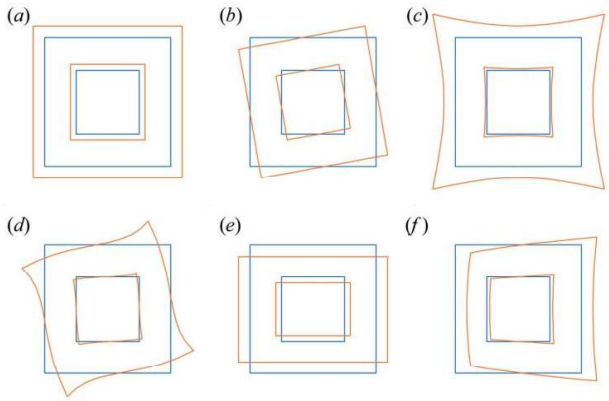

Figure 2.13: Distortions in static beam electron diffraction data. In blue the unaltered pattern is represented, while in orange the effect of the distortion. (a) magnification error, (b) in-plane rotation, (c) barrel-pincushion distortion, (d) spiral distortion, (e) elliptical distortion, (f) parabolic distortion [59]

the computed case (Fig. 2.14). A good fit between the two indicates a good data quality and a correct integration of the diffraction peaks.

The V-shaped trend, typical of precession experiments, arises from the fact that at high resolution a larger amount of peaks will probed for high values of excitation error, thanks to the movement of the Ewald sphere. For the same resolution, at higher precession semi-angles we will therefore find the maximum intensity at higher values of excitation error. On the contrary, at $\phi = 0°$, a single maximum will be observed for all resolution values [55].

Optimizations

At this point, parameters such as the rocking curve width, the mosaicity as well as the diffraction pattern center and the frame orientation (angle α) can be refined. These optimizations can significantly improve the diffraction peaks integration and therefore the rocking curve fit.

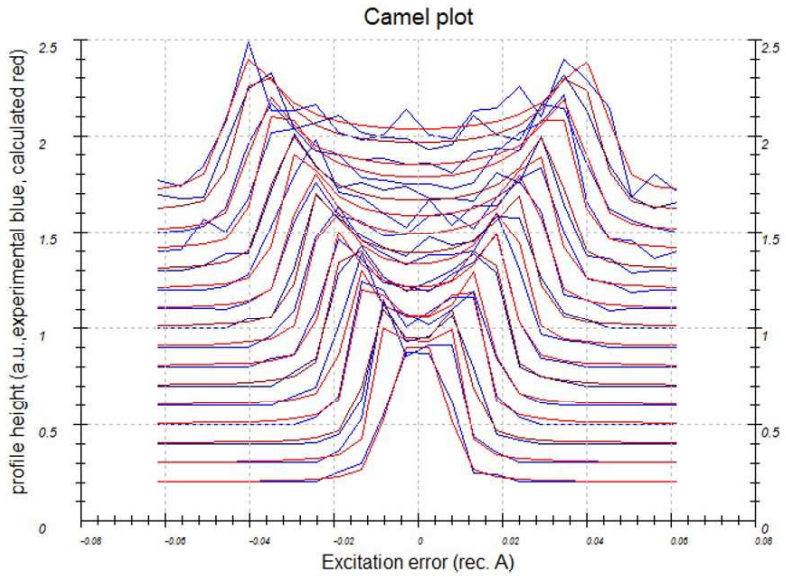

Figure 2.14: An example of rocking curve obtained after peak integration. The computed curve is displayed in red, while the experimental one in blue.

Integration finalization

The integration is finalized and the number of observed peaks ($I > 3\sigma$) versus the total is displayed, as well as a list of the Laue classes with the relative value of R int(obs). According to these values, the Laue class of the crystal can be determined, which is used to successively determine the possible space groups through the analysis of systematic absences in reciprocal space sections. At this stage, the files for structure solution and kinematical and/or dynamical refinement of the atomic structure are produced (*.hkl*, *.cif_pets*). In the *.hkl* file, the diffraction peaks are listed, as an average across all the dataset, with the relative *hkl* coordinates, intensity and sigma. In the two *.cif_pets* files we can firstly find a section containing the unit cell parameters and orientation matrix, as well as the used radiation wavelength and the parameters set for the data integration, followed by the list of the diffraction peaks with their *hkl* indices. In the first file, which is suitable for structure solution and refinement in kinematical approximation, each reflection is reported as an average across all the dataset, with the relative intensity, standard deviation. Instead, the

second file, which can be used for the so-called dynamical refinement, reports the reflections frame by frame with the corresponding intensity and standard deviation. In this way, the contribution of the dynamical effects can be estimated, and therefore a more accurate determination of the atomic coordinates can be achieved during the refinement of the structure.

2.1.4 Structure solution and refinements

The *.cif_pets* file can be used as an input to perform the structure solution on Jana2020 [60] through the Superflip tool, based on the Charge Flipping Algorithm (CFA) [60][61]. In this *ab initio* approach, the missing phase information is computed, recreating this way a complete Fourier map from which the elecrostatic potential density map, and hence the atomic structure according to the crystal symmetry can be extrapolated. The starting space group is specified by the user, and later the CFA will compute the most probable one relying on a score that is assigned to each symmetry element compatible with the crystal class.

On the same software, the obtained crystal structure can be refined both kinematically and dynamically according to the least squares method, which models a non-linear function that minimizes the sum of the squares of the differences in between observed and calculated parameters.

Alternatively, the *.hkl* file can be used as input, together with the expected unit cell content, for computing the structure solution on the software SIR2014/2019 [62]. Once the atomic structure has been obtained, the result is exported as a .res file in order to be refined separately on Shelxle [63], Jana2020 or an equivalent software. The .res input file contains information about the used wavelength, the formula unit repetitions, the atomic scattering factors of the species in the crystal structure and their thermal factors, the symmetry, the estimated atomic positions and the computed Fourier peaks. Using these data, the atomic structure can be refined, and the final R value is displayed.

In all the cases, the quality of the refinement is estimated by considering several

reliability factors (R values). The R value can be defined as follows:

$$R = \frac{\sum_{\mathbf{k}} |I_{\mathbf{k}}^{\mathrm{exp}} - I_{\mathbf{k}}^{\mathrm{calc}}(x)|}{\sum_{\mathbf{k}} |I_{\mathbf{k}}^{\mathrm{exp}}|} \tag{2.8}$$

and can be computed both on observed reflections (R_{obs}), i.e. on reflections usually limited to $I/\sigma(I) > 3$ and on all the reflections (R_{all}).

The computed Fourier peaks can be converted into atoms to complete the structure. Moreover, various restraints can be applied to the structure, such as distances and angles among the atoms, in order to facilitate the computations convergence and therefore the structure refinement.

In figure 2.15, the result of the kinematical refinement performed on Jana2020 on PEDT data acquired on an epidote sample is shown as an example. On the left, an example of computed Fourier maxima is reported, while on the right we can see the solved crystal structure visualized on Vesta. The Fourier peaks are visible in yellow superimposed to the structure.

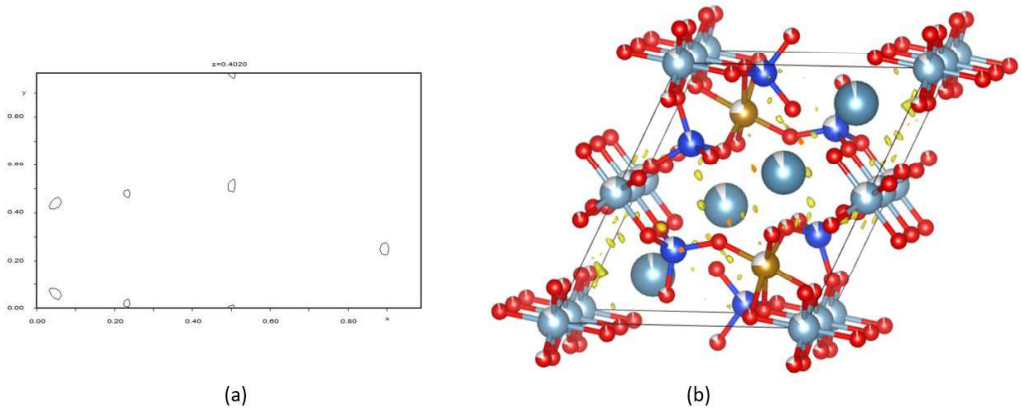

Figure 2.15: The result of kinematical refinement performed on Jana2020 on PEDT data acquired on an epidote sample. (a) Fourier Contour on the (x, y) plane for the desired value of z, (b) the atomic structure visualized in Vesta superimposed to the computed Fourier peaks.

Once the refinement is completed, the result can be exported in .cif extension in order to easy visualize it on Mercury [64] or Vesta [65].

While kinematical approximation is suitable for X-Ray Diffraction data, in real cases, while impinging a sample, electrons undergo more than one scattering event, generating the so called *dynamical diffraction*. This phenomenon breaks the direct proportionality between the diffracted intensity and the Fourier transform of the electrostatic potential that we described in equation 2.2, it becomes stronger with thicker specimens and significantly affects the measured diffracted intensities which are used to compute and refine the crystal structure. Therefore, in order to obtain an accurate structure solution, it is necessary to consider dynamical scattering events [66].

Two different methods can be used to compute the scattered intensities for dynamical diffraction model: in the first one, known as multi-slice method, the crystal is divided into fine slices in a direction perpendicular to the incident beam, and, for every slice, the electrostatic potential is projected onto a plane. Electrons are considered to travel in vacuum in between each slice and to be diffracted as they pass through a slice. In this case, the scattering is numerically integrated and propagation of the electron wave is carried out. This method is suitable when applied to oriented zone-axis diffraction patterns and for simulating high-resolution transmission electron microscopy (HRTEM) images [67].

The second model is the Bloch wave formalism, which relies instead on the solution of the Schrödinger equation for high-energy electrons [68]. In this case the wavefunction is expanded on the basis of Bloch waves describing the propagation states of electrons in a periodic crystal.

In particular, the software Jana2020, which is exploited in the present work for structure solution and refinements, uses the Bloch-wave formalism to compute the diffracted intensities, that are later employed for the least-square refinement [69].

In Bloch wave formalism, the process for calculating intensities can be divided into several steps: The first step is to define all reflections contributing to diffraction, i.e., those close enough to the Ewald sphere (with an excitation error S_g less than a threshold value to be defined) and involved in the refinement. To do this, a structure

matrix A needs to be constructed, which is independent of the crystal orientation. This matrix A is a square matrix with the number of columns equal to the number of beams considered in the calculation. For example, for three beams, the matrix A can be written as follows:

$$A = \begin{pmatrix} 2K & U_{-g} & U_{-h} \\ U_g & 2KS_g & U_{g-h} \\ U_h & U_{h-g} & 2KS_h \end{pmatrix} \tag{2.9}$$

where the diagonal and off-diagonal elements are, respectively:

$$a_{ii} = \frac{|\mathbf{K}|^2 - |\mathbf{K} + \mathbf{g}_i|^2}{(1 + g_{n,i}/K_n)^{1/2}} \tag{2.10}$$

$$a_{ij} = \frac{U_{g_i - g_j}}{(1 + g_{n,i}/K_n)^{1/2}(1 + g_{n,j}/K_n)^{1/2}} \tag{2.11}$$

$\{\mathbf{g}_i,\ i = 1...n\}$ = set of n diffraction vectors considered for the calculation
$\mathbf{n}$ = the normal to the crystal surface pointing to the electron source
$\mathbf{K}$ = wavevector of the incident beam
$i,\ j = 1...,\ N_{beams},\ i \neq j$
g_n = projection onto $\mathbf{n}$ of the vector g_i of the incident beams
K_n = projection onto $\mathbf{n}$ of the wavevectors of the incident beams
$U_{g,i}$ = calculated structure factors

If electron backscattering is neglected, the diffracted waves for a thickness t can be represented by the elements of the first column of the scattering matrix denoted as S:

$$\mathbf{S} = \exp\left(\frac{2\pi i t}{2K_n}\mathbf{A}\right) \tag{2.12}$$

$$I_{h,i} = |S_{i,1}|^2 \tag{2.13}$$

Intensities are obtained as the square amplitudes of these elements, each intensity depending on the thickness, crystal orientation, structure factors, and considered beams. Once the intensity model is calculated, the rest of the procedure will be the same as for structure refinements in the kinematical approximation involving the least squares method.

Parameters for Reflection Selection

The selection of reflections that are involved in the refinement is a crucial step to ensure the success of the dynamical refinement. The choice is made based on parameters characterizing these reflections. The most important parameters are described below and schematized in Figure 2.16. Most are specific to electron diffraction dynamical refinement and are not found in the case of kinematical refinement from X-ray diffraction data. Generally, they can be classified into two categories, i.e. parameters related to observed intensities I_{obs} and related to calculated intensities I_{calc}.

Parameters related to observed intensities I_{obs}:

- $S_g^{\max}$(data): the excitation error S_g of a reflection is independent from the integration method. The limit applied to all reflections will be denoted as S_g^{max}(data). It defines a constant thickness band around the Ewald sphere (Fig. 2.16), and only reflections with S_g^0 close enough to the allowed limit are considered. By increasing the value of this parameter, more reflections are included, but they are also further away from the Ewald sphere and therefore generally have lower intensities.

- R_{S_g}: this parameter is specific to the integration method (precession or continuous rotation). It does not only impose a distance limit by selecting a reduced portion of the Ewald sphere, but this distance is also compared to the precession movement amplitude. This amplitude, denoted S_g^{ϕ} (Figure 2.16), can be described as a maximum and minimum excitation error reached by the precession movement around a reflection. It is derived from the precession geometry and is defined by equation 2.14 for a reflection g and a precession semi-angle ϕ.

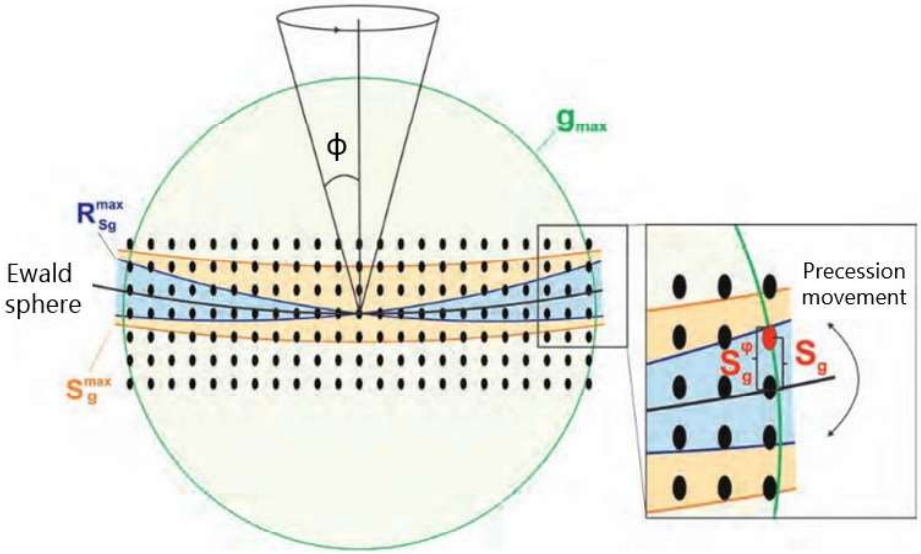

Figure 2.16: Schematic representation of the Ewals sphere, where the different parameters for reflection selection during integration and dynamical refinement are indicated: g_{max} : maximal resolution of experimental data[Å^{-1}], S_g^{max}: maximal excitation error of experimental data, $R_{S_g^{max}}$: ratio between S_g and the precession movement amplitude at the point g [70].

$$|S_g^{\phi}| \simeq S_g^0 \pm |g|\phi \tag{2.14}$$

R_{S_g} can then be defined as the ratio between the maximum excitation S_g^0 for a given reflection g and the amplitude S_g^{ϕ} (eq. 2.15), marked in blue zone in Fig. 2.16.

$$R_{S_g} = \frac{S_g}{S_g^{\phi}} \tag{2.15}$$

Only reflections close enough to the Ewald sphere with a certain ratio R_{S_g} of the precession movement amplitude will be considered in the refinement.

Concretely, this ratio describes how a reflection is covered by the precession movement. In Fig. 2.16, reflections located in the blue zone are those for which the ratio between the maximum excitation error and the amplitude allowed by the precession movement is less than the selected value of $R_{S_g^{max}}$ (see below). If R_{S_g} of a

reflection is less than 1, the Bragg condition is met during the precession movement. The reflection will pass into exact diffraction condition twice during the precession circuit. With $R_{S_g} = 1$, a reflection will pass into Bragg condition at a single point, and if R_{S_g} is greater than 1, the reflection will not reach the Bragg condition during the precession circuit. This reflection is not necessarily absent or weak on the image. Indeed, a reflection can give a significant signal relatively far from the Bragg condition under certain conditions, especially for very thin samples. Finally, a reflection in exact Bragg position (located on the Ewald sphere) will have $R_{S_g} = 0$.

By setting the parameter $R_{S_g^{max}}$ to a value less than 1, the selected reflections will be less influenced by crystal imperfections. This is because the effect of these imperfections in reciprocal space can be described as the convolution of the perfect diffraction pattern and an attenuation function. Considering almost the totality of the reflection intensity (i.e., with R_{S_g} much less than 1) makes them less sensitive to this disturbance. By integrating only part of the reflection, the influence of this disturbance is greater. In the electron diffraction parameters panel in Jana 2020 (Fig. 2.17), by increasing the parameter $R_{S_g^{max}}$, more reflection will be considered in the calculation. By default in Jana2020, R_{S_g} is set at a value of 0.66.

Parameters related to the calculated intensities I_{calc}:

The parameters S_g^{max}(matrix) and g^{max}(matrix) determine the number of beams entering the structure matrix, which will then be used in the calculation of intensities. They are the counterparts of S_g^{max}(data) and g^{max}(data), but related to calculated and not observed intensities. S_g^{max}(matrix) is determined from the vectorial equation 2.16:

$$\mathbf{S_g} = \frac{|\mathbf{K}|^2 - |\mathbf{K} + \mathbf{g}|^2}{\mathbf{2K}} \tag{2.16}$$

In the electron diffraction parameters panel in Jana 2020 (Fig. 2.17), default values are applied for these two parameters and are generally not modified. g^{max}(matrix) is set with respect to the value g^{max}(data) used during the integration (g^{max}(data)

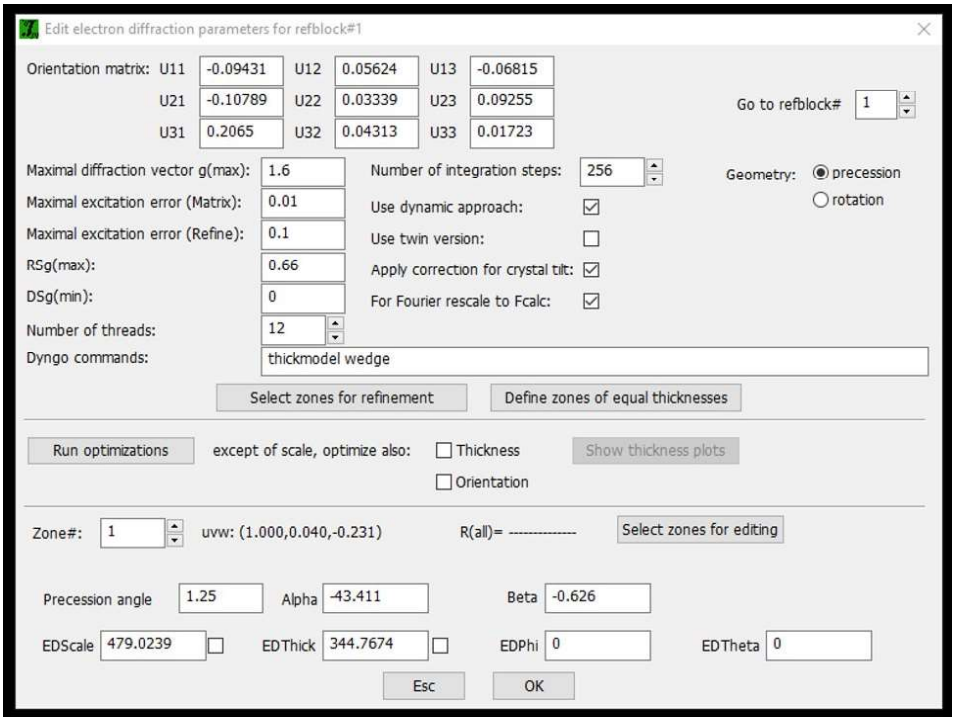

Figure 2.17: Jana2020 panel for setting the selection parameters for dynamical refinements. g_{max} = maximal diffraction vector, maximal excitation error

+ 0.2). S_g^{max}(matrix) is set to 0.01.

The parameter denoted N_{step} is related to the integration method. It is a calculation parameter that indicates the number of evaluations of diffracted intensities along the integration circuit (a circle for precession or a line for continuous rotation). The higher the value is the more accurate the evaluation will be. However, this will significantly increase the computation time.

Determination of the Average Crystal Thickness

During a 3D ED acquisition, the thickness of the crystal crossed by the electron beam will vary with the inclination angle of the sample holder. Moreover, the chosen crystal may not necessarily have a uniform thickness over the entire probed area.

Describing diffracted intensities from an irregularly shaped crystal is challenging. Studies by L. Palatinus et al.[71] demonstrate that in most electron diffraction experiments, the crystal can be approximated as a collection of small sections parallel

to each other with constant widths and variable thicknesses (Fig. 2.18).

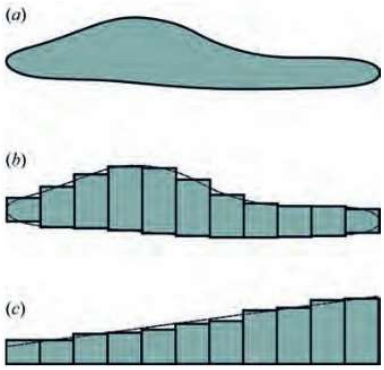

Figure 2.18: (a) Schematic representation of an irregularly shaped crystal. (b) Approximation of the crystal by sections of constant width (c) Approximation of the crystal shape after rearrangement of the sections giving the same diffraction pattern [71].

Diffracted intensities can be calculated as an incoherent sum of all diffraction patterns emerging from each of these small sections. Therefore, the relative positions of the sections are not important, and knowledge of the exact shape of the crystal is not required. The crystal shape can be simplified by approximating it with a few simple geometric shapes such as a cylinder, wedges, or lenses. In the case of electron precession data, intensities are not too sensitive to variations in crystal thickness, and therefore, approximating the crystal as a simple geometric shape is sufficient to describe thickness variations.

The crystal thickness must be refined for each diffraction frame in a PEDT dataset (or each virtual frame in cRED). This procedure is included in the Dyngo program associated with Jana2020 (Fig. 2.17). It involves calculating the weighted factor on the amplitudes wR1(all) as a function of thickness and allows obtaining the type of curve presented in Fig. 2.18. This calculation can be performed considering the structural model obtained directly at the structure solution step or after a structure refinement assuming kinematical approximation. It provides an initial estimation of the quality of both the dataset and the structural model. When the

thickness optimization works well, the wR1(all) curve as a function of thickness exhibits a single minimum for the considered diffraction pattern. Once the thickness optimization is performed for all patterns, an average thickness for the crystal is determined during an initial calculation cycle. Since all patterns come from the same crystal, it is assumed to have a constant thickness, and a correction will then be applied to account for thickness variations due to the crystal shape and its inclination during data acquisition. This is an option activated by default in the electron diffraction parameters panel in Jana2020 (Fig. 2.17). The thickness model can be also changed by passing the command to Dyngo.

Optimization of Image Orientations

The orientation of a 3D ED patterns is initially determined by the chosen lattice and the crystal orientation matrix during the integration step. However, many effects can cause a difference between the calculated orientation and the actual orientation. These effects include the lack of precision in the orientation matrix due in part to the lack of precision in the exact position of the goniometer or to the small movements of the crystal during the acquisition. It is thus necessary to adjust the orientation for each pattern in the dataset. Unlike the average thickness, which is a parameter included in the least squares refinement, orientation is optimized separately. Indeed, a change in orientation induces a change in the excitation error S_g. Since this parameter is a reflection selection parameter, the number of reflections considered in the refinement (in matrix A) can be modified. Consequently, intensities are not monotonic functions of orientation parameters, and the least squares refinement, which is based on the assumption of a continuous gradient, could be destabilized. Importanlty, it was shown that without an integration method (PEDT or cRED), the ED intensities are heavily influenced (wR1(all) factor) by a slight misorientation. The use of an integration method helps to reduce the influence of misorientations on the intensities and thus on the wR1(all) factor. This is a major requirement for sucessful dynamical refinements.

During the refinement in Jana2020, an orientation optimization can be performed

based on the stuctural model where the orientation deviation is described by two Euler angles : EDPhi: rotation around the z-axis during data acquisition. This is the axis pointing from the sample to the electron beam and defines the direction of the inclination angle. EDTheta: deviation of the sample inclination angle across the 3D ED dataset.

Initially, and before any optimization procedure, the crystal orientation is defined by the orientation matrix. This condition corresponds to EDPhi and EDTheta = 0. To optimize the orientation, the program starts by searching for a minimum of the wR1(all) factor around the initial orientation The procedure used by the Dyngo software is based on the "downhill simplex method" . It is a heuristic optimization algorithm adapted to minimize continuous functions in N-dimensional spaces.

The deviation EDTheta from the initial rotation angle is expected to be about a few tenths of a degree. This is generally the case, but it can happen that the orientation parameters diverge towards higher values exceeding 1 degree. This is particularly the case for structures with small lattice parameters since there are, on average, fewer reflections per frame and therefore less information or sensitivity in certain directions. Moreover, the optimization process may fail when frames are dominated by a few very strong reflections. To avoid aberrant results, frames for which the calculated deviation EDTheta are too large should be excluded from the structure refinement.

For users of the program PETS2.0, an option is available to perform a first orientation optimization based on geometry during the 3D ED data integration.

Various tests have shown that the orientation optimization benefits the refinement by providing structures closer to the references and better figures of merit.

2.2 3D ED applied to nanosized domains in functional materials

As an initial observation, of the two major 3D ED approaches (precession-assisted electron diffraction tomography and continuous rotation) the former has been predominantly used for characterizing nanosized domains in materials science. The primary reason is historical, since PEDT has been in use longer than cRED. The second reason is technical: cRED was developed specifically for studying compounds that are sensitive to observation conditions in a TEM, such as pharmaceuticals or organics. While it allows for very short acquisition times, it is more challenging to keep the region of interest within the beam during acquisition. This makes cRED more suitable for 'larger' isolated crystals (greater than 100 nm) with correspondingly large beams (over 300 nm), making it less ideal for studying nanodomains in materials science. PEDT, on the other hand, is better suited for investigating small domains embedded within a matrix or thin films.

We will now see some cases where 3D ED provided significant results in the analysis of challenging samples, providing information on their crystal structure which was not possible to obtain with other characterization techniques, firstly outlining the procedure of sample preparation for performing TEM analysis.

2.2.1 Sample preparation for TEM analysis

Powder grinding

Concerning bulk samples, they are usually prepared for TEM analysis by firstly grinding it in an agate mortar with or without a solvent, in order to reduce the mean dimensions of the crystals. Because electrons interact much stronger with matter than x-rays, very small crystals are sufficient (and required) for electron diffraction. The dimensions of the crystals normally fall in the range from tens to hundreds of nm. The obtained powder or dispersion is then transferred onto a

metal TEM grid (Cu, Au) covered with a carbon film and dried in air when needed. Afterwards, the grid is fixed onto the sample holder, and it is finally inserted into the TEM column under vacuum. It can be useful to check the grid by optical

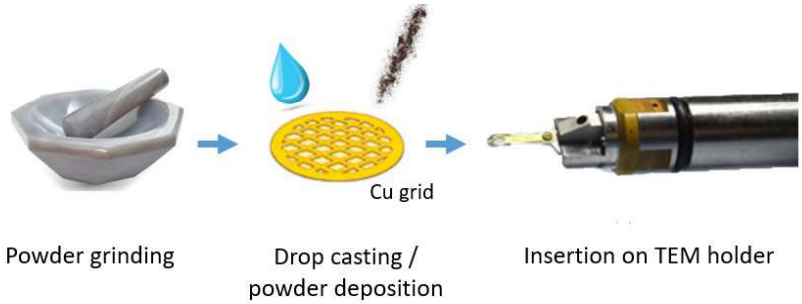

Figure 2.19: Steps of TEM powder sample preparation.

microscopy ensuring that the crystals are not too large in size and are well spread across the grid, so that single nanocrystals can be analysed through diffraction in the TEM. This is an important advantage of 3D ED over PXRD, as it allows to analyse the individual components of polyphasic samples [72]. In case the crystals tends to create aggregates, the sample in solution can be better dispersed through sonication.

Grinding bulk samples is a straightforward and commonly used method for TEM investigations, particularly for ceramics and minerals. This is suitable when there is no need to target a specific area of the sample, meaning that any sufficiently thin fragment of bulk material can be considered representative of the entire compound. This preparation technique has also been adopted for 3D ED to characterize embedded nanodomains, as will be illustrated later. By using this approach, 3D ED data acquisition can be carried out still providing valuable information about the various domains. This is dependent on the ability to collect diffraction data in parallel beam mode over a sufficiently small area to avoid contributions from adjacent grains. When working with selected area diffraction (SAED), the limitation on the size of accessible domains is greater compared to using a nano-beam (NBED), which generally offers more flexibility in achieving smaller beam sizes and, consequently, exploring smaller areas.

FIB cutting for lamellae preparation

When there is a need to target a specific area of the sample, more advanced techniques can be employed. Bulk samples can be prepared as thin, electron-transparent lamellae through methods such as electrochemical, mechanical, or ion thinning. Today, one of the most popular approaches for creating these TEM lamellae is using a focused ion beam (FIB). In the case of epitaxial thin films for instance, this represents one of the most effective methods for analyzing the structure of a film preserving its interactions with the substrate, such as strain.

FIB cutting can be performed with a SEM-FIB system, usually using a Ga beam or a Xe plasma source. As a first step, a protective layer (usually Pt) is deposited on the desired area of the sample in such a way to avoid damages during the cutting stage. Afterwards, the area around the deposited Pt is excavated (trench milling at $\simeq$ 20 nA current) in order to expose a thin vertical layer of the sample (2.20a). At this point, a first polishing of the lamella is performed with a lower current ($\simeq$ 10 nA). After the polishing, un undercut is performed to detach two of the three edges of the lamella from the bulk sample (bottom and one side). The free side is then attached to a needle by Pt deposition and the remaining edge is then cut (2.20b).

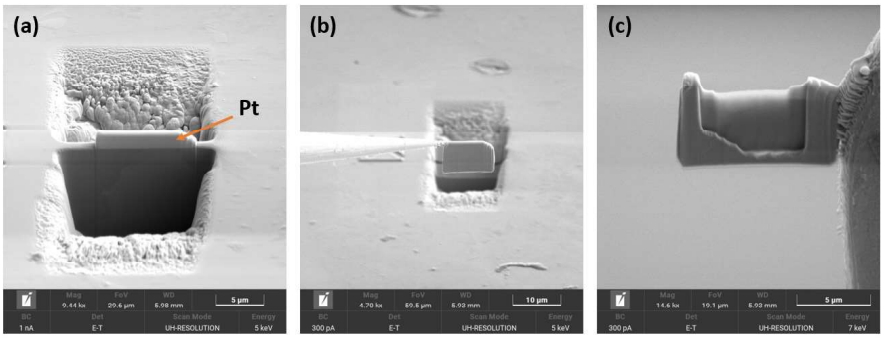

Figure 2.20: Steps of FIB lamella preparation with the TESCAN Amber X SEM-FIB system: a) trench mill, b) lamella extraction, c) polishing.

At this point, the lamella can be lifted out and attached to the TEM grid through Pt deposition, before detaching the needle.

Once the lamella is positioned on the grid, the final polishing can be performed (2.20c) lowering step by step the beam current (from $\simeq$ 250 pA to 150 pA, down to $\simeq$ 50 pA) until reaching the desired thickness (under 100 nm).

2.2.2 3D ED on nanodomains

As we previously outlined, when samples cannot be found or synthesized in the form of single crystals big enough for SC XRD measurements, ED techniques come into play, being very effective for structure solution on single crystals from hundreds of nm down.

In many cases where, apart from the dimensions of the crystals, other features provide additional challenges to X-ray characterization, 3D ED was proven to be successful. For instance, the samples may be found together with other phases, as domains embedded in a matrix with another composition, they may form polymorphs appearing in different order-disorder arrangements, whose reflections may severely overlap; or being characterized by pseudo-symmetries, which can lead to errors in the crystal system assignment [73].

We find as an example the case of $Eu_2Si_2O_7$. The Eu-doped silica glass sample was observed to be composed by Eu-rich nanoparticles, which could be found in small size (30–70 nm) and surrounded by an amorphous matrix, or large (100– 500 nm) and embedded in a nanocrystalline quartz matrix (highlighted in Fig. 2.21a) [73]. While the small nanoparticles composition could be identified by PXRD acquired on an aggregate, the same approach could not be applied for the larger ones, because of the superposition of the diffraction peaks with the ones from the quartz matrix. Moreover, the large particle size lead to incompleteness of the diffraction rings, which can lead to an incomplete indexing. By probing an inclusion with PEDT as a single crystal, their crystal structure could be finally determined as $Eu_2Si_2O_7$ (triclinic, SG: $P\bar{1}$).

In the same study, it is outlined how, through PEDT, it was possible to solve the crystal structure of a phase referred as the 11.2 Å, whose crystallites were character-

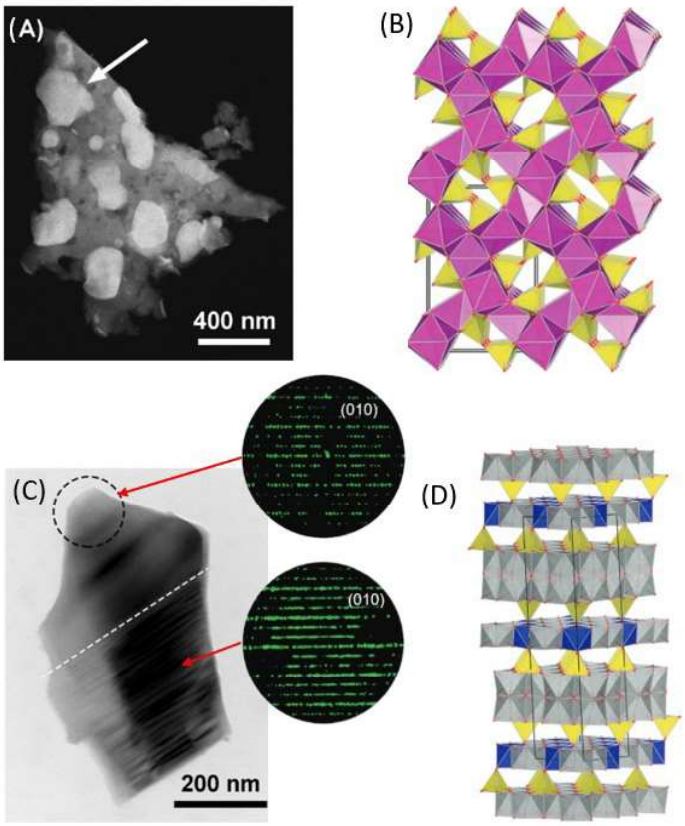

Figure 2.21: a) HAADF-STEM image of Eu-doped silica glass. From EDT performed on the inclusion highlighted with the arrow, the $Eu_2Si_2O_7$ crystal structure (b) was solved. c) BF image of a crystal grain of the phase referred to as 11.5 Å. The ordered area at the top was used for structure solution by PEDT. The difference is visible in the corresponding insets showing the disorder in the reciprocal space sections. d) 11.2 Å phase solved from EDT on the indicated area [73].

ized by randomly stacked layers which provide an important disorder in reciprocal space (Fig. 2.21c). Once an ordered area of the suitable dimension was found, it was possible to perform structure solution obtaining the structure in Fig. 2.21d.

3D ED has later on been applied in the field of cultural heritage. In 2019, Nicolopoulos et al. [74] employed PED-ADT, in combination with other TEM techniques (EELS, EDX, ASTAR), for determining the origin of the pigments in several samples, such as a pottery fragment from a Greek glass amphorisk and a glass Ro-

man Tesserae. The samples showed small crystalline inclusions (around 200 × 200 nm in the first case and 200-400 nm in the second) embedded in an amorphous glass matrix (Fig. 2.22). 3D ED performed on the single inclusions allowed to identify the respective crystal structures, proving how this combination of TEM techniques can be successfully employed to characterize samples which incorporate several crystal phases.

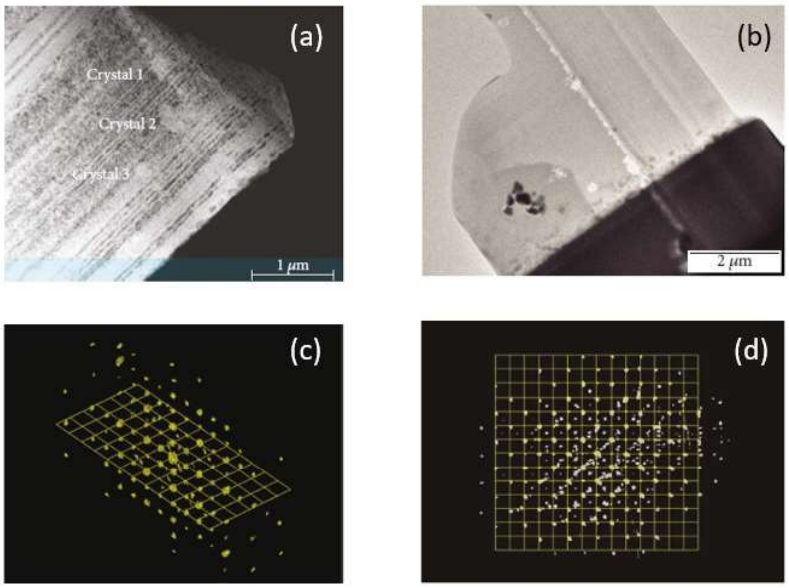

Figure 2.22: (a,b) TEM samples containing crystalline inclusions: pottery fragment from a Greek glass amphorisk and glass Roman Tesserae, (c,d) reconstructed reciprocal space from inclusions in (a) and (b), respectively [74].

More recently, Gollé-Leidreiter et al. [75] (2022) successfully applied PED-ADT to characterize the structure of even smaller crystalline inclusions in a glass ceramic from the MgO–Al_2O_3–SiO_2 system. The sample was synthesized from the parent glass by using as additives La_2O_3 and P_2O_5, which are usually employed in order to lower the melting point making it easier to eventually crystallize into glass-ceramics, in addition to ZrO_2 and TiO_2 as nucleating agents. The thinned sample appeared, as shown in Fig. 2.23, characterized by nano-sized inclusions surrounded by an amorphous matrix. The presence of La and P was observed in the inclusions. However, the known structure of $LaPO_4$ was not fitting the acquired PXRD data. Therefore,

in order to elucidate the structure of the La-containing inclusions, they were probed with PED-ADT in NBED configuration, which allowed to acquire diffraction data with a 10 nm electron beam. This way, the unknown phase was correctly solved *ab initio*, revealing a distorted barite structure.

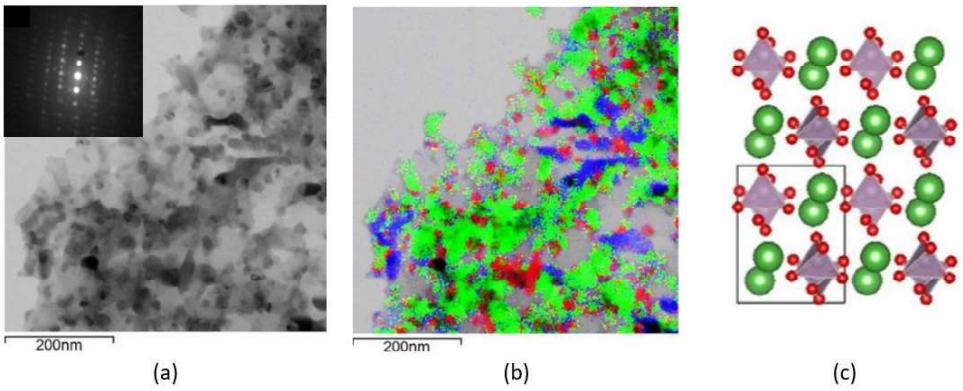

Figure 2.23: a) BF-STEM image of the glass ceramic sample. In the inset, an example of diffraction pattern collected on one of the La-containing inclusions is reported. b) EDX map collected on the same area (green = spinel, blue = $LaPO_4$, red = $ZrTiO_4$, light grey area = SiO_2. c) obtained distorted barite structure, view along b axis. [75].

Following the lead of these examples, we can therefore think of expanding the applications of 3D ED from minerals to a whole range of materials which are characterized by a complex nanodomain structure, from ceramics [76] to planetary samples [77] and, as we will see in the next section, epitaxial thin films. 3D ED performed with a small beam of the domains of interest can in fact provide, by considering dynamical effects in the refinements, accurate structure solutions. This can help us understand the link with their physical properties and in turn to the ability of tuning them by acting on their structure.

2.2.3 Case of study on $Cu_{2+x}Mn_{1-x}GeS_4$ thermoelectric nanocomposites

As a first proof of concept, we will here report our case of study on the series of self-doped thermoelectric compounds $Cu_{2+x}Mn_{1-x}GeS_4$. In literature, it is reported how the family of sulfides with generic formula Cu_2MGeS_4 (with M = Fe, Co, Hg), characterized by tetragonal sphalerite-derived structure, has displayed good thermoelectric figures of merit (ZT). This is not the case of the sulfides Cu_2MGeS_4 with M = Mn, Zn, Cd, showing an orthorhombic enargite structure, a derivation from wurzite. Nevertheless, the physical performances showed by the enargite $Cu_3P_{1-x}Ge_xS4$ compounds (ZT = 0.5 at 673 K) makes this a potentially interesting series to study.

In our case, Cu was substituted to Mn in different quantities, and the resulting self-doped samples were characterized in order to understand the role of the crystal structure features in tuning their thermoelectric properties. PXRD measurements highlighted the presence of two crystal structures in different ratios according to the sample doping, namely the tetragonal stannite (SG: $I\bar{4}2m$) and the orthorhombic enargite (SG: $Pmn2_1$), as we can derive by comparing the experimental diffractograms and the corresponding theoretical peaks shown below (Fig. 2.24).

More specifically, decreasing the value of x, we can observe the progressive appearance of the orthorhombic structure at the expense of the tetragonal one, reaching the single enargite phase at $x = 0$ as expected from other studies on the compound $Cu_2MnGeS4$. However, a more detailed structural analysis was necessary in order to establish whether the samples were biphasic or characterized by a more complex framework.

Notably, all the peaks in the acquired diffractograms appear to be broadened and displaying an asymmetry which is not related to the instrumentation and their intensities deviated significantly from the theoretical ones, indicating the possible presence of structural defects in the crystallites. As a result, Rietveld refinement on

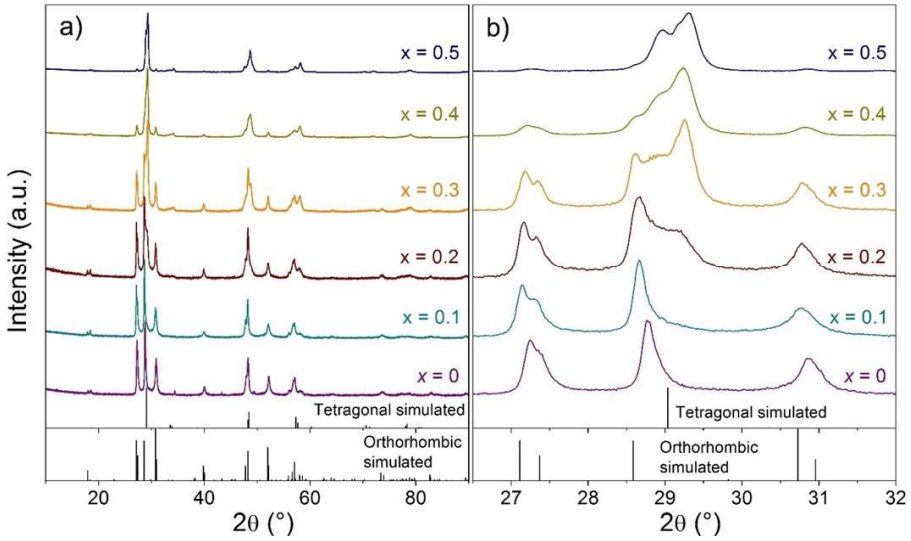

Figure 2.24: a), PXRD patterns for the $Cu_{2+x}Mn_{1-x}GeS_4$ series. The simulated peaks for tetragonal stannite and orthorhombic enargite are shown below. b) an enlarged area of the PXRD patterns [78].

these powder diffractograms failed in all the cases.

In order to confirm the presence of the two phases in the synthesised samples and possibly their microstructural defects, TEM characterizations were performed.

Sample Cu_2MnGeS_4 (x = 0) characterization

Firstly, the pristine sample Cu_2MnGeS_4 was analysed by TEM using the Jeol F200 microscope. It was prepared in form of a powder by grinding it in an agate mortar and then transferred to a Cu grid with C amorphous film and inserted in the TEM. From the acquired Bright Field TEM images (Fig. 2.25) we can see the typical size of the fine isotropic grains (typically smaller than 100nm), where contrast shows stripe-like features, indicating the possible presence of stacking fault or crystal twins.

PEDT was performed on the sample at room temperature on three different crystallites in order for the acquired series to be statistically representative. The experiments were performed in quasi-parallel NBED configuration using the smallest condenser aperture (10 µm). The crystal areas were selected because of the reduced presence of stripe-like contrast. The corresponding lower incidence of defects allows

in fact an easier structure solution and stable refinements.

An electron beam with a diameter of about 70 nm was used, whose dimension was observed to be small enough to probe the desired sample areas. PEDT datasets were acquired respectively on 88, 97 and 93 orientation angles with a tilt step of 1° and a precession semi-angle $\phi = 1.2°$.

The results shown below refer to the probed area in Fig. 2.25c.

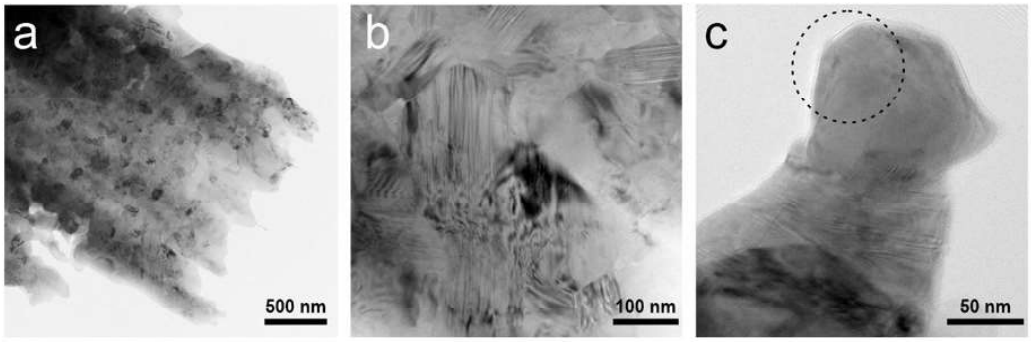

Figure 2.25: Bright Field TEM imaging of sample $Cu_2MnGeS4$. a) typical grain size, b) the presence of stripe-like features across the grains is visible, c) dimension of the area explored with PEDT depicted as a dashed circle [78].

Looking closely at the reciprocal space sections reconstructed from the acquired PEDT series on PETS2, we can observe the presence of two types of reflections, namely the more intense ones, relative to the wurtzite subcell, and the weaker ones, corresponding to the enargite-type supercell (2a, 2b-a, c, [1/2, 0, 0]) (Fig. 2.26).

Structure solution was performed *ab initio* from the acquired tilt series, and successively, kinematical and dynamical refinements of the structure were carried out on Jana2020 [60]. The results are listed in Table 2.1 together with the experimental conditions, while the obtained crystal structure is shown in Fig. 2.27.

In the obtained enargite structure, we find the Cu, Mn and Ge cations tetrahedrally linked to S atoms. The challenge in this case was to identify the atomic positions occupied by the cations Ge^{4+}, Mn^{2+} and Cu^{+}. Determining the localization of these cations is difficult due to their proximity in the periodic table and their similar electronic configurations. While electron diffraction can probe the elec-

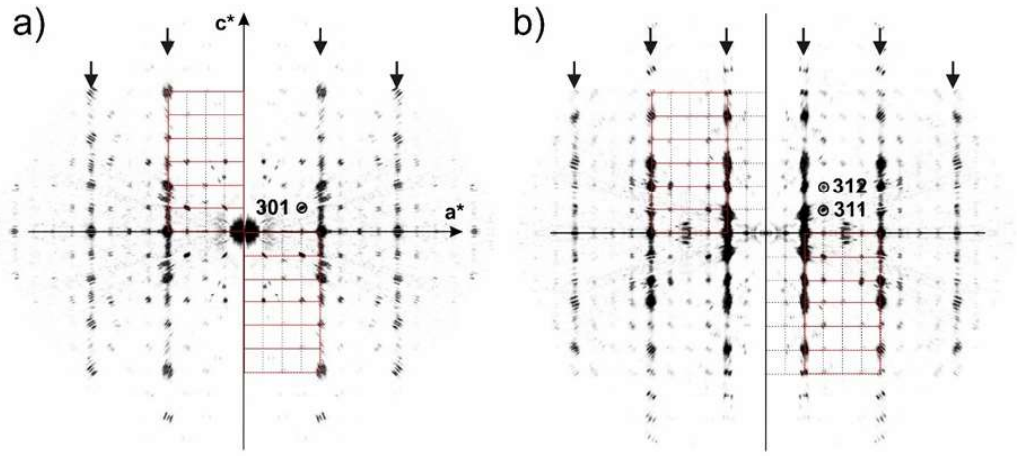

Figure 2.26: Reciprocal space sections reconstructed from PEDT data for the pristine sample Cu_2MnGeS_4, a) h0l section and b) h1l, respectively. The more intense reflections, related to the wurtzite subcell, are highlighted using red lines while weaker reflections, characterizing enargite, are highlighted using black dotted lines.[78].

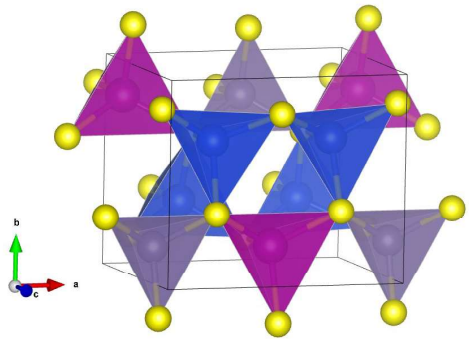

Figure 2.27: Crystal structure of orthorhombic enargite solved *ab initio* from PEDT data on the pristine sample Cu_2MnGeS_4. Color key: Cu in blue, Mn in pink, Ge in gray, S in yellow.

trostatic potential, it has limitations in this context. Bond valence sums (BVS) calculations were performed, based on the results of the structure refinement, in order to estimate the most probable positions occupied by the cations Ge^{4+}, Mn^{2+} and Cu^{+}. BVS calculation relates the bond lengths around an atomic center to its oxidation state, allowing to assign the correct species to each atomic position.

However, as we can observe from the reciprocal space sections, some disorder

Structure type	Enargite
Crystal system	Orthorhombic
Space group	$Pmn2_1$ (SG: 31)
a, b, c (Å)	7.69(1), 6.541(7), 6.340(9)
V (Å^3)	318.9
Number of frames	88
Tilt range (°)	87.7
Resolution $sin(\theta_{max})/\lambda$ (Å^{-1})	0.85
Cumulative coverage (%)	89.5
Measured, observed[I>3σ(I)] reflections	3682, 2342
No. of refined parameters, restraints	100, 0
g_{max} (Å^{-1}), $S_{g,max}$ (Å^{-1}), R_{S_g}, steps	1.9, 0.01, 0.4, 128
R(obs), R(all), wR(all), GoF(all)	0.142, 0.183, 0.179, 6.9

Table 2.1: Crystallographic details of data reduction and dynamical refinement obtained for the orthorhombic phase observed in the sample Cu_2MnGeS_4.

is also present in the crystallite. In fact, diffuse scattering is visible along the c^* direction in *h0l* and *h1l* sections for the rows with index $k - 2h = 4n$ (highlighted with black arrows in Fig. 2.26).

High Resolution TEM images were also acquired on several areas of the sample (Fig. 2.28). These show that the stripe-like patterns visible in numerous grains in BF at low magnification are due to planar defects such as stacking faults and nanotwins, as well as dislocations at the grain boundaries which cause local lattice disorder (Fig. 2.28). These factors are likely to be the main reason for the broadness of the diffraction peaks in Fig. 2.24. Although, other causes cannot be excluded.

Sample $Cu_{2.3}Mn_{0.7}GeS_4$ ($x = 0.3$) characterization

Analyzing then sample $Cu_{2.3}Mn_{0.7}GeS_4$, we could observe by BF TEM that the higher Cu content, corresponding to a lower Mn quantity, leads to the growth of larger and more elongated grains. Also in this case, the vast majority of the grains show stripe-like contrast in BF imaging (Fig. 2.29).

From the HAADF image shown in Fig. 2.30a, in this case we can see, other than

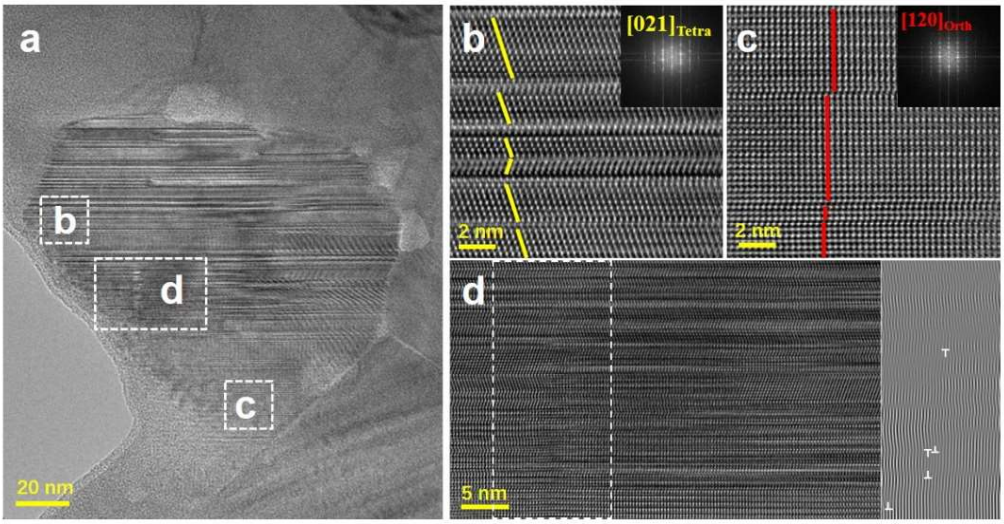

Figure 2.28: HRTEM images of sample $Cu_2MnGeS4$ acquired with a Thermoscientific Talos F200S TEM working at 200 kV. (b-d) enlarged views of the dotted ares in (a). In images (b-c) nanotwins and stacking faults are observable in both the orthorhombic and the tetragonal phase. Dislocations at the boundaries are also highlighted in the filtered HRTEM image at the right panel of (d).

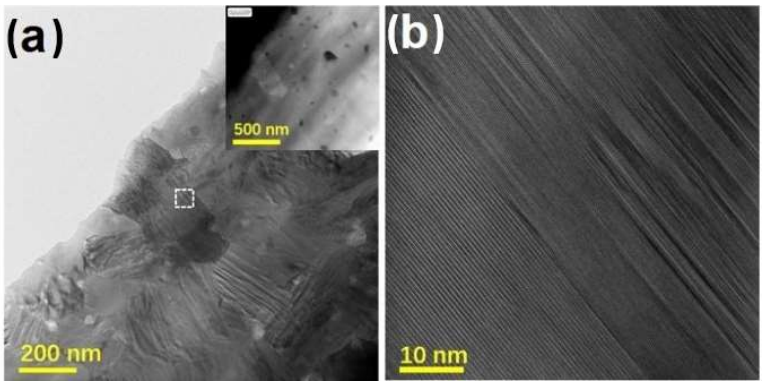

Figure 2.29: (a, b) TEM BF images of sample $Cu_{2.3}Mn_{0.7}GeS_4$.

the dense presence of stacking faults and twins, different crystal lattices coexisting in the same crystallite. The left part, in fact, corresponds to the orthorhombic enargite phase, while on the right portion we find the tetragonal lattice compatible with the stannite phase. The two lattices exhibit in between them specific orientation relationships, namely $[120]_{\mathrm{Ortho}}//[021]_{\mathrm{Tetra}}$ and $(001)_{\mathrm{Ortho}}//(11\overline{2})_{\mathrm{Tetra}}$. This is visible

in Fig. 2.30b, representing the SAED pattern of the area showed in Fig. 2.30d, where the sets of peaks corresponding to both the lattices are present.

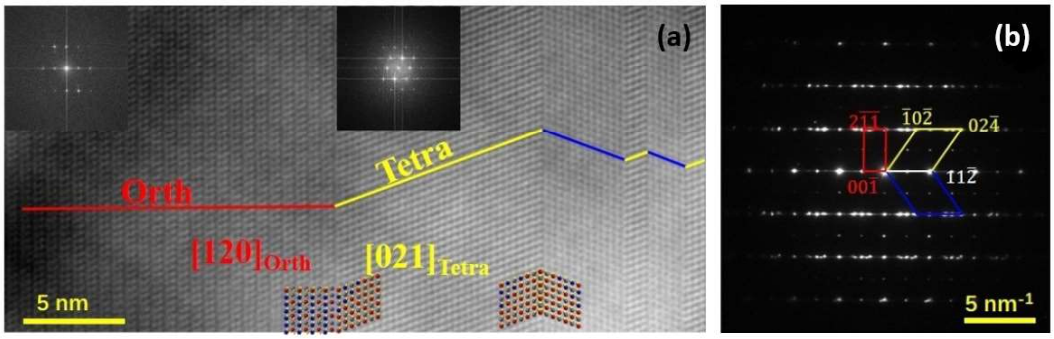

Figure 2.30: Microstructure characterization of sample $Cu_{2.3}Mn_{0.7}GeS_4$. (a) HAADF image and (b) the corresponding SAED pattern of the specimen.

PEDT was also performed at room temperature on different portions of crystallites in the sample in order to confirm the presence of the two phases. The experiments were performed, as in the previous case, in quasi-parallel NB configuration by using the smallest condenser aperture (10 µm) for an electron beam size of about 70 nm. The datasets were acquired with a precession semi-angle of 1.2° respectively on 102 and 99 frames collected with a tilt step of 1°. Both enargite and stannite phases were identified (Fig. 2.31) and structural refinements were carried out. The results of the data processing and dynamical refinements are reported, together with the experimental conditions, in Table 2.2.

Also in this case, bond valence sums (BVS) calculations allowed to identify the correct atomic positions for the different cations in the crystal structure (Ge^{4+}, Mn^{2+}, Cu^{+}). While the refinements allow to distinguish the cationic sites, the stoichiometry Cu_2MnGeS_4 was imposed considering that the potential Mn^{2+} substitution by Cu^{+} would be difficult to probe given their relatively similar atomic number.

We can notice that the cationic arrangements projected along $[010]_{\text{Ortho}}$ and $[111]_{\text{Tetra}}$ projections of the two structures coincide (see Fig. 2.32), which should account for the perfect orientation relationships by sharing coherent interfaces between

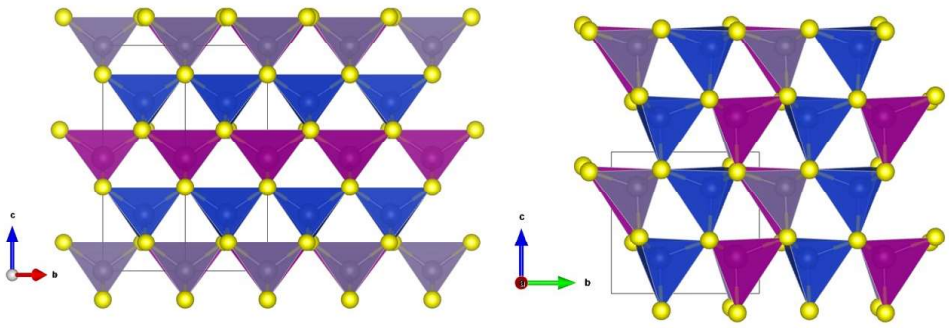

Figure 2.31: Crystal structure representation of Cu_2MnGeS_4 phases with (left) tetragonal stannite-type structure and (right) orthorhombic enargite-type structure. Key: Cu = blue; Mn = violet; Ge = grey; S = yellow.

Structure type	Phase 1: Enargite	Phase 2: Stannite
Crystal system	Orthorhombic	Tetragonal
Space group	$Pmn2_1$ (SG: 31)	$I\bar{4}2m$ (SG: 121)
a, b, c (Å)	7.634(6), 6.558(3), 6.238(3)	5.393(6), 5.393(6), 10.44(1)
V (Å^3)	312.3	303.6
Number of frames	102	99
Tilt range (°)	100.5	97.5
Resolution $sin(\theta_{max})/\lambda$ (Å^{-1})	1.00	0.90
Cumulative coverage (%)	82.2	100
Measured, observed[I>3σ(I)] reflections	7212, 4753	2041, 916
No. of refined parameters, restraints	115, 0	78, 0
g_{max} (Å^{-1}), $S_{g,max}$ (Å^{-1}), R_{S_g}, steps	2.2, 0.01, 0.4, 256	2.0, 0.01, 0.4, 256
R(obs), R(all), wR(all), GoF(all)	0.130, 0.160, 0.157, 5.6	0.129, 0.157, 0.160, 7.8

Table 2.2: Crystallographic details of data reduction and dynamical refinement obtained for the two phases observed in the sample $Cu_{2+x}Mn_{1-x}GeS_4$ ($x = 0.3$)

these two phases. By rotating the grain of about 30° along the direction parallel to the coherent interface, the two phases and nanotwins cannot be distinguished anymore and a single-crystal-like domain appears.

While from PXRD we could suggest a phase mixing between enargite and stannite, TEM investigations revealed a more complex situation. Small areas of (tens of nm) can be associated to either enargite or stannite structure, the majority of the sample shows a fine and coherent intermixing of these two phases within one single grain through the formation of nano-twins. Note that coherent interfaces and

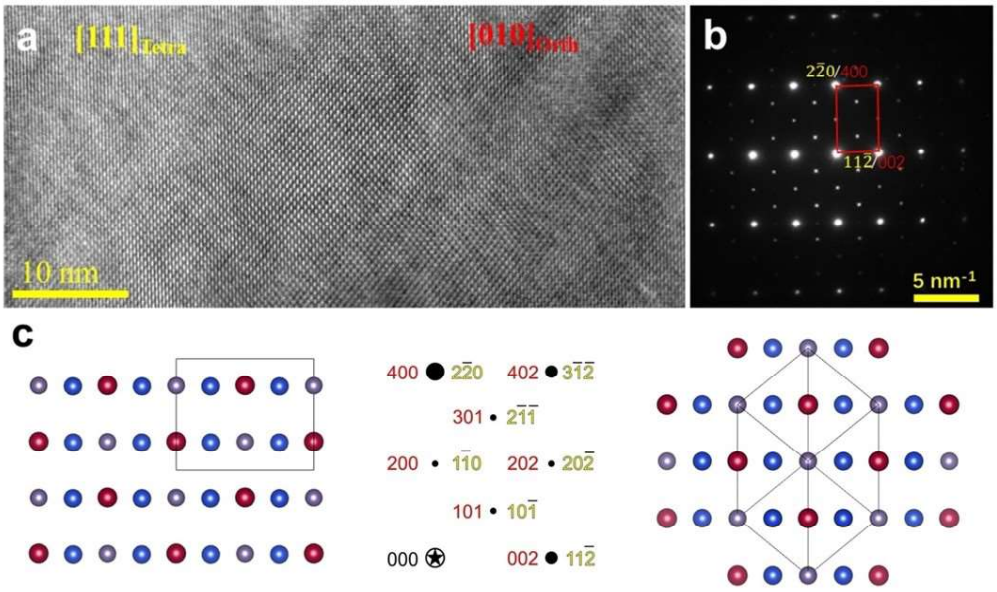

Figure 2.32: a) HRTEM image and b) SAED pattern of sample $Cu_{2.3}Mn_{0.7}GeS_4$ along the direction where the projection of enargite and stannite structures lead to a coincidence in the patterns (highlighted in red), c) cationic positions of enargite (left) and stannite (right) as obtained from the structure refinement against PEDT data. Mn, Cu and Ge are respectively represented in red, blue and grey. In the central part of c), the coincidence lattice in reciprocal space is indexed using both lattices: red for enargite and yellow for stannite.

stacking faults were also reported in enargite-luzonite minerals [79].

A non-periodic approach, based on the general recursion method for crystals containing coherent planar faults developed by Treacy et al. [80] and implemented in the software FAULTS was then used to create a model for a layered structure in which the layer sequence and their stacking vector are determined by a probabilistic law.

The stacking between the two phases was built along the c axis of the enargite cell (corresponding to $(11\bar{2})$ for stannite) in agreement with the direction of the diffuse line in the reciprocal space reconstruction. Using an enargite-derived cell ($a_{\text{layer}} = a_{\text{enargite}}$, $b_{\text{layer}} = b_{\text{enargite}}$ and $c_{\text{layer}} = \frac{1}{2}c_{\text{enargite}}$) both structures could be represented as the stacking of layers depending on the applied shift in directions a and b (see Fig. 2.33).

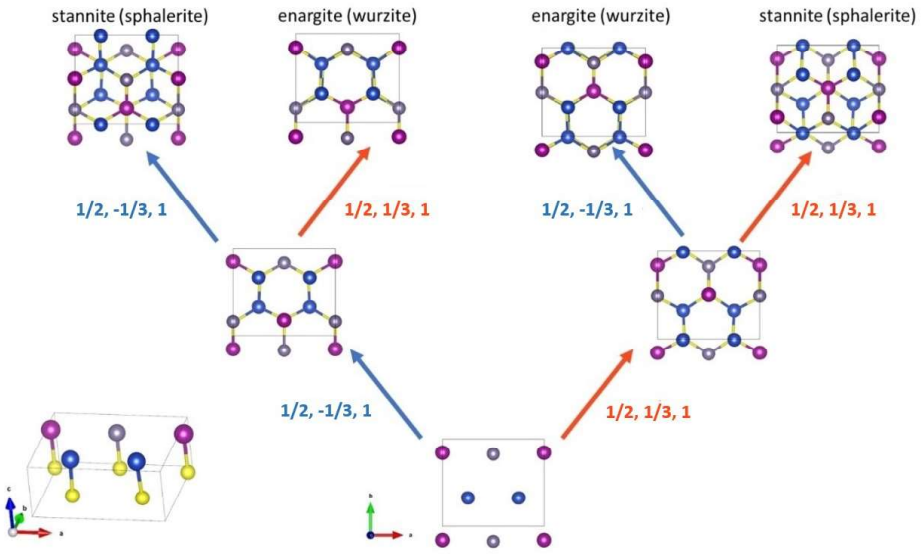

Figure 2.33: Layer cell used to build the composite crystal enargite/stannite and stacking vector used during refinement.

This way, it was found that, depending on the sequence of the applied shift vectors ($v_1 = (1/2, 1/3, 1)$ and $v_2 = (1/2, -1/3, 1)$), we can obtain one of the two phases or the other. By using a sequence $v_1 - v_1$ or $v_2 - v_2$, the stannite structure is obtained, while alternating the two vectors the enargite structure is produced. As a result of the stacking simulation, a probability of about 4% of passing from enargite to stannite was determined, and of about 15% of passing from stannite to enargite.

After physical measurements, it was found an increase in the carrier concentration passing from the pristine sample ($x = 0$), which showed a semiconducting behavior (electrical resistivity $\rho = 5$ Ω·cm) to the Cu-rich samples, which resulted to be metallic with an electrical resistivity $\rho = 1$ mΩ·cm for $x = 0.5$. This observation is consistent with previous studies which relate a Cu hyper stoichiometry with an increase in the hole carrier concentration, and consequently a decrease in the electrical resistivity, in sphalerite systems [81, 82, 83, 84].

This improvement results from the mixed valence Cu^{2+}/Cu^{+}, caused by the substitution of Cu to Mn, by providing a *p*-type carrier delocalization over the Cu-S

network, as already proven for various Cu-rich sulfides [18]. This trend in the electrical resistivity leads to an overall substantial increase of the thermoelectric figure of merit ZT, which makes this newly characterized materials interesting candidates for applications in energy recovery from waste heat.

2.2.4 3D ED applied to thin films

A combination of X-ray, High Resolution (S)TEM techniques and spectroscopy is often employed for the structural characterization of epitaxial thin films to evaluate the effect of the strain imposed to the structure of the film and/or the morphology of the domains. With this approach, relevant quantitative information can be obtained, such as the atomic shift in the unit cell and defects in the structure, which are of fundamental interest for engineering this kind of materials [85]. However, these were generally not used, at least in the recent past, for determining the crystalline structure of thin films through least-squares refinement. On the other hand, 3D ED approaches are primarily employed for solving the structures of unknown compounds and conducting structure refinements. For thin films, the need for structure solution is rare because encountering an unknown structure deposited as a thin film is uncommon.

Nevertheless, when this situation occurs and since the establishment of PED, Electron Diffraction has been introduced as a complementary characterization technique for thin films, considering the significant advantages that it can offer with respect to the widely used X-rays techniques. PED is in fact able to probe a larger portion of the reciprocal space without having the contribution from the substrate, provided that a suitable electron beam size is used. The precession, by integrating the reciprocal space rods, allows *ab initio* crystal structure solution, despite the occurring of dynamical scattering effects [86].

In 2009, Boullay et al.[86] firstly applied PED in Selected Area for probing the cross-section of a $Ca_2Co_2O_5$ (CCO) perovskite thin film grown by PLD on (101)-oriented $NdGaO_3$ (NGO), using a JEOL 2010 (LaB6 cathode) microscope

equipped with a precession module (Spinning Star—Nanomegas). The diffraction patterns were acquired from several zone axis patterns (ZAPs) using the Pleïades (Nanomegas) point detector electrometer. The sample, of about 130 nm thick, was prepared both by scratching the film depositing it on the copper grid dispersed in alcohol and by mechanical polishing followed by ion-milling. In this case the diffraction patterns contained both contributions from the film and the substrate, due to the limits in the available selected area aperture. Nonetheless, from the acquired zone axis PED patterns, the average crystal structure was solved, and the Brownmillerite crystal structure (orthorhombic, SG: $Ibm2$) was refined (kinematical approximation) with an R value around 25%. The limit of this result lies in the low data completeness and in the lack of a refinement method able to account for the significant amount of dynamical scattering which was present is the data, given the thickness of the sample.

From our best knowledge, it is only in 2016 [87] that PEDT was firstly applied to a complex structure in the form of a thin film lamella, allowing to perform *ab initio* structure solution and kinematical refinement. The sample was represented by a heteroepitaxial oxide $Bi_3Fe_2Mn_2O_{10+\delta}$ (BFMO) thin film with a supercell, which was grown on $LaAlO_3$ (LAO) (001) substrate, deposited by PLD. Structure solution performed on Jana2006 revealed that the superstructure was composed by a intergrowth of Bi_2O_2 and $FeMnO_4$ infinite layers (SG: $Amm2$) stacked regularly along the growth direction of the film, after a first 5 nm of interlayer (Fig. 2.34).

Remarkably, this structure has no counterpart in bulk form and exists only in thin films. Following this work, two additional studies were conducted on related systems, where PEDT proved its effectiveness in solving unknown crystal structures deposited in the form of thin films [88, 89].

As state earlier, need for structure solution is rare and scientists working on thin films typically know the expected structure and are more interested in understanding how the structure of the film differs from its bulk counterpart due to strain imposed by the substrate. With this in mind, PEDT was firstly applied at CRISMAT for

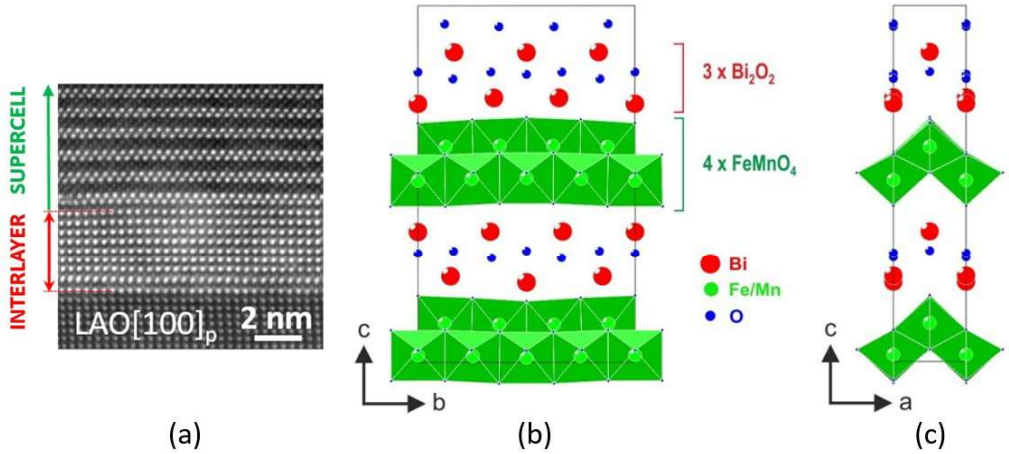

Figure 2.34: (a) STEM HAADF image of the sample, (b) and (c) BFMO SC structure along [100]p and [010]p, respectively, the edge-sharing $[Fe_{0.5}Mn_{0.5}]O_6$ octahedra being represented in green. [87]

the study of perovskite-related thin films. In 2015, PEDT was in fact applied for structural characterization of a 200 nm $LaVO_3$ (LVO) epitaxial thin film deposited on (001)-oriented STO (cubic, SG: $Pm\bar{3}m$, a = 3.905 Å) substrate cut in a cross-section [25]. At room temperature, LVO shows an otrhorhombic structure with the following lattice parameters, a=5.5529(2) Å, b=7.8447(3) Å and c=5.5529 (SG: $Pnma$). From PEDT data, solution of the average structure and refinements in kinematical approximation were performed, obtaining results comparable to the XRD observations with R(obs) $\simeq$ 19%. At that time, the results lacked accuracy for two main reasons: the use of only the kinematical approximation in structure refinement and the presence of twinning. Accurate structure refinement only became feasible in 2015 (Palatinus et al. [71]), and was later applied to the study of CuMnAs thin films [90]. However, challenges remained when twinning was present, an issue that was only addressed starting in 2019 (Steciuk et al. [23]).

In this study, NB-PEDT data were acquired on a 450 nm thick $CaTiO_3$ (CTO) thin film deposited on a $SrTiO_3$ (STO) substrate, and firstly performed accurate structural refinements by accounting for dynamical scattering. PEDT acquisitions were performed both close to the interface with STO and close to surface of the film.

The CTO film appeared constituted by several domains growing in a columnar way with respect to the substrate interface, of about 50-60 nm in width each. Given that the smallest achievable electron beam size was around 60 nm, it was not possible to probe a single non-twinned domain. However, taking into account the twin law, they proved that an R value comparable to the ones of non-twinned data is achievable for dynamical refinement (R(obs) $\simeq$ 13%).

From previous XRD measurements performed on films with different thicknesses, the structural relaxation of CTO was estimated to take place in the first 80 nm from the interface with STO. These observations are in agreement with the Ti-O-Ti angles obtained from the refinements of the structures from the datasets acquired at the interface and at the top of the film. In fact, in this last case the Ti-O-Ti angles were found to be closer to the reference values of bulk CTO. In this case it was therefore

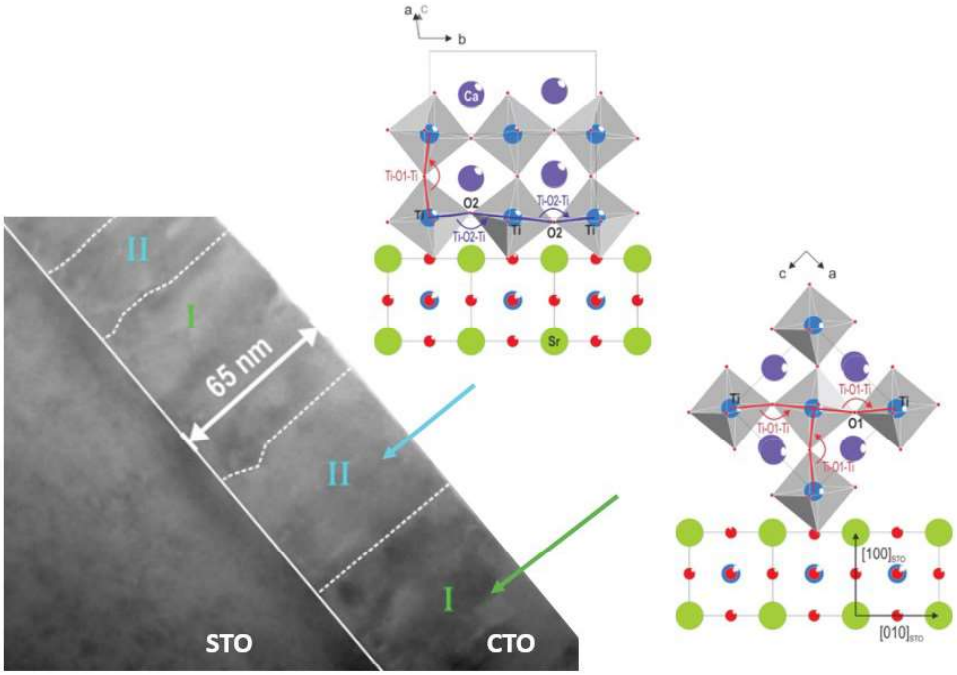

Figure 2.35: TEM BF image of an equivalent CTO film deposited on STO, highlighting the columnar domains with the corresponding refined CTO crystal structure and its epitaxial relation with the substrate. [23].

possible to assess the octahedral tilting characterizing these perovkite structures by PEDT. In this study, the results were accurate, and the idea of investigating the evolution of the structure with respect to film thickness was already in place. However, this study was conducted on a 450 nm thick film, intentionally synthesized for the experiment, which is not representative of typical oxide thin films, which are usually less than 100 nm thick (Fig. 2.35). Additionally, the study was limited by the size of the probed area, which was approximately 60 nm in diameter.

2.2.5 Expected contribution of this thesis

As we previously introduced, this research work is focused on pushing forward the current limits in the characterization of nanodomains in crystalline structures using electron diffraction with a TEM. While cRED or PEDT acquisitions are easy and fast to perform on isolated single crystals, these become hard to implement in samples that show domains in their microstructure as their size goes down the range of 100 nm. These difficulties are caused by the necessity of tracking with the electron beam the specific domain under investigation while tilting the sample with the goniometer. So far, by cRED it is possible to track only single crystallites automatically while tilting the sample with specific software (ex: fastADT, implemented in DigitalMicrograph [91]) while concerning PEDT on smaller domains, advances are under development with precise tracking systems such as the one implemented in TESCAN Tensor analytical 4D-STEM [92].

Apart from the capacity of tracking a small nanodomain while performing tomography experiments, at this stage where accurate structure refinements accounting for dynamical effects has been successfully implemented on software as Jana2020, the main limit to the possibilities of 3D ED is therefore set by the minimum beam size achievable in quasi-parallel configuration.

As in the last years great improvements have been done in the field of TEM functionalities, achieving a significantly smaller electron beam while maintaining a quasi-parallel configuration is now possible. With the arrival of a new JEOL F200 in

CRISMAT Laboratory in 2019, which allows NB-PEDT acquisitions in quasi-parallel configuration with an electron beam down to 10 nm, we have now the possibility of studying much more in detail the crystal structure of nanodomains in functional materials.

As a matter of fact, the question that we want to address in this work is how the available TEM facilities can be exploited in order to obtain a more detailed information about these functional materials by analyzing nanodomains which were until recently precluded from probing singularly, or, in the case of thin films, studying the development of the relaxation that the film undergoes by growing further from the substrate interface.

CHAPTER 3

SPET: combining 3D ED and 4D-STEM

Conventional 3D ED techniques are very effective for structure solution of bulk single crystals. When combined with dynamical refinements, they proved to be effective for accurate structure determination of crystals down to 10 nm in size [93]. However, when the samples under analysis are composed of domains of tens of nm in dimension or we are interested in probing a specific area of a crystal, they show some limitations that need to be addressed. It is in fact difficult to track a specific nanodomain or area of a domain while performing a tomography, even considering the stability of modern goniometers and the available crystal tracking routines. Therefore, in the present work of thesis we are considering whether combining 3D ED performed with a small electron beam size and a scan across the Region of Interest (ROI) of the sample can help us overcome the limits of 3D ED and access a larger amount of information from the sample under test at the same time. In fact, scanning the electron beam across the sample, not only we can bypass the necessity of a high-precision tracking system, but we could as well perform structural analysis of multiple ROIs in our sample with a single acquisition. In the considered approach, the electron beam is

therefore scanned across a defined region of the sample, which can be a line or a 2D area, at each tilt angle during a PEDT acquisition (Fig. 3.1).

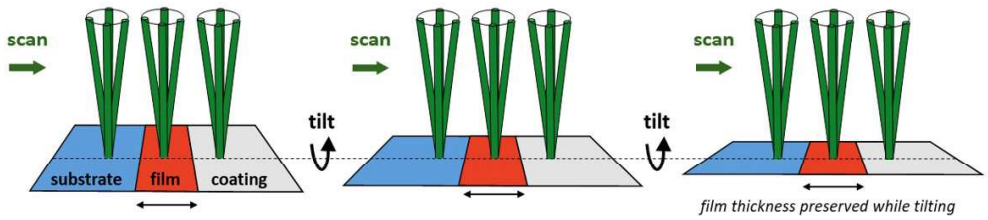

Figure 3.1: Representation of SPET procedure performed on a thin film lamella.

Eggeman et al. [94] actually exploited a similar approach for analyzing the domain volume and orientation in crystalline Ni-based superalloys and used the acronym SPET for Scanning Precession Electron Tomography data acquisition. This concept was also recently used by Rauch et al. [38] in order to reconstruct in 3D the different domains composing a sample using parallel beam illumination. In these above-mentioned works, SPET and 4D-STEM are used for microstructure analysis and, essentially, map known crystalline phases and orientations over an area (2D) or, less often, on a volume (3D) of multi-domain materials. Conversely, in our case the objective is to be apply SPET in two different cases:

- to solve and refine the crystal structure from multidomain samples, i.e. specimen composed by adjacent irregular nanodomains whose dimensions can go below 100 nm, and whose phase could be unknown (e.g. ceramics, geological samples, ...)

- to obtain accurate structural analysis in order to track subtle structural changes within nano-sized domains. In this case, the crystal structure is usually known. These structural modifications can be for example induced by strain, as in the case of epitaxial thin films.

In the first case, it is sufficient to perform the scanning with coarse steps on a sufficiently extended area, while in the second case the step size should be very fine in order to be able to assess the evolution of the crystal structure in a nanodomain.

In both these cases, it is necessary to reconstruct afterwards the diffraction tilt series for each one of the desired domains or regions inside a single domain, and by successively performing structure solution and accurate refinements. We should therefore:

(a) separate the Regions Of Interest (ROIs) at a given tilt angle

(b) relate the diffraction patterns of equivalent ROIs across the tilt series

Considering that usually multidomain samples show very different diffraction patterns on the various domains, the first step can be considered "easy", while the second can constitute a challenge. Conversely, thin films usually show a similar diffraction pattern with respect to their substrate, which could make separating the ROIs on a single scan more difficult.

In CRISMAT Laboratory, the available equipment resulted ideal for testing SPET as a characterization technique for functional materials. The new JEOL F200 TEM allows in fact to perform 3D ED experiments in quasi-parallel configuration with an electron beam size down to 10 nm. In addition, the hybrid-pixel CheeTah M3 direct electron detector from ASI enables fast diffraction data acquisitions, combined with a high dynamic range. The precession movement of the electron beam is controlled and aligned with a NanoMEGAS DigiSTAR unit, which can also manage the scanning of the beam (size of the steps, area dimension and orientation), while the diffraction pattern acquisition is managed by the ACCOS software by ASI. Notably, no synchronization between the scan movement and the acquisition is up to now implemented in the TEM, being the two procedures controlled independently. Thanks to this advanced setup, we are now able to explore new frontiers in the structural analysis of complex structures, paving the way for detailed three-dimensional characterization of nanodomains in functional materials.

3.1 Automatic diffraction pattern sorting of SPET data for structure analysis

Considering the large amount of data that can be collected by SPET, the first problem that rises is how to reconstruct the PEDT series for the Regions Of Interest (ROIs), from which structure solution and accurate structure refinements can be carried out. Notably, our aim is to perform this step without previous knowledge of the phases which are present in the sample, therefore with a different approach with respect to ACOM, based on template matching. This way, it would be possible to apply this method to unknown materials. In our case, the diffraction data was stored as a sequence of .tiff files for each tilt step. Therefore, in order to perform structural characterization of determined areas/domains in the scanned area, it is fundamental to be able to (semi)automatically reconstruct their corresponding tilt series. Despite it is possible to perform this step by manually checking the diffraction patterns, it would make this approach extremely time-demanding. For this reason, different approaches for sorting the diffraction patterns acquired with SPET have been tested. These methods rely on the generally observed resemblance of diffraction patterns acquired on the same crystal on adjacent orientation angles. The choice of the approach is strongly sample-dependent, therefore, rather than trying to find a universal method which is suitable for every kind of acquisition, we focused on customizing the approach for making it optimal for each one of our dataset. The two tested approaches rely, respectively, on NMF (Non-negative Matrix Factorization) decomposition and the direct comparison of the diffraction peaks coordinates ("similarity index computation"), and will be outlined below.

3.1.1 Similarity index computation

An approach based on the direct comparison of the Euclidean coordinates of the diffraction peaks detected on every acquired frame was implemented in Python [95].

The aim in this case was to correlate a determined frame in a scan series with the ones acquired on the following tilt angle. By computing a similarity index in between the reference diffraction patters and the ones on the following scan acquisition, we can in fact not only find the most similar frame and extract this way a PEDT series for the selected domain, but also visualize the similarity percentage across the dataset (on a plot or on a 2D color map) obtaining information about the distribution of crystallographically equivalent domains.

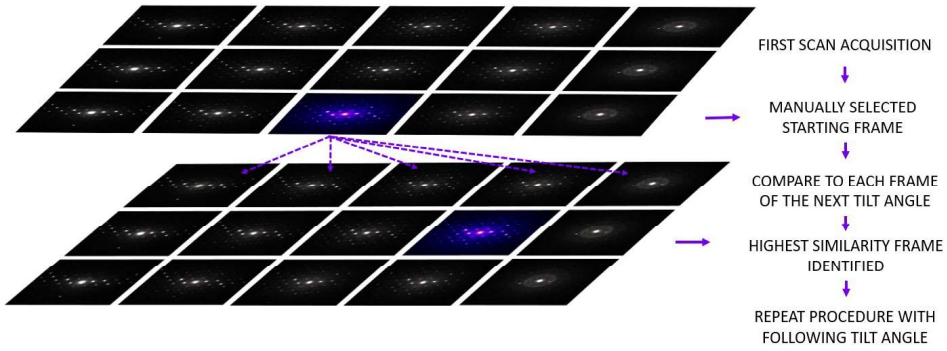

Figure 3.2: Representation of PEDT series reconstruction from SPET data based on the similarity index computation.

The peak detection is performed through PETS2, therefore the first step consisted in the generation of a .pts file for every tilt step of the SPET acquisition. This was then opened on PETS2 and the peak search was performed using the automatic mode with the desired I/σ. This way, for every tilt step, an .rpl file containing the list of the detected peaks for every frame was obtained. For every peak, its coordinates are indicated, together with the number of the frame where it was detected. Using this last index, it is therefore possible to create a peak list for every frame in a specific scan sequence.

It is then possible to re-center the diffraction patterns in order to have a higher reliability on the similarity percentage that will be later on computed. In fact, the central beam (and consequently all the diffracted beams) can undergo a shift during the scan if the first intermediate lens focus does not lie exactly on the back focal

plane. This can be taken into account by extracting from the .logps file (output from the peak search performed on PETS2) the deviation of the central beam from the image center (x, y) detected for every frame. By applying this correction to all the frames, the comparison in between peak positions will result more reliable, since a smaller shift will be detected for matching diffraction peaks.

The procedure requires the user to manually select the starting diffraction pattern among the frames of the first tilt angle, according to the domain of interest. Its peak list is then compared to the peak lists of all the frames on the next tilt angle in order to find the most similar one (Fig. 3.2). When comparing two frames (1 and 2), for every peak of the first diffraction pattern, we check for a match in the second one by computing the Euclidean distance in between their coordinates. The desired tolerance for considering two peaks as matching can be set in pixels (fixed in our case to 4 pixels). The similarity percentage of one frame versus the other one (1 vs 2) can then be computed as a ratio in between the number of matching peaks and the total number of peaks in the reference frame:

$$\text{Similarity } (\%) = \frac{\text{matching peaks}}{\text{total peaks reference frame}} \tag{3.1}$$

Optionally, for a couple of frames, an alternative similarity index can be defined as the average of the two cross-similarities:

$$\text{Similarity } (\%) = \frac{\text{similarity 1 vs 2} + \text{similarity 2 vs 1}}{2} \tag{3.2}$$

The diffraction pattern obtaining the highest score will be selected as match and will become the new reference frame. The two matching diffraction patterns can optionally be displayed as in Figure 3.3, by highlighting the matching peaks.

The choice of how to define the similarity index can be made according to the sample under test and the specific user necessities, since different samples may require one approach over the other to obtain a more reliable identification of the similar frames. In the case of thin film lamellae, where the diffraction patterns of

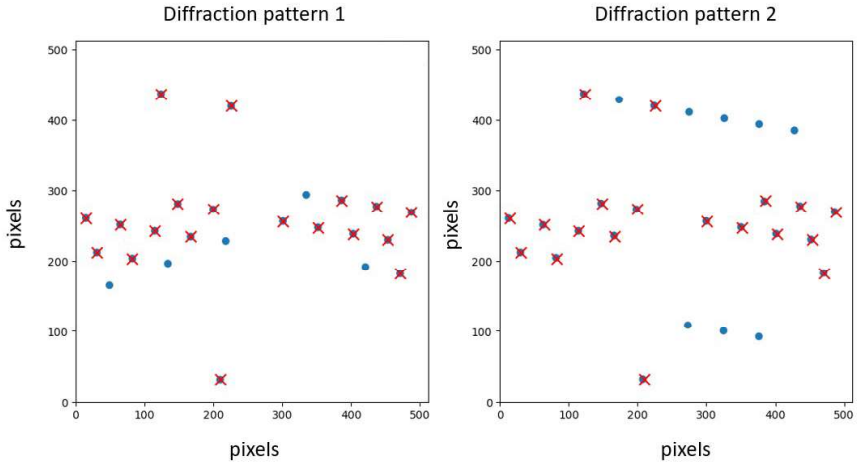

Figure 3.3: Example of diffraction pattern comparison for computing the similarity percentage. On the two images, the position of the detected diffraction peaks is shown as blue circles. The peaks that are found to be matching in between the two are highlighted with a red cross.

the film and the substrate usually have a significant amount of common peaks, definition 3.1 of the similarity index has proved to be more efficient in distinguishing the two domains. Let us take as example the PVO thin film deposited on STO (see section 4.1), where the film shares with the substrate a significant amount of diffraction peaks, showing as well additional ones. When comparing the reference film frame to a diffraction pattern corresponding to the substrate, by considering also the similarity of the substrate frames to the reference, the final score would be higher, being similarity #2 close to 100%. This would make differentiating the two domains more difficult, and in turn, the selection process less reliable. In other cases where the sample is constituted by randomly oriented domains, definition 3.2 may be more reliable instead, since it would decrease the score of the frames where more than one domain gives the contribution to the diffraction pattern. This would lead in turn to a higher data quality and to avoid the risk of shifting from one domain to the other while reconstructing the tilt series. After the most similar frame is chosen, the procedure is repeated again for the following tilt angle, using as a reference frame the selected most similar diffraction pattern.

From the computations, color maps can be displayed in order to visualize the computed similarity percentage across each one of the scans, in order to obtain information about the shape and position of the domains. The map is constructed with the shape of the scan (ex: 50 steps on x, 5 steps on y), and the color of each pixel will represent the computed similarity with that specific diffraction pattern on the scan grid. In Fig. 3.4a, an example of similarity maps computed starting from three different reference frames are shown, from which we can identify the different domains. The maps can then be combined into a single one using a RGB scale to display for every pixel the percentages from the three components (Fig. 3.4b).

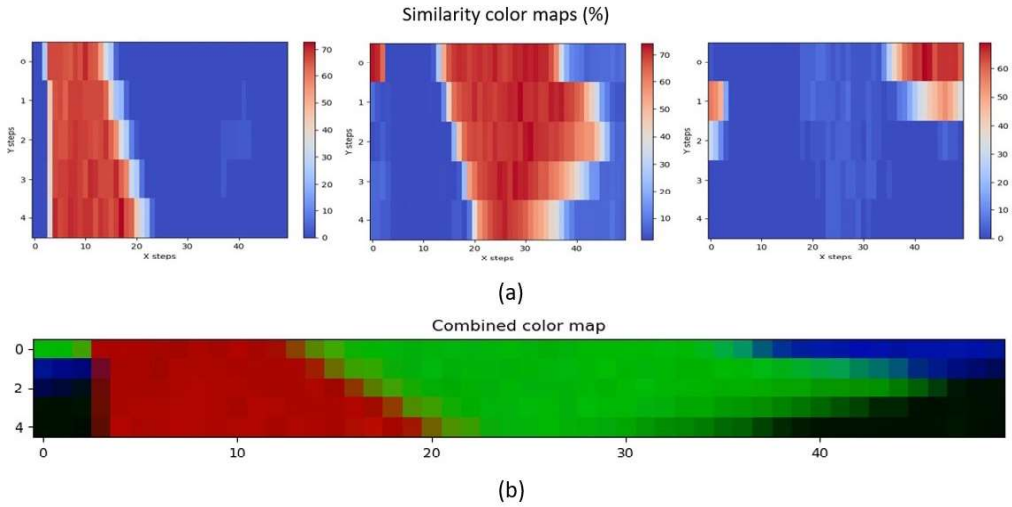

Figure 3.4: (a) Similarity maps (in percentage) computed at the same orientation angle on the scanned area of sample $Al_2O_3/MgAl_2O_4$. The three maps are derived starting from frames associated with different domains. (b) RGB combination of the three previous similarity maps computed on the scanned area of the sample.

Frame-by-frame domain reconstruction

The same approach can be used, with some adjustments, to automatically sort the diffraction patterns generated by the different ROIs of a single domain. By reconstructing the PEDT series for adjacent areas, it is then possible to evaluate potential evolutions in the crystal structure of the domain of interest.

The first step consists, as in the previous case, in selecting, from the first line scan acquisition, a frame positioned around the center of the selected domain. At this stage, it is useful to estimate the extent of the whole domain region in terms of acquired frames by evaluating the frame sequence. This information will be later used to set the amount of diffraction patterns that has to be extracted in order to obtain a list of tilt series that cover the whole extension of the domain.

Setting the selected diffraction pattern as starting reference frame, we can then compute the similarity index by comparing it to the diffraction patters of the following tilt angle, as previously outlined. Afterwards, the trend of the similarities can be smoothed by computing the moving average in a suitable window size, i.e. selecting an adequate amount of neighbours data to consider for computing the average (in our case 4), which is defined as follows:

$$\overline{x}_i = \frac{1}{2M+1} \sum_{j=-M}^{j=+M} x[i+j] \tag{3.3}$$

The average data point is computed by averaging the values contained in the moving window defined as $\pm M$ and centered around x_i. We expect to observe a similarity trend such as the one reported in Fig. 3.5 as an example, which was computed on SPET data from a line acquisition on a thin film lamella starting from a reference frame picked from the film region. In the plot we can see the similarity index (defined as eq. 3.1) computed for each frame in blue and the moving average in orange. Here, we can see that the range of frames showing high similarity corresponds to the region of the film. Before this, we can also observe how the substrate region shows a reasonable average similarity percentage to the film, considering that, in this case, the two unit cells display some common diffraction peaks.

At this point, the derivative of the trend can be computed on the average. By identifying the points corresponding to the maximum and the minimum of the derivative, the frame range corresponding to the domain of interest (in this case the thin film) can be defined. The frame corresponding to the center of the domain

is then set as the medium point in the found range (Fig. 3.5). The highest score frame is then taken as a new reference, and the calculation is performed again for the diffraction patterns acquired on following tilt angle.

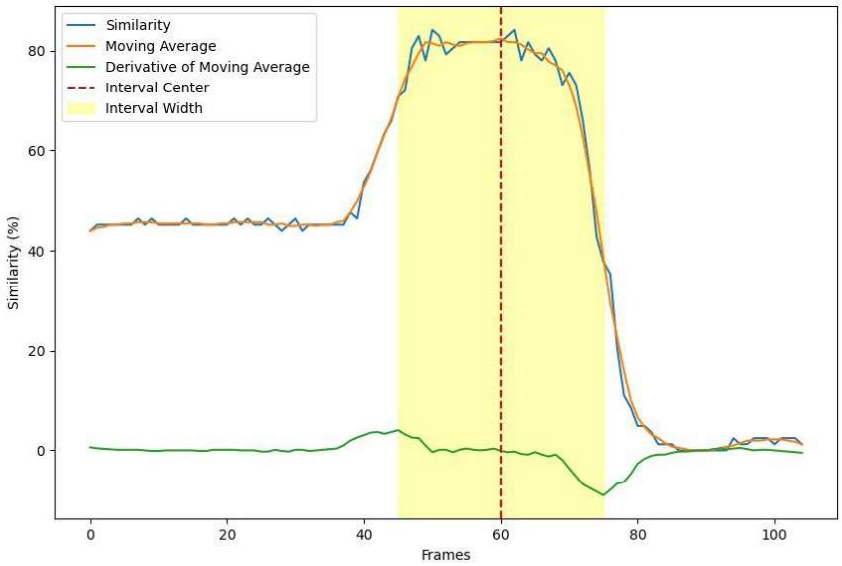

Figure 3.5: The derivative computed on the moving average trend of the similarities is shown in green. Taking into account its minimum and maximum values, the film frame interval is defined (yellow region) and its central frame determined (dotted red line).

By proceeding this way, a list of frames representing the central frame of the film for each tilt angle can be stored. Starting from this central frame, the corresponding tiff files can be extracted in order to reconstruct the tilt series for the middle region of the film. In the same way, the neighbouring ROIs tilt series can be reconstructed by adding or subtracting to the central frame the desired amount of frames. Combining the initially estimated width of the domain region and the average value of the computed width, we can have an indication of how much shift we have to apply to the central diffraction pattern in order to reach the edges of our ROI. At this point, according to how detailed the analysis of the ROI has to be, we can chose to extract all the tilt series or just some of them.

3.1.2 Non-negative Matrix Factorization (NMF) decomposition

Considering a scan sequence of diffraction patterns on a single tilt angle from a SPET acquisition, Non-negative Matrix Factorization (NMF) can be used in order to identify and separate its components. This approach treats every scan acquisition independently identifying frames which are similar to each other, therefore it is then necessary to correlate the components that were found on adjacent tilt angles in order to reconstruct the diffraction tilt series for the desired domains.

NMF is an unsupervised learning algorithm which can decompose a complex dataset into two simpler, non-negative matrices: **W** (basis components) and **H** (coefficients). More specifically, **W** contains information about the individual diffraction patterns of each component in the sample, while **H** tells us how much of each pure signal is present in the mixed signals. It requires positivity constraints to the input matrix (therefore suitable for diffraction data where the signal is a positive intensity) as well as on the derived components. Given a $m \times n$ matrix **A** of rank $r \leq \min(m, n)$, representing our 4D dataset the NMF decomposition approximates **A** as:

$$A_{n,m} \approx \mathbf{W}_{m,k}\mathbf{H}_{k,n} \quad \text{with } \mathbf{k} < min(m, n) \text{ and } \mathbf{W}, \mathbf{H} > 0 \tag{3.4}$$

where rank **k** gives the total number of components. The factorization in NMF is iterative and the goal is to minimize the residual between **A** and **WH** [96].

In order exploit NMF, the Python libraries Hyperspy [97] and py4DSTEM [98] have been exploited. As a first step, it is necessary to convert the series of acquired tiff files in a Hyperspy 2D signal having the shape of the scanned grid. Afterwards, the signal can be imported as a DataCube with py4DSTEM. Afterwards, it is possible to perform a peak search on all the frames in the dataset by cross-correlating a template to the experimental patterns. The template is represented by a synthetic vacuum probe in real space (2D array), whose radius and width can be customized. During the peak search, parameters such as the minimum correlation peak inten-

sity, both absolute and relative to the brightest peak, the the minimum acceptable spacing between detected peaks and the maximum number of peaks can be tuned as required. In Fig. 3.6, an example of peak search performed on three diffraction patterns originated from different sample domains in reported.

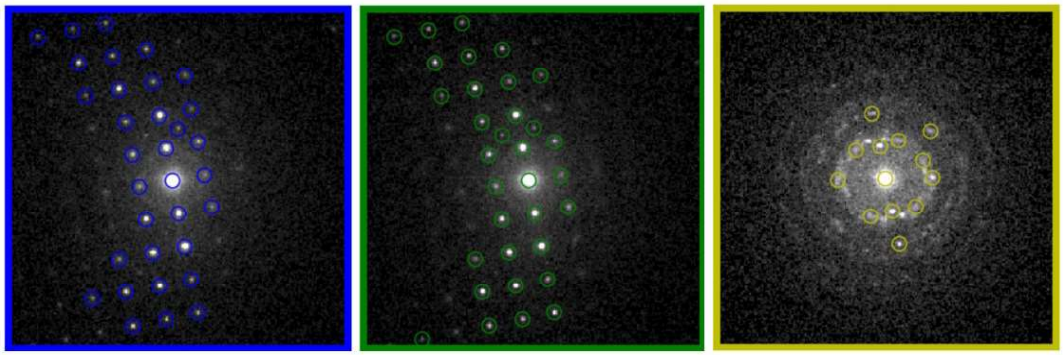

Figure 3.6: Example of peak search performed with py4DSTEM library on three diffraction patterns extracted from a single tilt scan of a SPET experiment.

Once the procedure is completed, an .h5 file containing the list of the found Bragg peaks can be saved and used for the following steps of the analysis. This procedure allows us to eliminate the background noise and to strongly decrease the amount of information that has to be treated, since every frame is reduced to the coordinates of its diffraction peaks, speeding up the following steps of the data analysis.

At this point, it is possible to visualize the raw Bragg peaks map, representing the detected diffraction spots in all the frames projected onto a 2D map. The Bragg peak map can then be centered by computing the origin in each diffraction pattern by exploiting the Friedel pairs and calculating the mean position of these pairs. The origins are then used to re-center all the Bragg peaks positions. Elliptical distortion can also be corrected by fitting a 1D elliptical curve, which is defined by selecting the desired range of distances with respect to the origin, to the data inside the annulus. In case a polycrystalline or amorphous region has been probed, its diffraction rings can be exploited for this purpose. In Fig. 3.7, an example of Bragg peak map before and after the corrections is shown.

At this point, the decomposition can be performed on the dataset through the

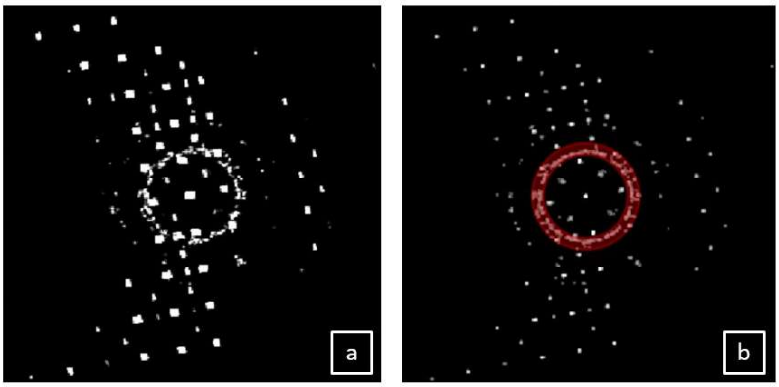

Figure 3.7: a) Example of raw Bragg peak map, representing all the detected diffraction spots projected in 2D, b) the same Bragg peak map after the centering and correction of the elliptical distortion procedure, carried out using the data contained in the selected annulus (highlighted in red).

NMF algorithm. In this case, for every tilt angle, a map representing the scanned area and the relative components found are displayed, which gives information about the domain distribution within the ROI. An example of resulting NMF component map is shown in Fig. 3.8. Here, every pixel corresponds to an acquired diffraction pattern, while the presence of the different found components is represented by the different colors.

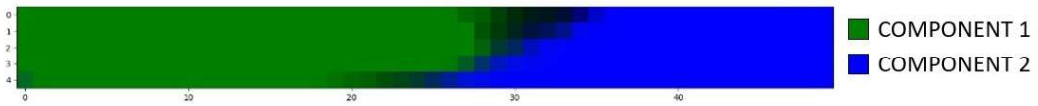

Figure 3.8: Example of NMF components map obtained from the decomposition of one of the area scans performed during the SPET experiment on sample $Cu_{2.3}Mn_{0.7}GeS_4$. Each acquired diffraction pattern is represented by a pixel, whose color is related to the components that it presents.

These results were used to perform the diffraction pattern sorting, by moving to separate folders ("1" and "2") the frames presenting a component higher than the average across the dataset. The following step consisted in reconstructing the tilt series for both domains by checking that to each folder "1" was assigned to the patterns associated with the same domain, as well as for folder "2". Since every scan acquisition is treated independently, there is in fact no correlation at this point in

between the frames being associated with component 1 or 2 at different tilt angles. The tilt series are reconstructed by using the similarity index computation (see previous section).

As a first thing, all the frames in each folder were averaged in intensity to obtain a single average image. All the mean images from the folders "1" and "2" were then put in two directories, and a .pts2 file was created for each one in order to read the sequence of the average images on PETS2. From the peak search on PETS2, an .rpl file containing the list of the diffraction spots detected in each image was produced. This file was then used in order to compare the peaks coordinates of each frame to the following one in order to determine their similarity. In particular, each image of folder 1 was compared to the following one in folder 1 and folder 2. Their similarity was computed following eq. 3.2.

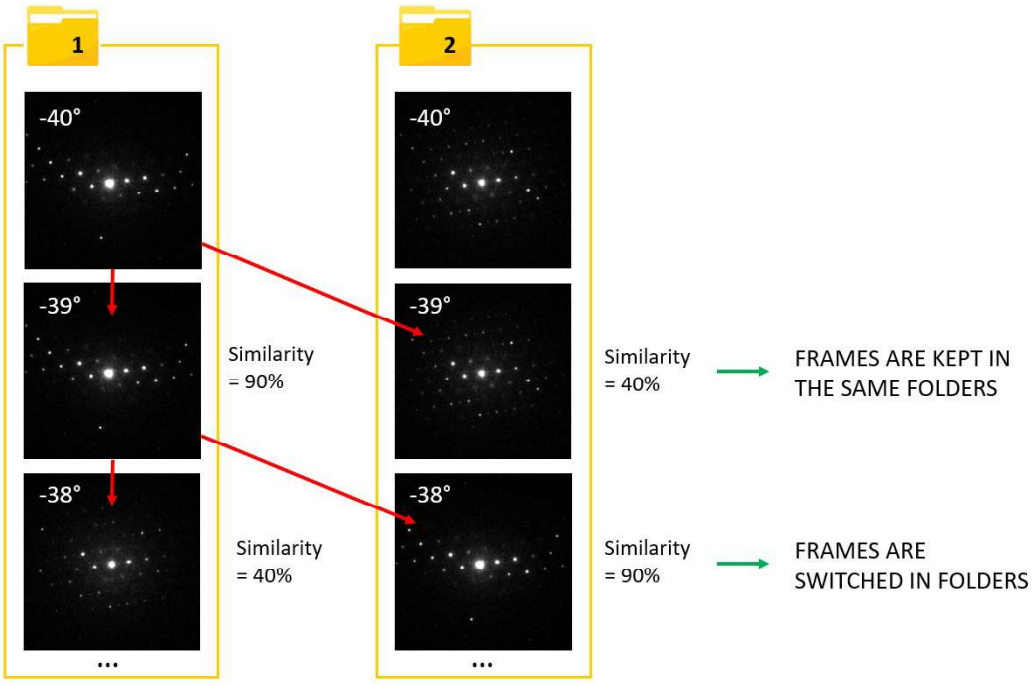

Figure 3.9: Schematic representation of the procedure for the tilt series reconstruction from the average diffraction pattern computed after performing NMF decomposition on every scan acquisition.

If a similarity lower than 50% was found in between two following images in the same folder, and at the same time a similarity higher than 50% was computed with the frame located in the opposite folder, the images are switched directory. The procedure is schematized in Fig. 3.9.

3.2 Automatic data processing of SPET tilt series

Once the acquired frames have been sorted into tilt series according to the regions of interest, being able to process the data consistently and in a fast manner becomes an important objective to achieve. In this section we will outline how the procedure of peak indexation, intensity extraction, structure solution and refinements was optimized for analyzing the SPET tilt series.

3.2.1 PETS2 batch processing

For the automatic peak indexation and intensity extraction on PETS2, a script was implemented for the creation of a .pts file for each one of the extracted tilt series. The preamble containing the information relative to the experimental conditions and commands specifying the parameters for the refinements as well as for the peak integration can be customized according to necessity, while the image list is created by reading the names of the .tiff files contained in each folder. The *autotask* option was exploited in order for the software to automatically go through the whole data analysis process. This was achieved by inserting in the .pts2 file the list of steps to be performed, from the peak search to the integration. If all these commands are properly set, the data processing can be performed exploiting the autotask option without the need of carry out manually each step for every tilt series. An example of the generated .pts2 files is reported in Appendix B.

In case the region of interest covers an area characterized by the same crystal

structure, as in the case of the analysis of thin films along their thickness, we firstly process a single tilt series by choice, and afterwards copy the obtained "petsdata" folder to the directories of the other ROIs. This way, we will make sure that the indexation of the peaks is correct and that the setting of the unit cell parameters is the same throughout all the datasets.

Once all the .pts file have been generated, a Python [95] script was developed for automatically process all the ROIs. Once the main path containing all the extracted ROIs and their corresponding PETS2 data is specified, it accesses each directory in it, opens the .pts file on PETS2 and carries out the processing following the *autotask* sequence.

3.2.2 Structural refinements on Jana2020

In order to perform structural refinements on all the selected ROIs, the *cyclic refinement* tool included in Jana2020 was exploited. This option is meant for refining either powder or single crystal datasets acquired at different temperatures, times or pressures. Therefore, it can be exploited to perform kinematical or dynamical refinements on more than one ROI at a time, sensibly reducing the amount of time needed for analyzing all the datasets from SPET acquisitions.

The process starts by performing structure solution and refinements on a single ROI chosen as a reference. Afterwards, the cyclic refinement file can be created and the .cif_pets files corresponding to the other ROIs can be imported and ordered by appropriately setting the different times (or temperatures/pressure). In our case, the ROIs were ordered according to their position on the sample with the increasing time (see Fig. 3.10). The refinement will be carried out for each ROI by using the atom list from the reference file. The Jana2020 window displayed during the cyclic refinement is shown in Fig. 3.10. At the end of the process, it is possible to visualize the global trends of the obtained R values, as well as coordinates of atoms or angles in between them.

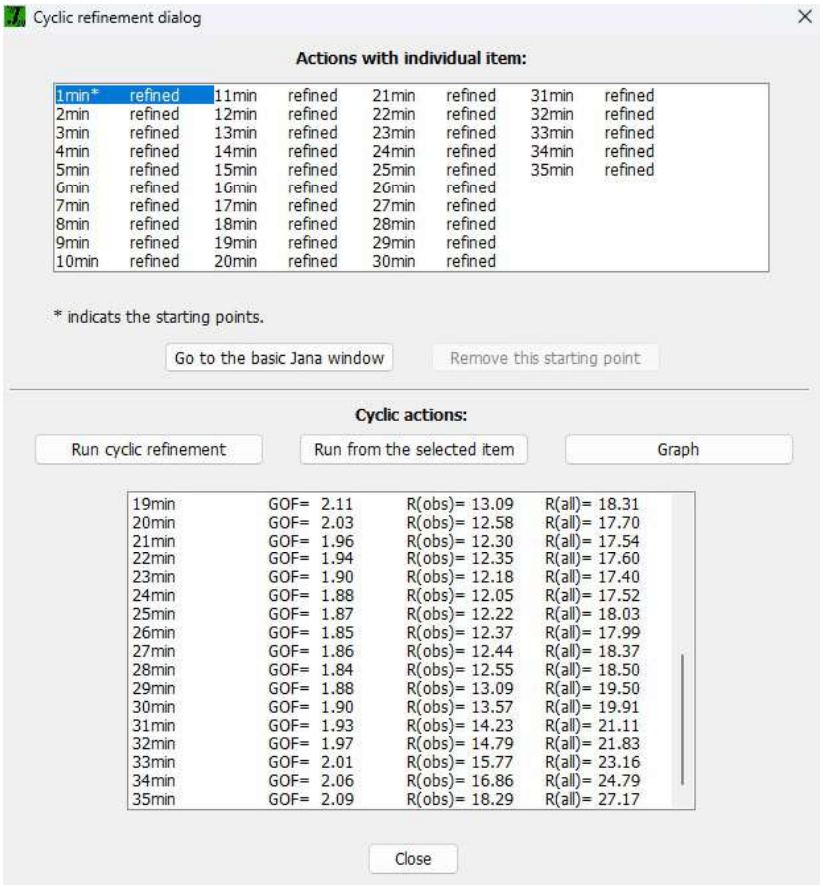

Figure 3.10: Example of cyclic refinement window on Jana2020. On the top panel, the selected files can be visualized, together with the advancement of their refinement. On the bottom panel, the results for each refinement is shown.

3.2.3 Testing SPET on functional materials

In the next chapters, we will apply the previously outlined procedure to process SPET data acquired on the test samples in order to evaluate its potentialities for crystal structure characterization of nanodomains in functional materials as an alternative to classic 3D ED protocols. For this purpose, we choose as representative materials epitaxial perovskite thin films and ceramic materials composed by inhomogeneous domains. Thin film represent an ideal type of sample for testing SPET since their well defined crystallographic domains (substrate, film and eventually an amorphous coating), which makes in principle the identification of the ROIs easier.

However, given the epitaxial relation between the substrate and the film, usually the two share very similar diffraction patters, making the sorting process more challenging. On the other hand, in ceramic materials composed by irregular domains, the sorting procedure is in principle easier given the marked difference usually found in between the diffraction patterns of the different regions. Nevertheless, defects and polycrystallinity could represent challenges at the step of tilt series reconstruction, while their morphology could provide difficulties in probing all the domains of interest during the SPET acquisitions. These two classes of samples represent therefore different kinds of challenges to the characterization of nanodomains that we will try to address case by case.

CHAPTER 4

SPET characterization of epitaxial thin films

4.1 SPET on monodomain PVO thin films

As a first case of study for the application of SPET to functional materials, a perovskite epitaxial thin film was taken into account. The sample was represented by a [010]-oriented $PrVO_3$ (PVO) thin films deposited on $SrTiO_3$ (STO[110], cubic, SG: $Pm\overline{3}m$, a = 3.905 Å). At room temperature, bulk PVO shows an orthorhombic structure (a = 5.487 Å, b = 5.564 Å, c = 7.778 Å, SG: $Pbnm$ [99]). The aim was to perform SPET with a small electron beam by scanning in a direction perpendicular to the interface. This way, we wanted to determine whether it is possible to perform an accurate structural analysis of the thin film across its thickness, evaluating if we're able to appreciate the relaxation of the crystal structure, which can be associated to an evolution in the unit cell parameters and/or in the atomic positions. This sample represented an ideal case of study since it was observed to be composed by a single domain across its length. This limits the number of expected crystallographic ROIs to three (substrate, film and coating) and allows the probed area to be shifted

along the length of the film without significantly affecting the acquired data [100]. Another interesting point is that the film and substrate have distinct diffraction patterns with, notably, more peaks for the film.

In 2020, Kumar et al. [101] used HRTEM to characterize the crystal structure of this sample and other PVO films deposited on STO substrates of different orientations, with the aim to relate each morphology to its specific physical properties. The sample was synthesized by means of pulsed-laser deposition (PLD) using a KrF excimer laser ($\lambda = 248$ nm) with repetition rate of 2 Hz and laser fluence of 2 J/cm^2. The deposition was conducted at 650° and under oxygen partial pressure of 10^{-6} mbar. The samples were firstly characterized by XRD and reciprocal space mapping with a high resolution X-ray diffraction (HRXRD) Bruker D8 Discover diffractometer (Cu $K\alpha_1$ radiation, $\lambda = 1.5406$ Å). These measurements confirmed the quality of the deposited layers and their strained condition.

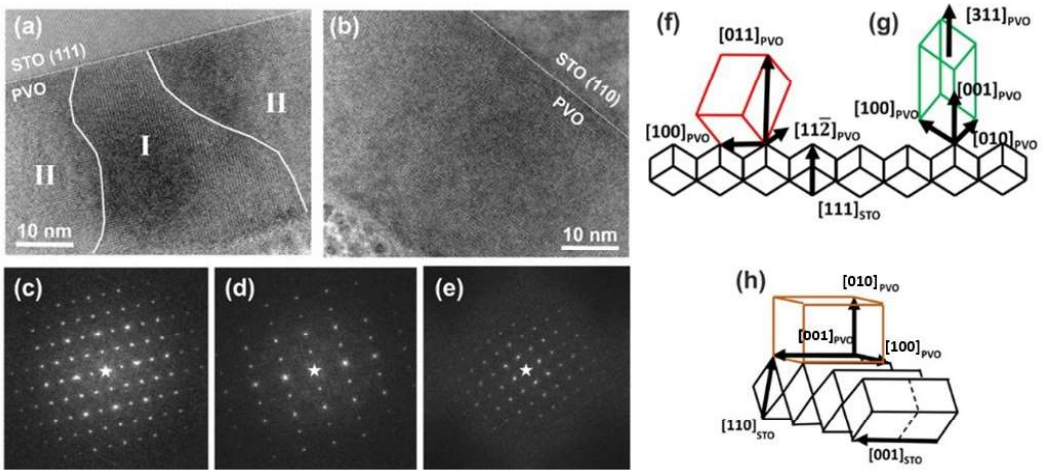

Figure 4.1: High Resolution TEM images of 35 nm PVO films grown on (a) STO(111) and (b) STO(110) substrates. Fourier Transforms obtained for the film on the (111)-oriented STO substrate, corresponding to domain I (c) and domain II (d), respectively. The zone axis pattern for (c) is [011]o and for (d) is [311]o (the subscript o refers to orthorhombic). (e) FT obtained for the film grown on (110)-oriented STO substrate, corresponding to [100]o ZAP. On the right: representation of the observed crystallographic domains in the film on STO(111) (f,g) and STO(110) (h) [101].

RSM investigations confirmed that the films were coherently grown on the substrates, showing completely strained in-plane parameters. According to TEM characterization of the samples cut in lamellae by FIB, the films were about 35 nm thick, and while the film deposited on STO(110) appeared as a uniform domain across its length, the one deposited on STO(111) featured columnar domains with two distinct preferential orientation (Fig. 4.1). Combining the HRXRD $\theta - 2\theta$ and RSM measurements the mismatch in between the STO substrate and the found in-plane lattice parameters in the PVO thin films were calculated ($[001]_o/[001]_{pc} = 0.41\%$; $[100]_o/[110]_{pc} = 0.65\%$, where the subscript o refers to the orthorhombic cell, while pc to the pseudocubic). Given that the bulk STO exhibits an $a^0b^0c^0$ tilting system according to Glazer's notation [102] (no tilt), while bulk PVO has an $a^-b^-c^+$ tilt pattern, we anticipated observing a completely strained segment of the film close to the substrate, as depicted in Fig. 4.2a. This implies that the V-O-V angles of PVO

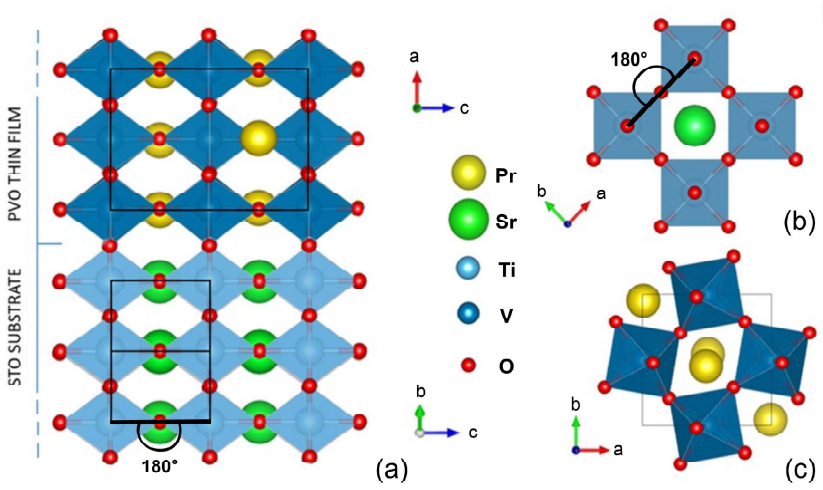

Figure 4.2: **(a)** Schematic representation of the expected strained structure of the PVO thin film on the STO substrate in the first deposited layers, viewed along the direction of the interface corresponding to the a axis of PVO. The unit cells of PVO and STO are represented in black. **(b,c)** Projections along the c axis of the STO and PVO unit cells in bulk, respectively, highlighting the difference in the tilting system of the BO_6 octahedra between the two.

would be close to 180°, as is the case in the perovskite structure of STO. As we moved away from the substrate, we expect a relaxation of the strain imposed on the

film, eventually returning to a configuration of the atoms close to the one observed in bulk PVO, including octahedral tilt amplitudes (Fig. 4.2).

4.1.1 Experimental procedure

As we introduced before, the aim of this study was to assess whether it's possible, by performing SPET with a nanobeam across the thickness of the film and later by performing accurate structure refinement on different ROIs of the sample, to observe and quantify the relaxation of the crystal lattice moving away from the interface with the substrate.

The scan was performed on three lines perpendicularly to the interface, going from the substrate across the film and to the coating. Choosing a scan extension which probed all the domains in the sample allowed us not only to make sure that the film was always fully probed, but also to use the substrate as an internal standard in order to enable, as we will see later, accurate determination of the unit cell parameters (Fig. 4.3). An electron beam with a diameter of about 10 nm was

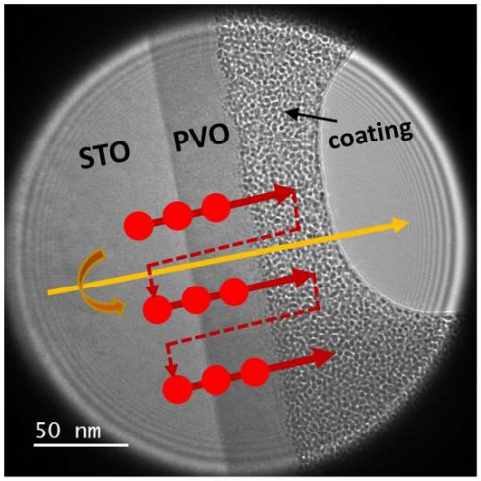

Figure 4.3: Representation of the SPET experiment on the PVO/STO sample. The red dots represent the scanning electron beam, following the red arrows across the defined sample area. The direction along which the lamella is tilted is indicated by the yellow arrow. TEM BF image acquired with Gatan Rio16 CMOS camera.

used, and a step of 1 nm was set in between two diffraction pattern acquisitions (x direction), resulting in oversampling of the specimen. In y direction, the three scan lines were spaced by 30 nm instead. The dimension of the beam was assessed by imaging with the Gatan Rio16 CMOS camera, while the step size was estimated afterwards from the acquired diffraction patterns by observing the moment where the electron beam enters and exits the film. By counting the number of frames included in the film region and comparing it to the dimension of the film, the step size could be finely estimated to 0.92 nm. The diffraction patterns were acquired with the ASI Cheetah M3 hybrid pixel detector (512 × 512 pixels) with an exposure time of 0.02 s. The precession semi-angle was set to 1.4° and aligned with the NanoMEGAS DigiSTAR system. A goniometer tilt step of 2° was applied after each line scan in the range [+44°,-34°], while a tilt step of 1° was used in the range [-34°,-50°]. In order to avoid shadowing of the film by the substrate or coating during the sample rotation, the tilt axis was aligned with the direction of scanning. This way, the observed thickness of the film could also be maintained constant across the tomography [23] (Fig. 4.4).

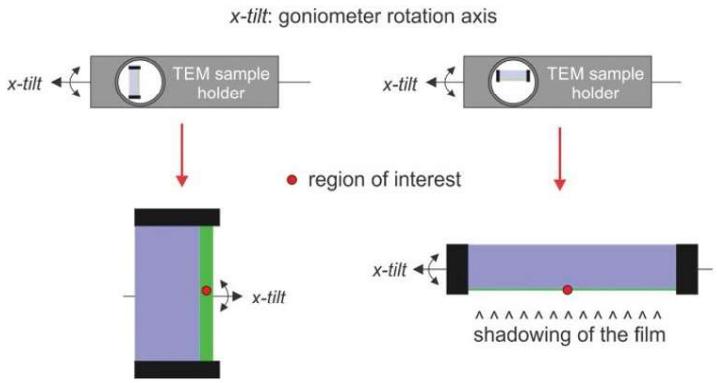

Figure 4.4: Schematic representation of the effect of rotation on the probed sample. In the case on the right the film (in green) is kept exposed, while on the right it gets shadowed by the substrate (in blue) [23].

Notably, no precise tracking of a specific area was performed between each goniometer rotation. This because, as we previously outlined, it would be difficult to

implement without a precise tracking system, and also because we assume the film being homogeneous throughout its length. Moreover, this approach represents a fast and easy way to acquire SPET data. Taking into account a scan of 2 minutes per acquisition, but a longer time to tilt the sample and ensure the right positioning of the electron beam on the desired area, globally a time span of 4h has to be considered. The term fast refers to the time that would require the acquisition of 3D ED data on every ROI. Before each acquisition, it was visually ascertained that the scanned area was centered on the thin film, in such a way to probe all the desired domains contained in the sample.

4.1.2 Data analysis and results

After the acquisition, each scan series was visually analysed in order to estimate the frames where the electron beam entered and exited the thin film, according to the changes in the observed diffraction patterns and, in particular, the presence of additional peaks for the film compared with the substrate (Fig.4.5). This way, the different scans could be aligned and the frames manually extracted for the given thickness of the film, thus reconstructing the diffraction pattern series for all the desired areas out of a single SPET dataset. At this stage, no sorting strategy for the

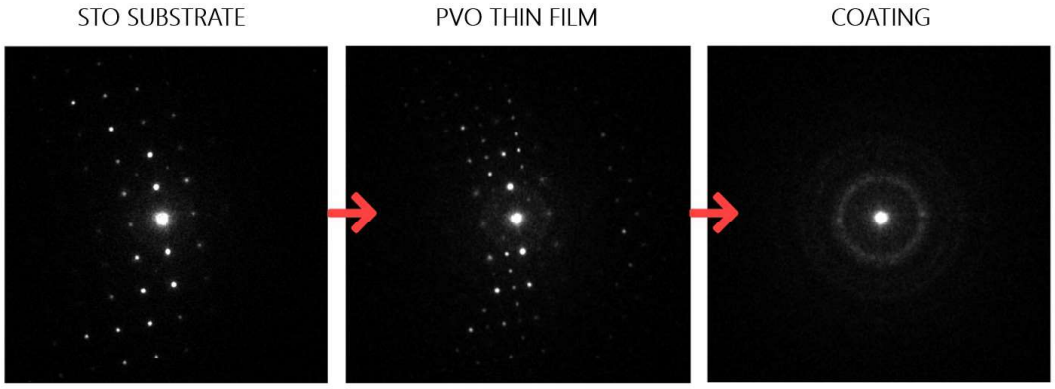

Figure 4.5: Example of diffraction patterns acquired during SPET experiment respectively on the STO substrate, PVO film and poly-crystalline coating at 0° orientation.

diffraction data was still implemented. Therefore, the tilt series reconstruction was done manually. Notably, the frame range where the film was observed showed some differences in number across the tilt steps, probably due to the slight misalignment of the tilt axis with the scan direction, or again the imperfections of the sample and its slight misalignment with the tilt axis. Therefore, some adjustments were needed while reconstructing each tilt series (ex: skip one frame or put the same diffraction pattern in two adjacent series).

Initially, only nine areas across the film thickness were selected for the analysis out of the 38 total from the first of the three scan lines, in order to check if we were able to observe any significant evolution in its crystal structure. The amount of film thickness at which a complete relaxation is observable is however highly dependent on the lattice mismatch between the substrate and the film. However, usually a rapid evolution in the cell parameters is expected in the region close to the interface with the substrate [23, 103]. Therefore, more ROIs were chosen in this part of the film. The second and the third scan lines were taken into account successively, once the automatic procedure for the data analysis was established, in order to validate the previously obtained results. Each ROI is referred to in relation to the distance in nm from the substrate interface, taking as a zero the position where the electron beam lies on the interface itself, as shown in Fig. 4.6.

The obtained results will be presented in this way, in comparison to the reference values for bulk STO and bulk PVO, indicated as squares respectively on the left and right y axis, in the color of the series they refer to. Concerning the unit cell parameters, the values of STO are transformed in order to fit the orthorhombic cell of PVO ($a_{\text{ortho}} = b_{\text{ortho}} = a_0\sqrt{2}$; $c_{\text{ortho}} = 2c_0$). Since a_{ortho} and b_{ortho} are equivalent and superimposed, only one of the two will be visible in the plots. A PEDT tilt sequence of the STO substrate was also considered, in order to use it as an internal reference. Notably, in the interface region the diffraction patterns will show a partial contribution from the substrate as well, which makes accurate information solely from the film hard to obtain. The interested region is highlighted on the results

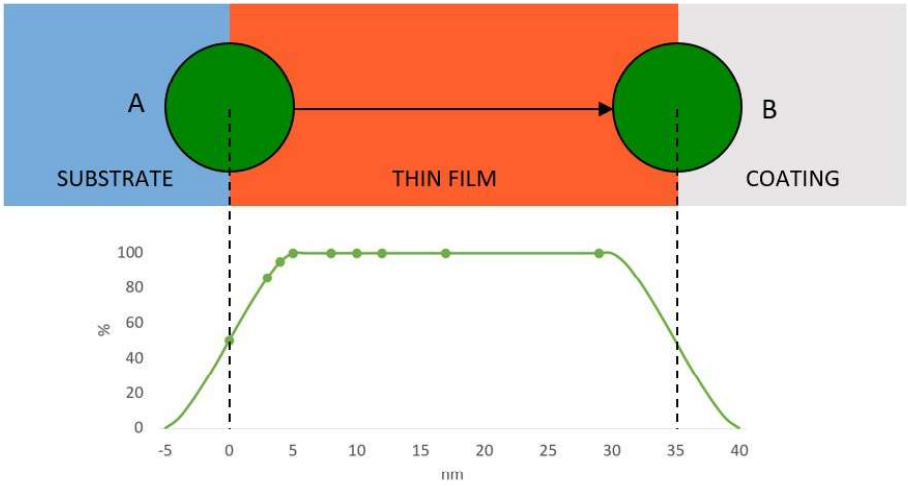

Figure 4.6: Schematic representation of the SPET experiment on the PVO thin film, with the electron beam depicted in green. The horizontal solid arrow indicates the scanning direction, while A and B configurations of the electron beam coincide, respectively, with 0 and 35 in the nm scale. Beneath the scheme, a graph representing the percentage of electron beam area impinging the film for every position is shown, considering a beam diameter of 10 nm. The ROIs that will later be selected for "manual" data analysis are highlighted as green dots.

plots in yellow.

As a first step, the dataset extracted from the bulk STO area was processes on PETS2[55] as previously described (see section 2.1.3), where we could determine the suitable calibration constant (estimated to 0.00708 Å/pixel) by imposing the known STO reference cell parameters and evaluate the refined distortion parameters. Afterwards, the PEDT data extracted from the various regions of the PVO film were processed one at a time using the program PETS2, imposing the previously determined calibration constant. At first, the data were processed by refining independently the distortion parameters of each ROI. After verifying that all of them were not deviating significantly from the values obtained for STO, the distortion parameters obtained from the substrate analysis were imposed to the film datasets and kept fixed.

As a first observation, we assessed the epitaxial relation in between the substrate

and the film. By comparing the reciprocal space of the datasets, we could confirm the alignment of the direction $[010]_{\mathrm{PVO}}$ with $[110]_{\mathrm{STO}}$, resulting in b being the out of plane parameter, while a and c lie on the interface plane. The resulting unit cell parameters for the different ROIs are reported in Fig. 4.7 together with the reference values for bulk STO and PVO. The reference bulk parameters are also reported in Table 4.1.

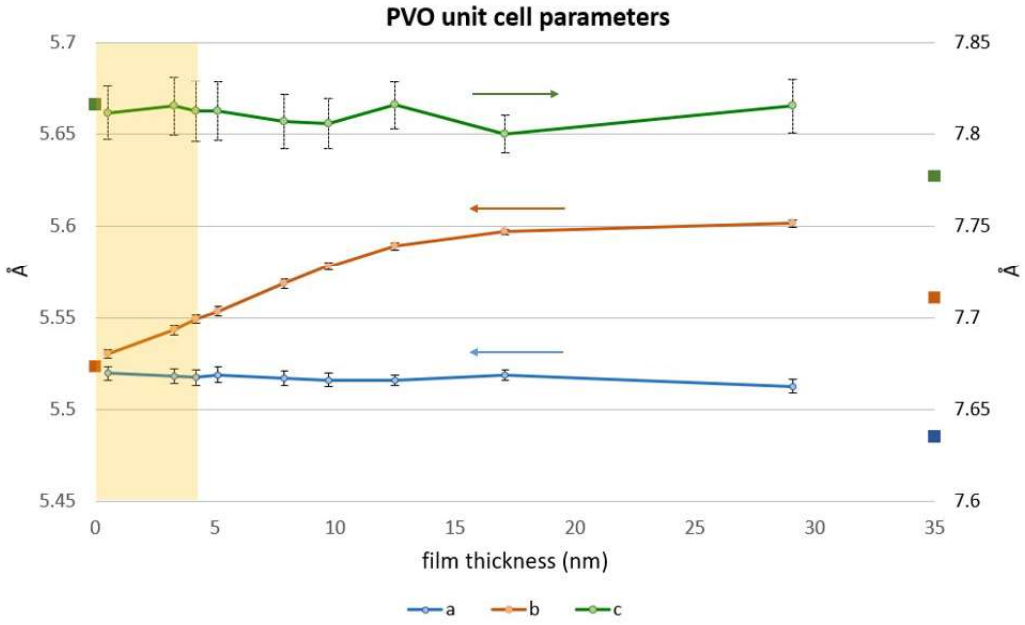

Figure 4.7: Refined unit cell parameters of PVO for different thicknesses of the thin film going from the interface to the surface, the arrow on top of each series indicating the vertical axis they refer to.

It can be noted that the standard uncertainties of the c parameter surpasses of about one order of magnitude the ones determined for a and b. This is due to the fact that, as confirmed at the data processing stage, c direction was the one probed the less during the tomography because of the conformation of the sample and the geometry of the experiment. We can observe that the in-plane parameters of the PVO film a and c exhibit no significant variation along the film thickness, in agreement with the fact that they are strained to match the unit cell of the substrate throughout the thickness, as supported by the Reciprocal Space Mapping (RSM)

	Substrate	Film
Composition	$SrTiO_3$	$PrVO_3$
crystal system	cubic	orthorhombic
SG	$Pm\bar{3}m$	$Pbnm$
a, b, c (Å)	3.905 3.905 3.905	5.486 5.561 7.777
α, β, γ (°)	90 90 90	90 90 90

Table 4.1: Reference crystal systems and unit cell parameters for the $SrTiO_3$ substrate and the $PrVO_3$ thin film [104, 99].

published in Kumar et al. [101]. At the interface, also the b parameter assumes the expected value, almost perfectly matching the a value, and, as a consequence, the cubic crystal structure of the underlying STO. Conversely, getting away from the substrate, we can observe a significant monotonous increase in the out-of-plane parameter, concentrated in the first 15 nm of film, as a result of the relaxation of the PVO. We have to remember that, at $x = 0$ nm, we have a 50/50 contribution to the diffraction patterns from the substrate and the film which affects the results. However, after the electron beam completely enters the film ($x = 5$ nm), we observe a coherent trend, confirming the observations at the interface. Globally, the obtained lattice parameters at the free surface of the film do not match the ones observed for bulk PVO. This can be firstly related to the strain imposed by STO for a and c lattice parameters across the whole film, and secondly to the progressive relaxation of VO_6 octahedra tilt across the film that produces an increase in the b lattice parameter, as it will be discussed later.

To assess whether the evolution of the lattice parameters as a function of the film thickness can actually be correlated to an evolution of the PVO atomic structure, we performed accurate structure refinements for the different ROIs along the film thickness. Kinematical and dynamical refinements were carried on Jana2020 [60] by importing the reference structure of bulk PVO in order to skip the unnecessary structure solution step. It is worth mentioning that, if desired, the PVO structure

can be determined *ab initio* from the experimental intensities recorded using SPET. The results of the dynamical refinements are reported for each one of the selected ROIs in Table 4.2. Notably, the kinematical R(obs) values typically fell within the range of 25 to 30%, while the use of dynamical refinements led to a significant reduction in these values (from 16 down to 12%), attesting a proper account for dynamical scattering effects, and, consequently leading to an improvement in the accuracy of structural parameters.

From the so obtained crystal structures, it was possible to reconstruct the trend followed by the tilt of the VO_6 octahedra across the thickness of the film. In figure 4.8, this tilt is reported as a variation over the angles $V_1 - O_1 - V_1$ and $V_1 - O_2 - V_1$. Close to STO, the strain imposed by the substrate to the PVO structure leads to

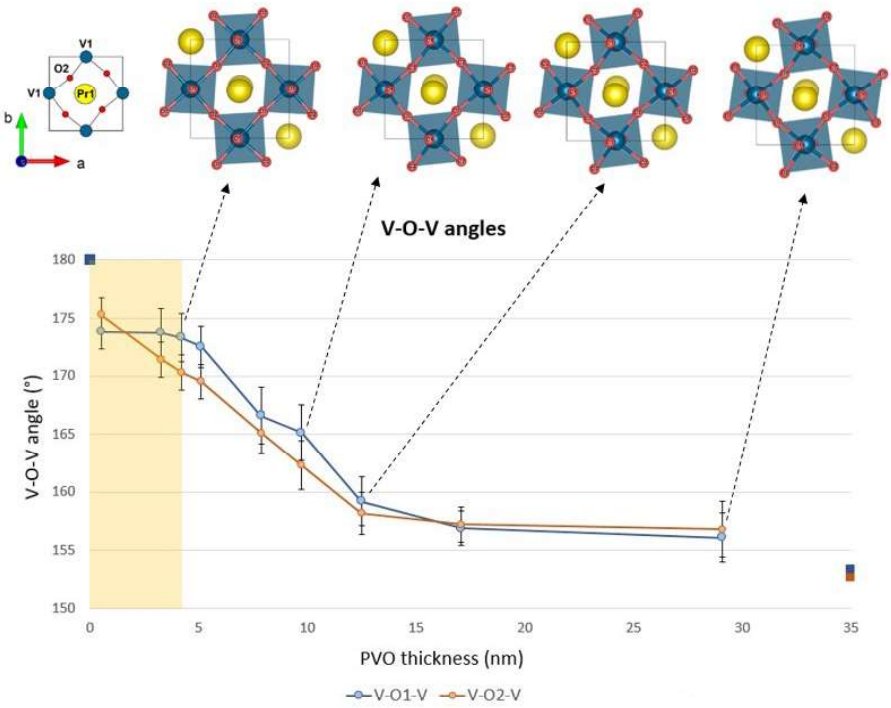

Figure 4.8: Angles for the series $V_1 - O_1 - V_1$ and $V_1 - O_2 - V_1$ obtained from dynamical refinements of PVO for different thicknesses of the thin film. Squares on the left and right y axis indicate the Ti-O-Ti angle for STO and the V-O-V angles in bulk PVO, respectively. Their color corresponds to the color of the series they refer to.

SPET data acquisition		
ROIs per scan in total / PVO	Tilt range	PED semi-angle
120 / 38	95° for 57 frames	1.4°

PEDT data analysis		
g_{max} = 1.6 Å^{-1}	RSg_{max} = 0.4	integration steps= 126
GoF(all) $^{min.}/_{max.}$ = $^{2.96}/_{3.84}$	Robs $^{min.}/_{max.}$ = $^{0.1247}/_{0.1610}$	wRall $^{min.}/_{max.}$ = $^{0.279}/_{0.3412}$

PVO atomic positions

ROI (nm)	x(Pr1)	y(Pr1)	x(O1)	y(O1)	x(O2)	y(O2)	z(O2)
0.52	0.998(2)	0.0078(6)	0.019(4)	0.498(2)	0.741(2)	0.258(2)	0.006(6)
3.28	0.996(2)	0.0140(6)	0.019(6)	0.495(3)	0.736(3)	0.261(3)	0.014(4)
4.20	0.995(2)	0.0161(6)	0.020(6)	0.495(3)	0.735(3)	0.263(3)	0.016(4)
5.12	0.995(4)	0.0182(9)	0.022(5)	0.493(3)	0.734(3)	0.264(2)	0.018(4)
7.88	0.994(2)	0.0257(9)	0.040(6)	0.488(5)	0.727(3)	0.270(3)	0.025(5)
9.72	0.993(2)	0.031(1)	0.046(9)	0.492(5)	0.725(4)	0.276(3)	0.030(6)
12.48	0.993(1)	0.0375(9)	0.063(6)	0.485(5)	0.719(3)	0.281(3)	0.037(5)
17.08	0.9919(9)	0.0428(9)	0.070(5)	0.480(4)	0.715(3)	0.285(2)	0.036(4)
29.08	0.994(2)	0.038(1)	0.073(5)	0.491(4)	0.714(4)	0.282(3)	0.032(6)

fixed coordinates: z(Pr1)=0.25, x(V1)=0.5, y(V1)=0, z(V1)=0, z(O1)=0.25

Table 4.2: SPET experimental specifics and results for dynamical refinements of PVO at different thicknesses. Fixed coordinates correspond to atoms positioned at special positions of the *Pbnm* space group.

V-O-V angles which tend to be close to 180°, implying no rotation. Going towards the coating, both the $V_1 - O_1 - V_1$ and $V_1 - O_2 - V_1$ angles show a decrease, that corresponds to an increment in the octahedra tilting amplitudes, up to 15 nm where a plateau is reached at about 156°, close to the values found in the bulk PVO structure. To illustrate the changes in PVO, a projection of the structure along the c axis is given, specifically emphasizing the evolution of the $V_1 - O_2 - V_1$ angles (as well as the Pr shift — see Fig. 4.9)

Likewise, we can observe the evolution on the Pr atom coordinates in the unit cell, reported in Fig. 4.9. Only the x and y coordinates are considered since z is fixed by symmetry in the space group $Pbnm$. Also in this case, the reference values for bulk STO and PVO are represented as square marks on the vertical axes. We can

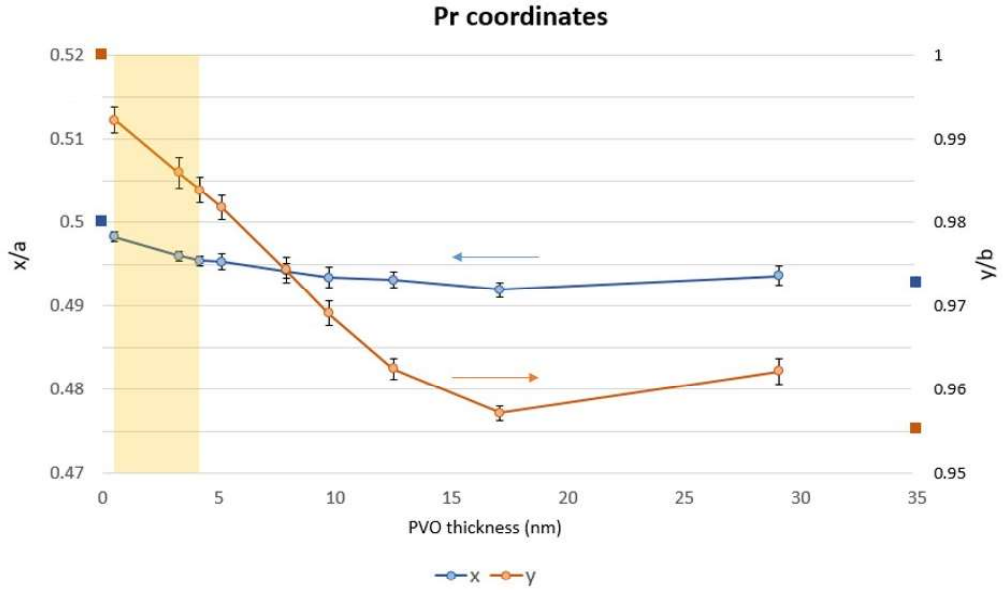

Figure 4.9: Refined coordinates of Pr atom in PVO unit cell for the selection of ROIs across the film thickness. The arrow under each experimental curve indicates the y scale to which the curve refers. z values were not plotted since the Sr atom lies on the special position $z = 0.25$. Squares on the left y axis indicate the Sr coordinates for STO, corresponding in PVO to the atomic site of Pr, while rhombuses on the right y axis indicate the Pr coordinates for bulk PVO, the color corresponding to the one of the series they refer to.

observed that the x coordinate doesn't variate significantly, remaining in the range in between the position assumed in STO ($x = 1$) and in bulk PVO ($x = 0.9928$). On

the contrary, a significant decrease can be observed on y coordinate, which relaxes from the state closer to STO to the one of bulk PVO. This variation is consistent with the strain relaxation along the film thickness observed for the b parameter, since it takes place in the same thickness range. As noted, for the last experimental point, the y coordinate deviates from the bulk PVO value by increasing, conversely to the overall observed trend. The reliability and implications of this result will be addressed more in detail in section 4.2, dedicated to the automatic analysis of all the ROIs probed on the thin film, which will provide a broader statistical basis to help interpret the data.

The evolution of the lattice parameters and structural features obtained using SPET are, globally, consistent with what we could expect considering the strain relaxation where the film tends to recover a structure close to bulk PVO.

4.1.3 DFT simulations

In order to validate the obtained results and have this way an insight into the reliability of the SPET method for extracting structural parameters across the thickness of thin films, *first-principles* simulations were performed on a [010]-oriented PVO film with respect to the orthorhombic cell. Density Functional Theory (DFT) simulations were used, exploiting the Vienna Ab initio Simulation Package [105] in combination with the meta-Generalized Gradient Approximation (meta-GGA) Strongly Constrained and Appropriately Normalized (SCAN) exchange–correlation functional [106]. The initial structure consisted in a *Pbnm* cell, corresponding to a 4 f.u. supercell with respect to the primitive high symmetry $Pm\bar{3}m$ cubic cell and characterized by an $a^-a^-c^+$ octahedral rotation pattern in Glazer's notation [107]. The structural relaxation was carried out until forces acting on the atoms were lower than 0.005 eV/Å. The epitaxial strain experienced by the film was then modeled by imposing the in-plane lattice parameters of PVO cell (a, c) to that of a (110)-oriented STO substrate while leaving b free to relax in amplitude and direction.

After the structural relaxation performed at 0 K, we observed elongated a and c lattice parameter with respect to the 0K DFT bulk structure (i.e., $a_{\text{strained}} = 5.5225$ Å and $c_{\text{strained}} = 7.8100$ Å vs $a_{\text{bulk}} = 5.4856$ Å and $c_{\text{bulk}} = 7.7771$ Å), in agreement with the experimental measurement presented in Fig. 4.7. This causes a contraction of the b lattice parameter in order to minimize the relative volume variation with respect to the bulk ($b_{\text{strained}} = 5.5230$ Å versus $b_{\text{bulk}} = 5.5606$ Å). At first glance, this result disagrees with the experimental value at 293 K reported in Fig. 4.7 (i.e., $b = 5.56$ Å). However, this mismatch may originate from the fact that our DFT simulations are performed at 0 K. A fair agreement is indeed recovered once using the experimental b parameter obtained at 5 K ($b = 5.6061$ Å [108]).

The octahedral rotation amplitudes were also estimated, obtaining $V - O_1 - V$ and $V - O_2 - V$ angles of 152.3° and 154.1°, respectively, fairly in agreement with the experimental observation for these two angles far from the interface, where no substrate effect may be experienced by PVO (Fig. 4.8). The evolution of the b lattice parameter can be put in relation to the V-O-V angles (Figure 4.10) by

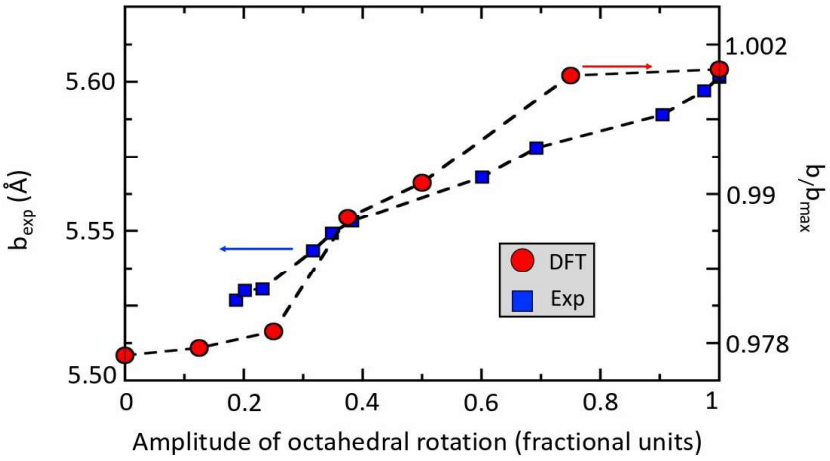

Figure 4.10: Evolution of the b lattice parameter (in Å) as a function of the octahedra rotation amplitude (in fractional units) from experiments (filled blue squares, left scale) and variations in b/b_{max} from DFT simulations (red filled circles, right panel). An amplitude of 1 corresponds to the largest value of octahedra rotation amplitude from theory and experiments, respectively. b_{max} is set to the largest value of b obtained for a rotation amplitude of 1 in the DFT simulations.

fixing a fractional amplitude of the relaxed atomic positions with respect to the high symmetry cell from 0 (no distortion) to 1 (total distortion appearing in the strained material) and performing relaxation of the b lattice parameter. Notably, an elongation of the b lattice parameter is observed as the amplitude of octahedral rotation increases. In the absence of octahedral rotation, the b value across the thickness is expected to be close to the value for $[110]_{STO}$. From 0.25 to 0.75, a progressive elongation of b is present, and above 0.75, b reaches a plateau with its maximal elongation. The overall trend of b versus the octahedral rotation amplitude is well reproduced by DFT, confirming the reliability of the experimental SPET measurements.

In conclusion, by performing SPET along the PVO film thickness, we could analyze the film structure at different thicknesses by properly sorting the acquired diffraction patterns. Cell parameters and atomic positions were accurately determined and an evolution along the thickness of the film was observed in the out-of-plane unit cell parameter, as well as in the tilting of the VO_6 octahedra and in the y coordinate of the Pr atoms. These variations are coherent with the expected constraint given by the substrate in the first layers, and afterwards with the expected gradual relaxation of the crystal structure. However, we have to take into account that it was not possible to obtain diffraction patterns exclusively from PVO within the first 5 nm of the film using a 10 nm electron beam, due to the non-negligible contribution from the substrate. Only an interpolation can be made between a non-tilted perovskite at thickness $x = 0$ and the PEDT data we obtained for thicknesses above 5 nm, where the beam is fully probing the film. DFT calculations were found to be in agreement with the ED data, supporting the results obtained by SPET and demonstrating its validity as a technique to obtain accurate information about subtle changes in the crystal structure of thin films.

At this stage, a faster and more efficient way of sorting the diffraction patters and process the diffraction tilt series is therefore needed in order to analyze with

more accuracy the interested areas of the sample and to obtain reliable results from SPET acquisitions in a reasonable amount of time. In the next section, we applied the automatic data processing strategy and the automatic diffraction data sorting procedure (implemented in Python) and compare the results to the manually processed data.

4.2 SPET on PVO thin film: automatic data processing

Once the ability to extrapolate useful structural information on the sample from SPET was verified, we focused our attention on making data analysis from SPET experiments faster and, as a consequence, more efficient. For this purpose, an automatic procedure for processing the diffraction patterns tilt series of the different ROIs was implemented in Python [95] as outlined in section 3.2.

Notably, in this section, for each scan the identification of the frames corresponding to the thin film will be still done. The problem of how to sort the diffraction patterns without the necessity to check them individually will be addressed later (section 4.2.4). A total of 33 ROIs were reconstructed starting from the interface ($x = 0$) and going across the thickness of the film, by selecting the neighbor frames with respect to the already extracted tilt series (sec. 4.1), and listing them into an Excel file. The tilt series were then reconstructed with a Python script implemented to read the file and copy the original frames into the suitable folders. This way, a step by step analysis of the thin film could be performed. The frames where the contribution from the coating was starting to emerge were not taken into account. Considering that the relaxation of the film was previously observed to reach a plateau at about 15 nm, no significant deviation in the crystal structure from the previous ROIs is expected in this area.

4.2.1 Data processing strategy

As in the previous case (section 4.1), the first step to be performed was the processing of the data series of the STO substrate, used as an internal standard. This way, we could check once again the quality of the data, refine the distortion parameters and the tilt axis, as well as to find the suitable calibration constant. This was done by imposing the known reference parameters for bulk STO (cubic, $a = 3.905$ Å) and adjusting the calibration constant accordingly (0.00708 Å/pixel). The distortion parameters (barrel-pincushion, elliptical amplitude and phase, spiral and parabolic distortion) have been refined as well. These parameters will be later on used as constants for the analysis of the different ROIs of the thin film.

After all the .pts2 files for the different datasets have been created (section 3.2.1), the first step that has been carried out is the manual analysis of a ROI of choice (in our case ROI nr.9), in order to check the quality of the data and find the right unit cell and orientation matrix. The choice of the starting ROI is not expected to affect the results for all the others but just to give as an input the right unit cell. However, ROI nr.9 was selected considering its position in the middle of the observed relaxation region (at about 8 nm from the interface). Therefore, the unit cell parameters for this ROI are expected to lie in the middle of the observed range. Calibration constant and tilt axis orientation have been fixed to the values found for the substrate. The refined unit cell parameter are reported in Table 4.3, compared to the reference values for bulk PVO. The selected Laue class for the peak integration was *mmm*, in agreement with the *Pbnm* space group.

	a (Å)	b (Å)	c (Å)	α (°)	β (°)	γ (°)	vol (Å^3)
ROI 9	5.5268	5.5546	7.8142	90	90	90	239.89
bulk PVO	5.4856	5.5606	7.7771	90	90	90	237.23

Table 4.3: Structural parameters of PVO at the selected ROI, versus the unit cell of bulk PVO.

Afterwards, the processing files contained in the *petsdata* folder from ROI 9 have

been copied to all the other ROIs folders. The automatic analysis of all the layers will then start with the same reference cell with the suitable orientation matrix as an input. In this way, issues due to the automatic cell search, such as the choice of a different unit cell or the switch of the axes, can be avoided.

At this point, the automatic analysis of all the ROIs on PETS2 was launched using the previously described Python script (section 3.2). As a last step, structure solution and accurate structure refinements were performed by exploiting the cyclic refinement option provided by Jana2020 (section 3.2.2). In order to do so, it is firstly necessary to solve the crystal structure and perform the refinement of a dataset of choice, importing then the other ones and eventually launch the cyclic refinement. For each structure, the atom list will be imported from the first reference one.

4.2.2 Results of PETS2 analysis

During the PETS2 data analysis, several parameters have been tested in order to better understand their influence on the obtained results. In contrast with the manual data processing performed in section 4.1, the automatic analysis of the ROIs that is done at this stage allows in fact to carry out a large amount of trials in a reasonable time. The following tests were performed on the ROIs of the PVO film:

1. The ROIs were analysed by freely refining the unit cell parameters while keeping the distortion parameters (barrel-pincushion, spiral, elliptical amplitude and phase, parabolic distortion) to zero.
2. The ROIs were successively analysed by freely refining also the distortion parameters to assess their respective trends and their effect on the unit cell parameters.
3. The unit cell parameters were refined by imposing the distortion parameters calculated for the substrate dataset, serving as an internal reference.

In all the cases, the calibration constant and the tilt axis values were kept fixed to the ones refined on the STO substrate, while the frame orientation and the error

model were refined for each dataset. The results reported in the following plots are shown with the ROIs being ordered going from the region close to the substrate towards the coating, the point $x = 0$ nm representing, as in section 4.1, the ROI characterized by a 50/50 contribution from the substrate and the film.

In Fig. 4.11, the obtained unit cell parameters with distortions fixed to zero are shown. A defined trend can be observed in the b parameter across the film thickness, while a and c appear to remain steady in the whole range. As much as the trends are reasonable, the obtained values for the ROIs close to the substrate don't match the expected strained values, mainly for what concerns a and b parameters, implying a lack of accuracy in the refined unit cell parameters. Therefore, it is reasonable to suppose that the data need a more accurate calibration of the distortion parameters in order to obtain reliable results.

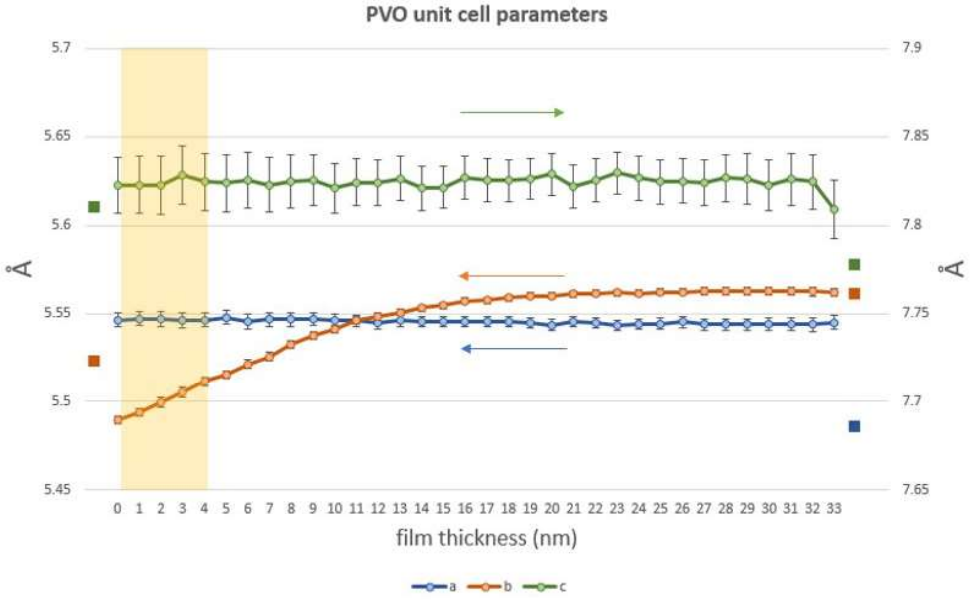

Figure 4.11: Obtained unit cell parameters for PVO in the different ROIs (going from the substrate to the coating) by keeping the distortion parameters to zero. Each curve refers to the vertical axis indicated by the arrow of the same color.

The ROIs were thus successively analyzed by freely refining the distortion parameters, the frame orientations and the error model. Only the calibration constant

and the tilt axis values were kept fixed to the ones refined on the STO substrate. In Fig. 4.12 and 4.13, the resulting unit cell and distortion parameters are reported for all the analyzed layers.

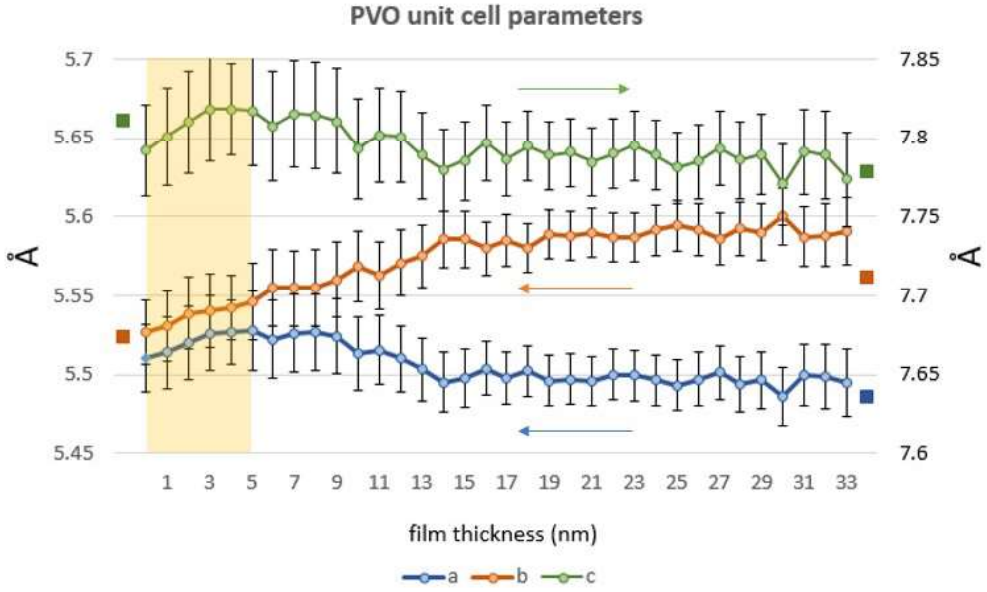

Figure 4.12: Obtained unit cell parameters for the PVO thin film in the different ROIs across its thickness by freely refining the distortion parameters. Each curve refers to the vertical axis indicated by the arrow of the same color.

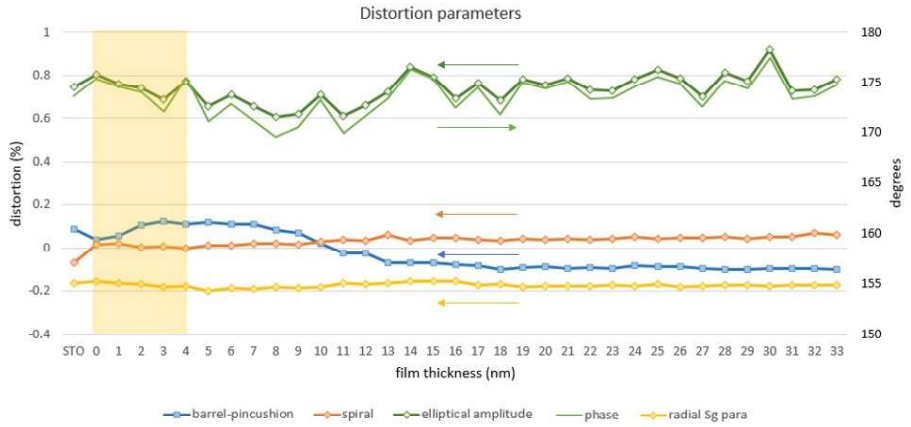

Figure 4.13: Refined distortion parameters the PVO thin film in the different ROIs across its thickness. Each curve refers to the vertical axis indicated by the arrow of the same color.

By comparing these results to the previous ones obtained by fixing the distortion parameters to zero, we can firstly observe how the standard deviations are significantly larger (one order of magnitude) with respect to the ones obtained in the previous case. This clearly indicates how the distortions refinement plays a fundamental role in the unit cell determination and in its resulting uncertainty. Globally, we can also state that a and c parameters lie in the expected range, coherently with the previously obtained results. Looking at the distortions trend, it can be observed that the spiral distortion and the radial component of the parabolic distortion are constant along the whole thickness of the film, differently from the barrel-pincushion, which presents a bump in the first 15 nm of film, and the elliptical distortion in both amplitude and phase, which resulted to follow the same trend. Presumably, the elliptical distortion is therefore the main cause in the increment in the standard uncertainties of the unit cell parameters. To ascertain this hypothesis, the same trial was conducted, by fixing this time the elliptical amplitude and phase to the average values, computed across the whole thickness of the film. The resulting unit cell parameters are reported in Fig. 4.14.
We can notice how this time the standard deviations turn out to be lower in module with respect to the previous case, confirming that the fluctuations in the elliptical distortion values affect in a considerable way the error on the refined unit cell parameters.

As a second point, an overlap can be observed in between the barrel-pincushion and the trends of the unit cell parameter, which all show an increased value in he first 15 nm of film. In the region $33 < x < 13$ nm the barrel-pincushion is low (-0.1%), therefore it is compensated by a correction that makes the vectors in reciprocal space bigger, that in turn makes the unit cell parameters smaller, deviating from the expected strained values ($a = 5.52$ Å, $c = 7.81$ Å). The observed trend in the barrel-pincushion distortion is presumably linked to the strain in the thin film, which could make the computation of the distortion percentage less accurate. During this passage we could, most importantly, verify that the distortion values computed for

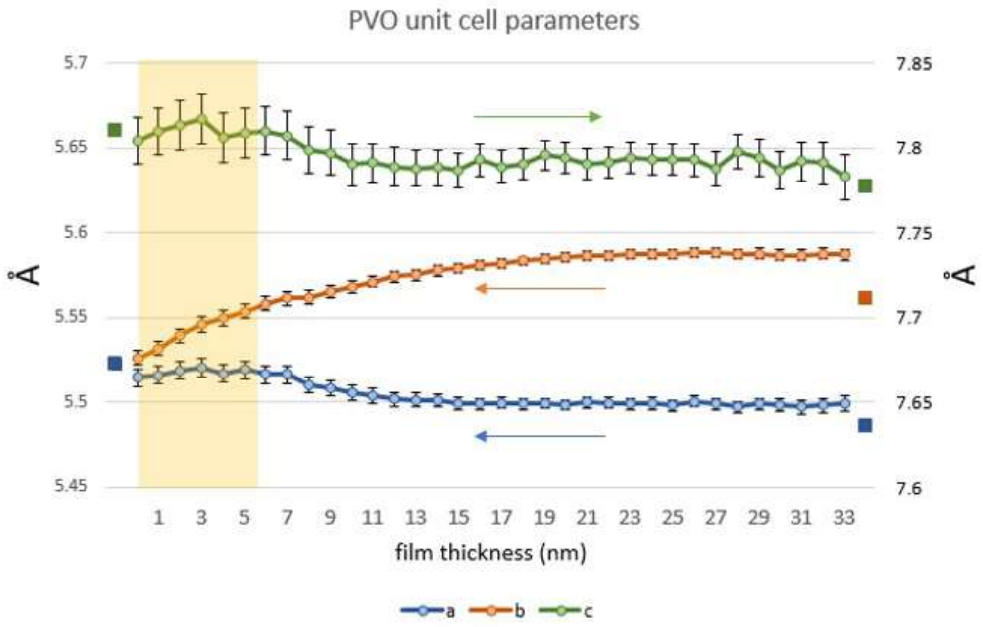

Figure 4.14: Obtained unit cell parameters for PVO in the different ROIs by fixing the elliptical distortion in amplitude and phase to the average value and freely refining the rest of the distortion parameters. Each curve refers to the vertical axis indicated by the arrow of the same color.

STO did not deviate significantly from the ones refined for each one of the single layers (apart for barrel-pincushion). This way, we could ascertain that the values for of STO represented a good approximation for each one of the film layers.

Afterwards, the procedure was repeated by fixing all the distortion parameters according to the substrate and refining the unit cell parameters. The results obtained from this analysis are shown in Fig. 4.15 in comparison to the previously obtained results for the the manual analysis (sec. 4.1). We can notice how the trend is much more stable for what concerns a and c parameters, while the increase in the b parameter appears to be more steady, as expected from the previously obtained results (Fig. 4.11). Also, the standard uncertainties show a minimal variability apart for c, as in the previous case, due to the geometry of the experiment. By comparing these results with the ones obtained by fixing the distortion parameters to zero (Fig. 4.16), we will notice that the global trend in the parameters is maintained, whereas

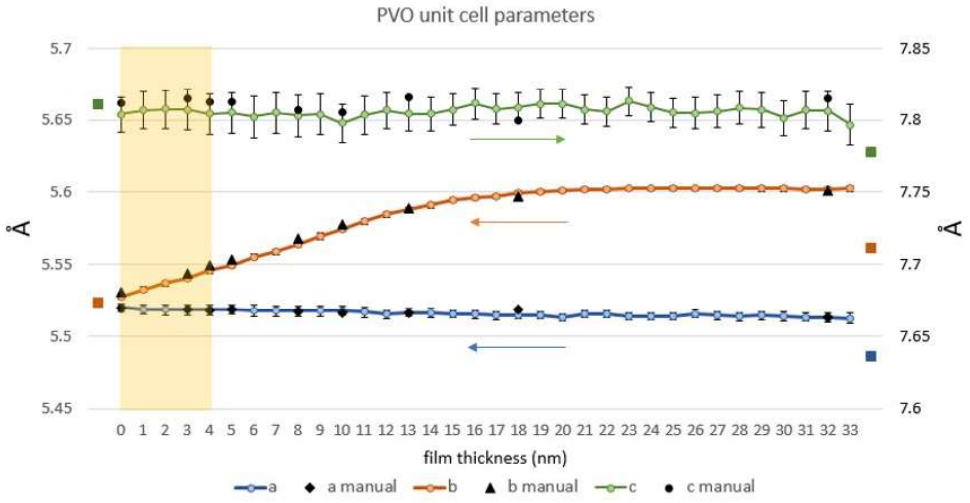

Figure 4.15: Obtained unit cell parameters for PVO in the different ROIs by fixing all the distortion parameters to the ones refined for the STO substrate. The cell parameters obtained via manual analysis (section 4.1) are shown superimposed to the corresponding curves as black markers. Each curve refers to the vertical axis indicated by the arrow of the same color.

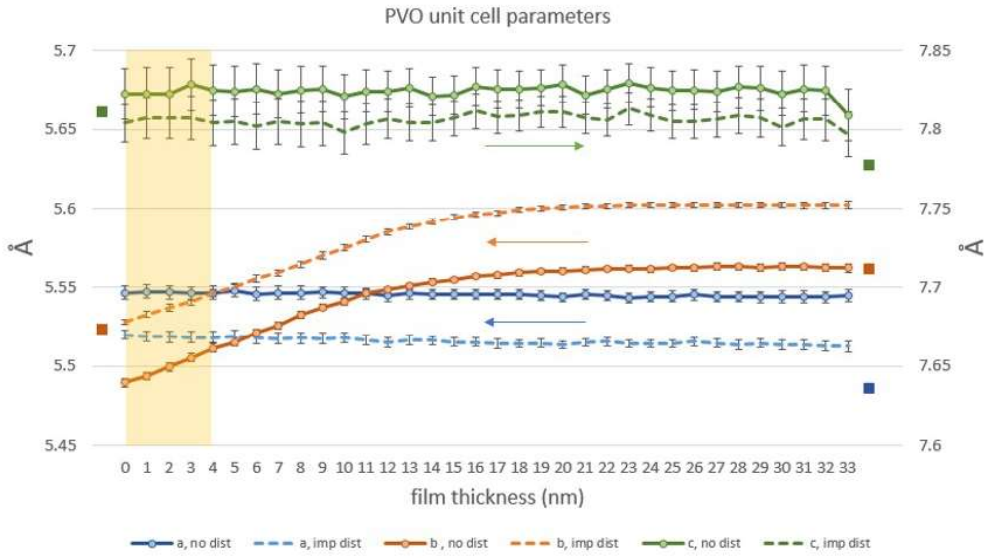

Figure 4.16: Comparison in between unit cell parameters obtained in the different ROIs of the PVO thin film across its thickness by imposing distortion parameters respectively refined from the substrate and equal to zero. Each curve refers to the vertical axis indicated by the arrow of the same color.

all the values underwent a constant shift across the film thickness, likely due mostly to the corrections in the barrel-pincushion and elliptical distortion, which sensibly affect the resulting lattice parameters. In this last case, a and b parameters take, in the ROIs next to the substrate, the expected strained parameters, matching the pseudo-octahedral values of cubic STO. For c parameter, no significant improvement in the fit with the reference parameter is observed instead, considering that the $c' = a * 2$ value falls in the range of compatibility of the two sets of measures. These results show how the choice of the calibration constant and distortion parameters plays a fundamental role in the absolute determination of the unit cell parameters of the structure in the considered ROI. By taking a look at the results obtained by imposing the parameters refined for STO, in all the cases they appear to be compatible with the results obtained with manual analysis, confirming the validity of the automatic data processing. From these results we can also see how, by imposing the barrel-pincushion distortion to all the film ROIs, the a and c parameters assume the expected strained values (and confirmed by previous RSM investigations). This observation indicates that using an internal standard (in our case the bulk substrate) is the correct approach for this kind of analysis.

In order to further confirm the reliability of the procedure, the same protocol was applied to the second and third scan lines of the SPET acquisition. For this purpose, the tilt series from the substrate have been extracted and processed on PETS2 for each one of the scan lines. For each refined parameter, the average among the three scan lines was computed and the deviations from the average values has been extracted (Fig. 4.17). As we can observe, the parameters show minimal deviation from their average values, with the phase of the elliptical distortion showing the maximum difference in between the scans (about 0.8°). Moreover, the frame orientation optimization is reported in Fig. 4.18, where the computed correction to the α angle of every frame is shown for the three line scan series. Globally, the three tilt series show a similar trend, and a maximum deviation from the average correction, calculated on the three scans, of 0.4° in absolute value is observed. The

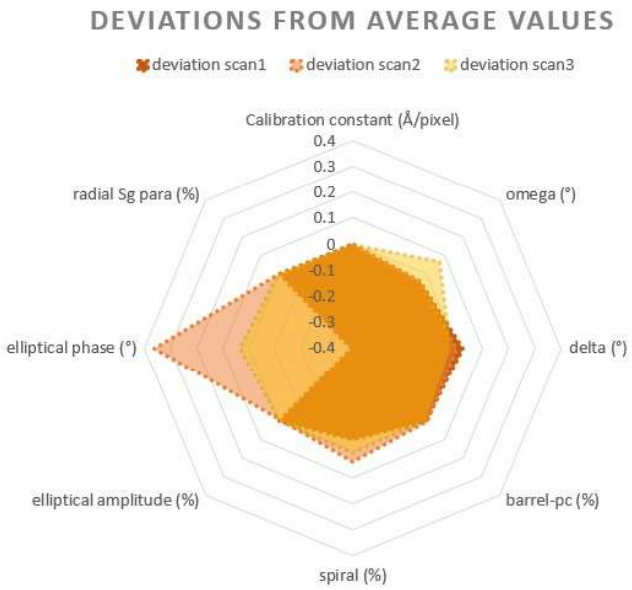

Figure 4.17: Deviation of the parameters refined for the STO tilt series for the three individual line scans from the average values.

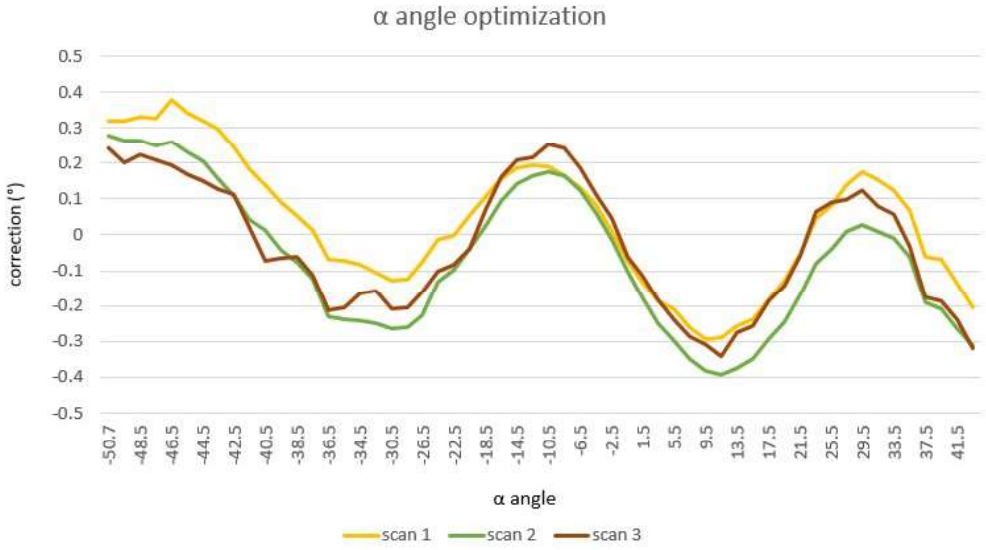

Figure 4.18: Optimizations of the frames orientation performed on the three tilt series for STO. The computed correction to α angles is reported in degrees for every for the three scans.

sinusoidal-like trend of the three line scans can be presumably traced back to the goniometer motor not being precise enough, causing small deviations in between the

reported and the effective value.

As a following step, each layer of the different scans was processed on PETS2 as previously described. The resulting unit cell parameters are plotted in Fig. 4.19.

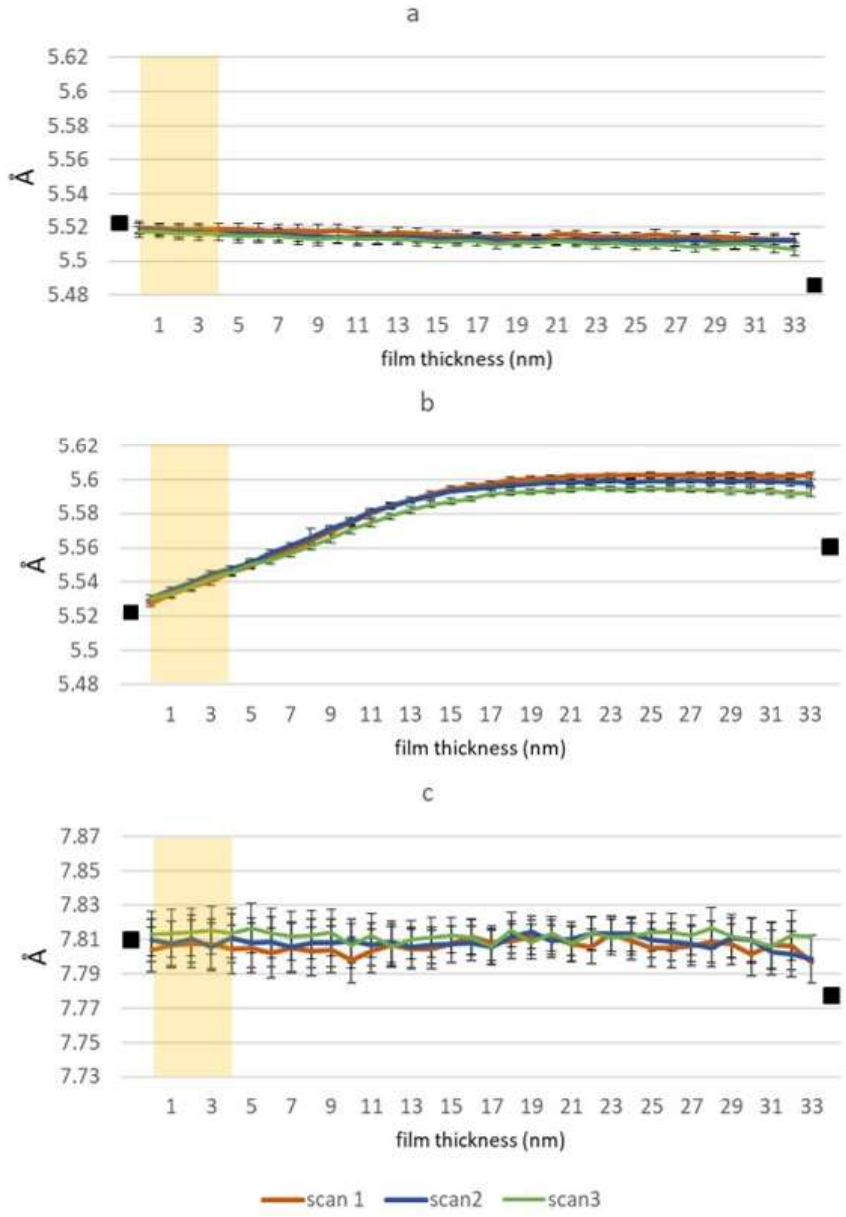

Figure 4.19: Obtained unit cell parameters for PVO in the different ROIs by fixing all the distortion parameters to the ones refined for the STO substrate, for the three different scans performed on the sample during the SPET experiment.

As we can see, the obtained values for a and c parameters, when considering the uncertainty ranges associated with the data, are compatible. Differently, taking a closer look to the obtained b parameters for the three scans, we can observe how the values for the third scan shows a small but significant difference in between the cell parameters of the other line scans. This slight deviations are likely attributable to the small differences in the parameters refined for the substrate at every scan line and then applied to the whole film range, such as the tilt axis (ω, δ) and the distortion parameters, or again the frame orientation optimization, which is performed singularly for each dataset. However, we can state that in general these observation confirm a good reproducibility of the results.

4.2.3 Results of Jana2020 structure refinements

The structural analysis was continued on the three line scans on PVO. In each case, ROI number 25 was selected as starting dataset for the structural refinements. Therefore, the refinements will start from the structure as we observe it close to the coating in the relaxed state. This way we can ascertain that the observed strain in the perovskite structure is not to be attributed to the starting atomic configuration. Using the output .cif_pets file from PETS2, the crystal structure of PVO was solved *ab initio* by means of Charge Flipping algorithm [61] and the kinematical refinement was performed. Afterwards, the remaining .cif_pets files were included in the cyclic refinement option and put in order by thickness, going from the interface with the substrate to the coating.

The R(obs) values resulting from the kinematical refinement lie in the range 22/31%, compared to the manual refinements performed in section 4.1 which fell in the range 25/30%. The values remain therefore stable for the whole film thickness in a standard acceptable range for what concerns electron diffraction data. The R(obs) values obtained for dynamical refinements of all the ROIs across the film thickness by cyclic refinement are reported in Fig. 4.20, in comparison with the results of the manual analysis of the ROIs on scan 1 (sec. 4.1). Moreover, the

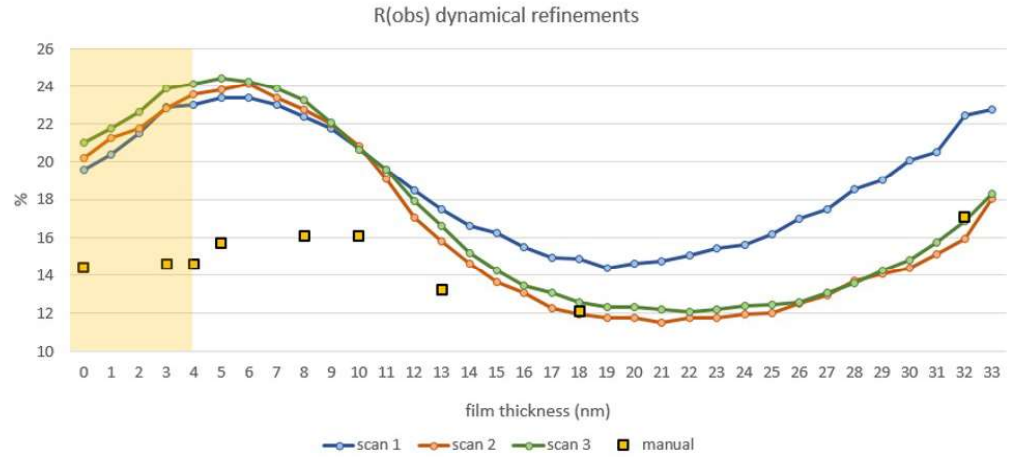

Figure 4.20: R(obs) values resulting from cyclic dynamical refinement for the three line scans along the film thickness, together with the results for the manual refinements done on the selected ROIs of the first line scan performed on Jana2020.

dynamically refined values of the sample thickness along the electron beam direction is reported in Fig. 4.21, in comparison to the values previously obtained for manual refinement of the selected ROIs. We can see how the best results were obtained

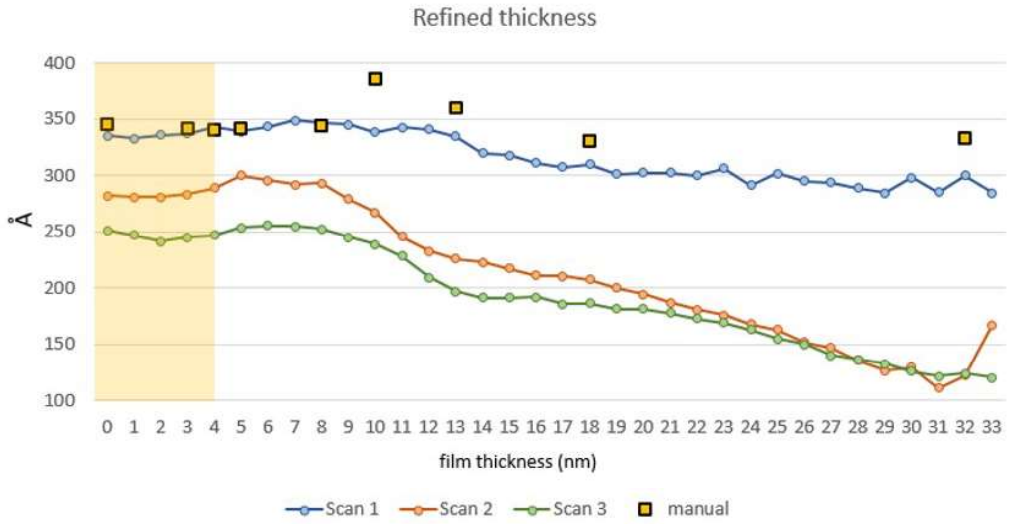

Figure 4.21: Values of the sample thickness refined dynamically for each ROI with the automatic cyclic refinement for the three line scans as well as for the manually refined ROIs of the first line scan.

for the manual analysis (see. 4.1), showing a fairly constant trend, while the cyclic refinements show a sinusoidal trend with equal results for R(obs) or higher, mostly in the first 15 nm of the thin film. In these regions, the single frames present on average higher R values. Therefore, discarding the outliers do not result in a total compensation of the difference in R values but rather a decrease of about 2% in the resulting R(obs). This significant increase in the R factors of the single frames is therefore likely attributable to the use of cyclic refinement, but a more thorough analysis is needed to understand the reasons behind it. Finally, we can observe a substantial similarity between the refined sample thickness values for manual and automatic analysis for scan 1, which result quite constant, while scan 2 and 3 show a decreasing trend. Being the scan lines spaced 30 nm in between each other, we can assume that, since the probed area of the sample did not undergo large shifts during the SPET acquisition, the difference could be due to an effective thinning of the sample towards the surface of the film. This is in agreement with TEM BF observations, which revealed areas of the polycristalline coating inhomogeneous in thickness, as visible in Fig. 4.3.

From the resulting crystal structures obtained for scan 1, the V-O-V angles, accounting for the octahedra tilting in the perovskite cage, were calculated and compared to the values obtained for the manual analysis (sec. 4.1). In Fig. 4.22, the resulting values for dynamical refinements are shown. In the kinematical case, both the V_1-O_1-V_1 and the V_1-O_2-V_1 angles remain steady along the whole sample thickness, respectively in the ranges 151.80/151.9° and 152.08/152.15°. On the contrary, from the dynamical refinement, we can appreciate a significant evolution of the angles, going from a strained condition (angles close to 180°), to a configuration closer to the structure of bulk PVO. In this case, the previously obtained results, where the refinements were carried out independently for each ROI, are indicated as rhombuses of the same color as the corresponding trend. The comparison show a substantial match in between the results, validating this way the cyclic refinement as a tool for efficiently performing sequential structural refinements of multiple diffrac-

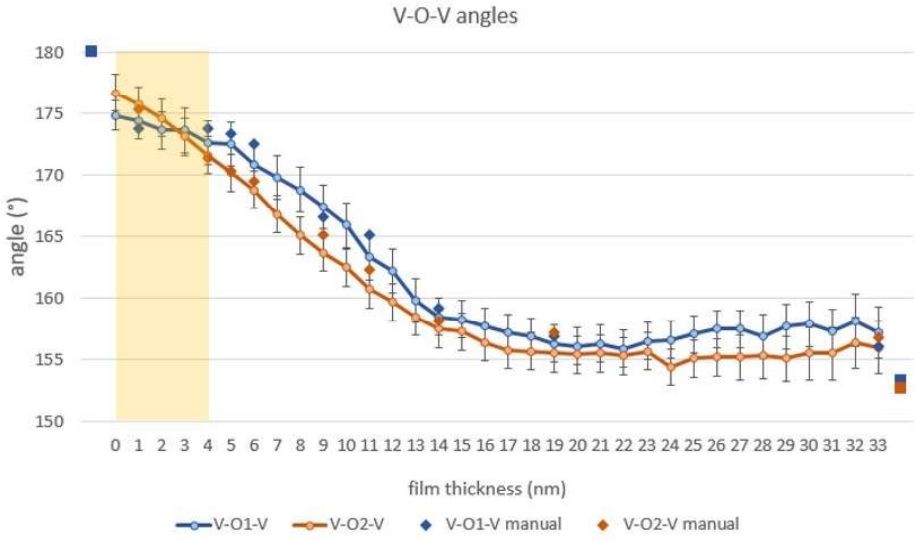

Figure 4.22: V-O-V angles resulting from cyclic dynamical refinement on Jana2020 of PVO along the film thickness. The values obtained by manual analysis are shown for comparison as rhombuses of the same color.

tion tilt series.

As a final observation, the Pr coordinates were plotted as a function of the film thickness and compared to the values obtained with the manual analysis (Fig. 4.23). Also in this case, the manually obtained values are shown as rhombuses of the same color as the corresponding curve for comparison. Similarly to the case of the octahedra tilting, we can see an evolution of the Pr coordinates, mainly concerning y, going from values close to (0.5, 1), as Sr in STO (transformed in the orthorhombic cell), to a configuration closer to bulk PVO (0.4928, 0.9928), and compatible with the results obtained for manual analysis considering the slight differences in the data processing. The coordinates evolution is also compatible with the other observed trends (unit cell parameters and octahedra tilting), reaching a plateau after 15 nm from the interface.

In Fig. 4.24, the PVO structures obtained respectively from the refinement of the first (close to the substrate) and the last (close to the coating) ROI are compared. From the projections along c (a, b) and a (c, d) we can observe the effect that the

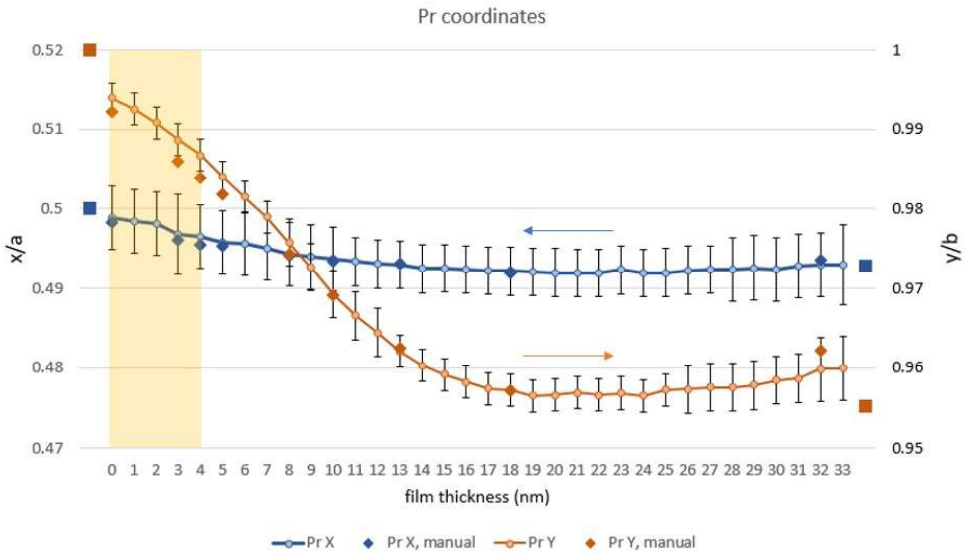

Figure 4.23: *(x,y)* coordinates of the Pr atom in the perovskite cage of PVO dynamically refined for each ROI along the film thickness. The values obtained by manual analysis are shown for comparison as rhombuses of the same color. Each curve referes to the vertical axis indicated by the arrow of the same color.

evolution of the $V - O - V$ angles has on the crystal structure of PVO.

These outcomes highlight the importance of performing dynamical refinements when the accurate crystal structure is of primary interest. Even if some ROIs did not obtain satisfying R values in dynamical refinement, the resulting structures are observed to be compatible with the ones obtained by manual processing of each dataset. Therefore, we can conclude that the tested procedure for automatic analysis is effective for providing information about the evolution of the crystal structure from SPET data in a reasonable amount of time. Then, if better R values are needed, or if we want to check the quality of the results, a manual analysis of the ROIs can be performed.

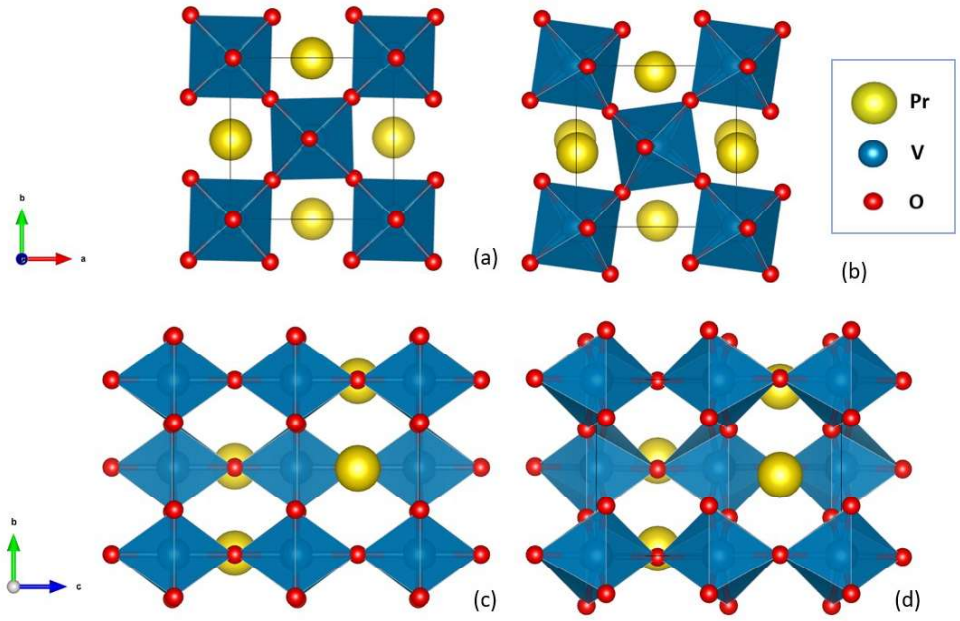

Figure 4.24: Comparison of the refined PVO structure the first and last ROIs taken into account, respectively along c (a, b) and along b (c, d). The color key is shown in the panel on top-right.

4.2.4 Automatic diffraction pattern sorting procedure

After establishing an effective procedure for automatically detecting the central frame of the film region at every tilt step of a SPET acquisition, and consequently sorting the diffraction patterns into different folders in order to reconstruct the single tilt series (see section 3.1.1), we could compare the results thus obtained with the ones previous analysis performed after manual sorting. This would allow us to evaluate the compatibility of the results and therefore to validate the automatic sorting routine. In Fig. 4.25, the computed central frames of the PVO thin film is reported in blue for every tilt step of the SPET acquisition, while the manually determined frames are shown in orange. The automatic procedure was started by selecting as a starting diffraction pattern, among the ones acquired at the first tilt angle (-50°), the frame which represented the center of the thin film in the manually determined sequence. By starting from the same frame, we can in fact observe

whether the automatic sorting procedure is able to reconstruct equivalent PEDT sequences as the manually defined ones or not. As we can observe, the central

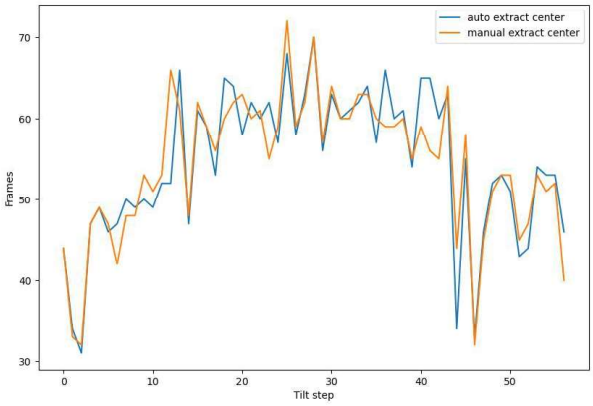

Figure 4.25: Central frames of PVO film on each tilt angle the SPET acquisition determined manually (blue) and automatically (orange).

frames display an overlapping trend with few significant differences throughout the dataset, demonstrating the globally satisfying proficiency of the script in identifying the frame intervals corresponding to the region of interest. Notably, in this case the sorting was performed solely based on the computed central frame of PVO for each tilt step, therefore not considering, as in the manual case, the total width of the thin film in terms of number of observed diffraction patterns. In this case, ROIs were reconstructed also at thickness $x < 0$, therefore entering the substrate, in order to evaluate the unit cell parameters in this region.

After sorting the frames in the tilt series, each one of them was automatically processed as before, by imposing to the film the distortion parameters refined for the STO substrate. In Fig 4.26, the results for the unit cell parameters throughout the thickness of PVO are shown (solid lines), in comparison to the previously obtained values by manual data sorting (triangles of the same color). Globally, we can see that the trends for the unit cell parameters are compatible in the two cases. Nevertheless, in the case of manually sorted series we observe a deviated from the automatically sorted ones, reaching faster the convergence of the a and b parameters

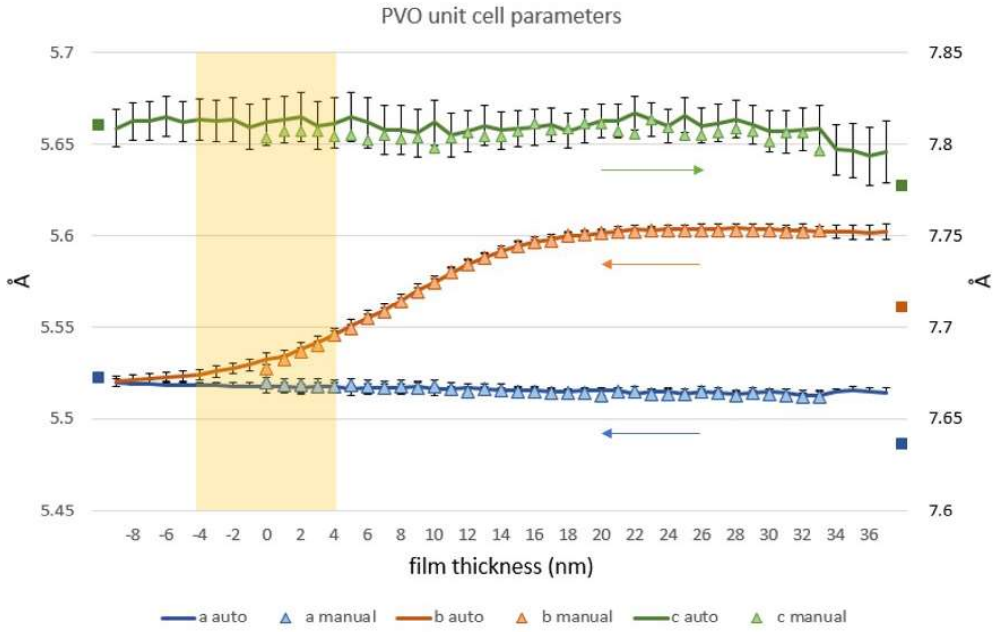

Figure 4.26: Unit cell parameters obtained by automatic data processing on PEST2 of the tilt series sorted both manually and automatically, respectively as solid lines and triangles. Each curve refers to the vertical axis indicated by the arrow of the same color.

to the values of bulk STO. This can be likely attributed to the different approach for data sorting, by taking into account the width of the film through the observed frame number or not. However, being the resulting difference moderate, we can confirm the success of the automatic approach for data sorting, which can make the analysis of SPET data significantly faster (5 minutes vs. 2/3 hours for manual data sorting). After the automatic sorting has been performed, the obtained ROIs can be singularly evaluated in order to check for possible mistakes in the procedure, and some adjustments can be done if considered necessary.

4.3 SPET on epitaxial LVO thin film

As a further proof of concept, we considered as a sample the epitaxial $LaVO_3$ (LVO) thin film deposited on a $DyScO_3$ (DSO) substrate, analyzed in collaboration with the Institute Jean Lamour (IJL - Nancy) in the framework of the ANR project design & Control of spIn, orbiTal and chaRge Orders in vaNadates - CITRON (ANR-21-CE09-0032) coordinated by O. Copie. In the context of research for less energy intensive multifunctional materials, the project aims at exploring new paradigms and design of multiferroic oxide-based systems (RVO_3 heterostructures) at the nanometer scale towards potentially short time scale spin dynamics. In this context, we aimed at exploiting SPET to analyze the samples and therefore to obtain accurate structure solutions that can help in better understanding how these affect the physical properties of the heterostructures.

A lamella was cut by FIB with Ga+ ion milling (FEI-Helios Nanolab 600i) from the thin film for TEM characterization. As we can see from the BF TEM image in Fig. 4.27, the LVO sample is estimated to be around 45 nm in thickness.

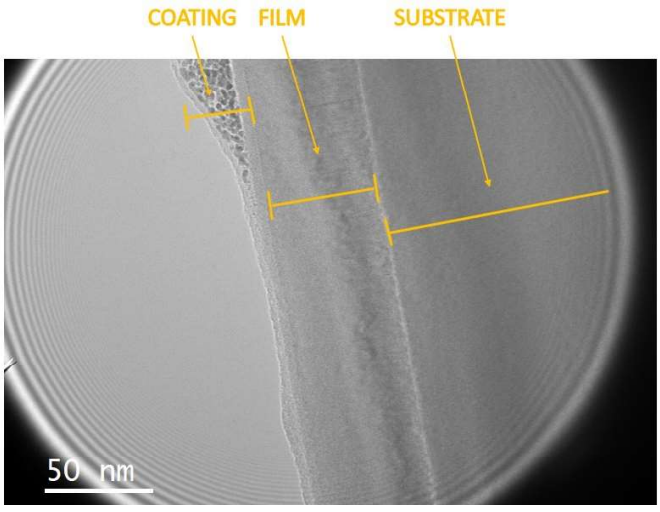

Figure 4.27: TEM BF image of LVO thin film lamella on DSO substrate.

Both the substrate and the film are characterized by a tilted orthorhombic *Pbnm*

perovskite structure, whose epitaxial relation is shown in Fig. 4.28, alongside with a STEM ADF image of the sample. LVO and DSO show [110] as out-of-plane direction, while [001] lies in the plane of the substrate-film interface. Being parameters a

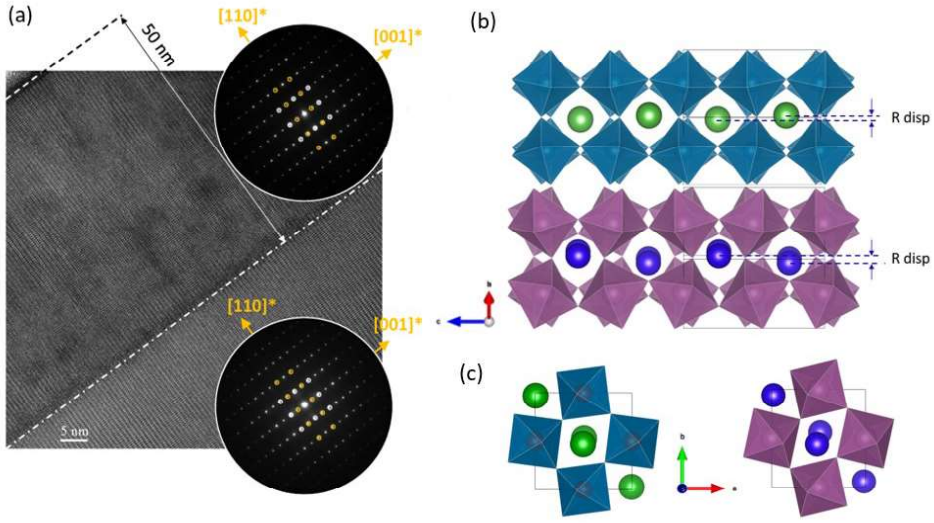

Figure 4.28: (a) STEM ADF of the LVO/DSO lamella sample. In the inserts, the diffraction patterns of the corresponding areas are shown, indicating the orientation of the crystal lattices. (b) Epitaxial relation between LVO and DSO crystal structures, viewed along the projection of the HR image. R disp parameter, indicating the shift in between the rare-earth elements in the perovskite cage, is also indicated. O atoms placed at the vertices of the octahedra. (c) LVO and DSO structures projected along c. Color key: La in green, V in blue, Dy in purple, Sc in light purple.

and b not directly constrained by the substrate, a distortion of the γ angle is possible, leading to a deviation from the orthorhombic structure which would bring the lattice to monoclinic-c, SG: $P2_1/m$. Therefore, both possibilities have been explored by XRD and electron diffraction.

XRD measurements were performed with a PANalitycal X'pert Pro MRD diffractometer using monochromatic Cu $K\alpha_1$ radiation (λ = 1.54056 Å). The unit cell parameters determined using RSM (Fig. 4.29) and refined the value with CelRef highlighted a c parameter in the LVO film strained to the c value of DSO, in agreement with [001] direction being in-plane with the substrate interface.

The reference bulk parameters for DSO and LVO are reported in Table 4.4, as

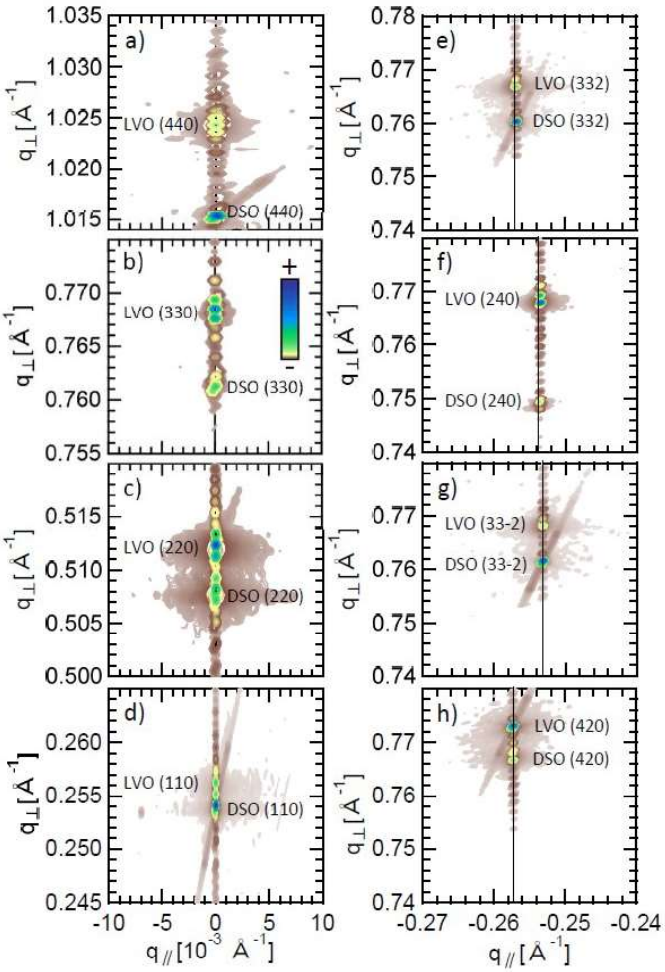

Figure 4.29: Reciprocal Space Maps acquired on sample LVO/DSO with a PANalitycal X'pert Pro MRD diffractometer.

	a, b, c (Å)	α, β, γ (°)
bulk DSO ($Pbnm$)	5.44, 5.71, 7.89	90, 90, 90
bulk LVO ($Pbnm$)	5.5535, 5.5555, 7.8487	90, 90, 90
XRD LVO ($Pbnm$)	5.5207(50), 5.5274(49), 7.9082(22)	90, 90, 90
XRD LVO ($P2_1/m$)	5.5484(15), 5.5527(20), 7.8910(22)	90, 90, 89.41(18)

Table 4.4: Reference lattice parameters for bulk DSO and LVO at room temperature [109], with the lattice parameters obtained from XRD measurements both with SG $Pbnm$ and $P2_1/m$.

well as the lattice cell parameters obtained for the thin film with XRD measurements, both refined as orthorhombic and monoclinic.

As in the case of PVO, this thin film is constituted by a single domain across its length, as no variations of the generated diffraction pattern is notable in the different regions. This constitutes an advantage for SPET data acquisition and analysis, making it an ideal sample for testing the capacities of this technique. Nevertheless, the similarity in between the lattice parameters of DSO and LVO, being both characterized by a perovskite structure with tilted octahedra, makes the data sorting procedure more difficult. In fact, during the passage from the substrate to the film, only a slight shift of the diffraction peaks is visible.

4.3.1 Experimental procedure

SPET was performed on the sample in order to examine its unit cell parameters and to perform accurate refinements of the structure along the thickness of the film. The scan was performed in this case on a single line, perpendicular to the film/substrate interface, spanning 250 nm in total, with a step size of 2.5 nm. The acquisitions were performed in the tilt range $\alpha = -48/+26°$ with a precession angle $\phi = 1.4°$. The sample tilt was performed, as in the case of PVO/STO, around an axis perpendicular to the film/substrate interface, in order to avoid the shadowing of the film. A beam size of about 15 nm was used, whose diameter was assessed by BF imaging.

In this case, the ROIs diffraction series was reconstructed by manually identifying the frames where the electron beam enters and exits the thin film area, and sorting them accordingly, since the automatic procedures for data sorting were not still optimized. The same procedure as the case of PVO thin film was followed, by extracting the series corresponding to the substrate as a first step, in order to refine the calibration constant and the distortion parameters, exploiting DSO as an internal standard.

4.3.2 Data analysis and results

The automatic processing on PETS2 was launched for the different thin film ROIs by only imposing the calibration constant derived from the analysis of the substrate. The distortion parameters were instead freely refined for every layer. The film structure was firstly refined as orthorhombic. The obtained unit cell parameters across the film thickness are reported in Fig. 4.30, while the refined distortion are shown in Fig. 4.31. As in the case of PVO, the results will be here shown for the selected ROIs as a function of the film thickness going from the substrate to the coating, being the zero fixed to the position where the beam accessed the film by 50% of its area. The reference parameters given for comparison are represented by the lattice constants of bulk DSO and the LVO parameters computed from XRD measurements, and are represented as squares on the left and right y axis, respectively. The area around the interface where both the film and the substrate contribute to the diffraction patterns is also highlighted in yellow.

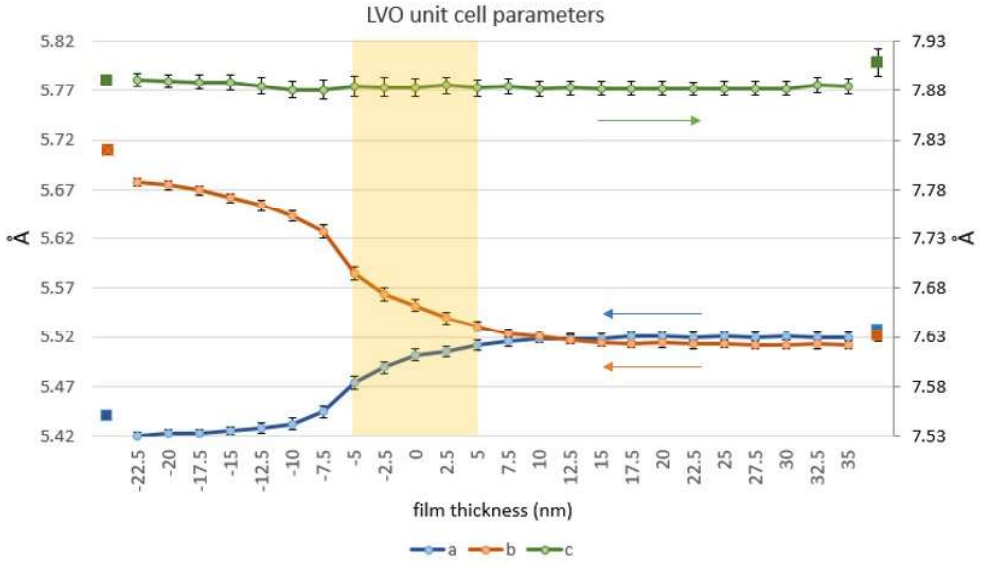

Figure 4.30: Unit cell parameters obtained with free refinement of the distortion parameters for every film layer. The area around the interface where both the film and the substrate contribute to the diffraction patterns is highlighted in yellow.

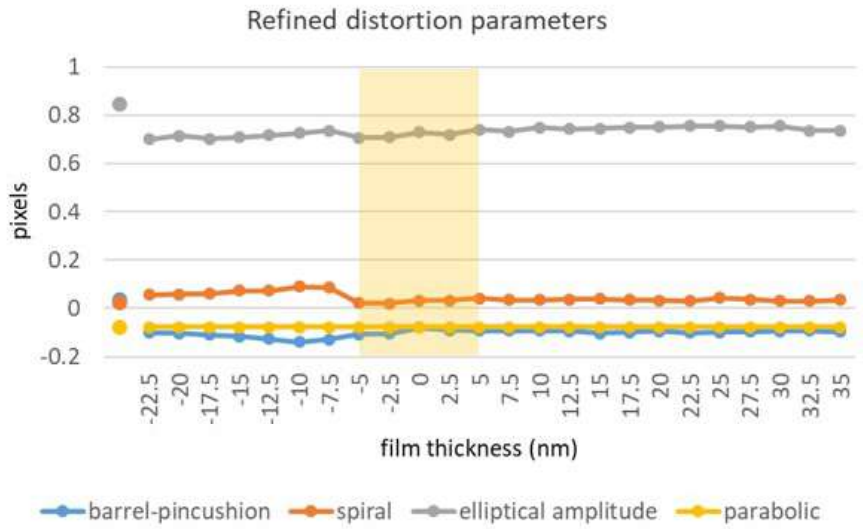

Figure 4.31: Refined distortion parameters for each LVO layer. The first experimental point represent the obtained values for DSO substrate. The area around the interface where both the film and the substrate contribute to the diffraction patterns is highlighted in yellow.

In this case, differently from the example of PVO thin film, ROIs before the zero point (in the substrate) were also taken into account, since the parameters were observed to vary but not reaching a plateau.

We can observe an evolution of a and b cell parameters in the area around the interface, which go from values close to the ones for bulk DSO (although with a small shift) to the ones observed for LVO through XRD. Although, we have to keep in mind that across the area around the interface (highlighted in yellow in the plots), we have in the diffraction patterns contributions from both the film and the substrate. Being the two structures very similar and thus their peaks almost superimposed, it is possible that the obtained cell parameters are affected by the partial indexation of peaks attributable to both domains. Notably, a trend is still observable at thicknesses equal to -7.5 nm and smaller when the beam is entirely probing the substrate, suggesting that a distortion could be present in the DSO parameters. A constant trend is observed for LVO c parameter instead, whose range of values don't result to be compatible with the reference value from XRD. However,

the obtained results are in agreement with the expectations, being c parameter in-plane with DSO and therefore strained by the substrate. We can also see how the distortion parameters remain mostly steady in the whole range and in line with the ones refined for the substrate series, which supports the imposition of distortion parameters obtained from the substrate.

The ROIs were then processed by imposing to all of them the distortion parameters refined for the reference substrate dataset. The unit cell parameters thus obtained are reported in Fig. 4.32. In this case, we see a and b parameters globally

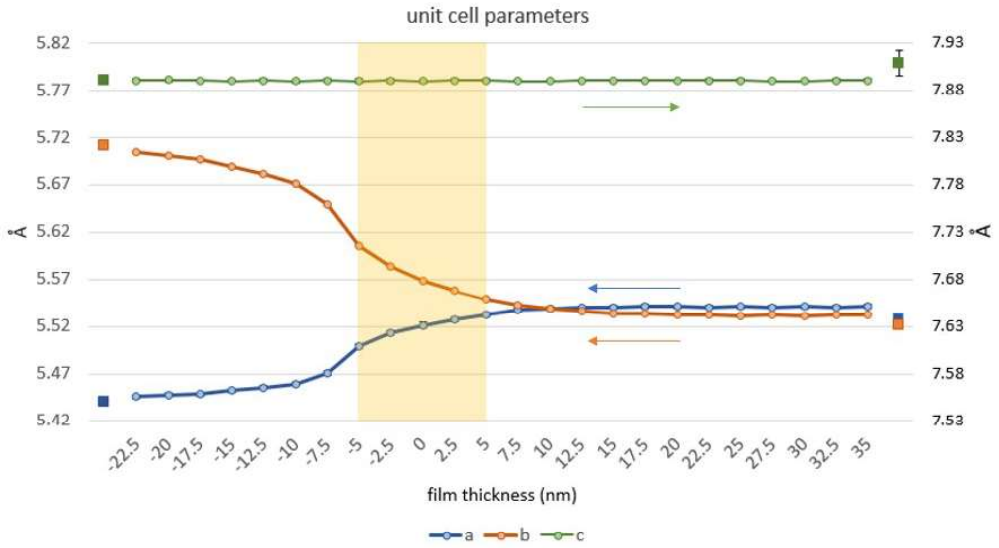

Figure 4.32: Unit cell parameters for LVO for the different analyzed ROIs by fixing the distortion parameters to the ones obtained for the substrate.

maintaining the same trend, but showing a slight shift towards bigger values. In the first ROIs in the region close to the interface, both the parameters better converge to the reference values of DSO, and still reaching at the surface values close to the reference LVO parameters. Parameter c still shows a constant trend across the film thickness matching the the corresponding value for DSO.

Being [110] the out-of-plane crystallographic direction, in this case parameters a and b are not directly constrained by the substrate, possibly giving a certain degree of freedom to their orientation and therefore to angle γ. In order to evaluate this

possibility, the ROIs were processed again by imposing the distortion parameters from the substrate, but refining the lattice as monoclinic-c. The resulting unit cell parameters (a, b, c, γ) are reported in Fig. 4.33. By comparing the results obtained

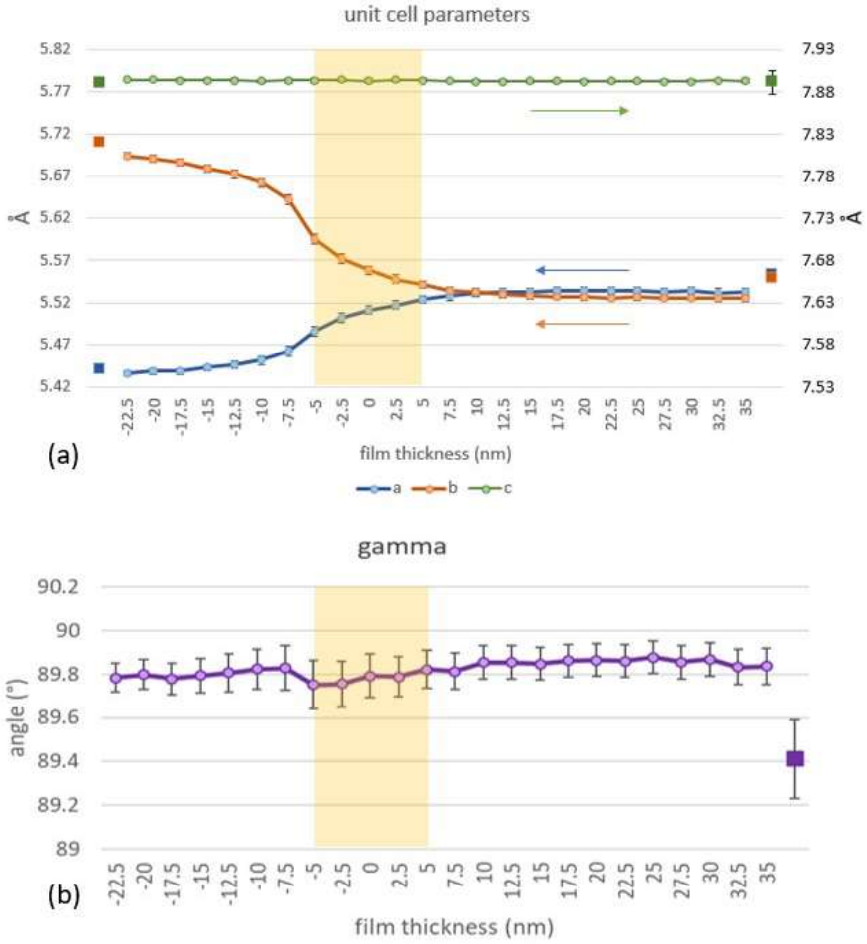

Figure 4.33: Unit cell parameters of the sample for the different analyzed ROIs by fixing the distortion parameters to the ones obtained for the substrate fixing the cell as monoclinic-c, the first and the last points (squares) representing, respectively, the reference parameters for bulk DSO and LVO from XRD measurements (SG: *Pbnm*). The area around the interface where both the film and the substrate contribute to the diffraction patterns is highlighted in yellow.

by fixing the lattice as orthorhombic and monoclinic, it seems reasonable to take the former as model which better represents the structure of the thin film. Refining

LVO as monoclinic-c, in fact, resulted in a trend for γ angle constant and close to 90°, in fair agreement with the value obtained from XRD measurements. Moreover, although concerning c parameter in the monoclinic case we have a better match with the observed value from XRD, the results show a small deviation from the expected values of DSO. The same is valid by looking at the results for parameters a and b, since they show a similar trend with respect to the orthorhombic refinement but with a small shift towards smaller values.

The crystal structure of the sample was therefore further evaluated by carrying out kinematical and dynamical refinements on Jana2020 as orthorhombic (SG: *Pbnm*) using the cyclic refinement option in order to process all the ROIs at once. In both cases, the structure was imported as a model from the reference .cif file instead of obtaining it through Charge Flipping calculations in order to make the process faster. The refinements of the datasets corresponding to the substrate ($x \leq 0$) were carried out by imposing DSO as crystal structure, while in the area of the film ($x \geq 0$) the LVO composition was used. Dataset at $x = 0$ was thus analyzed with both crystal structures to highlight potential differences in the results.

In Fig. 4.34, the R(obs) values resulting respectively from kinematical and dynamical refinements of the sample across the film thickness are reported, going from the ROIs corresponding to the substrate to the ones close to the coating. We can observe how, in the two cases, the R values stay mostly constant in all the analyzed ROIs, and how, passing from kinematical to dynamical refinement, a reduction of about 50% of the R(obs) value is obtained, except for a range of ROIs at the interface where the difference is lower. The reason for the higher R(obs) obtained in this region is likely to be attributed to the contribution of both the film and the substrate to the diffraction patterns, which provokes a spitting of the peaks and as a consequence different integrated intensities. However, the obtained R values fall in all the cases in the expected ranges for kinematical and dynamical refinements. The values of the sample thickness refined during the dynamical refinement are also shown in Fig. 4.35, globally comprised in between 276 and 455 Å. The trend is in

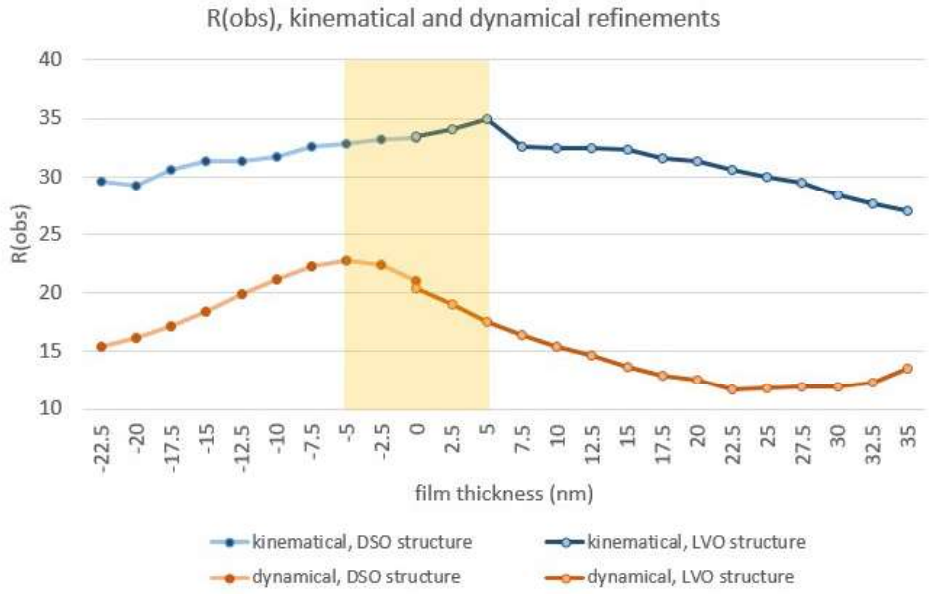

Figure 4.34: R(obs) values obtained respectively from kinematical and dynamical cyclic refinements of the sample structure across the film thickness, going from the substrate to the coating. The area around the interface where both the film and the substrate contribute to the diffraction patterns is highlighted in yellow.

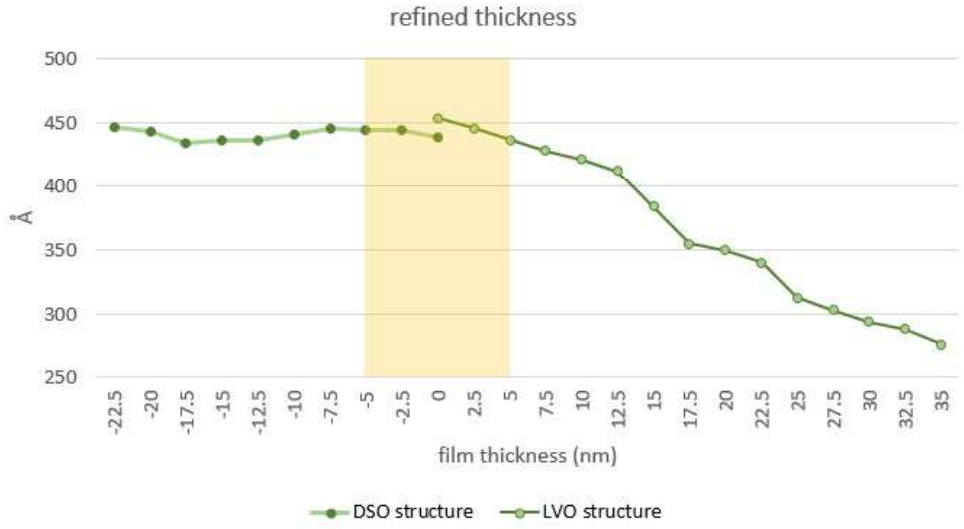

Figure 4.35: Refined thickness value for every ROI. The area around the interface where both the film and the substrate contribute to the diffraction patterns is highlighted in yellow.

line with the expected shape of the sample, considering it was thinned by FIB. In fact, it shows lower values close to the surface of the film, where the sample can show a thinner section.

From the refined structures, it was possible to extract the values of the V-O-V/Sc-O-Sc angles, which indicate the tilting system of the perovskite cage. In Fig. 4.36 and 4.37, the $V_1 - O_1 - V_1/Sc_1 - O_1 - Sc_1$ and $V_1 - O_2 - V_1/Sc_1 - O_2 - Sc_1$ angles obtained respectively for the sample in all the ROIs from respectively kinematical and dynamical refinements are reported. The values are shown for both the refinement as DSO and as LVO crystal structure. The results for kinematical refinement (Fig. 4.36) show an evolution across the analyzed area which is not coherent with the reference values for bulk DSO and LVO, reported in the plots as squares respectively on the left and on the right of the experimental points. Moreover, for what concerns angles $Sc_1 - O_1 - Sc_1/V_1 - O_1 - V_1$, the values are not coherent in between structure solution as DSO and as LVO. Contrarily, looking at

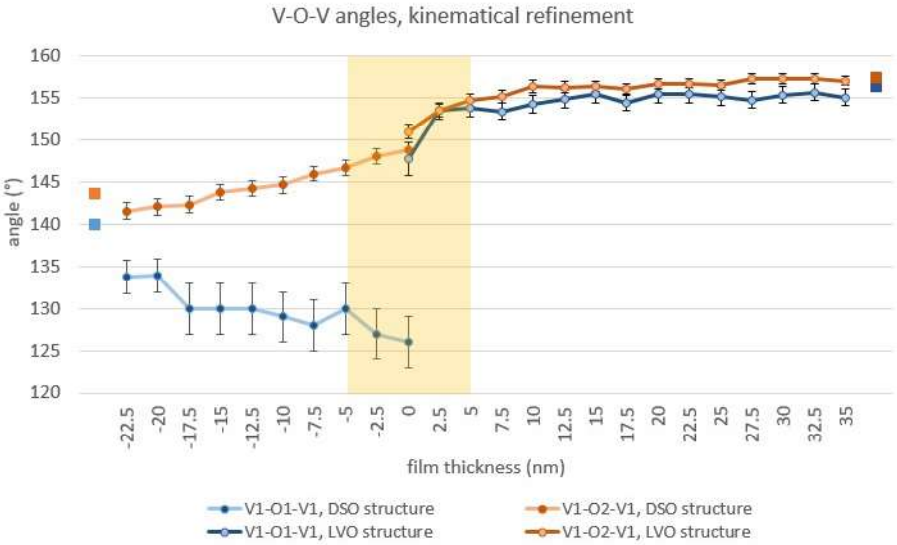

Figure 4.36: $V_1 - O_1 - V_1$ and $V_1 - O_2 - V_1$ angles for kinematically refined sample structures across the thickness of the film, going from the substrate to the coating. The area around the interface where both the film and the substrate contribute to the diffraction patterns is highlighted in yellow.

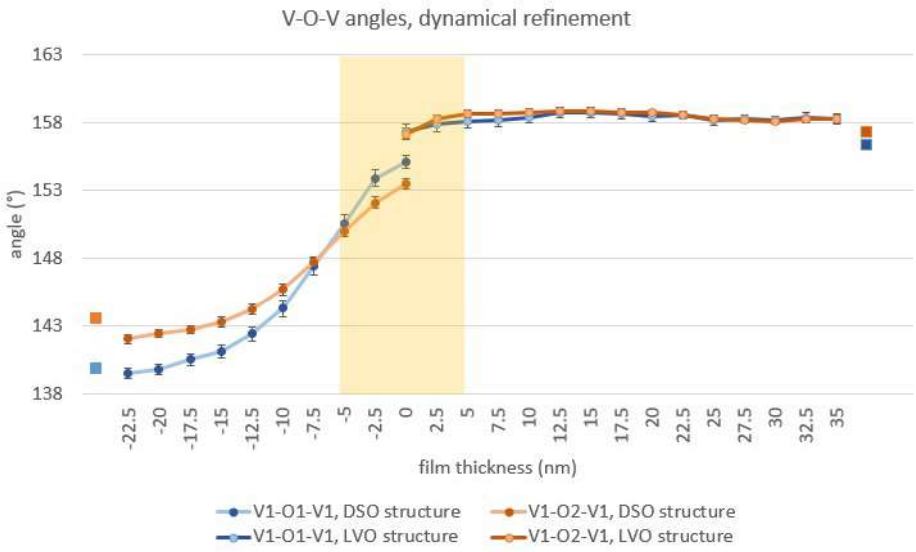

Figure 4.37: $V_1 - O_1 - V_1$ and $V_1 - O_2 - V_1$ angles for dynamically refined sample structures across the thickness of the film, going from the substrate to the coating. The area around the interface where both the film and the substrate contribute to the diffraction patterns is highlighted in yellow.

the results for dynamical refinements (Fig. 4.37), we can see a better coherence of the obtained values, which evolve from angles close to the ones of bulk DSO to values compatible with bulk LVO. These observation prove the importance of considering dynamical effects, especially for thick samples as TEM lamellae. Notably, all the evolution is visible before $x \leq 0$, suggesting that the structure of DSO could be affected by the overlying LVO film. Nevertheless, we still have to consider that the contribution of both domains in the diffraction patters could give as a result an average value over the probed area, affecting this way the observed evolution over the selected area. From XRD measurements it is not possible perform accurate structure refinements, and thus to extract information about the position of V and O atoms in the unit cell. Therefore, by comparing the obtained values to the references, we have to take into account that the bulk values reported in Fig. 4.36 and 4.37 do not actually represent the experimental ones for the thin film but the reference ones from bulk LVO.

The (x, y) coordinates of the rare-earth element in the perovskite structure were

also extracted for every ROI and reported in Fig. 4.38 and Fig. 4.39, respectively for the kinematically and dynamically refined structures of DSO and LVO. The z coordinate was not taken into account since fixed by symmetry restrictions to 0.25. In this case we can observe a similar but smoother trend for both x and y by performing dynamical cyclic refinements, with values matching the ones of bulk DSO in the first ROIs and going towards the bulk values of LVO reaching a plateau at about 10 nm into the thin film. As for the octahedra tilting trends, we observe the majority of the evolution in the range $x \leq 0$, even in the region where the beam completely probes the substrate.

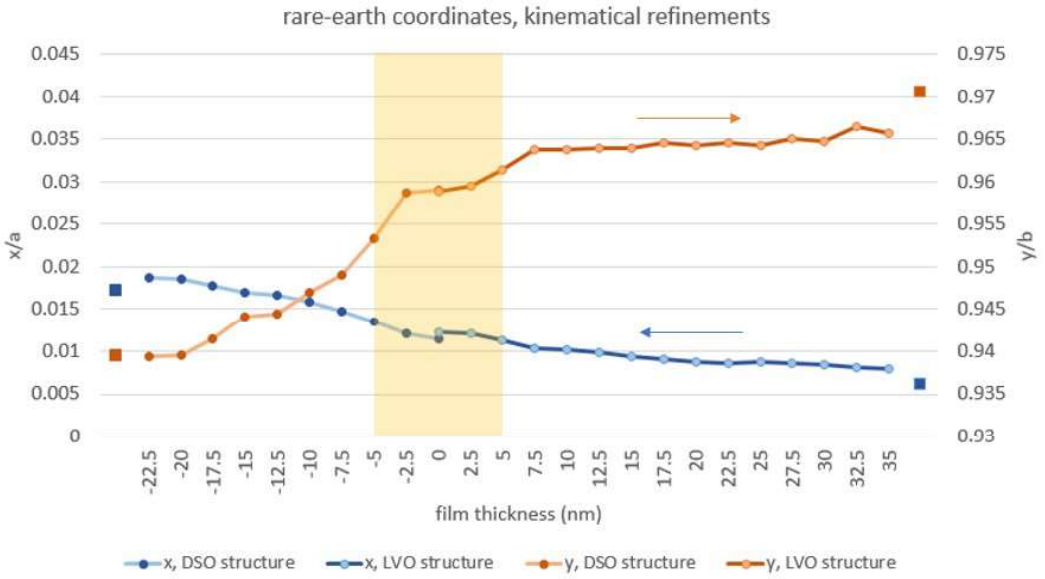

Figure 4.38: x and y coordinates of the rare-earth element in the perovskite cage for kinematically refined sample structures across the thickness of the film, going from the substrate to the coating.

In Fig. 4.40, the LVO crystal structures obtained from dynamical refinement of the first (substrate) and last (film) ROIs are shown, respectively along c (a, b) and a (c, d) directions. From the comparison we can see how the two structures show different atomic positions and tilting of the octahedral perovskite cage, as expected from the previously shown results.

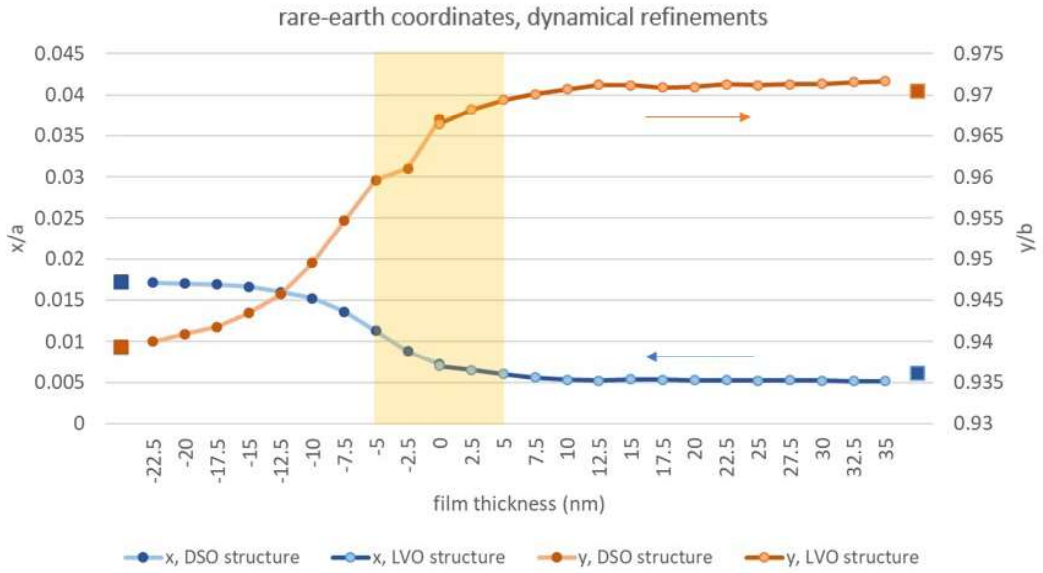

Figure 4.39: x and y coordinates of the rare-earth element in the perovskite cage for dynamically refined sample structures across the thickness of the film, going from the substrate to the coating.

In order to confirm these observations, High Resolution imaging was performed on the sample for estimating the position of the rare-earth element in the unit cell, and thus to compare the results with the coordinates obtained from SPET data. From HAADF STEM atomic resolution imaging, performed with a double-aberration corrected JEOL ARM microscope operated at 200 kV, the R displacement of the rare-earth element in the perovskite cage (see Fig. 4.28) was computed using the Python library Atomap [110]. The R displacement indicates twice the deviation in pm of the rare-earth element from its average position along the direction of growth, in our case [110]. As a first step, the software finds the initial atomic positions. From these, it extracts the position and shape of the atomic columns in the image, and creates a sublattice containing the information about the atomic positions and the 2D array representing the image. Afterwards, the positions are refined using the center of mass, and 2D elliptical Gaussian function is used to fit the atomic columns. At this point, the desired atom planes and zone axes can be found in the sublattice, and the average displacements from the fit line can be computed

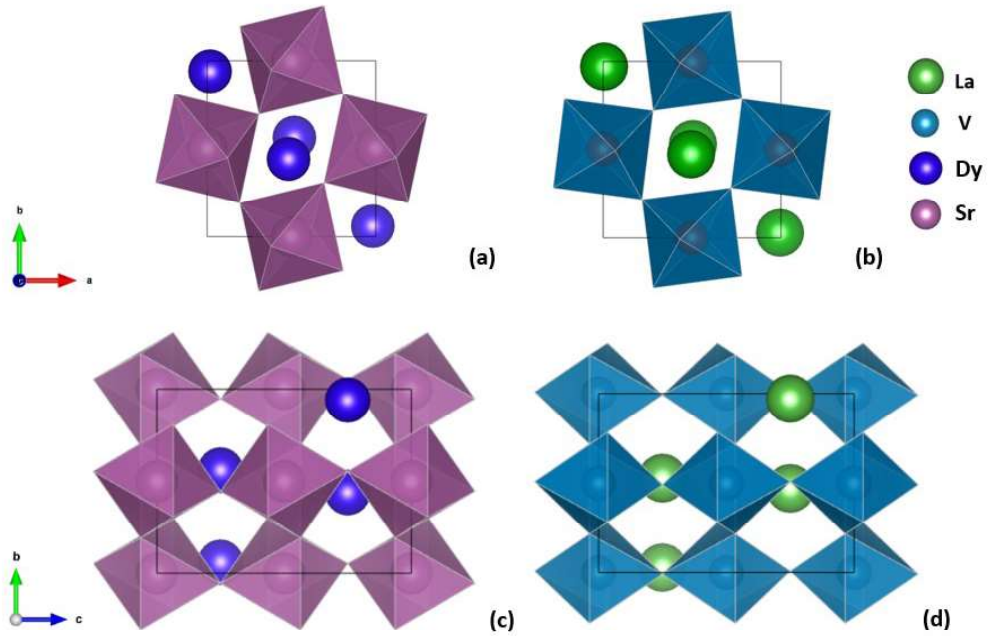

Figure 4.40: Comparison of the refined LVO structure the first and last ROIs taken into account, respectively along c (a, b) and along a (c, d). The color key is shown in the panel on top-right (O atoms placed at the vertices of the octahedra)

for every atomic plane in that direction. In Fig. 4.41, the ADF image (a) from which the displacement map (b) was calculated is reported. A plot showing the mean deviation in pm for every atomic plane is also reported (c), from which we can see an R displacement in the range (20-30 pm) for DSO and (5-15 pm) for LVO.

The R displacements were then computed from the atomic positions of the structures resulting from the aforementioned dynamical refinement of each ROI from SPET data. The results are reported in Fig. 4.42 for the ROIs corresponding to the LVO film and DSO substrate, as well as the substrate dataset which was extracted far from the interface in order to be used as a internal reference (shown as the first experimental point). As we can notice, there is a general agreement in between the values obtained from SPET and from high resolution STEM, which validates the reliability of the analysis. Nevertheless, with STEM imaging a much more rapid change in the R displacement is notable with respect to the evolution

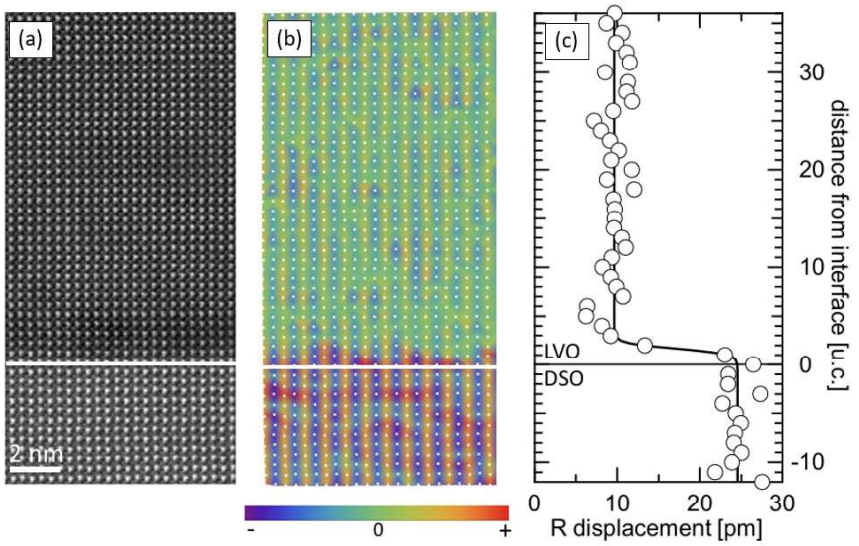

Figure 4.41: (a) High resolution STEM image of LVO/DSO. The film/substrate interface is indicated with a white line. (b) Displacement map resulting from Atomap.

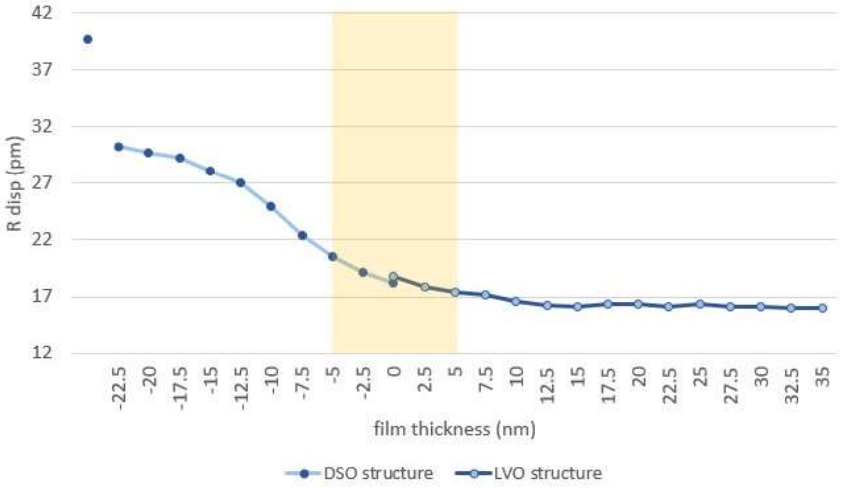

Figure 4.42: R displacement in pm computed on the refined crystal structures of DSO and LVO across the sample thickness, the first experimental point representing the results for the dataset extracted from the substrate to be used as internal reference. The area around the interface where both the film and the substrate contribute to the diffraction patterns is highlighted in yellow.

observed through electron diffraction. As reminded before, this could be likely due to the larger electron beam size, which, probing a more extended area of the sample, would likely lead to obtain an average result over it.

In conclusion, the analysis of adjacent ROIs in the sample through SPET data acquisition allowed us to observe an evolution in the unit cell parameters along the direction perpendicular to the sample interface, attributable to the relaxation of the structure from the strain it underwent. Looking at the trends of both the unit cell parameters and the atomic positions, we can observe that the relaxation reaches a plateau at about 10 nm in the LVO film. However, a significant evolution is notable in these trends also in the portion of analyzed ROIs which are dominated by the contribution of the substrate. These observations may suggest that the crystal structure of the DSO substrate is in turn affected by the above structure of the film. Although the majority of the evolution of the structural parameters is visible in the region where both domains contribute to the diffraction patterns, the observation are confirmed in the region where the electron beam completely entered the substrate, supporting the validity of our results. However, we have also to consider the possibility of an error in the determination of the interface position ($x = 0$). An shift of one or two frames to the left would in fact mean an evolution more equally distributed between the film and the substrate. We remind about this point the difficulty in accurately determining the position of the electron beam, given the similarity between the diffraction patterns of the two structures (LVO and DSO).

Globally, the observations are in line with the expectations, being all the parameters evolving from values which are close to the bulk DSO parameters to the ones of bulk LVO. The slight discrepancies that we observe in between electron diffraction data and XRD data are likely due to the uncertainties given by both the measurements. It is in fact difficult to accurately estimate the structural parameters of thin films by XRD, given the very limited amount of observable diffraction peaks and the superposition of the signal from the substrate. Concerning electron diffraction

instead, a certain amount of distortions is intrinsically provided by the TEM setup, which, if wrongly calculated, will affect the accuracy obtain structural parameters of the sample. Regarding the structural refinements, a wrong peak integration or a wrong estimation of the dynamical effects can lead to errors in the obtained atomic positions and therefore in the possible structural strain. In any case, being the different ROIs of the sample processed by imposing fixed distortion parameters, and being the refinements carried out in the same way across all the ROIs, we can state that an evolution is certainly present in the sample.

Being the acquired patterns an average signal coming from the probed ares, as a following step we could try to study the influece of the beam size on the results of SPET. The use of a smaller electron beam size would provide a more local information, allowing us to determine with a higher accuracy the structural parameters, and to avoid as much as possible the contribution from both domains to the diffraction patterns in the region close to the interface.

Being able to estimate with high accuracy the evolution of the parameters and to visualize the whole crystal structure across this relaxation process will hopefully help to understand its link with the physical properties of the samples, leading in turn to the ability of finely tune the features of these materials in order to obtain the desired functionalities.

CHAPTER 5

SPET characterization of 2D ROIs of functional materials

Up until now we saw how SPET can be used in order to obtain accurate structural information from thin films. The samples are characterized by ordered domains and limited in number, namely a mono-crystalline substrate, a mono-crystalline film and a polycrystalline coating, and the aim in this case was to observe an evolution of the structural parameters along the film growth direction.

In this chapter we will see which are other possible cases where SPET can provide useful information about the samples. More specifically, we will focus on the use of SPET to probe 2D areas of ceramic materials, which are characterized by domains inhomogeneous in phase, shape and orientation.

In this case, the ultimate objective would be, by performing SPET on an area composed by multiple domains, to be able to accurately solve the crystal structure for all of those we are interested in within a single acquisition, and possibly to detect, also this time, evolutions in the crystal structures.

In order to do so, it is firstly necessary to try to scan the same area across all the tilt steps of the SPET acquisition, in such a way to have access to a complete

diffraction tilt series for each one of the ROIs.

To extract the frames from the scan grid, we can both rely on the position of the diffraction patterns within the scanned grid (e.g. position 1,1), which we will address as "blind extraction", or on a sorting approach such as NMF decomposition or the similarity percentage (section 3.2). This way, it is possible to process datasets coming from different domains and perform *ab initio* structure solution and accurate refinements. A schematic representation of the process is reported in Fig. 5.1.

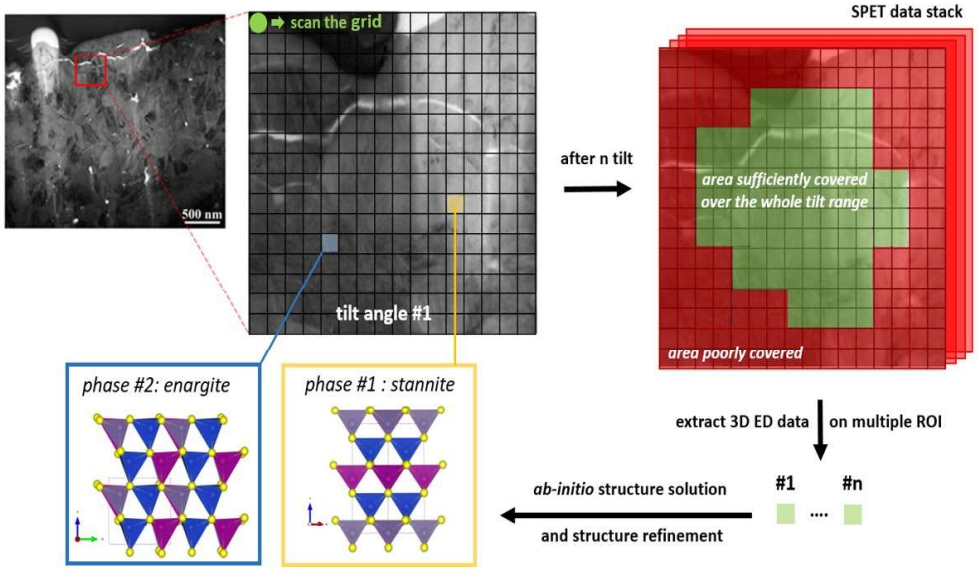

Figure 5.1: Illustration of the procedure of SPET data acquisition, extraction and analysis showed on sample $Cu_{2.3}Mn_{0.7}GeS_4$ as a TEM lamella. Even if the scan grid is not placeed exactly in the same place at every tilt step, some parts of the interested area shall be scanned and used for structure solution.

In the following section we will find these different methods applied for the analysis of ceramic materials prepared as TEM lamellae. SPET applied to these kind of samples can this way be useful to analyze them by electron diffraction in the form they were synthesized in to have a more accurate overview of their features, mostly when the size of the domains becomes too small to easily keep track of their position during the tilting.

5.1 $Cu_{2.3}Mn_{0.7}GeS_4$ lamella

SPET was used to probe a 2D area on the thermoelectric sample $Cu_{2.3}Mn_{0.7}GeS_4$, previously described in chapter 2.2.3, prepared in the form of a TEM lamella by Focused Ion Beam (FIB) cut, in collaboration with Electron Crystallography group at IIT (Istituto Italiano di Tecnologia) in Pontedera, Italy (Fig. 5.2).

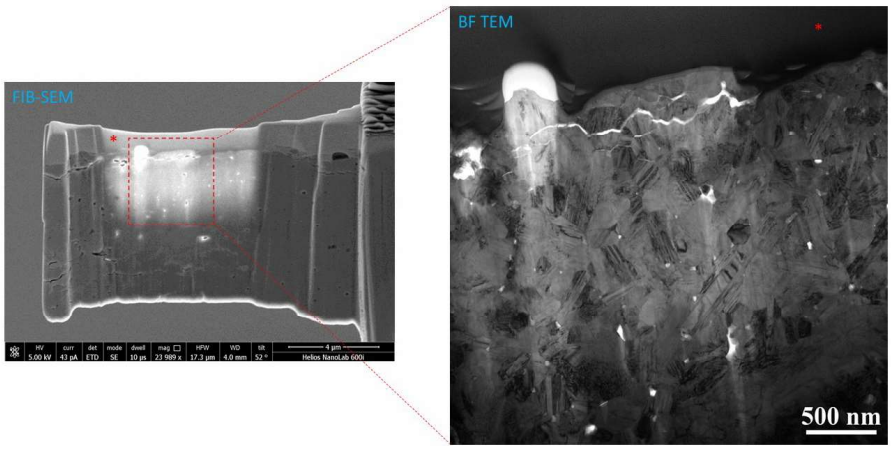

Figure 5.2: Left: SEM image of sample $Cu_{2.3}Mn_{0.7}GeS_4$ prepared as a TEM lamella by FIB. Right: TEM BF image of the area of the sample contoured in red in the SEM image, highlighting the well defined domains present in the sample.

The crystal structures of the two phases which are present in the sample, together with the unit cell parameters previously obtained through PEDT on single crystals (section 2.2.3), are reported as a reminder in Fig. 5.3.

An area of the sample at the interface between two sufficiently large domains was selected, in such a way that a SPET dataset including only two different diffraction pattern could be obtained. This simple dataset could then be used for testing the efficiency of the diffraction pattern sorting method.

As in the previous cases, the scan was controlled with the NanoMEGAS Digistar unit, while the diffraction pattern acquisition was performed with the ASI ACCOS software. The area selected for the SPET experiment, measuring 250 x 100 nm, was probed with a (x, y) 50 x 5 grid, with a step size of 5 and 20 nm, respectively,

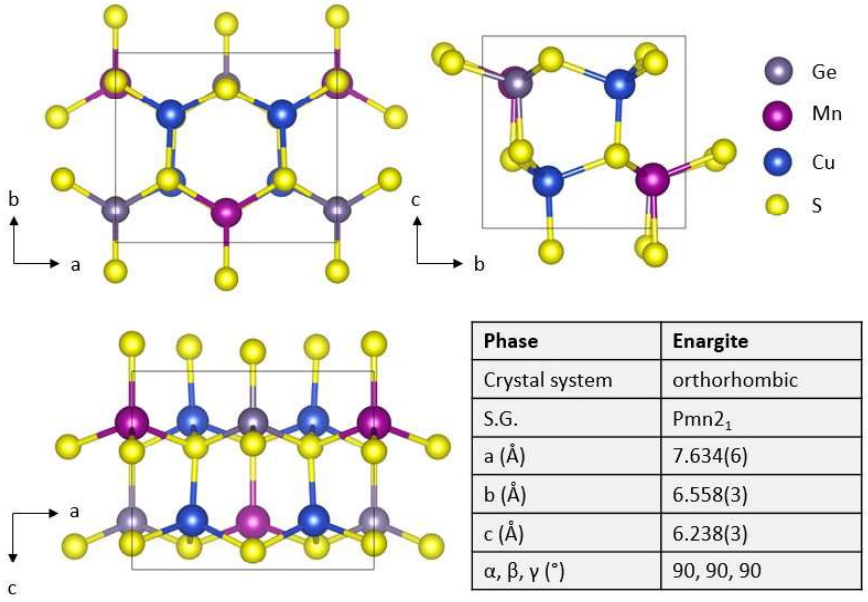

Phase	Enargite
Crystal system	orthorhombic
S.G.	$Pmn2_1$
a (Å)	7.634(6)
b (Å)	6.558(3)
c (Å)	6.238(3)
α, β, γ (°)	90, 90, 90

(a)

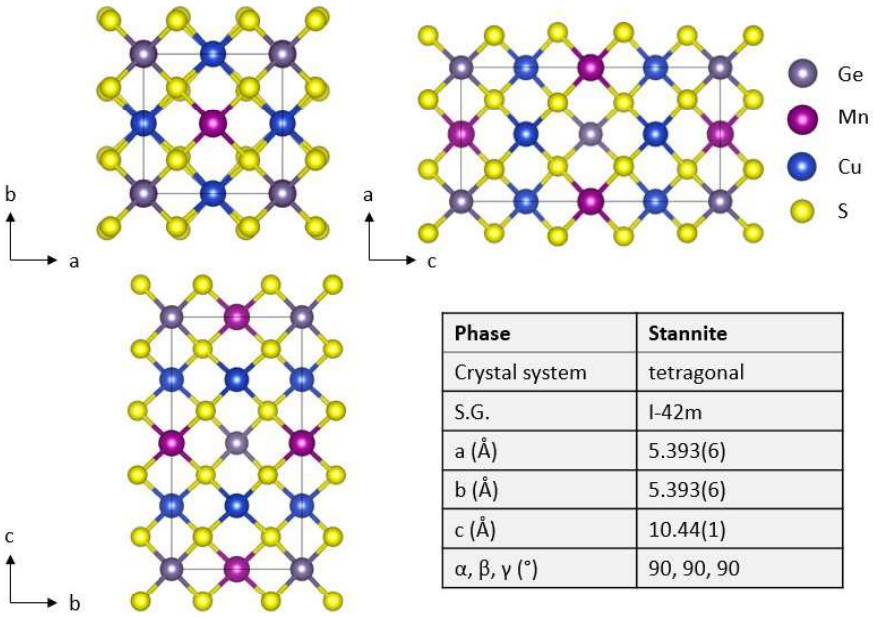

Phase	Stannite
Crystal system	tetragonal
S.G.	I-42m
a (Å)	5.393(6)
b (Å)	5.393(6)
c (Å)	10.44(1)
α, β, γ (°)	90, 90, 90

(b)

Figure 5.3: Crystal structures and lattice parameters of the two phases observed by PEDT in the sample, (a) enargite and (b) stannite, respectively.

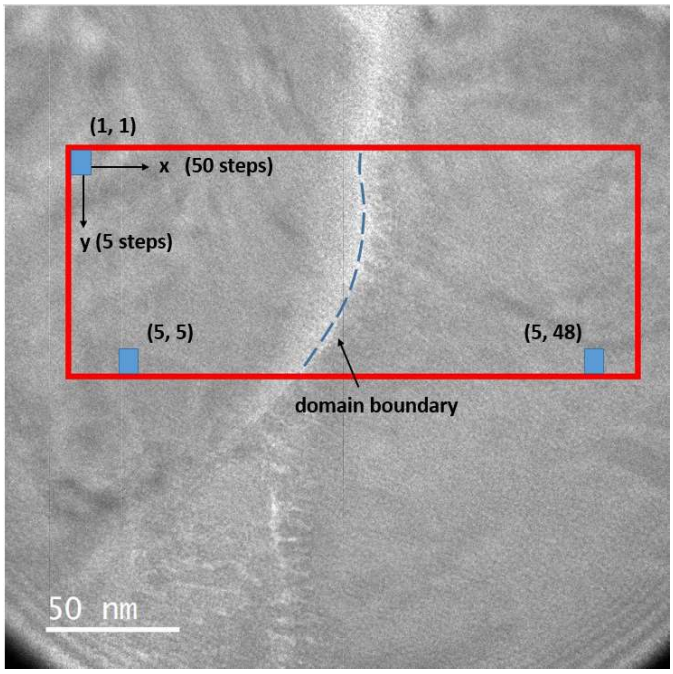

Figure 5.4: TEM BF image of the lamella sample $Cu_{2.3}Mn_{0.7}GeS_4$ acquired with Gatan Rio16 CMOS detector. The area probed by SPET is contoured in red, while the domain boundary is indicated with a blue dotted line.

for a total of 250 frames per tilt angle (Fig. 5.4). An electron beam of about 20 nm was used, whose diameter was assessed by TEM BF imaging. Acquisitions were performed in the range α = -40/+50°, with a tilt angle of 1°. An approximate tracking of the area was performed during the tilting by visual check, ensuring that roughly the same area was probed at every tilt step of the acquisition. Taking into account about 2 minutes per acquisition, but a longer time to tilt the sample and ensure the right positioning of the electron beam on the desired area, globally a time span of 4h has to be considered.

At this point, different approaches for tilt series reconstruction were compared, in order to inspect whether a significant difference was present, and, in case, to determine which one lead to the best results. In all the cases, although the phases which are present in the sample were known, the SPET datasets were processed as if they were not, in order to test the potentialities of the technique.

5.1.1 Data sorting and preliminary results

Blind extraction

As a first step of the analysis, we attempted to extract tilt series from the acquired SPET data solely relying on the position of the diffraction patterns within the scanned grid (ex: position (1,1), see Fig. 5.4). We will refer to this approach as "blind extraction". In this case, it was possible to perform tilt series extraction this way from single domains. In fact, the domain size was sufficiently large and the shift of the probe on the sample in between the different tilt steps was small enough to maintain certain portions of the scan grid on the same ROI.

Tilt series from the left (#1) and right (#2) domain were extracted, respectively from grid positions (5,5) and (48,5) (indicated in Fig. 5.4) and processed on PETS2 for cell indexation and intensity extraction.

In both cases, the diffraction peaks were successfully indexed by the orthorhombic $Pmn2_1$ enargite unit cell (SG: 31), revealing that the two domains were composed by the same phase. Structure solution and accurate structure refinements were performed for both datasets on Jana2020. The results are summarized in Table 5.1.

NMF decomposition

Additionally, NMF decomposition was used as a method to perform the diffraction pattern sorting automatically, indicating a number of components equal to two. As outlined in section 3.2, the frames were sorted in two folders according to their domain, and then the average frame in each folder was computed. It was then necessary to correctly reconstruct the tilt series for each domain. Therefore, the average frames were compared to the ones of the following tilt step in order to find the most similar one. The average frames were moved then to folder #1 or #2 accordingly.

After the correct sequences composed by the average diffraction patterns were reconstructed for the two components, they were normally processed on PETS2,

where both tilt series were once again indexed by the orthorhombic $Pmn2_1$ enargite structure (SG: 31). Afterwards, structure solution and accurate refinements were carried out on Jana2020. The obtained unit cells, as well as the results of the refinements, are reported in Table 5.1.

	Domain 1	**Domain 2**
Phase	Enargite	Enargite
	Blind extraction	
a, b, c	7.747(15) 6.460(12) 6.260(14)	7.659(13) 6.473(14) 6.233(16)
Kin ref R(obs)	0.291	0.215
Dyn ref R(obs)	0.210	0.169
	NMF deocomposition	
a, b, c	7.780(4) 6.454(4) 6.247(3)	7.609(5) 6.467(4) 6.199(4)
Kin ref R(obs)	0.297	0.218
Dyn ref R(obs)	0.198	0.157
	Similarity extraction	
a, b, c	7.765(3) 6.445(3) 6.227(2)	7.622(2) 6.460(1) 6.209(4)
Kin ref R(obs)	0.303	0.222
Dyn ref R(obs)	0.177	0.153

Table 5.1: Unit cell parameters and refinement results for the two domains probed by SPET on sample $Cu_{2.3}Mn_{0.7}GeS_4$ obtained from blind extraction, automatic sorting by NMF and averaging of the diffraction patterns of each domain, and finally extracted by similarity computation.

Sorting by similarity

A tilt series for each domain was also reconstructed by the similarity method. The similarity index method was applied to identify the regions of the scan area belonging to the same domain. Starting from a reference frame chosen among the images acquired at the first tilt angle, the script identifies the most similar diffraction pattern in the following tilt angle and consequently the frame range where the domain

of interest is located, determining then its center. Continuing in such fashion, a list of frames identifying the computed center of our domain is created, from which we can reconstruct its diffraction tilt series. In Fig. 5.5, an example of similarity computation in between a reference frame and the diffraction patterns of the following tilt angles is shown. Being the scan grid $(x,y) = (5,50)$, we can identify the regions where the domain of interest is located as the ones were the similarity is higher. The results from peak indexation on PETS2 and refinements performed on Jana2020 are reported in Table 5.1.

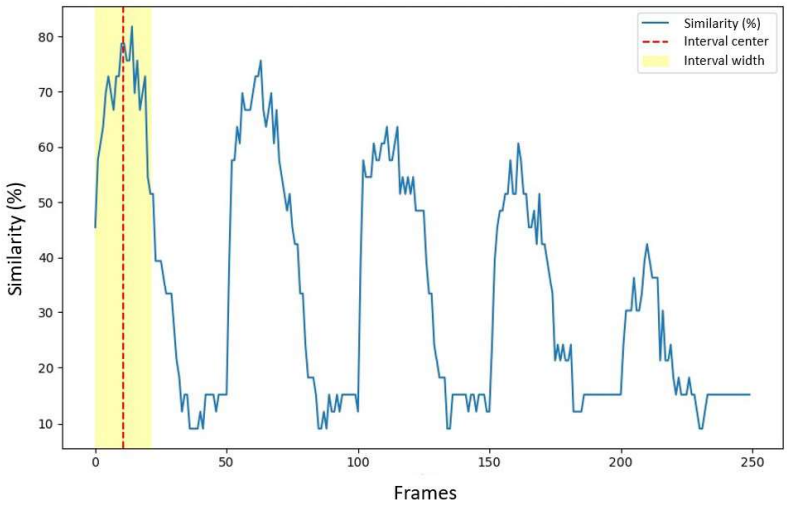

Figure 5.5: Similarity computation in between a reference frame and the diffraction patterns of the following tilt angles for the SPET acquisition on sample $Cu_{2.3}Mn_{0.7}GeS_4$.

In all the cases, the data integration was performed treating each dataset singularly, by refining the distortion parameters, adapting the resolution (in $Å^{-1}$) and choosing the most suitable method for intensity estimation. This has to be considered when comparing the obtained results for the three cases, since it can be a source of slight discrepancies.

In general, we can say that the matching results in between the three approaches suggest that it is possible to perform structure determination and accurate refinements by sorting the acquired frames through NMF and by similarity computation.

Therefore, using either one of these approaches (provided that the number of probed domains remains constant in the case of NMF) a precise tracking of the scanned area by visual check is not strictly necessary. Nevertheless, some differences can be noted.

Firstly, we can observe how the obtained R(obs) values are higher in all cases for domain 1. This can be likely attributed to the higher level of disorder in this area of the sample, evident in the diffraction pattern series because of the elongation of the peaks, in addition to the higher number of unindexed peaks due to twin-like patterns, whose presence was already stated in section 2.2.3 (Fig. 5.6).

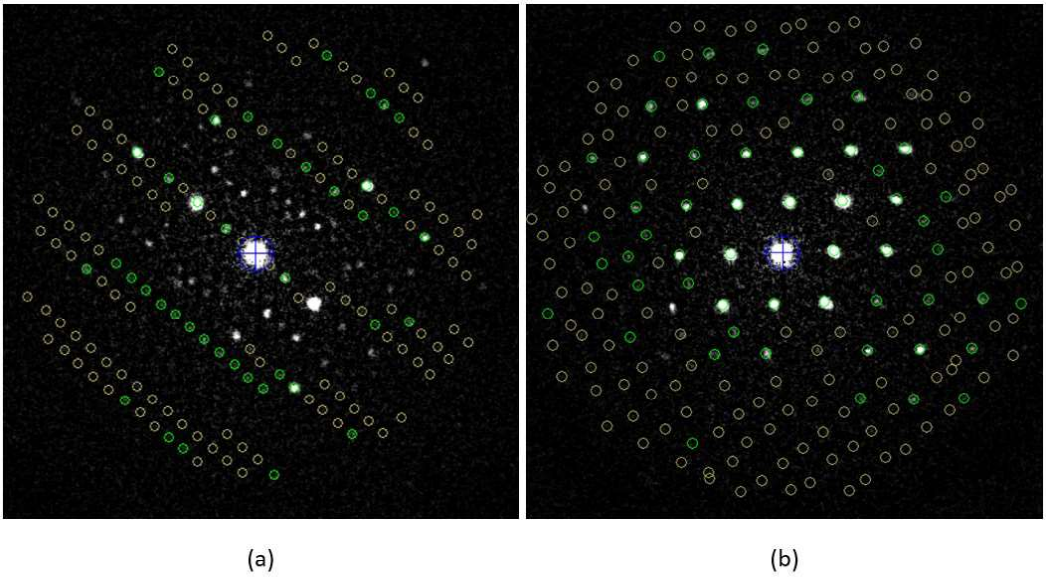

Figure 5.6: Comparison between diffraction patterns extracted from (a) domain 1 and (b) domain 2 of sample $Cu_{2.3}Mn_{0.7}GeS_4$, showing the better quality of the latter. Green circles: reflections matching the orientation matrix with observed intensities orange circles: reflections matching the orientation matrix with non observed intensities.

Despite being quite high, the R(obs) values for dynamical refinements are comparable with the ones previously obtained on the same sample by 3D ED on crushed powder (section 2.2.3), and in line with the abundant presence of defects in the specimen. As we can see, the best results were obtained for the extraction by similarity computation. This is likely linked to the precise tracking of the domain position, which allowed us to perform an accurate analysis of a specific area of the sample,

while the analysis on data sorted by NMF was performed on averaged diffraction patterns. Secondly, while the unit cell parameters of domain 2 are in line with the previous observations done by PEDT (section 2.2.3), a significant difference, mainly for what concerns the a parameter, was found in all of the three cases. Taking into account the models obtained from the extraction by similarity computation, we can observe that this difference translates, for domain 1, in a deviation from the hexagonal motif visible by projecting the structure along the c axis (see Fig. 5.7). In particular, the tetrahedra centered on the Cu, Mn and Ge atoms result stretched in direction [100], with the angles deviating more from the standard value of 109.5° (Table 5.2).

	Domain 1	**Domain 2**
$S_1 - Ge - S_1$	105.0(3)	107.1(3)
$S_1 - Mn - S_1$	115.8(3)	111.3(3)
$S_2 - Cu - S_3$	113.2(2)	111.0(3)
$Mn - S_1 - Ge$	110.4(3)	109.2(3)

Table 5.2: Individual angles observed in domain 1 and domain 2 of sample $Cu_{2.3}Mn_{0.7}GeS_4$ from dynamical refinement on datasets extracted by similarity computation.

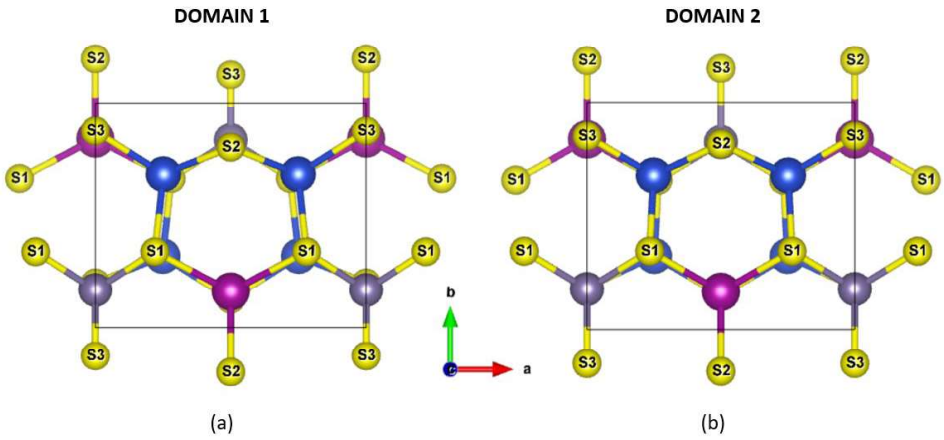

Figure 5.7: Crystal structures of enargite obtained from dynamical refinement on datasets extracted by similarity computation from SPET data on sample $Cu_{2.3}Mn_{0.7}GeS_4$ for (a) domain 1 and (b) domain 2.

5.1.2 Analysis of domain evolution

In order to go more deeply into the study of this difference between the two probed domains, we reconstructed the tilt series across all the ROIs of the two domains horizontally going from domain #1 to domain #2 (Fig. 5.8). The aim in this case was to check the consistency of the results and the potential presence of an evolution in the unit cell parameters.

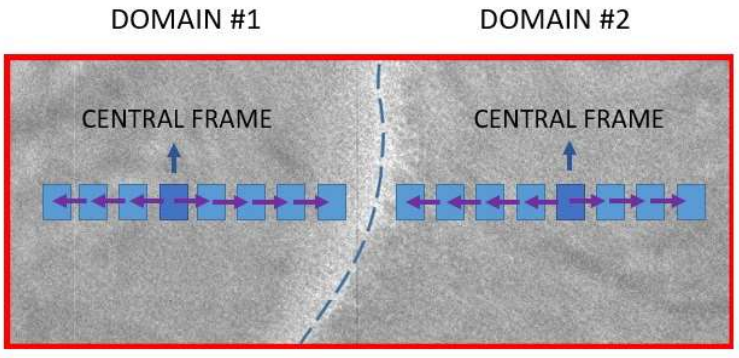

Figure 5.8: Scheme representing the desired ROI dataset extraction, for evaluating the evolution of the lattice parameters on the probed area of sample $Cu_{2.3}Mn_{0.7}GeS_4$.

The reconstruction of the tilt series for every ROI was done by extracting the neighbor frames with respect to the central ones previously found with the similarity approach (both to the left and to the right). As shown in Fig. 5.8, once the central frame of the domain of interest is determined, by shifting horizontally of the desired amount of frames, we could extract the diffraction pattern corresponding to the regions nearby. This is done for every tilt angle in such a way that the whole tilt series are reconstructed.

The procedure was applied to both domains with shifts of one frame in between every ROI. Being the step of the electron beam set to be 5 nm on x direction, we can consider each analysed ROI being 5 nm apart from each other. The central ROIs of the two domains were firstly analyzed manually in order to obtain the unit cell parameters and UB matrix that will later on be used as starting values for the

other tilt series.

In order for the results to be consistent and comparable, we decided to impose the same distortion parameters in all the ROIs, in such a way that every observed difference in the lattice would not be attributed to variations in these parameters (as previously validated in sections 4.1 and 4.3). For this reason, the central ROI of one of the two domains was chosen as a reference for the refinement of the distortion parameters. In this case, the choice fell on the domain on the right, since its diffraction pattern series showed a higher indexing percentage.

All the reconstructed ROIs were then automatically processed on PETS2, as previously outlined in section 3.2, by fixing the distortion parameters to the ones refined for the reference series of the right domain.

The effective vicinity of the two series defining the domain boundary was assessed through the observation of the respective diffraction patterns, where contributions from both domains were visible, as we can see in Fig. 5.9. Therefore, the selected frames for these ROIs can be attributed to the domain boundary.

The resulting unit cell parameters are reported in Fig. 5.10, where the gap in between the first and the second half of the experimental point indicates the boundary in between the two domains.

We can firstly state that, while in the right domain no significant evolution in any of the parameters is present, in the left one an evident increasing trend is observable in the case of the a parameter. Moreover, we can notice a significant discrepancy in between the parameters obtained at the domain boundary, mainly concerning a and b parameters.

In this case, we cannot rely on an internal standard for the determination of distortion parameters as the substrate for thin films, making harder the calibration to the correct values. Therefore, we should take into account the possibility of getting slightly shifted unit cell parameters with respect to the correct ones. Nevertheless, since the imposed values are the same for all the ROIs, we can state that the difference in between the parameters, as well as their evolution in the case of domain 1,

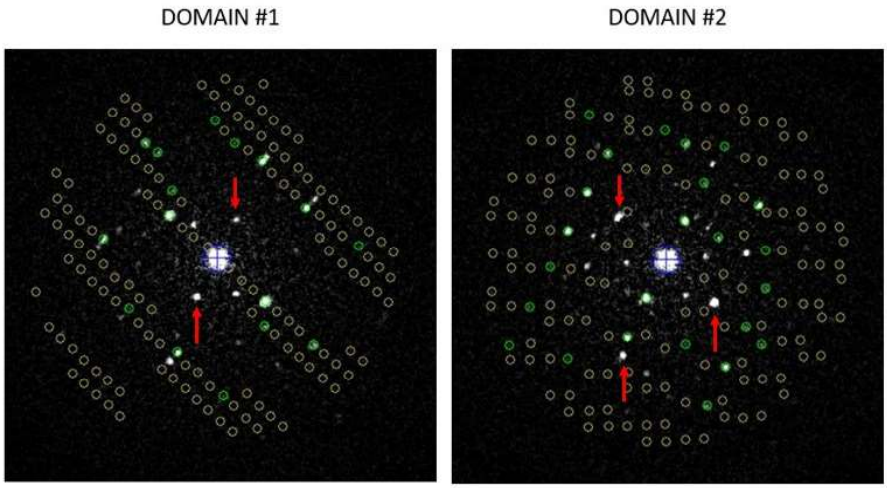

Figure 5.9: Selected diffraction pattern for domain #1 and domain #2 of sample $Cu_{2.3}Mn_{0.7}GeS_4$ at the same orientation angle. The peak integration is visible for both, the non-indexed peaks highlighting the contribution of both domains. Green circles: reflections matching the orientation matrix with observed intensities orange circles: reflections matching the orientation matrix with non observed intensities. The non-indexed peaks which are instead indexed on the other frame are indicated by a red arrow.

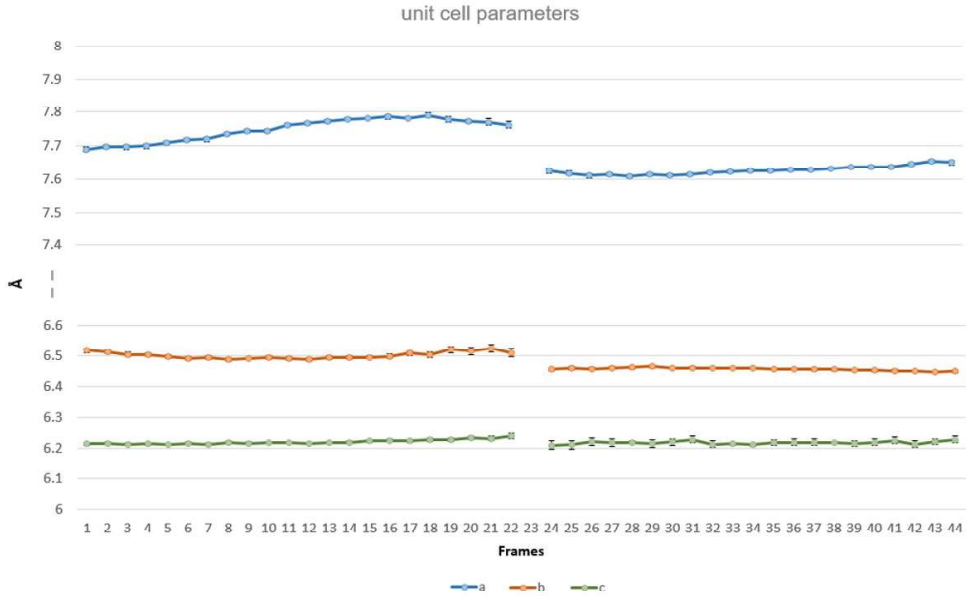

Figure 5.10: Unit cell parameters obtained from the automatic data processing of the tilt series reconstructed from the SPET acquisition on sample $Cu_{2.3}Mn_{0.7}GeS_4$.

are real.

Moreover, the results are in agreement with the different values previously obtained by single dataset extraction with the different approaches, considering the mismatch among the a parameters in domain 1. In fact, the blind extraction was performed on the left side of the area, the similarity method extracted frames from the center of the domain and the series reconstructed from NMF decomposition was composed of the average frames of the domain. This explains the initial difference on a parameter obtained in the three cases.

It is interesting to notice how these differences are appreciable with such an experiment on a TEM lamella, where the domains appear as they are in the bulk material, contrarily to conventional PEDT performed on single crystals in the grinded sample. Moreover, what is usually obtained with conventional PEDT is unit cell parameters which are averaged over a wider area, since the normally used beam diameter is larger. This way, we lose the ability of discerning fine details such as their evolution across a region (if present). Finally, the different experimental conditions could make the comparison of the results obtained by different PEDT acquisitions on different crystals complicated.

These variations on the unit cell parameters are likely causing the peak broadening that we observe in PXRD and that make Rietveld refinement of the diffractograms hard to perform.

5.1.3 ACOM phase mapping

ACOM measurements were performed as well on the sample using the Jeol F200 TEM. The scans were performed and later processed with the ASTAR system by NanoMEGAS. From the previously solved crystal structures of stannite (by PEDT, section 2.2.3) and enargite phases (by SPET), it was possible to generate the templates that were later on used to index the diffraction patterns acquired on the probed area.

The maps were indexed using, other than stannite, the enargite structure resulting from SPET analysis on domain #1 and domain #2, respectively. This way, we could verify whether the varying unit cell parameters of the structures have an effect on the obtained maps or not. The results are shown in Fig. 5.11. From

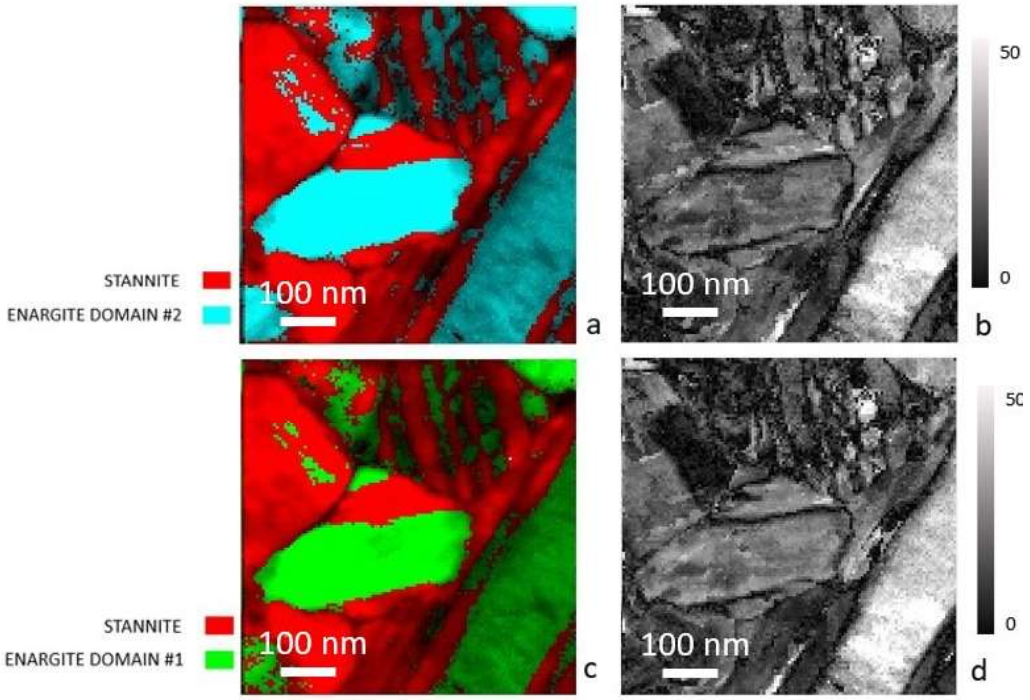

Figure 5.11: Left column: phase maps superimposed with index map of the scanned area (being the index representative of the match between the recorded diffraction pattern and one of the generated template giving a specific crystal orientation), using as templates, respectively: stannite and enargite #2; stannite and enargite #1; stannite, enargite #1 and #2. Right column: Correspondent reliability index of the phase identification.

the obtained maps we can see how the domains characterized by enargite phase are correctly identified using as a template both the unit cells derived from the previous SPET experiment (*a,c*), maintaining globally the same reliability indices (*b,d)*, confirming that the indexation procedure is not significantly affected by such differences in the unit cell parameters of the reference structures. We can therefore derive that small changes in the crystal lattices as the ones detected by SPET are not appreciable with ACOM approach.

5.2 $Al_2O_3/MgAl_2O_4$ lamella

As a last case of study, we took into account an α-alumina ceramic sample, synthesized by microwave-sintering, for which a 430 x 430 x 490 mm^3 multimode cavity and a 2.45 GHz (600 W to 6 kW) generator (SAIREM) was used [111]. The used thermal cycle was 25°C/min to 1550°C, with a dwell duration of 5 min. The specimen, once prepared as a TEM lamella by FIB cutting, appears characterized by large Al_2O_3 domains (500-1000 nm), constituting the matrix, and nano-sized $MgAl_2O_4$ inclusions, as previously observed by TEM imaging and EDX (Fig. 5.12) [112]. In

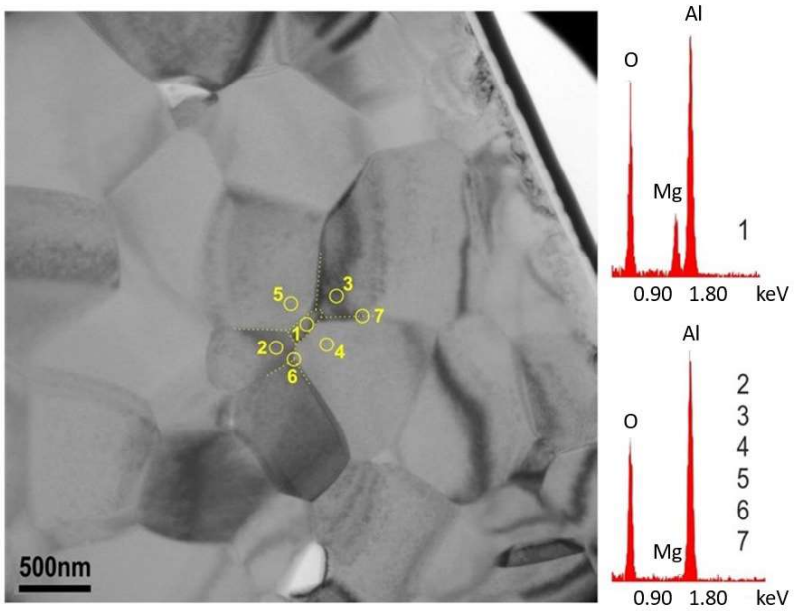

Figure 5.12: TEM bright field imaging of sample $Al_2O_3/MgAl_2O_4$, the EDX spectra on the right corresponding to the areas indicated in yellow.

Table 5.3, the reference parameters for the matrix and inclusion crystal structures are reported. The respective structures are shown in Fig. 5.13.

TEM BF imaging observations suggested an average dimension of 300 nm for the $MgAl_2O_5$ inclusions (as visible in Fig. 5.14), where the presence of Mg was confirmed through EDX analysis.

SPET was performed on the sample with a precession semi-angle $\phi = 1.4°$ and an

	Matrix	Inclusion
Composition	Al_2O_3	$MgAl_2O_4$
crystal system	hexagonal	cubic
SG	$R\bar{3}c$	$Fd\bar{3}m$
a, b, c	4.761 4.761 12.995	8.085 8.085 8.085
α, β, γ	90 90 120	90 90 90

Table 5.3: Reference crystal systems and unit cell parameters for the Al_2O_3 matrix and the $MgAl_2O_4$ inclusion of the lamella [113, 114].

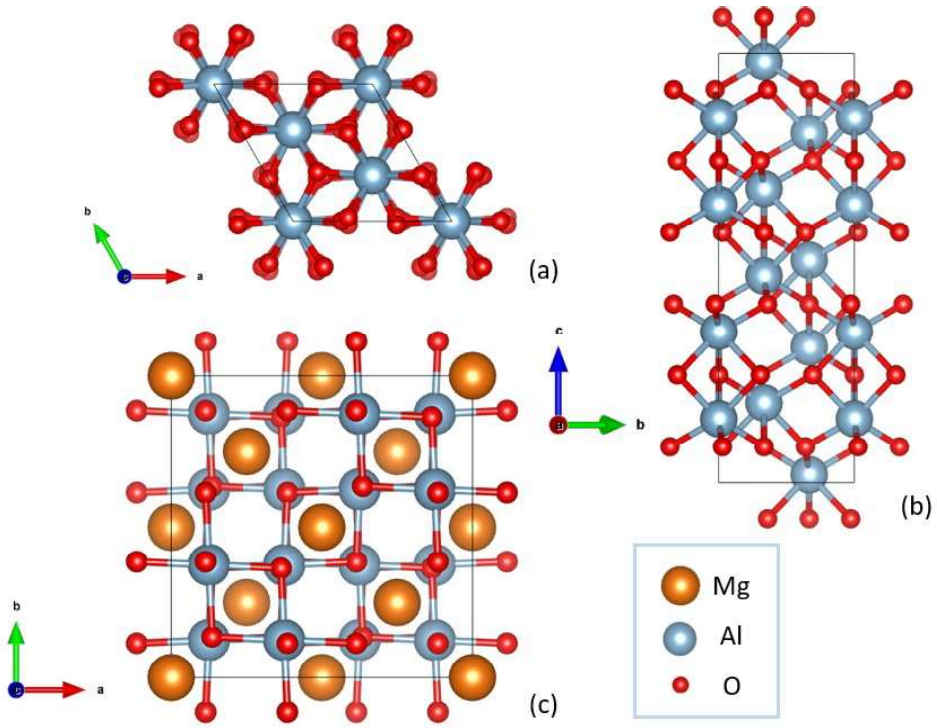

Figure 5.13: Crystal structure of both the Al_2O_3 matrix viewed along c and a axes (a, b) and the $MgAl_2O_4$ inclusion (c). Color key in the bottom-right panel.

electron beam size of 50 nm, whose diameter was estimated with BF imaging. The selected scan area measured (1000 x 250) nm, sampled in a (50 x 5) grid (highlighted in Fig. 5.14) having step size of 20 nm in X direction and 50 nm in Y direction. Acquisitions were performed in the range $\alpha = -41/+35°$ with a tilt step of 1° by visually checking the sample at each orientation angle in order to probe roughly

the same area. ACCOS software from ASI was used for the diffraction patterns acquisitions.

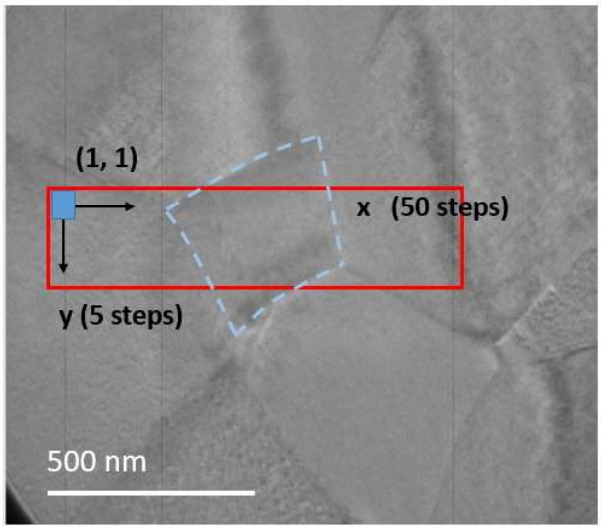

Figure 5.14: Bright Field TEM image of sample $Al_2O_3/MgAl_2O_4$, acquired with Gatan Rio16 CMOS detector. The scanned area during the SPET experiment is highlighted in red, while the $MgAl_2O_4$ inclusion is framed with a light blue dotted line.

PEDT was also performed on both the Al_2O_3 matrix and an $MgAl_2O_3$ inclusion in order to compare the results to the ones obtained by SPET, with a precession semi-angle $\phi = 1.4°$, an exposure time of 0.5 s in the range $\alpha = -41/+35°$, and a camera length equal to the value used for the SPET acquisition (CL = 200 mm).

5.2.1 Data sorting strategy

From the SPET acquisition, we firstly tried blind extraction, therefore to reconstruct diffraction tilt series from both domains by only relying on the position on the scan grid (for example extracting from every tilt step frame nr.100). This way, two datasets were obtained, representing respectively the matrix and the inclusion.

Secondly, one tilt series for the matrix and one the inclusion were reconstructed with automatic extraction by selecting, as outlined in the previous section, a starting frame from the first scan, and then searching for the most similar frame among the

diffraction patterns collected on the following tilt step. From the computations, color maps were constructed in order to visualize the computed similarity percentage across each one of the scans, in such a way to obtain information about the shape and position of the domains. In Fig. 5.15, the similarity maps at +1° orientation from three different reference frames are shown, from which we can observe the different domains identified by the computation. The maps can then be combined into a single one using a RGB scale to display for every pixel the percentages from the three components (Fig. 5.16).

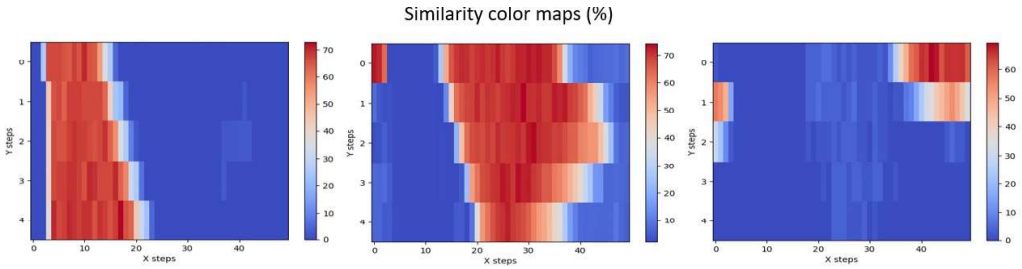

Figure 5.15: Similarity maps (in percentage) computed at the same orientation angle on the scanned area of sample $Al_2O_3/MgAl_2O_4$. The three maps are derived starting from frames associated with different domains.

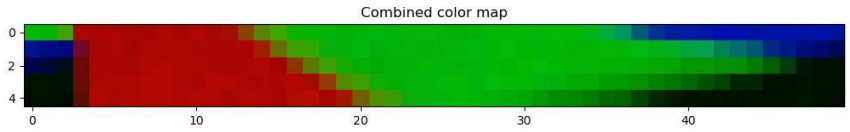

Figure 5.16: RGB combination of the three previous similarity maps computed on the scanned area of sample $Al_2O_3/MgAl_2O_4$.

In this case, the shift observable in the first columns of the reconstructed maps is due to the lack of synchronization in between the scan and the acquisition. The electron beam is positioned at the center of the scan grid at the beginning of each acquisition and then proceeds to move to position (0, 0) in order to start the scan. Therefore, the first frames can show a high similarity with respect to the central domain (in this case the inclusion), according to the time difference in between the initiation of the two processes. As a consequence, the dataset might show a shift of the first or last frames of each scanned row to the previous or following row.

For what concerns this sample, it was not possible to apply the sorting through NMF decomposition. In fact, the variable amount of domains probed across the tilt series, due to slight differences in the starting position of the beam, lead to incorrect identification of the components and consequently a wrong image sorting.

5.2.2 Results of data processing

The reconstructed tilt series of both the Al_2O_3 matrix and the $MgAl_2O_4$ inclusion were then processed and the results compared to highlight possible discrepancies in between them. As in the previous cases, the data were processed on PETS2 for indexation and intensity extraction and Jana2020 for structure solution and refinements.

The datasets (PEDT and SPET, both by blind extraction and similarity computation) were processed by freely refining, in addition to the unit cell, the distortion parameters. The results thus obtained are reported in Table 5.4. By comparing the lattice parameters obtained from the PEDT series to the ones obtained from the SPET series, both by blind and automatic extraction, we can observe that the obtained unit cell parameters for the matrix and the inclusion show some differences.

	Al_2O_3 Matrix	$MgAl_2O_4$ Inclusion
Reference	4.761 4.761 12.995	8.085 8.085 8.085
PEDT	4.754(7) 4.7543(7) 13.20(2)	8.012(5) 8.012(5) 8.012(5)
Blind extraction	4.758(5) 4.758(5) 13.05(2)	8.104(7) 8.104(7) 8.104(7)
Similarity extraction	4.774(6) 4.774(6) 13.096(6)	8.135(5) 8.135(5) 8.135(5)

Table 5.4: Unit cell parameters resulting from PETS2 indexation of both the Al_2O_3 matrix and the $MgAl_2O_4$ inclusion of the lamella, in comparison with the respective reference values [113, 114].

In Table 5.5, the results for kinematical and dynamical refinements on both the matrix and the inclusion structures are reported, for the three different datasets.

Globally, we can state that the results for the lattice parameters are compatible in

	Al_2O_3 matrix	$MgAl_2O_4$ inclusion
PEDT		
Kinematical refinement R(obs)	0.183	0.228
Dynamical refinement R(obs)	0.073	0.098
SPET blind extraction		
Kinematical refinement R(obs)	0.209	0.256
Dynamical refinement R(obs)	0.112	0.094
SPET automatic extraction		
Kinematical refinement R(obs)	0.207	0.265
Dynamical refinement R(obs)	0.086	0.094

Table 5.5: Results of kinematical and dynamical refinements on PEDT and SPET data from both the Al_2O_3 matrix and the $MgAl_2O_4$ inclusion of the lamella.

between each other and with the reference crystal structures. The slight differences among the various parameters can be in fact attributed to the intrinsic uncertainties linked to TEM electron diffraction, as well as to the computation of distortion parameters. Moreover, we have to take into account that, inside the probed domains, there could be slight variations of the unit cell parameters. In this case, the PEDT acquisition and the different dataset extraction from SPET series could be sensitive to this phenomenon. An analysis region by region of the areas, by extracting all the diffraction data series of each domain, as we performed on sample $Cu_{2.3}Mn_{0.7}GeS_4$ in section 5.1, could highlight such variations.

Finally, looking at the results for structural refinements, in all the cases the obtained R(obs) values are coherent and reasonable for electron diffraction data. In this case, the slight differences in the results are likely due to the variations in peak integration, computation of the frame orientations, estimation of the sample thickness, as well as to the exclusion of the specific frames showing high R values during the refinements.

As a general consideration, we can consider the obtained results from SPET

acquisition satisfying and in line with the expectations, confirming the efficiency of the dataset extraction approach by similarity computation as well. It was in fact possible to perform accurate structure refinements from more than one nano-sized domain with a single SPET acquisition obtaining comparable results with respect to PEDT. Therefore, this approach paves the way for an easy way to characterize through 3D ED a variety of materials composed by nanodomains. In fact, it allows to probe the desired ROIs of the sample with a narrow electron beam and without the need of a sophisticated method for crystal tracking. Moreover, reconstructing the diffraction tilt series from a SPET data stack containing several ROIs, gives us the opportunity to use one of them as an internal reference in case the phase is known, which will finally bring more accuracy to the results (cell parameters).

Conclusions and perspectives

In this thesis, we proposed Scanning Precession Electron Tomography (SPET) as an approach to collect 3D ED data from different ROIs of a sample using a single acquisition, in order to analyze structural changes within nanodomains.

Through data processing on PETS2 and the refinements performed on Jana2020, we were able to analyze nano-sized domains and observe structural evolutions in the analyzed samples, both expitaxial thin films and ceramic materials, performing accurate structural refinements. However, some final considerations about the faced challenges and possible approaches to overcome them in the future can be made.

Challenges concerning the experimental setup

Firstly, we remind that in our experimental setup, the synchronization between the scanning and the acquisition was not implemented. The scan was in fact manged through the ASTAR system from NanoMEGAS, while the acquisitions were controlled by the ACCOS software by ASI. While the lack of synchronization was not detrimental to our test regarding the potentiality of SPET, some benefits could derive from its implementation. This would bring a greater ease during the data acquisition, since it would not be necessary to manage two different software. More-

over, at the stage of data sorting, the maps reconstructed at each tilt angle by similairity index or NMF decomposition would not suffer of possible shifts, as mentioned in section 5.2. This would avoid problems in the location of the domain of interest in the case of similarity computation. In fact, the shift observable in Fig. 5.15 could give issues in locating the center of the domain of interest and in the pattern sorting if we're interested in a frame-by-frame reconstruction as we did in the cases of the thin films or the ceramic sample $Cu_{2.3}Mn_{0.7}GeS_4$.

Challenges in SPET data sorting

Concerning the diffraction tilt series processing from a SPET dataset, the main challenge that was found consisted in the SPET data sorting, problem which we addressed in the previous chapters. In particular, two approaches have been taken into account and exploited in different experimental cases, namely similarity computation through direct comparison of the diffraction peaks coordinates (homemade Python script), and NMF decomposition by using already existing Python libraries (py4DSTEM, Hyperspy). Already from the first trials, it became clear that a universal method for diffraction pattern sorting would have been difficult to develop, considering the differences in between the tested samples and the varying processing necessities. Therefore, we focused on customizing the data sorting method for each case, in order to obtain the best results for every sample.

In the case of epitaxial thin films our aim was directed towards a detailed analysis of a single domain to assess potential variations of the crystal structure, which required the ability of tracking and separating the frames representing specific ROIs of the sample (e.g. ROI close to the substrate and ROI close to the coating). On the contrary, concerning multi-domain samples the main focus was being able to separate the frames representing different domains in order to reconstruct the reciprocal space for all the significant crystallographically equivalent regions of the sample. Therefore, in this last case, being able to track a specific area of the specimen while tilting is of secondary interest, as long as an equivalent ROI is probed. In this

context, attention should be payed to the possible presence of similar but not totally equivalent domains in the probed area. By using both approaches this could lead to errors in the reconstruction of the tilt series, by shifting from one domain to the other on different tilt angles or by averaging out frames not actually belonging to the same domain.

A possible further occurrence is the lack of frames corresponding to the domain of interest in one or more tilt steps of the acquisition due for example to bad positioning of the scan grid. In this case, the sorting methods will likely lead to mistakes in finding the best match in the scan series in question, affecting therefore the selection of all the following frames. If such an error is encountered, what can be done is to manually chose the desired frame from that scan series or the following one, and continue the procedure setting it as reference.

Moreover, each tested sample showed different challenges for the diffraction patter sorting, starting from the varying number of probed domains, to the diversity of the diffraction patterns to be sorted. More specifically, while for ceramic samples as the $Cu_{2.3}Mn_{0.7}GeS_4$ and $Al_2O_3/MgAl_2O_4$ lamellae the domains showed evidently different diffraction patterns, which facilitates the decomposition through NMF, the probed areas included, apart for the experiment reported in section 5.1, a varying number of domains depending on the tilt step. This constitutes a limit for exploiting NMF decomposition, since for automatizing the process the number of expected domains is set equal throughout the processing of all the scan acquisitions. Certainly, the decomposition can be performed separately for every tilt step of the SPET experiment. However, this will increase considerably the time invested for sorting the dataset, which is something we generally aim to minimize.

On the other hand, samples as the PVO and LVO thin films always showed across the SPET datasets the same domains, namely substrate, film and coating, also thanks to the homogeneity observable throughout their thickness. However, in the first case the difference consisted in additional peaks due to the larger unit cell parameters of PVO with respect to the STO substrate, while, for LVO/DSO,

only a slight shift of the peaks is observable by passing from one domain to the other. In this case in fact, the structures of both the film and the substrate were tilted perovskites with a similar orthorhombic lattice. In these cases the similarity in between the diffraction patterns of film and substrate constituted a challenge for NMF decomposition, since a single component could be assigned to both the film and the substrate. In Fig. 5.17, the aforementioned differences in between the diffraction patterns or the PVO and LVO epitaxial thin films and their substrates is highlighted through red circles and arrows.

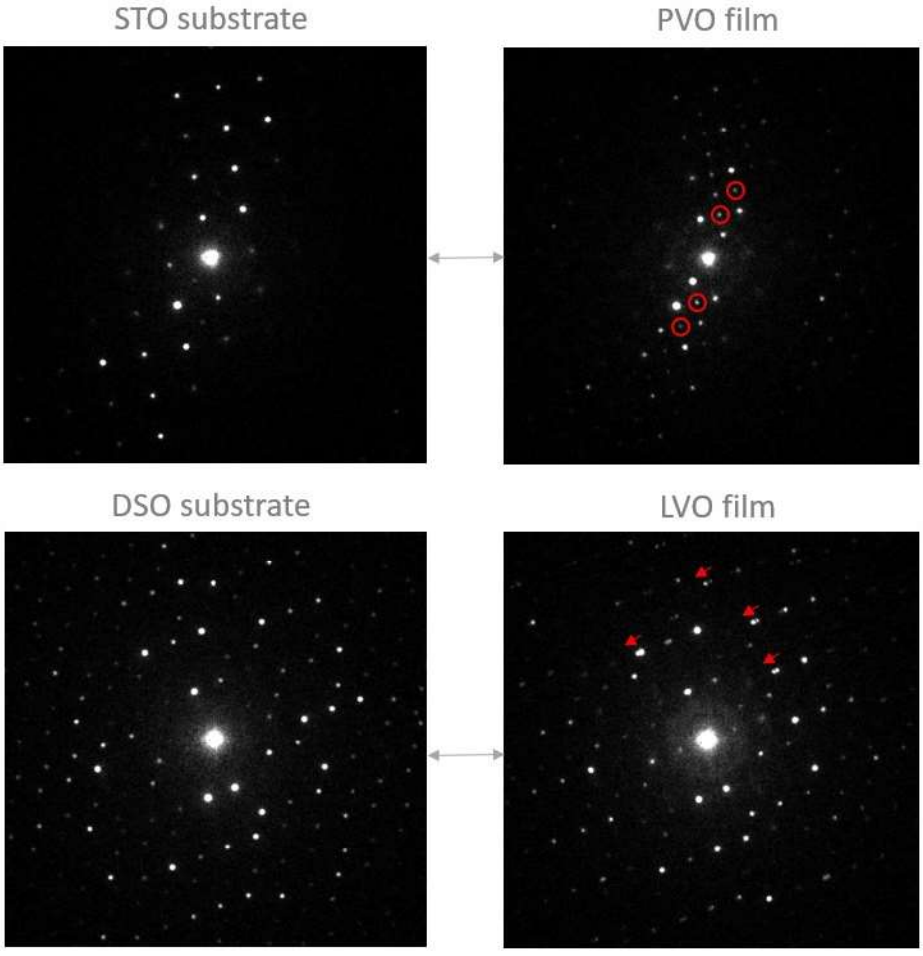

Figure 5.17: Comparison in between diffraction patterns generated by the PVO and LVO epitaxial thin films and their respective substrates. Differences are highlighted with red circles and arrows.

In addition, if NMF decomposition is used, another challenge is represented by the polycrystalline coating of thin films. Since variable peaks are usually detected in this area, identifying a single component in this region is not trivial. To circumvent the problem, what can be done in this case is, previous to the NMF decomposition, substituting all the frames corresponding to the coating with a reference frame of this region, in such a way that the detected peaks will be the same across all the dataset, making this way the decomposition easier. Directly eliminating the concerned frames instead should be avoided, since it would likely lead to SPET scans on the various tilt angles with different sizes, which would make in turn the construction of the 2D signal (.hspy), which takes as input the dimensions of the scan grid, harder and more time consuming. However, this implementation did not make the sorting by NMF decomposition totally effective for thin film samples.

Furthermore, the structure of the dataset as it is required for computing NMF decomposition on py4DSTEM makes hard accessing to information such as the peaks position and modifying it according to the necessities, which is a crucial step in the optimization of the procedure. As a final consideration, it is noteworthy that even if the NMF decomposition proceeded correctly at every step of the SPET acquisition, is it however necessary to correlate the frames to the ones of the following tilt angle, since the sorting is independent for each scan dataset. Therefore, a homemade method for relating the frames at different tilt angles and reconstructing the PEDT series was required in any case.

Given the previously listed difficulties, the development of a homemade script for data sorting was thus taken into account as an option. Despite the time invested in implementing it, the code brought significant advantages with respect to the NMF decomposition procedure. Firstly, this script directly searches for the most similar frame in the following tilt angle with respect to the one chosen as a reference, which reduces the steps to follow for the PEDT series reconstruction to one instead of two. Also, this approach makes the computation independent from the number of domains which are present in each scanning acquisition. Therefore, no issues will

arise if the probed domains vary by passing from a tilt angle to the other, or if polycrystalline regions are present. This allows the user to focus on the reciprocal space reconstruction for the domains considered as ROIs, just by having to identify the suitable frames in the first tilt scan, and disregarding the rest. Secondly, by directly working with the peaks list of every acquired diffraction pattern, information is more easily accessible, and the comparisons in between the frames can optionally be visualized on plots to check every step in the procedure. This allows the user to quickly optimize the comparison calculation according to the necessities, for example by tuning the tolerance in shift for considering two peaks as matching. Moreover, the method for the similarity percentage computation can be customized as well as needed according to the features of the sample and its diffraction patterns (see eq. 3.1, 3.2). In the cases of randomly distributed domains, a more accurate calculation would take into account both the similarity of frame #1 to #2 and the similarity of frame #2 to #1, since the ROIs normally show very different diffraction patterns in between each other. Differently, in epitaxial thin films, where we usually have a high resemblance in between the diffraction pattern of the film and the one of the substrate, only consider the similarity in between the selected frame and each test frame was proven to be more efficient. In the case of PVO for instance, the average in between the two computed percentages was raised by the total correspondence of the peaks of STO to the ones of PVO, making the separation less reliable. Lastly, for every tilt step, a map can be visualized showing the similarity percentage of every frame to the reference one, and optionally combine the ones created starting from different diffraction patterns in order to create a global phase map of the probed area, similarly to the NMF components map that can be visualized with py4DSTEM, offering an equivalent overview of the sample.

Nevertheless, to this day some issues remain open when using the similarity computation to sort SPET data, as a mistake in the assignment of the most similar frame, as previously mentioned. Also in this case, This problem can be manually solved by re-starting the procedure from the tilt step where the mistake took place

by setting as a reference the frame selected as correct from the user, or skipping the acquisition in question in case the desired ROI does not appear.

Despite at this stage it needs some amount of supervision from the user, the automatic data sorting procedure developed for this work of thesis already offers a quicker and more convenient way to reconstruct the PEDT tilt series from SPET datasets with respect to the manual sorting. This protocol, together with the automatic data processing routine, can provide reliable structure solution and accurate structural refinements in a reasonable amount of time.

Some improvements can be implemented which could make the sorting method by similarity computation more reliable. As we saw in section 4.2.4, to this day the automatic procedure for reconstructing thin film ROIs only takes into account the found central frame of the domain, and then extracts the neighboring regions by adding or subtracting frame to it. This way, the effective thickness of the film is not taken into account, incurring possible errors. If the observed film thickness varies across the SPET dataset for misalignment reasons, the frames position with respect to the interface could be this way wrongly estimated, as depicted in Fig. 5.18.

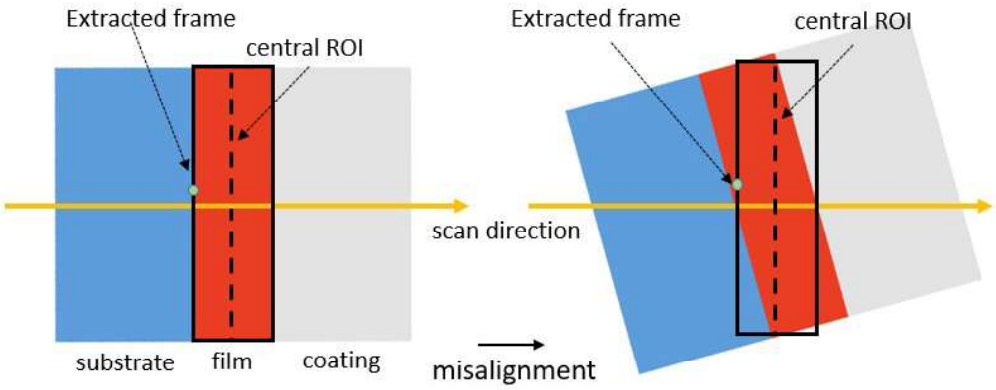

Figure 5.18: Illustration of the effect of misalignment is SPET acquisitions on frame extraction.

Therefore, by actually taking into account the number of frames where the film

appears, we can obtain a more accurate ROIs reconstruction. This would imply some adjustments in case the number of frames varies across the SPET datasets in order to maintain the same number of diffraction patterns in all the ROIs, for example, by averaging out two frames (Fig. 5.19).

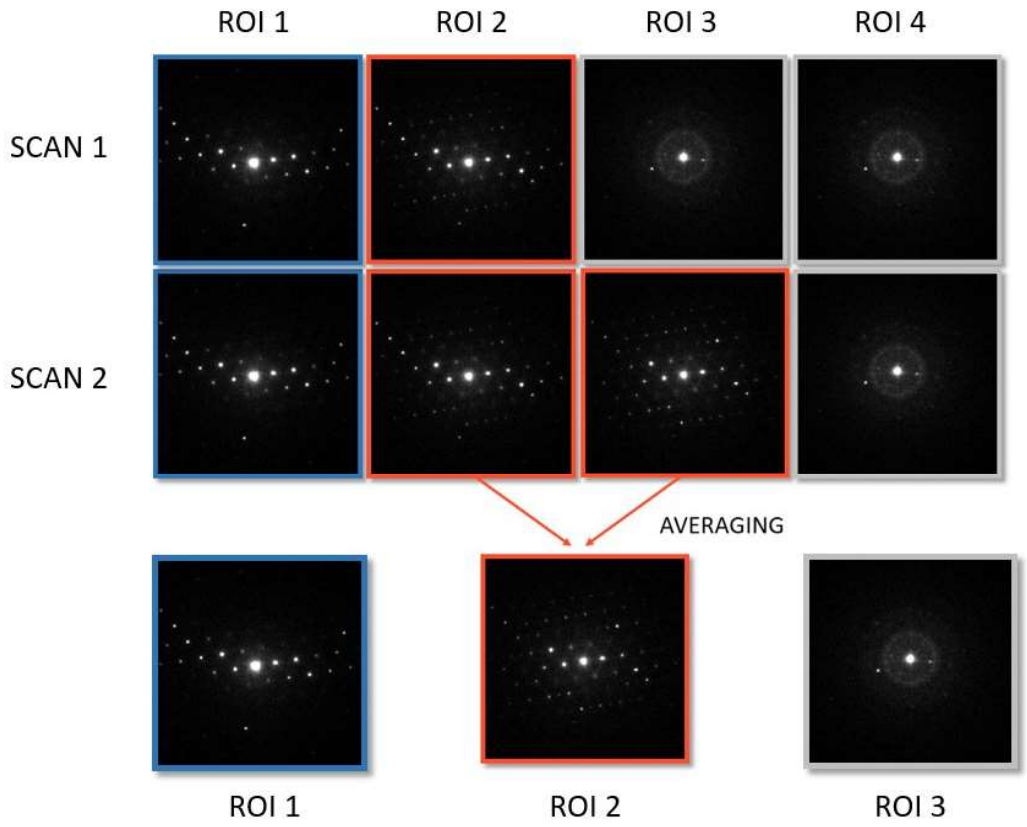

Figure 5.19: Illustration of the procedure of frame averaging for maintaining the same number of frames across the scan series in a SPET dataset.

Challenges in the data processing strategy

A fast and effective way of automatically processing the datasets on PETS2 (for refinement of the unit cell and peak integration) and Jana2020 (for structure solution and refinements) was implemented, in order to analyze several extracted ROIs automatically. In the first case, the procedure relied on the imposition of a starting unit

cell to be refined, together with the distortion parameters if needed. On Jana2020, the cyclic refinement option was exploited instead. As we saw, this approach can give good results in a reasonable amount of time, allowing to evaluate possible evolutions in the unit cell parameters, as well as in atomic coordinates, across a certain area of the specimen. However, it is important to take into account that, being the processing done automatically, the quality of the results is not necessarily the best achievable, and therefore it could be improved.

During the PEST2 processing, By assessing each dataset singularly, we can in fact chose an integration method that gives as a result a better rocking curve fit or discard possible bad frames. Moreover, the autotask offered by PETS2 requires fixed settings (ex: peak integration method or parameters to be refined) which can not be modified during the process. Moreover, it is not possible to change the parameters to be refined during the procedure, by fixing some of them and freeing others. This limits the reachable quality of the data analysis, however providing good enough integrations for kinematical and dynamical refinements. This could be overcome by defining a procedure for performing some steps with the autotask option and closing the file before modifying the .pts and setting new commands for the autotask procedure. This way, the procedure followed for the manual analysis of the first reference ROI could be accurately reproduced.

Concerning instead the cyclic refinements on Jana2020, some more test can be performed in order to optimize the procedure and understand the origin of the higher R values obtained for automatic vs manual analyses. As an example, we could try to perform the refinements starting from a different reference ROI, to assess whether this has an influence on the obtained structural parameters. Moreover, for the case of PVO thin film, cyclic refinements can be performed starting with the *.cif_pets* files obtained from manual analysis. This would highlight issues exclusively due to the automatic procedure.

SPET in the future

The listed optimizations could be tested on the previously analyzed materials in order to check the quality of the obtained data. Afterwards, SPET could be challenged by performing the experiments with a smaller electron beam to assess the effect of its size on the outcomes. Moreover, it would be valuable to conduct tests on different kinds of samples, as unknown bulk samples composed by naodomains or nano-sised inclusions, or multidomain thin films. In this last case, their morphology, constituted by nano-sized domains that usually show a limited amount of orientations represent a case where we have crystallographically equivalent regions. While solving *ab initio* the structure of each type of domain could be straightforward, analyze the evolution of the crystal lattice as we did for monodomain films could be more challenging, given the difficulty in reconstructing of a specific domain.

Once a more defined and efficient procedure for data acquisition and data processing has been implemented, SPET will have the possibility to become a routine characterization technique for obtaining accurate details on the crystal structure of nanodomains in functional materials.

APPENDIX A

List of NanED Secondments

TESCAN France, Fuveau 13-25/02/2023

TEM lamellae preparation through SEM-FIB using TESCAN Amber X

Local supervisor: A. Morvan

TESCAN Brno, 06-25/03/2023

Diffraction data acquisition with TESCAN Tensor analytic 4D-STEM

Local supervisor: B. Clarke

Johannes-Gutenberg Universität, Mainz, 02/05-29/07/2023

3D ED on defective materials; development of a routine for SPET diffraction data sorting

Local supervisor: U. Kolb

FZU Institute of Physics of the Czech Academy of Sciences, Prague, 03/10-05/12/2023

Development of a routine for automatic processing of SPET diffraction data with PETS2 and Jana2020

Local supervisor: L. Palatinus

APPENDIX B

PETS2 input file for automatic PEDT series processing

```
# Steps for automatic data processing
autotask
peak search
peak analysis
refine cell
process frames
finalize integration
frame geometry
process frames
finalize integration
refine cell
process frames
frame geometry
process frames
finalize integration
quit
```

```
endautotask

# Experimental parameters
geometry precession
detector asitmp
noiseparameters 5 0 # parameters for calculating the sigma(count)
on every pixel. First: G*gamma (gain*cascade factor),
second: sigma**2 of the dark image
beamstop no
lambda 0.025079
center AUTO
Aperpixel 0.00708
phi 1.4
omega 16.4015
delta 0.1658
bin 1

# Parameters for refinements and peak integration
dstarmax  1.7  # max. resolution for peak integration (1/Å)
dstarmaxps  1.7  # max. resolution for peak search
i/sigma    5.00    5.00  # Minimal intensity for peak
detection and for the calculation of the camel plot
reflectionsize 10  # diameter of integration circle of the
reflections (pixels, unbinned)
integrationmode fit 1 5 3 1.000  # integration mode, frame
scaling (0 = no scaling, 1 = optimize against reflection
profile, 2 = optimize against R(int)), Laue class number
for frame scaling, range for frame scale restraints,
weight of the frame scale restraint.
intensitymethod profilefit  # method for peak intensity
determination
```

```
orientationparams 1 1 0 1 -3 0 1  # keys of the orientation
optimization. 1=apply, 0=don't apply optimization to tilt
angles, frame centers, RC width, mosaicity,
frame-by-frame distortions (binary code - 1st bit
magnification, second elliptical, third parabolic),
transfer average distortions to global distortions.
The last key selects integrated intensities (=1) or
uniform (=2)
interpolationparams  2  3  0  # keys for interpolation of
orientation optimization values: mode of interpolation
(0 = none, 1 = polynomial, 2 = moving average), order
(polynomial order for poly fit, half-range formoving
average), level for outlier rejection (in sigma).
distortunits percent  # units in which distortions are
displayed and stored
distortions  # distortion parameters
0.0000      0.0000      0.0000      0.0000
0.000000    0.000000    0.087994    0.000000
0.000000    0.000000    0.000000    0.000000
0.746720    0.000000    0.000000  173.671494
0.000000    0.000000   -0.069004    0.000000
0.000000    0.000000    0.000000  -90.000000
0.746700    0.000000    0.000000  128.977493
-0.162968    0.000000    0.000000    0.000000  0.0000 0.0000
enddistortions
distortionskeys # refinement keys for distortion parameters
0  0  0  0
0  0  1  0
0  0  0  0
1  0  0  1
0  0  1  0
```

```
0  0  0  0
2  0  0  2
1  0  0  0  0  0
enddistortionskeys
cellrefinemode cellanddistort  # algorithm for cell refinement.
cellandub = refinement from 3D peak coordinates (standard),
cellfromd = refinement against lengths of the diffraction
vectors, cellanddistort = cell from 2D peak positions plus,
optionally, distortion parameters.
cellrefineparameters  4 1 1  # parameters for cell refinement:
crystal system index, key to refine cell in cellanddistort
(0/1), key to refine distortions in cellanddistort (0/1).

imagelist
path_tiff_1  alpha_angle_1
path_tiff_2  alpha_angle_2
...
path_tiff_n  alpha_angle_n
endimagelist
```

APPENDIX C

List of Author's contributions

Peer-reviewed Publications

Pavan Kumar, V., Passuti, S., Zhang, B., Fujii, S., Yoshizawa, K., Boullay, P., Le Tonquesse S., Prestipino C., Raveau B., Lemoine P., Paecklar A., Barrier N., Zhou X., Yoshiya M., Suekuni K., Guilmeau, E. (2022). Engineering Transport Properties in Interconnected Enargite-Stannite Type $Cu_{2+x}Mn_{1-x}GeS_4$ Nanocomposites. Angewandte Chemie, 134(49), e202210600.

Passuti, S., Varignon, J., David, A., Boullay, P. (2023). Scanning precession electron tomography (SPET) for structural analysis of thin films along their thickness. Symmetry, 15(7), 1459.

Oral Presentations

Workshop on Electron Crystallography SIG4, Antwerp University, 30-31/05/2023
"SPET as a tool to investigate nanodomains in functionals materials "

18^e Colloque de la Société Français des Microscopies (SFμ 2023) Rouen, 03-07/07/2023
"SPET as a tool to investigate nanodomains in functional materials"

34^{th} European Crystallography Meeting (ECM34), Padova, 26-30/08/2024
"Structural analysis of functional materials through Scanning Precession Electron Tomography (SPET)"

Poster presentations

33^{th} European Crystallography Meeting (ECM33), Versailles, 23-27/08/2022
"3D scanning precession electron diffraction analysis of nanodomains in thin films"

Intenational Workshop on Thermoelectrics (IWT2023), Caen, 12-14/04/2023
"3D Scanning Precession Electron Diffraction Tomography of nanodomains in thermoelectrics"

Scientific Workshop Participation

Electron Crystallography School (ECS2022), Caen, 29/08-01/09/2022

NanED Workshop I - data processing and structure refinement
Prague, 25-27/05/2022

NanED Workshop II - Imperfect crystals, complementarity with XRPD, Intellectual properties and patent in Science
Mainz, 06-08/12/2022

NanED Workshop III - TEM Imaging and Spectroscopy
Antwerp, 01-02/06/2023

NanED Workshop IV - NanED Meets Industry
Caen, 06-07/12/2023

Bibliography

[1] Breakthrough of the year 2018 Runners-up: Molecular structures made simple. Science Magazine. URL: https://vis.sciencemag.org/breakthrough2018/finalists/#cell-development.

[2] Daniel Sando. "Strain and orientation engineering in ABO_3 perovskite oxide thin films". In: *Journal of Physics: Condensed Matter* 34.15 (2022), p. 153001.

[3] Kurt E Geckeler and Hiroyuki Nishide. *Advanced nanomaterials*. John Wiley & Sons, 2009.

[4] Ibrahim Khan, Khalid Saeed, and Idrees Khan. "Nanoparticles: Properties, applications and toxicities". In: *Arabian journal of chemistry* 12.7 (2019), pp. 908–931.

[5] Saisai Yuan and Qitao Zhang. "Application of one-dimensional nanomaterials in catalysis at the single-molecule and single-particle scale". In: *Frontiers in Chemistry* 9 (2021), p. 812287.

[6] Chaoliang Tan et al. "Recent advances in ultrathin two-dimensional nanomaterials". In: *Chemical reviews* 117.9 (2017), pp. 6225–6331.

[7] Zong-Yang Shen and Jing-Feng Li. "Enhancement of piezoelectric constant d33 in BaTiO3 ceramics due to nano-domain structure". In: *Journal of the Ceramic Society of Japan* 118.1382 (2010), pp. 940–943.

[8] Peter Maksymovych et al. "Tunable metallic conductance in ferroelectric nanodomains". In: *Nano letters* 12.1 (2012), pp. 209–213.

[9] Tony JA Richardson. *Shreir's corrosion*. Elsevier, 2009.

[10] George F Harrington and José Santiso. "Back-to-Basics tutorial: X-ray diffraction of thin films". In: *Journal of Electroceramics* 47.4 (2021), pp. 141–163.

[11] Josep Fontcuberta. "Multiferroic RMnO 3 thin films". In: *Comptes Rendus. Physique* 16.2 (2015), pp. 204–226.

[12] Hélène Béa et al. "Investigation on the origin of the magnetic moment of $BiFeO3$ thin films by advanced x-ray characterizations". In: *Physical Review B—Condensed Matter and Materials Physics* 74.2 (2006), p. 020101.

[13] KH Ahn, T Lookman, and AR Bishop. "Strain-induced metal–insulator phase coexistence in perovskite manganites". In: *Nature* 428.6981 (2004), pp. 401–404.

[14] Deepak Kumar et al. "Magnetism tailored by mechanical strain engineering in PrVO 3 thin films". In: *Physical Review B* 99.22 (2019), p. 224405.

[15] Rajasekhar Madugundo et al. "Recent developments in nanostructured permanent magnet materials and their processing methods". In: *Magnetic Nanostructured Materials* (2018), pp. 157–198.

[16] Anindita Chatterjee, Tanmay Basak, and KG Ayappa. "Analysis of microwave sintering of ceramics". In: *AIChE Journal* 44.10 (1998), pp. 2302–2311.

[17] Pierric Lemoine et al. "Crystal structure classification of copper-based sulfides as a tool for the design of inorganic functional materials". In: *Angewandte Chemie* 134.2 (2022), e202108686.

[18] Bernard Raveau. “Copper mixed valence concept:“Cu(I)-Cu(II)” in thermoelectric copper sulfides—an alternative to “Cu(II)-Cu(III)” in superconducting cuprates”. In: *Journal of Superconductivity and Novel Magnetism* 33 (2020), pp. 259–263.

[19] Harith Hasoon Al-Moameri et al. “A review on the biomedical applications of alumina”. In: *Journal of Engineering and Sustainable Development* 24.5 (2020), pp. 28–36.

[20] M Kobayashi et al. “Three-dimensional structure of high-performance heat insulator produced with micro and nano particle alumina”. In: *Materials Characterization* 154 (2019), pp. 424–436.

[21] Fei Zuo et al. “Comparison of the microwave and conventional sintering of alumina: effect of MgO doping and particle size”. In: *Journal of the American Ceramic Society* 96.6 (2013), pp. 1732–1737.

[22] DANIEL K Unruh and TORI Z Forbes. “X-ray diffraction techniques”. In: *Analytical geomicrobiology: a handbook of instrumental techniques* (2019), pp. 215–237.

[23] Gwladys Steciuk et al. “Precession electron diffraction tomography on twinned crystals: application to $CaTiO_3$ thin films”. In: *Journal of Applied Crystallography* 52.3 (2019), pp. 626–636.

[24] Toru Mitsunaga. “X-ray thin-film measurement techniques”. In: *Rigaku J* 25 (2009), pp. 7–12.

[25] Hélène Rotella et al. “Structural analysis of strained LaVO3 thin films”. In: *Journal of Physics: Condensed Matter* 27.17 (2015), p. 175001.

[26] Jian Min Zuo and John CH Spence. *Advanced transmission electron microscopy*. Springer, 2017.

[27] *JEM-F200 Multi-purpose Electron Microscope*. URL: https://www.jeol.com/products/scientific/tem/JEM-F200.php.

[28] C Barry Carter and David B Williams. *Transmission electron microscopy: Diffraction, imaging, and spectrometry*. Springer, 2016.

[29] U Kolb, E Mugnaioli, and TE Gorelik. "Automated electron diffraction tomography–a new tool for nano crystal structure analysis". In: *Crystal Research and Technology* 46.6 (2011), pp. 542–554.

[30] E Spiecker et al. "Advantages of aberration correction for HRTEM investigation of complex layer compounds". In: *Journal of microscopy* 237.3 (2010), pp. 341–346.

[31] Colin Ophus. "Four-dimensional scanning transmission electron microscopy (4D-STEM): From scanning nanodiffraction to ptychography and beyond". In: *Microscopy and Microanalysis* 25.3 (2019), pp. 563–582.

[32] EF Rauch et al. "Automatic crystal orientation and phase mapping in TEM by precession diffraction". In: *Microscopy and Analysis-UK* 128 (2008), S5–S8.

[33] P Moeck et al. "High spatial resolution semi-automatic crystallite orientation and phase mapping of nanocrystals in transmission electron microscopes". In: *Crystal research and technology* 46.6 (2011), pp. 589–606.

[34] Robert A Schwarzer and J Sukkau. "Automated crystal orientation mapping (ACOM) with a computer-controlled TEM by interpreting transmission Kikuchi patterns". In: *Materials science forum*. Vol. 273. Trans Tech Publ. 1998, pp. 215–222.

[35] A Kobler et al. "Combination of in situ straining and ACOM TEM: A novel method for analysis of plastic deformation of nanocrystalline metals". In: *Ultramicroscopy* 128 (2013), pp. 68–81.

[36] EF Rauch and MJMC Véron. "Automated crystal orientation and phase mapping in TEM". In: *Materials Characterization* 98 (2014), pp. 1–9.

[37] Joaquim Portillo et al. “Precession electron diffraction assisted orientation mapping in the transmission electron microscope”. In: *Materials science forum*. Vol. 644. Trans Tech Publ. 2010, pp. 1–7.

[38] Edgar F Rauch et al. “New features in crystal orientation and phase mapping for transmission electron microscopy”. In: *Symmetry* 13.09 (2021), p. 1675.

[39] Christopher Hammond. *The basics of crystallography and diffraction*. Vol. 21. Oxford University Press, USA, 2015.

[40] Andrew R Barron. “Physical methods in chemistry and nano science”. In: (2015).

[41] H Stanjek and WJHI Häusler. “Basics of X-ray Diffraction”. In: *Hyperfine interactions* 154.1 (2004), pp. 107–119.

[42] Rosa Chierchia. “Strain and crystalline defects in epitaxial GaN layers studied by high-resolution X-ray diffraction”. PhD thesis. Universität Bremen, 2007.

[43] Neil W Ashcroft, N David Mermin, et al. *Solid state physics*. Vol. 2005. holt, rinehart and winston, new york London, 1976.

[44] *Ewald sphere | Glossary | JEOL Ltd.* URL: https://www.jeol.com/words/emterms/20121023.010900.php#gsc.tab=0.

[45] Mauro Gemmi and Arianna E Lanza. “3D electron diffraction techniques”. In: *Acta Crystallographica Section B: Structural Science, Crystal Engineering and Materials* 75.4 (2019), pp. 495–504.

[46] U Kolb et al. “Towards automated diffraction tomography: Part I—Data acquisition”. In: *Ultramicroscopy* 107.6-7 (2007), pp. 507–513.

[47] Mauro Gemmi et al. “Fast electron diffraction tomography”. In: *Journal of Applied Crystallography* 48.3 (2015), pp. 718–727.

[48] Igor Nederlof et al. “A Medipix quantum area detector allows rotation electron diffraction data collection from submicrometre three-dimensional protein crystals”. In: *Acta Crystallographica Section D: Biological Crystallography* 69.7 (2013), pp. 1223–1230.

[49] Brent L Nannenga et al. “High-resolution structure determination by continuous-rotation data collection in MicroED”. In: *Nature methods* 11.9 (2014), pp. 927–930.

[50] R Vincent and PA Midgley. “Double conical beam-rocking system for measurement of integrated electron diffraction intensities”. In: *Ultramicroscopy* 53.3 (1994), pp. 271–282.

[51] E Mugnaioli, T Gorelik, and U Kolb. ““Ab initio” structure solution from electron diffraction data obtained by a combination of automated diffraction tomography and precession technique”. In: *Ultramicroscopy* 109.6 (2009), pp. 758–765.

[52] Dipanwita Chatterjee et al. “Nucleation of Metal Nanoparticles on Amorphous Substrate: Insights into Orientation Preference and Heterogeneous Catalysis”. In: *Microscopy and Microanalysis* 23.S1 (2017), pp. 2038–2039.

[53] U Kolb and E Mugnaioli. “Complementarities between precession electron and X-ray powder diffraction”. In: *European Powder Diffraction Conference; August 2010, Darmstadt, Germany*. OLDENBOURG WISSENSCHAFTSVERLAG. 2011, pp. 1–14.

[54] S Plana-Ruiz et al. “Quasi-parallel precession diffraction: Alignment method for scanning transmission electron microscopes”. In: *Ultramicroscopy* 193 (2018), pp. 39–51.

[55] Lukáš Palatinus et al. “Specifics of the data processing of precession electron diffraction tomography data and their implementation in the program PETS2. 0”. In: *Acta Crystallographica Section B: Structural Science, Crystal Engineering and Materials* 75.4 (2019), pp. 512–522.

[56] Ute Kolb, Yaşar Krysiak, and Sergi Plana-Ruiz. "Automated electron diffraction tomography–development and applications". In: *Acta Crystallographica Section B: Structural Science, Crystal Engineering and Materials* 75.4 (2019), pp. 463–474.

[57] Wolfgang Kabsch. "xds". In: *Acta Crystallographica Section D: Biological Crystallography* 66.2 (2010), pp. 125–132.

[58] *PETS2 webpage*. URL: http://pets.fzu.cz/.

[59] Petr Brázda et al. "Accurate lattice parameters from 3D electron diffraction data. I. Optical distortions". In: *IUCrJ* 9.6 (2022).

[60] Václav Petříček et al. "Jana2020–a new version of the crystallographic computing system Jana". In: *Zeitschrift für Kristallographie-Crystalline Materials* 0 (2023).

[61] Lukáš Palatinus. "The charge-flipping algorithm in crystallography". In: *Acta Crystallographica Section B: Structural Science, Crystal Engineering and Materials* 69.1 (2013), pp. 1–16.

[62] Maria Cristina Burla et al. "Crystal structure determination and refinement via SIR2014". In: *Journal of Applied Crystallography* 48.1 (2015), pp. 306–309.

[63] Christian B Hübschle, George M Sheldrick, and Birger Dittrich. "ShelXle: a Qt graphical user interface for SHELXL". In: *Journal of applied crystallography* 44.6 (2011), pp. 1281–1284.

[64] Ian J Bruno et al. "New software for searching the Cambridge Structural Database and visualizing crystal structures". In: *Acta Crystallographica Section B: Structural Science* 58.3 (2002), pp. 389–397.

[65] Koichi Momma and Fujio Izumi. "VESTA: a three-dimensional visualization system for electronic and structural analysis". In: *Journal of Applied crystallography* 41.3 (2008), pp. 653–658.

[66] Lukáš Palatinus, Václav Petříček, and C Antunes Corrêa. "Structure refinement using precession electron diffraction tomography and dynamical diffraction: theory and implementation". In: *Acta Crystallographica Section A: Foundations and Advances* 71.2 (2015), pp. 235–244.

[67] JG Allpress et al. "n-beam lattice images. I. Experimental and computed images from W4Nb26O77". In: *Acta Crystallographica Section A: Crystal Physics, Diffraction, Theoretical and General Crystallography* 28.6 (1972), pp. 528–536.

[68] Lukas Palatinus et al. "Structure refinement from precession electron diffraction data". In: *Acta Crystallographica Section A: Foundations of Crystallography* 69.2 (2013), pp. 171–188.

[69] Lukáš Palatinus et al. "Structure refinement using precession electron diffraction tomography and dynamical diffraction: tests on experimental data". In: *Acta Crystallographica Section B: Structural Science, Crystal Engineering and Materials* 71.6 (2015), pp. 740–751.

[70] Gwladys Steciuk. "Application de la précession des électrons en mode tomographie à l'étude de phases apériodiques et de films minces d'oxydes." PhD thesis. Université Caen Normandie, 2016.

[71] Lukáš Palatinus, Václav Petříček, and C Antunes Corrêa. "Structure refinement using precession electron diffraction tomography and dynamical diffraction: theory and implementation". In: *Acta Crystallographica Section A: Foundations and Advances* 71.2 (2015), pp. 235–244.

[72] Mauro Gemmi et al. "3D electron diffraction: the nanocrystallography revolution". In: *ACS central science* 5.8 (2019), pp. 1315–1329.

[73] Enrico Mugnaioli and Mauro Gemmi. "Single-crystal analysis of nanodomains by electron diffraction tomography: mineralogy at the order-disorder borderline". In: *Zeitschrift für Kristallographie-Crystalline Materials* 233.3-4 (2018), pp. 163–178.

[74] Stavros Nicolopoulos et al. “Novel TEM microscopy and electron diffraction techniques to characterize cultural heritage materials: from ancient greek artefacts to maya mural paintings”. In: *Scanning* 2019.1 (2019), p. 4870695.

[75] Philipp Gollé-Leidreiter et al. “Crystal structure determination of a new LaPO4 phase in a multicomponent glass ceramic via 3D electron diffraction”. In: *Ceramics International* 48.3 (2022), pp. 3790–3799.

[76] Mojca Otonicar, Sreco D Skapin, and Bostjan Jancar. “Tem analyses of the local crystal and domain structures in $(Na_{1-x}K_x)_{0.5}Bi_{0.5}TiO_3$ perovskite ceramics”. In: *IEEE transactions on ultrasonics, ferroelectrics, and frequency control* 58.9 (2011), pp. 1928–1938.

[77] Hugues Leroux et al. “Phyllosilicates with embedded Fe-based nanophases in Ryugu and Orgueil”. In: *Meteoritics & Planetary Science* (2023).

[78] V Pavan Kumar et al. “Engineering Transport Properties in Interconnected Enargite-Stannite Type $Cu_{2+x}Mn_{1-x}GeS_4$ Nanocomposites”. In: *Angewandte Chemie* 134.49 (2022), e202210600.

[79] Mihaly Posfai and Margareta Sundberg. “Stacking disorder and polytypism in enargite and luzonite”. In: *American Mineralogist* 83.3-4 (1998), pp. 365–372.

[80] Montse Casas-Cabanas et al. “FAULTS: a program for refinement of structures with extended defects”. In: *Journal of Applied Crystallography* 49.6 (2016), pp. 2259–2269.

[81] Yosuke Goto et al. “Enhanced Thermoelectric Figure of Merit in Stannite–Kuramite Solid Solutions $Cu_{2+x}Fe_{1-x}SnS_{4-y}$ (x= 0-1) with Anisotropy Lowering”. In: *Inorganic Chemistry* 52.17 (2013), pp. 9861–9866.

[82] Christophe P Heinrich et al. “Tetragonal tungsten bronzes $Nb_{8-x}W_{9+x}O_{47-\delta}$: optimization strategies and transport properties of a new n-type thermoelectric oxide”. In: *Materials Horizons* 2.5 (2015), pp. 519–527.

[83] V Pavan Kumar et al. "A new wide band gap thermoelectric quaternary selenide $Cu_2MgSnSe_4$". In: *Journal of Applied Physics* 118.15 (2015).

[84] Ventrapati Pavan Kumar et al. "Copper Hyper-Stoichiometry: The Key for the Optimization of Thermoelectric Properties in Stannoidite $Cu_{8+x}Fe_{3-x}Sn_2S_{12}$". In: *The Journal of Physical Chemistry C* 121.30 (2017), pp. 16454–16461.

[85] Piu Rajak et al. "Evidence of Mn-ion structural displacements correlated with oxygen vacancies in La0. 7Sr0. 3MnO3 interfacial dead layers". In: *ACS Applied Materials & Interfaces* 13.46 (2021), pp. 55666–55675.

[86] P Boullay et al. "Structure determination of a brownmillerite $Ca_2Co_2O_5$ thin film by precession electron diffraction". In: *Physical Review B* 79.18 (2009), p. 184108.

[87] Wenrui Zhang et al. "Two-dimensional layered oxide structures tailored by self-assembled layer stacking via interfacial strain". In: *ACS Applied Materials & Interfaces* 8.26 (2016), pp. 16845–16851.

[88] Leigang Li et al. "Novel layered supercell structure from Bi2AlMnO6 for multifunctionalities". In: *Nano letters* 17.11 (2017), pp. 6575–6582.

[89] Leigang Li et al. "Self-assembled two-dimensional layered oxide supercells with modulated layer stacking and tunable physical properties". In: *Materials Today Nano* 6 (2019), p. 100037.

[90] M Veis et al. "Band structure of CuMnAs probed by optical and photoemission spectroscopy". In: *Physical Review B* 97.12 (2018), p. 125109.

[91] S Plana-Ruiz et al. "Fast-ADT: A fast and automated electron diffraction tomography setup for structure determination and refinement". In: *Ultramicroscopy* 211 (2020), p. 112951.

[92] Dirk Van Der Wal. "Scanning Transmission Electron Microscopy Done Right". In: *Microscopy Today* 31.2 (2023), pp. 15–17.

[93] Erica Cordero Oyonarte. “3D electron diffraction of nanoparticles”. PhD thesis. Université de Caen Normandie, 2024.

[94] Alexander S Eggeman, Robert Krakow, and Paul A Midgley. “Scanning precession electron tomography for three-dimensional nanoscale orientation imaging and crystallographic analysis”. In: *Nature communications* 6.1 (2015), p. 7267.

[95] Guido Van Rossum and Fred L. Drake. *Python 3 Reference Manual*. Scotts Valley, CA: CreateSpace, 2009. ISBN: 1441412697.

[96] Daniel Lee and H Sebastian Seung. “Algorithms for non-negative matrix factorization”. In: *Advances in neural information processing systems* 13 (2000).

[97] Francisco De La Peña et al. “hyperspy/hyperspy: HyperSpy 1.3”. In: *Zenodo* (2017).

[98] Benjamin H Savitzky et al. “py4DSTEM: A software package for four-dimensional scanning transmission electron microscopy data analysis”. In: *Microscopy and Microanalysis* 27.4 (2021), pp. 712–743.

[99] MJ Martinez-Lope et al. “Evolution of the crystal structure of RVO3 (R= La, Ce, Pr, Nd, Tb, Ho, Er, Tm, Yb, Lu, Y) perovskites from neutron powder diffraction data”. In: *Inorganic chemistry* 47.7 (2008), pp. 2634–2640.

[100] Sara Passuti et al. “Scanning precession electron tomography (SPET) for structural analysis of thin films along their thickness”. In: *Symmetry* 15.7 (2023), p. 1459.

[101] Deepak Kumar et al. “Strong magnetic anisotropy of epitaxial $PrVO_3$ thin films on $SrTiO_3$ substrates with different orientations”. In: *ACS applied materials & interfaces* 12.31 (2020), pp. 35606–35613.

[102] Anthony M Glazer. “The classification of tilted octahedra in perovskites”. In: *Acta Crystallographica Section B: Structural Crystallography and Crystal Chemistry* 28.11 (1972), pp. 3384–3392.

[103] PE Janolin et al. “Strain engineering of perovskite thin films using a single substrate”. In: *Journal of Physics: Condensed Matter* 26.29 (2014), p. 292201.

[104] Martin Schmidbauer, Albert Kwasniewski, and Jutta Schwarzkopf. “High-precision absolute lattice parameter determination of SrTiO3, DyScO3 and NdGaO3 single crystals”. In: *Acta Crystallographica Section B: Structural Science* 68.1 (2012), pp. 8–14.

[105] Georg Kresse and Jürgen Hafner. “Ab initio molecular dynamics for liquid metals”. In: *Physical review B* 47.1 (1993), p. 558.

[106] Jianwei Sun, Adrienn Ruzsinszky, and John P Perdew. “Strongly constrained and appropriately normed semilocal density functional”. In: *Physical review letters* 115.3 (2015), p. 036402.

[107] MH Sage et al. “Competing orbital ordering in RVO_3 compounds: High-resolution x-ray diffraction and thermal expansion”. In: *Physical Review B* 76.19 (2007), p. 195102.

[108] Marie-Hélène Sage. “Orbital, charge and magnetic order of RVO_3 perovskites”. In: (2006).

[109] P Bordet et al. “Structural aspects of the crystallographic-magnetic transition in $LaVO_3$ around 140 K”. In: *Journal of solid state chemistry* 106.2 (1993), pp. 253–270.

[110] Magnus Nord et al. “Atomap: a new software tool for the automated analysis of atomic resolution images using two-dimensional Gaussian fitting”. In: *Advanced structural and chemical imaging* 3 (2017), pp. 1–12.

[111] Daniel Żymełka et al. “Contactless monitoring of shrinkage and temperature distribution during hybrid microwave sintering”. In: *Advanced Engineering Materials* 13.9 (2011), pp. 901–905.

[112] Fei Zuo et al. “Investigation of the mechanism (s) controlling microwave sintering of α-alumina: Influence of the powder parameters on the grain growth, thermodynamics and densification kinetics”. In: *Journal of the European Ceramic Society* 35.3 (2015), pp. 959–970.

[113] Larry W Finger and Robert M Hazen. “Crystal structure and compression of ruby to 46 kbar”. In: *Journal of Applied Physics* 49.12 (1978), pp. 5823–5826.

[114] Haipeng Ji et al. “Ultrabroadband red luminescence of Mn^{4+} in $MgAl_2O_4$ peaking at 651 nm”. In: *Dalton Transactions* 49.17 (2020), pp. 5711–5721.

Electron Crystallography of nanodomains in functional materials

keywords: 3D ED, epitaxial thin films, ceramics, multidimensional data analysis, automatic data processing

Abstract: The investigation of functional materials has increasingly focused on samples characterized by nanodomains (ranging from submicron sizes to tens of nanometers) due to their interesting physical properties, such as those observed in thin films and ceramic materials. When unknown phases need to be determined or detailed information on the crystalline structure of these materials is required, this presents challenges for both X-ray diffraction and transmission electron microscopy (TEM). To address this, a novel electron diffraction (ED) technique, Scanning Precession Electron Tomography (SPET), has been employed. SPET combines the established precession-assisted 3D ED data acquisition method (a.k.a. Precession Electron Diffraction Tomography – PEDT) with a scan of the electron beam on a region of interest (ROI) of the specimen at each tilt step. This procedure allows to collect 3D ED data from multiple ROIs with a single acquisition, facilitating structure solution and accurate structure refinements of multiple nanodomains or distinct areas within a single domain, at once. In this thesis, the potentialities of SPET are explored on both oxide thin films and ceramic thermoelectric materials prepared as TEM lamellae. Additionally, a novel methodology was developed to efficiently analyze the large amount of data collected. This method involves sorting the diffraction patterns according to their region of origin, reconstructing the diffraction tilt series of the ROI, and automatically processing the obtained tilt series for structure solution and accurate refinements. This work demonstrates the potential of SPET for the fine crystallographic characterization of complex nanostructured materials. This approach appears to be complementary to what can be done in imaging or spectroscopy by (S)TEM or, in diffraction, by the so-called 4D-STEM and ACOM approaches.

mots-clés: 3D ED, films minces épitaxiales, céramiques, analyse de données multidimensionnelles, traitement automatique des données

Résumé: L'étude des matériaux fonctionnels se concentre de plus en plus sur des échantillons caractérisés par des nano-domaines (allant de tailles submicroniques à des dizaines de nanomètres) en raison de leurs propriétés physiques intéressantes, telles que celles observées dans les films minces ou les matériaux céramiques. Lorsqu'il faut déterminer des phases inconnues ou obtenir des informations détaillées sur la structure cristalline de ces matériaux, la diffraction des rayons X et la microscopie électronique à transmission (MET) se heurtent à des difficultés. Pour résoudre ce problème, une nouvelle technique de diffraction électronique (ED), dite « Scanning Precession Electron Tomography » (SPET), a été employée. La SPET combine la méthode établie d'acquisition de données 3D ED assistée par la précession (également connue sous l'acronyme PEDT) avec un balayage du faisceau d'électrons sur une région d'intérêt (ROI) de l'échantillon et ce à chaque angle d'inclinaison du porte objet. Cette procédure permet de collecter des données 3D ED à partir de plusieurs ROIs en une seule acquisition, ce qui facilite la résolution et l'affinement précis de la structure cristalline de plusieurs nano-domaines ou de zones distinctes à l'intérieur d'un seul domaine. Dans cette thèse, les potentialités de la SPET sont explorées à la fois sur des films minces d'oxyde et sur des matériaux thermoélectriques (céramiques) préparés sous forme de lamelles TEM. En outre, une nouvelle méthodologie a été développée pour analyser efficacement la grande quantité de données collectées. Cette méthode consiste à trier les diagrammes de diffraction en fonction de leur région d'origine, à reconstruire la série 3D ED selon les différentes ROIs et à traiter automatiquement ces données pour la résolution et l'obtention d'affinements précis de la structure. Ce travail démontre le potentiel de la SPET pour la caractérisation cristallographique fine de matériaux nano-structurés complexes. Cette approche est complémentaire de ce qui peut être fait en imagerie ou en spectroscopie par (S)TEM ou, en diffraction, par les approches dites 4D-STEM et ACOM.